

The University of Sheffield



Investigation of High-Speed Permanent Magnet Motors with Toroidal Windings

Fan Xu

A thesis submitted for the degree of Doctor of Philosophy

Department of Electronic and Electrical Engineering

The University of Sheffield

Mappin Street, Sheffield, S1 3JD, UK

April 2022

ABSTRACT

This thesis investigates the electromagnetic performance of low-power and small-size toroidally wound 2-pole high-speed permanent magnet (HSPM) motors.

The influence of various design parameters, such as stator slot number, split ratio, slot ratio, and stator iron flux density, has been investigated. It is found that 6-slot/2-pole HSPM motor with toroidal windings is eminently suitable for high-speed applications due to no UMF and low rotor eddy current loss. The analytical predictions show that when the slot ratio, i.e. the ratio of the inner slot area to total slot area, is 0.5, the maximum torque can be achieved, and the optimal split ratio increases with the decrease of slot ratio, as confirmed by the finite element (FE) analyses.

Considering modular design for auto-manufacturing, the influence of stator gap and misalignment on the electromagnetic performance is investigated. It shows that the stator gap results in unbalanced three phase back-EMFs, not only amplitudes, but also phase angles. The stator gap increases the equivalent air-gap length and PM flux leakage, which lead to lower air-gap flux density, back-EMF, and average torque. Moreover, the stator gap results in asymmetric air-gap length, which results in large cogging torque. Further, it shows that the misalignment of two stator parts mainly affects the uneven equivalent air-gap length and symmetry of winding configuration, which lead to unbalanced three phase back-EMFs, especially phase angles, and self-/mutual-inductances, as well as rotor PM loss. Experimental results of a prototype motor with/without stator gap and/or misalignment are given to validate the finite element predicted analyses.

The electromagnetic performance between 2-pole slotted and slotless HSPM motors with toroidal and tooth-coil windings, together with the influence of the tooth-tip, has been compared. It is found that the slotless motor with 6-coil toroidal windings has advantages of low stator iron loss and rotor eddy current loss due to no slotting effect, but has significantly higher AC copper loss and lower output torque. In addition, considering the thermal limitation, compared to the motor with tooth-coil windings, toroidal windings have the advantage of relatively large torque due to smaller stator core volume and stator iron loss.

ACKNOWLEDGMENTS

First and foremost, I would like to express my special thanks of gratitude to my supervisor, Professor Z. Q. Zhu, for his invaluable guidance, continuous support, and encouragements during my PhD study, particularly for offering this opportunity to start a brand new life in Sheffield and not giving up on me when my health condition was terrible. His immense knowledge, impressive wisdom, and plentiful experience have encouraged me in all the time of my academic research and daily life.

I would like to thank all members of Electrical Machines and Drives Group for their support, especially Dr. Nathan Porter who shared his chocolate drawer with me. I would like to extend my sincere gratitude to Dr. Zhenping Xia for her attentive care and support, also Dr. Tianran He, Dr. Dawei Liang, Dr. Yu Wang, Dr. Yanxin Li, Mr. Ji Qi, Mr. Fangrui Wei, Mr. Zhitong Ran, and Ms Xinyi Wang for their inspired suggestions and generous help.

I would also like to thank Mr. Hong Bin, Dr. D. Wu, Dr. L. M. Gong, and Dr. J. T. Chen at Midea Welling Motor Technology (Shanghai) Co., Ltd., China, for their technical support.

Finally, I would like to express my thanks to my parents without their love and generous support in the past few years, it would be impossible for me to complete my study.

CONTENTS

ABSTRACT	I
ACKNOWLEDGMENTS	II
CONTENTS	III
NOMENCLATURE	VIII
CHAPTER 1 GENERAL INTRODUCTION	1
1.1 Introduction.....	1
1.2 Stator Topologies and Winding Configurations.....	2
1.2.1 Slotless stator structure	2
1.2.2 Slotted stator structure	9
1.2.3 Comparison	18
1.3 Rotor Topologies.....	19
1.3.1 Surface-mounted PM (SPM).....	20
1.3.2 Interior PM (IPM).....	25
1.3.3 Solid PM	29
1.3.4 PM material.....	30
1.4 Other Design Consideration.....	31
1.4.1 Stator iron loss	31
1.4.2 Copper loss (AC and DC).....	32
1.4.3 Rotor eddy current loss	33
1.4.4 Windage loss	34
1.4.5 Thermal and demagnetization.....	34
1.4.6 Rotor dynamics and vibration.....	35
1.4.7 Optimization method (Electromagnetic/ Multiphysics).....	35
1.5 Scope of Research and Contributions of the Thesis	36
CHAPTER 2 INFLUENCE OF SLOT NUMBER ON ELECTROMAGNETIC PERFORMANCE OF 2-POLE HIGH-SPEED PERMANENT MAGNET MOTORS	

WITH TOROIDAL WINDINGS.....	39
2.1 Introduction.....	39
2.2 Motor Topologies.....	41
2.3 Winding Configuration and Winding Factor.....	42
2.4 Optimal Design.....	44
2.5 Analysis of Electromagnetic Performance.....	48
2.5.1 Air-gap flux density.....	48
2.5.2 Open-circuit flux linkage.....	51
2.5.3 Back-EMF.....	55
2.5.4 Cogging torque and electromagnetic torque.....	56
2.5.5 Winding inductances.....	57
2.5.6 Loss analysis.....	58
2.5.7 Unbalanced magnetic force.....	60
2.6 Experimental Validation.....	61
2.7 Conclusion.....	65
CHAPTER 3 SPLIT RATIO OPTIMIZATION FOR 6-SLOT/2-POLE HIGH-SPEED PERMANENT MAGNET MOTOR WITH TOROIDAL WINDINGS.....	66
3.1 Introduction.....	66
3.2 Motor Topology.....	68
3.3 Design and Optimization.....	70
3.4 Influence of Design Parameters on Optimal Split Ratio.....	75
3.4.1 Influence of slot ratio.....	75
3.4.2 Influence of maximum stator iron flux density.....	78
3.4.3 Influence of tooth-tips.....	80
3.5 Experimental Validation.....	83
3.6 Conclusion.....	87
CHAPTER 4 INFLUENCE OF STATOR GAP ON ELECTROMAGNETIC PERFORMANCE OF 6-SLOT/2-POLE MODULAR PERMANENT MAGNET	

MOTOR WITH TOROIDAL WINDINGS	88
4.1 Introduction.....	88
4.2 Topologies of HSPM Motors with Toroidal Windings	90
4.2.1 Winding factor	91
4.2.2 End-winding.....	91
4.3 Electromagnetic Performance without Stator Gap	92
4.4 Electromagnetic Performance with Stator Gap.....	97
4.4.1 Air-gap flux density	98
4.4.2 Flux linkage	99
4.4.3 Back-EMF.....	101
4.4.4 Cogging torque.....	103
4.4.5 On-load torque	104
4.4.6 Inductance	106
4.4.7 Losses.....	107
4.5 Electromagnetic Performance with Misaligned Stator Structure.....	118
4.5.1 Air-gap flux density	118
4.5.2 Flux linkage	120
4.5.3 Back-EMF.....	122
4.5.4 Cogging torque.....	124
4.5.5 Electromagnetic torque	125
4.5.6 Inductance	126
4.5.7 Loss	127
4.6 Influence of Both Gap and Misalignment.....	128
4.6.1 Air-gap flux density	128
4.6.2 Flux linkage	130
4.6.3 Back-EMF.....	131
4.6.4 Cogging torque.....	132

4.6.5 Electromagnetic torque	133
4.6.6 Inductance	134
4.6.7 Losses.....	134
4.7 Influence of Tooth Tip.....	135
4.8 Experimental Validation.....	141
4.8.1 Back-EMF	142
4.8.2 Phase resistance and winding inductance	145
4.8.3 Static torque	146
4.9. Conclusion	149
CHAPTER 5 COMPARISON OF 2-POLE HIGH-SPEED PERMANENT MAGNET MOTOR WITH DIFFERENT STATOR STRUCTURES AND WINDING CONFIGURATIONS.....	150
5.1 Introduction.....	150
5.2 Comparison of Slotted and Slotless Motors with Toroidal Windings.....	152
5.2.1 Toroidal winding motor topologies.....	152
5.2.2 Optimal designs	153
5.2.3 Electromagnetic performance	158
5.3 Comparison of Slotted Motor with Toroidal and Tooth-coil Windings	168
5.3.1 Motor topologies.....	168
5.3.2 Optimal designs	169
5.3.3 Electromagnetic performances.....	173
5.4 Conclusion	180
CHAPTER 6 GENERAL CONCLUSION AND FUTURE WORK	182
6.1 Motor Design and Comparison.....	183
6.2 Manufacturing Tolerances.....	186
6.3 Future Work	187
REFERENCES.....	189
APPENDIX I PUBLICATION RESULTED FROM PHD STUDY	212

NOMENCLATURE

Symbol

A_{cond}	Cross section area of conductors	m^2
A_{fe}	Stator iron cross-section area	m^2
A_g	Air-gap area	m^2
A_m	Permanent magnet cross section area	m^2
A_{sin}	Inner slot area	m^2
B_{fe}	Maximum stator iron flux density	T
B_g	Maximum air-gap flux density	T
B_r	Remanence	T
D_g	Diameter of middle of equivalent air-gap	m
D_i	Stator inner diameter	m
D_o	Stator outer diameter	m
F_{PM}	Magneto-motive force of PM	A
f	Fundamental frequency	Hz
h	Overall heat transfer coefficient	$W/(m^2k)$
h_{in}	Inner tooth height	m
h_o	Outer winding height	m
h_{out}	Outer tooth height	m
h_{sy}	Stator yoke height	m
h_{tt}	Tooth-tip height	m
I_a	Amplitude of phase current	A
J_s	Current density	A/m^2
k	Harmonic index	
K_a	Slot ratio	
K_d	Distribution factor	
k_{ec}	Excess loss coefficient	W/m^2
k_{ex}	Eddy current loss coefficient	W/m^2
k_{hy}	Hysteresis loss coefficient	W/m^2
K_p	Pitch factor	
k_{tw}	Ratio of stator tooth width to stator yoke height	
K_w	Winding factor	

l_a	Stator active length	m
l_e	Total end-winding length	m
l_{er}	Radial end-winding length	m
l_{ex}	Extra part of end-winding length	m
l_g	Air-gap length	m
m	Misaligned distance	m
m_{fe}	Stator iron mass	Kg/m ³
N_s	Number of series turns per phase	
N_{slot}	Stator slot number	
P_0	DC component of permeance	H
P_{cu}	DC copper loss	W
P_{fe}	Stator iron loss	W
P_{kNslot}	Amplitude of Fourier coefficient for k_{Nslot} th harmonic	H
P_{limit}	Stator thermal limitation	W
P_{stator}	Maximum allowed stator loss	W
q	The number of slots per pole per phase	
R_i	Stator inner radius	m
R_m	Rotor outer radius	m
R_{shaft}	Shaft radius	m
T_{em}	Electromagnetic torque	Nm
U_{dc}	Terminal voltage	V
v	Harmonic order	
v_m	Maximum allowed temperature	°C
W_{fe}	Iron loss density	W/kg
w_{it}	Inner tooth width	m
w_t	Stator tooth width	m
δ	Skin depth	m
θ	Air-gap circumferential angular position	Mech. Deg.
θ_0	Phase difference	Mech. Deg.
λ	Split ratio	
μ_c	Permeability of the conductor	H/m
μ_r	Relative recoil permeability	H/m
ρ_{cu}	Resistivity of copper	Ω/m

ρ_{fe}

Iron mass density

Kg/m³

Acronym

3s/2p	3-slot/2-pole
6s/2p	6-slot/2-pole
6s/4p	6-slot/4-pole
AC	Alternating current
Back-EMF	Back electromotive force
BLDC	Brushless direct current
CFD	Computational fluid dynamics
EAT	Electrically assisted turbocharger
FE	Finite element
FEA	Finite element analysis
FRPM	Flux reversal permanent magnet
HSPM	High-speed permanent magnet
IM	Induction machines
IPM	Interior permanent magnet
LPTN	Lumped-parameter thermal network
MMF	Magneto-motive force
PM	Permanent magnet
PMM	Permanent magnet machines
SFPM	Switched flux permanent magnet
SPM	Surface-mounted permanent magnet
SR	Split ratio
SRM	Switched reluctance machines
TC	Tooth-coil windings
TO	Toroidal windings
TT	Tooth-tip
TWHSPM	HSPM motor with toroidal windings
UMF	Unbalanced magnetic force
VPM	Vernier permanent magnet

CHAPTER 1

GENERAL INTRODUCTION

1.1 Introduction

High-speed electrical machines have been developed for decades to meet requirements for various applications, for example, hand tools, compressors, vacuum cleaners, automotive superchargers, and micro gas turbines etc., due to their advantages of high efficiency and high power density [HES87] [ZHU97] [ZWY05] [NOG05] [GER14] [HON18] [SHE18] [HE21a].

The definition of high-speed electrical machine is related to not only the speed but also the power level due to the mechanical issue [GER14] [LIS16] [SHE18]. [GER14] ranks the high-speed induction machines and permanent magnet machines by the peripheral speed, but for high-speed switched reluctance machines, $n_r\sqrt{kW}$ (n_r is the rotor speed) has been used to define the high-speed. [LIS16] uses rotor tip-speed to define the high-speed electrical machines, based on the relationship between the rotor critical speed and the rotor outer diameter. The critical rotor tip-speed mostly depends on the sleeve material and its strength. [BIN06] shows that when using glass-fibre bandages, the critical rotor tip-speed should be less than 150m/s. When using carbon-fibre bandage, the critical speed can be higher than 200m/s. Therefore, a general definition of high-speed has not been made but the relationship between the machine power rating and high speed has been analysed in [SHE18].

There are different types of high-speed electrical machines, such as induction machines (IMs), switched reluctance machines (SRMs), and permanent magnet machines (PMMs). Among these machine types, PMMs are very popular due to high efficiency, high power density, and low vibration and noise. Therefore, high-speed permanent magnet (HSPM) machines will be researched in this thesis.

1.2 Stator Topologies and Winding Configurations

The stator topologies can be divided into slotted and slotless. The winding configurations for HSPM machines are categorised and introduced in this section. In literature, distributed, toroidal, concentrated, and skewed windings are employed in slotless structures. For convenience, two types of slotted stator topologies may be considered: the number of slots per pole per phase $q \geq 2$ (i.e. for a 2-pole machine, slot number ≥ 12) and the number of slots per pole per phase $q \leq 1$ (i.e. for a 2-pole machine, slot number ≤ 6). Stator structure with $q \geq 2$ is usually employed by large-size high-power HSPM machines with overlapping distributed and toroidal windings. HSPM machines with $q \leq 1$ usually employ concentrated and toroidal windings.

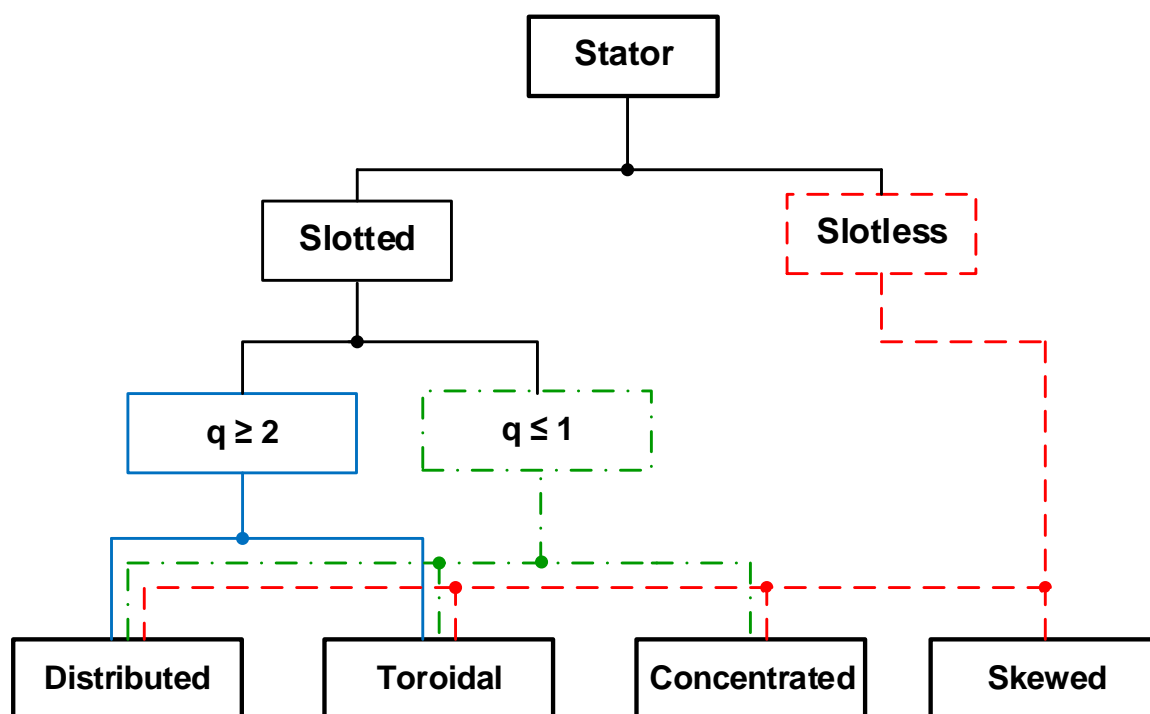


Fig. 1.1 Classification of stator topologies and winding configurations (q =the number of slots per pole per phase).

1.2.1 Slotless stator structure

For HSPM machines, both slotted and slotless stator topologies are widely used for different applications. Slotless stator structure is very popular in low-power small-size HSPM machines due to elimination of slotting effect and negligible cogging torque [CHE97]. In addition, without the slotting effect, the eddy current losses in rotor magnet and stator iron can be

reduced [ATA98] [CHE09]. However, the relatively large air-gap and flux leakage result in considerable small output torque.

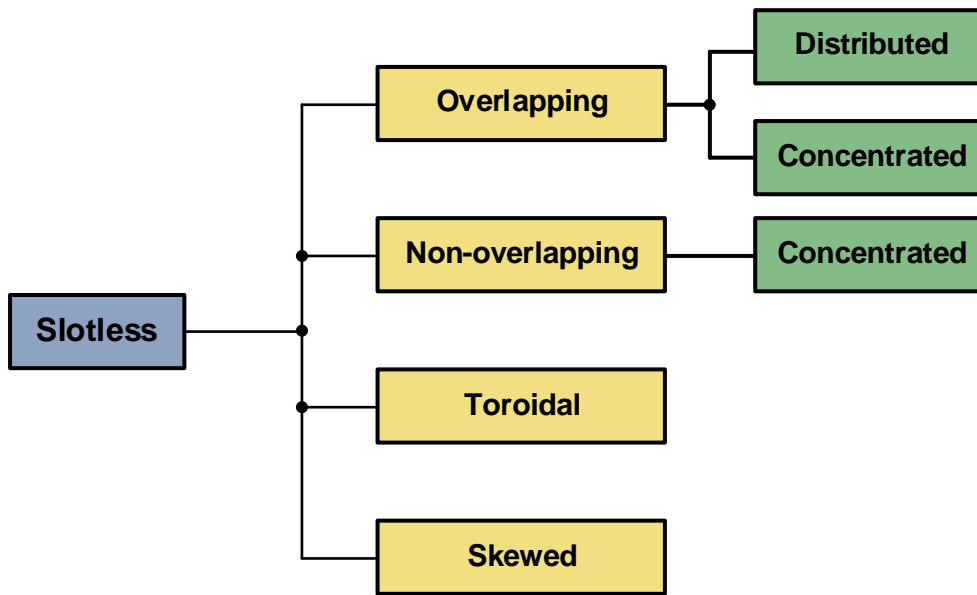


Fig. 1.2 Winding configurations of slotless stator structure.

In literature, slotless HSPM machines with different windings have been designed and analysed, including overlapping concentrated and distributed windings [BIA05] [BIA06] [CHE07] [CHE09] [CHE15] [LUO09] [PFI10] [WAL09] [YAN12] [WAN10b] [MIL16] [AHN17], non-overlapping concentrated windings [CHE98] [CHE99] [BUR19] [BUR20], toroidal windings [BOR14] [TUY15] [LEE17] [SCH17] [ISM18] [KOL13] [ZWY05] [JUM15] [GIL16] [GIL17] [SNE18], and slotless skew-type windings [ZHE05] [CHE97] [LOO10] [TUY17].

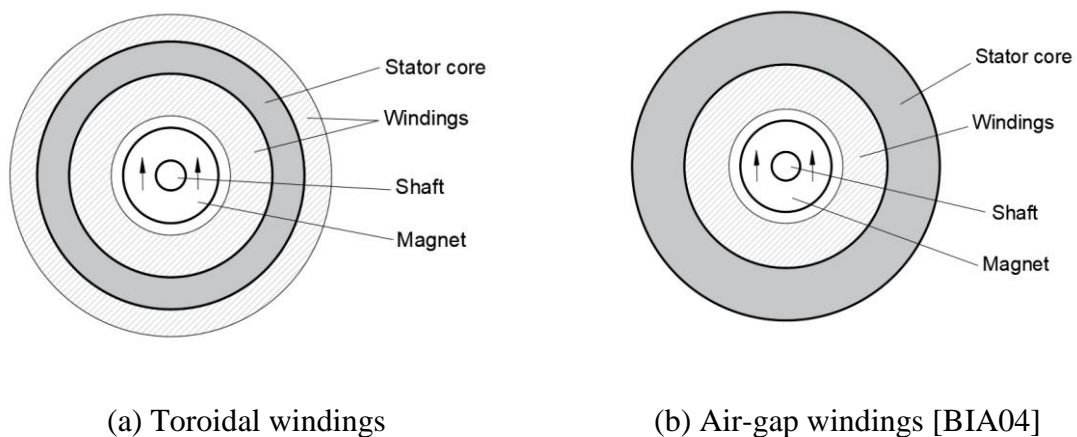
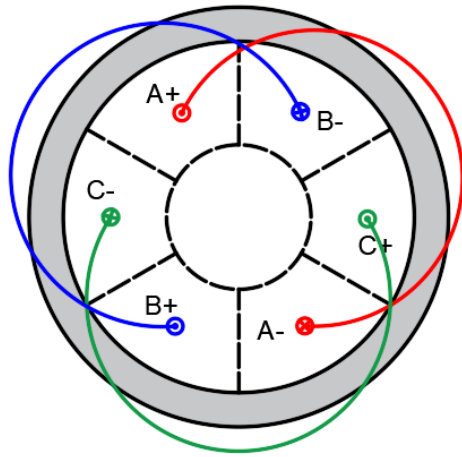


Fig. 1.3 HSPM machines with slotless structure.

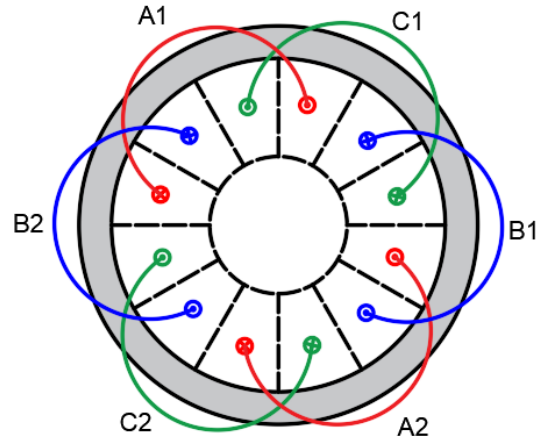
A. Overlapping concentrated and distributed windings

Overlapping concentrated and distributed windings are one of common winding configurations which have been widely employed in HSPM machines because of more sinusoidal electromotive force (EMF) waveform [ZHU08].

A comprehensive design and analysis of high-speed slotless machines with overlapping concentrated and distributed windings has been investigated in [BIA05] [BIA06]. The design consideration in terms of the input phase currents, the PM demagnetization, and the thermal limits, as well as typical control strategy and several methods for increasing the drive reliability are summarized. [CHE09] [CHE15] present analytical models of both PM and armature field distributions of a 500W, 20krpm, 2-pole, three phase slotless HSPM machine with overlapping distributed winding. In addition, the stator iron loss and conductor eddy current loss are calculated with improved accuracy. The iron loss measurement procedure for a 60 W, 40krpm, slotless HSPM motor with overlapping distributed winding has been proposed in [YAN12]. [WAL09] employs a simple end-winding model to calculate axial flux leakage of a 3-phase/2-pole HSPM motor with overlapping distributed windings for hand-tool applications. The experimental results indicate an approximately 2.5% reduction in back-EMF due to axial-leakage effects. The effect of shaft relative permeability on the rotor loss in a 2-pole slotless HSPM motor with overlapping distributed windings has been investigated by 3D model in [MIL16]. [PFI10] presents an analytical model including the magnetic field, the mechanical stress in the rotor, the electromagnetic power losses, the windage power losses, and the power losses in the bearings for a 2kW, 200krpm, HSPM motor. The windage loss has been taken into consideration in designing a 100 W, 500 krpm, 3-coil/2-pole HSPM motor with overlapping concentrated windings in [LUO09]. The analytical model has been employed to optimize the efficiency of this HSPM motor. [WAN10b] designs a 750W, 240krpm, 6-coil/2-pole three-phase slotless HSPM motor with soft magnetic ferrite stator core. This design verifies that although soft magnetic ferrite has low magnetic loading, the slotless structure can afford higher electrical loading to realize the high-speed operation. The rotor vibration, mechanical stress, and their correlation in an ultra-high-speed PM motor have been investigated and verified in [AHN17]. The 3-coil/2-pole slotless structure with overlapping concentrated windings has been adopted to eliminate the cogging torque.



(a) 3-coil [BIA05]

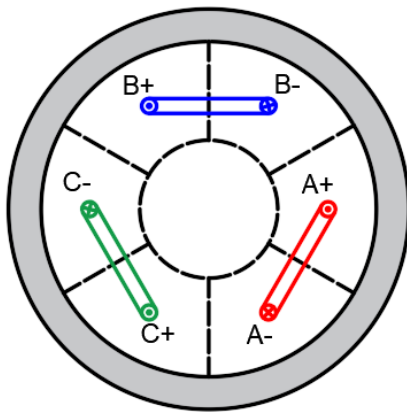


(b) 6-coil [WAN10b]

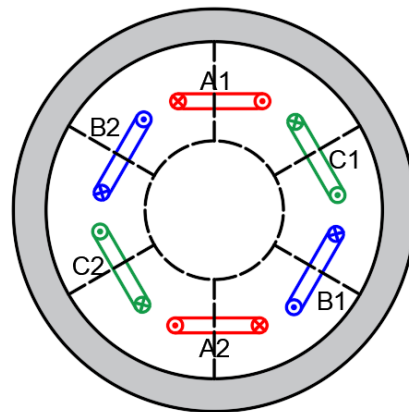
Fig. 1.4 Cross-section of 2-pole slotless HSPM machines with overlapping concentrated and distributed windings.

B. Non-overlapping concentrated windings

The slotless HSPM machines with non-overlapping concentrated windings have been designed and optimized in [CHE98] [CHE99] [BUR19] [BUR20]. The major advantage of this type of windings is that there is no issue of overlapping end windings.



(c) 3-coil [BUR19]



(d) 6-coil [BUR20]

Fig. 1.6 Cross-section of slotless HSPM machines with non-overlapping concentrated windings.

C. Toroidal windings

The slotless toroidal winding structure is usually investigated in small size, ultra-high-speed PM application [ZWY05] [BOR14] [TUY15] [LEE17] [KOL13] [GIL16] [GIL17] [JUM14] [JUM15] [SCH17] [ISM18] [SNE18]. Comprehensive designs including electromagnetic and mechanical consideration of a 6-coil/2-pole slotless HSPM motor with toroidal windings and solid PM rotor have been presented in [ZWY05] [SCH17] [ISM18]. [ZWY05] designs a 100W, 500krpm, HSPM motor for micro-gas turbines. [SCH17] designs a 1W, 160krpm, slotless HSPM motor with toroidal windings. [ISM18] designs a 2-pole slotless HSPM machine with toroidal windings, the rated power is 123W at 1200 krpm with 80% efficiency. A 160 krpm ultra-high-speed millimetre-scale slotless bearingless motor with toroidal windings has been designed in [SCH17], it shows the slotless structure is particularly well suited for high-speed low-power operation since the motor losses are below 1W and the temperatures in the hottest part of the motor are below 45 °C after operation. [KOL13] designs a 2-pole, 1kW, 70 krpm, slotless HSPM motor with toroidal windings by employing a stator core from the amorphous soft magnetic material. [JUM15] investigates the influence of the voltage harmonics resulting from PWM switching on rotor eddy current losses for a 6-coil/2-pole HSPM machine with toroidal windings by the analytical model. [BOR14] designs three 6-coil/2-pole slotless HSPM machines with toroidal windings for different applications, a 150W micro-milling spindle at 200 krpm, a 4.5 mNm air compressor at 30-90 krpm, and a 3.7 kW gas-turbine generator at 240 krpm. It is worth noting that the eddy current loss in the frame should be considered when employing the toroidal windings due to the external leakage of the armature field between the frame and outer windings. The frame eddy current loss remains unchanged when the frame thickness is bigger than its material skin depth at the operation speed. Therefore, the material and thickness of the frame are suggested to be selected carefully. [JUM14] compares the rotor eddy current losses in the slotless HSPM machines with concentrated, toroidal, and helical windings. It is worth noting that the direct contact between the windings and housing will benefit the reduction of operation temperature [JUM14]. For conventional motors, the housing must be in contact with or, at least, in close proximity to the stator core for good cooling of a machine [MLO15]. However, for slotless toroidal winding, if the housing is in contact with the external toroidal windings, the cooling properties of winding and stator core will be improved, although the induced losses of housing from neighbouring toroidal coils will be increased. If keeping air gap between the housing and the external toroidal windings, the induced losses of housing will be reduced, however, the cooling properties will be reduced due to the thermal

dissipation effect of air-cooling being less than that of housing heat transfer [DON14b]. Due to a rather short rotor and a very large gap between the magnet surface and stator inner surface in slotless HSPM machines with toroidal windings, it was anticipated that the flux leakage of the permanent magnet in the axial direction can have a significant influence on the motor performance [DON14a]. Furthermore, the effect of the external leakage of the armature field on the phase inductance was expected to be much higher than that calculated by the 2D FE model. The comparisons between slotless HSPM machines with toroidal windings and slotted HSPM machines with concentrated windings have been investigated in [GIL16] [GIL17]. The major difference is the slot. [GIL16] compares the efficiency and torque density of HSPM machines designed for electrically assisted turbocharger applications which required 15 kW at 150 krpm.

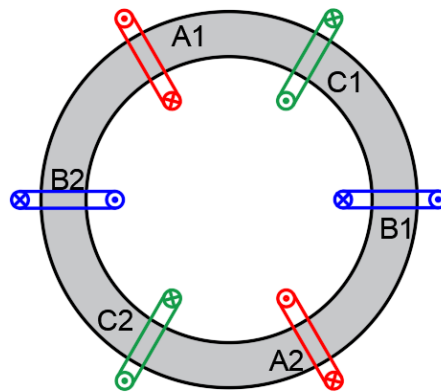


Fig. 1.5. Slotless toroidal winding structure [ZWY05].

D. Skewed windings

Slotless skewed structure is commercially used mainly in low-power HSPM machines for wide speed and torque ranges [CHE97] [JUM14] [LOO10] [ZHE05] [TUY17]. The primary advantage of this winding type is the reduction of manufacturing cost for miniature machines. Because the winding self-supporting construction allows manufacturing the winding separately from the iron core and placing it to the stator bore after it has been pre-formed. Moreover, helical winding can be adapted for multi-pole and single-/multi-phase requirements of either concentrated or distributed arrangements, as Fig. 1.7 shows. However, the major disadvantages of the helical windings are (a) the oblique current direction and torque which require design attention, and (b) the coils must be carefully assembled after the winding step is completed.

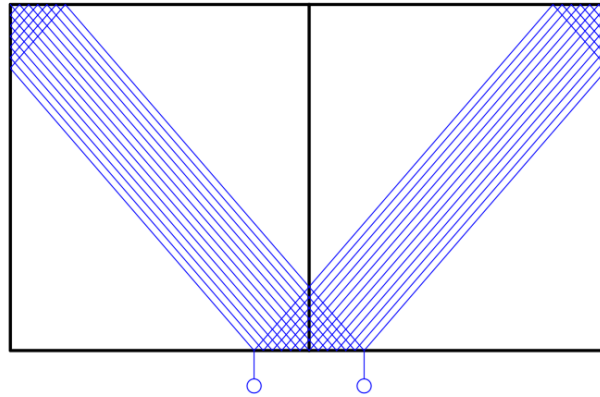


Fig. 1.7 One phase coil of helical slotless winding types [JUM14].

According to literature, considering 3-D winding model, the torque and force calculation methods of the helical windings have been analysed in [LOO10]. A phase inductance calculation method of the helical windings is thoroughly explained in [ARG10]. The rotor eddy current losses of toroidal, concentrated, and helical winding types are compared based on the different sleeve materials and thicknesses by [JUM14]. With the same power, the HSPM machine with concentrated windings has higher rotor eddy current losses than the HSPM machines with toroidal and skewed windings. In addition, the rotor eddy current losses in the HSPM machine with toroidal and skewed windings are nearly the same. The 3D models of three different shapes of slotless HSPM machines with skewed windings have been presented in [JUM16], as shown in Fig .1.8. [TUY15] and [TUY17] investigate a cooling method for slotless HSPM machine with skewed-type winding.

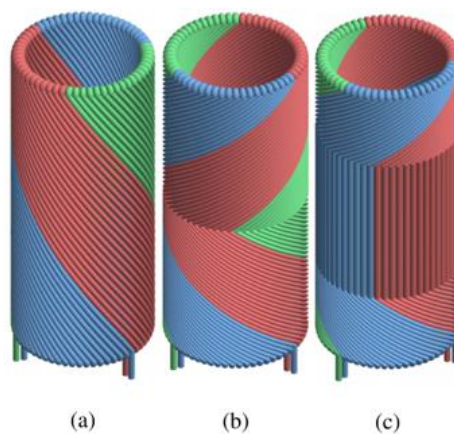


Fig. 1.8 3-D representation of a three-phase. (a) Faulhaber. (b) Rhombic. and (c) Diamond windings [JUM16].

1.2.2 Slotted stator structure

Slotted structure is a kind of conventional stator structure for HSPM machines and various slot/pole number combinations have been researched for different applications.

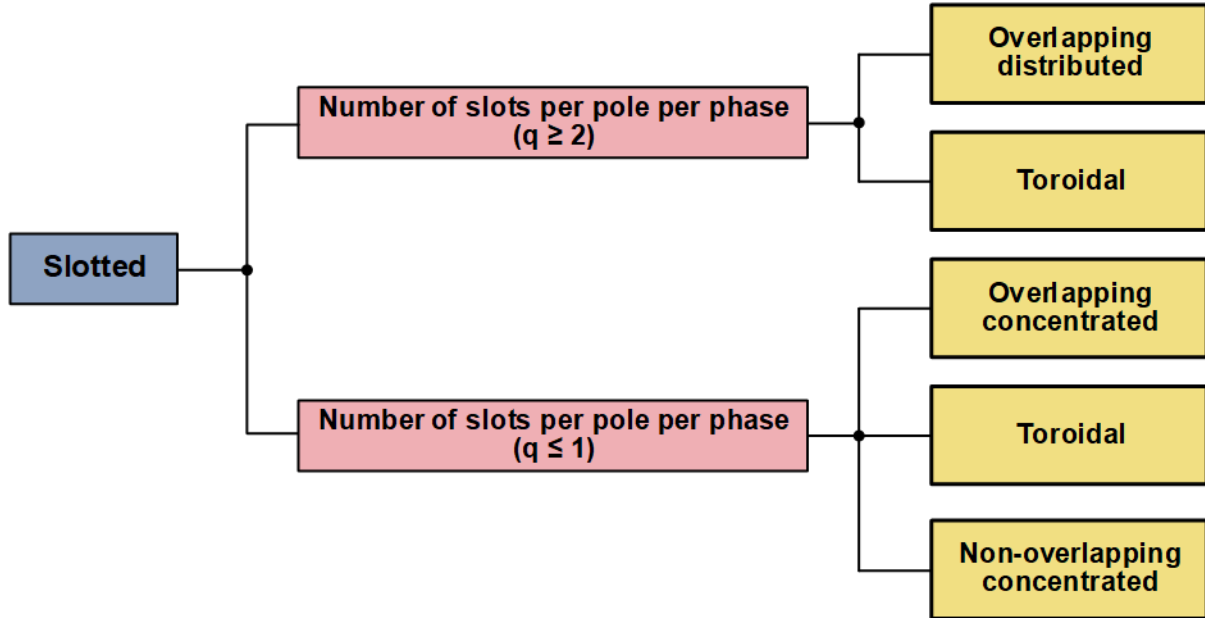


Fig. 1.9 Winding configurations of slotted HSPM machines.

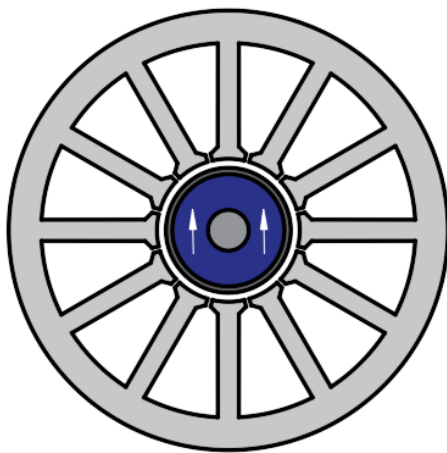
1) Number of slots per pole per phase $q \geq 2$

For large-size high-power HSPM machines, the large number of slots (Number of slots per pole per phase ≥ 2) has been employed such as for 2-pole HSPM machines, 12-slot [DON16a] [LIU18] [XU11] [SHE13] [ZHA21], 18-slot [FOD14] [DAM16] [ZHA15e] [BER16], 24-slot [CHE11] [WAN09] [XIN10] [DON14] [DON14a] [DON16c] [HUA16b] [HUY14] [FAN17] [LEE20], 27-slot [ZHA15a] [ZHA16a], 36-slot [HON97] [MUN10] [LIW14] [ZHA16c] [ZHA17a] [BEN18] [WAN20] and 48-slot [GAL15] [ZHA18b] [DUG20b]. The winding configurations employed by multi-slot HSPM machines are usually overlapping distributed and toroidal windings.

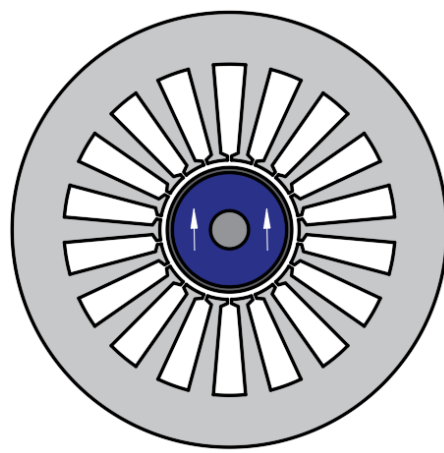
A. Overlapping distributed windings

For HSPM machines with slotted stator topologies, the overlapping distributed windings are usually employed in multi-slot (number of slots per pole per phase ≥ 2) large power HSPM machines in order to achieve the highest winding factor which is “1”, such as 12-slot [XUJ11] [SHE13], 18-slot [FOD14] [DAM16] [ZHA15e] [BER16] [FAN19], 24-slot [CHE19] [DON16c] [HUY15] [FAN17] [LEE20], 27-slot [ZHA15a] [ZHA16a], 36-slot [HON97]

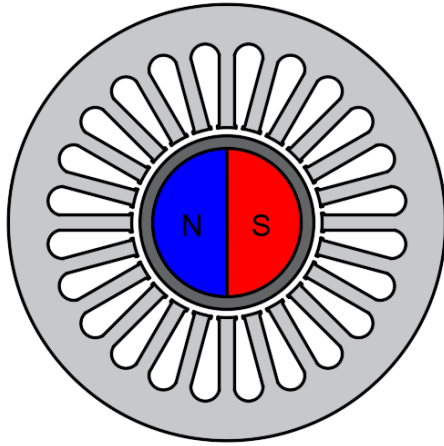
[MUN10] [ZHA15d] [ZHA17a] [BEN18] [MIR08], and 48-slot [GAL15] [ZHA18b] [DUG20]. The disadvantages of overlapping distributed windings are relatively long end-winding length and axial length, which reduce the rotor mechanical strength and critical speed. In [XU11], 500W, 100krpm, HSPM generators have been designed for miniature turbojet. [SHE13] investigates the rotor eddy current loss reduction with grooved sleeve for a 10 kW, 70krpm, 12s/2p HSPM machine with overlapping distributed windings. In [FOD14] [DAM16] [ZHA15e] [BER16], 18s/2p HSPM machines have been studied in terms of design methodology, rotor structure, mechanical stress, and cooling ability. The design methodology for a 25kW, 30 krpm, HSPM synchronous machines has been presented in [BER16]. [FOD14] compares different rotor topologies and PM magnetizations in three types of electrical machines for electric vehicle application. In [DAM16], the mechanical stress in the sleeve has been compared for different sleeve materials. In order to improve the cooling capability of HSPM generator, an optimization of the electromagnetic and thermal performances has been evaluated in [ZHA15e]. The 24s/2p HSPM machines with overlapping distributed windings have been designed by considering thermal and mechanical aspects in [HUY15] [JAN18] [LEE20], as well as 24s/4p HSPM machines with overlapping distributed windings in [DON16c] [FAN17] [CHE19]. For 36-slot HSPM machines with overlapping distributed windings, the researches mainly focus on the rotor design including the comparison of different rotor topologies, sleeve materials, PM segmentations, and influence of PM magnetization directions [HON97] [MUN10] [ZHA15d] [ZHA17a] [BEN18] [MIR08]. A comprehensive multi-physics and multi-objective optimization of 48s/4p HSPM machines have been analysed in [DUG20b].



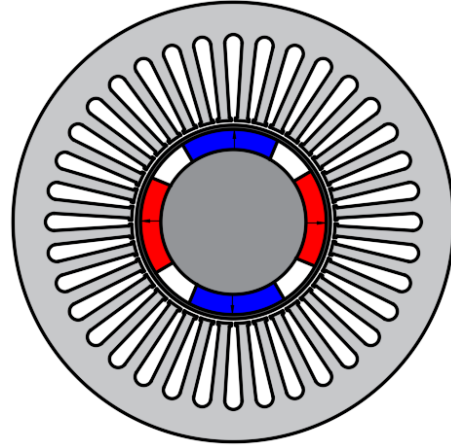
(a) 12s/2p [HON09]



(b) 18s/2p [BER16]



(c) 24s/2p [HUY15]



(d) 36s/4p [ZHA17a]

Fig. 1.10 Multi-slot HSPM machines with overlapping distributed windings.

Short-pitched overlapping distributed windings have been investigated for HSPM machines in [HON09] [JAN11b] [XUE12] [FAN19]. For large-power large-size HSPM machines, compared to full-pitched overlapping distributed windings, short-pitched windings have lower rotor eddy current loss, but have lower output torque due to smaller winding factor. In [FAN19], a solid PM rotor structure has been designed for an 18-slot 80 kW, 80 krpm, HSPM machine with short-pitched overlapping distributed windings for air blowers. [XUE12] designs a 24s/2p, 7.5kW, 20 rpm, HSPM motor with 4-coil pitch overlapping distributed windings which makes the stator winding factor 0.48. A multi-physics modelling for a multi-objective design of a 36s/6p HSPM synchronous machine with 5/6 short-pitched windings has been investigated in [JAN11b].

B. Toroidal windings

Toroidal windings, e.g. coils wound around stator core instead of stator teeth, are another kind of windings with short end-windings. This winding configuration can be employed for both slotless and slotted stator topologies. The slotted toroidal winding structure is widely adopted for multi-slot HSPM machines, such as 12-slot [ZHA21], 24-slot [WAN09] [XIN10] [CHE11] [DON14] [DON14a] [DON14b], 36-slot [LIW13] [LIW14] [ZHA16c] [WAN20], to shorten stator end-windings and reduce the rotor overall length for the better stiffness under high speed operation mode. In addition, the slotted toroidal winding structure has outside slots, which can increase the area for cooling if forced-air cooling is used [DON14a]. A 15kW, 120 krpm, 12-slot, slotted HSPM motor with toroidal windings has been designed and optimized by

considering winding friction loss for gas compressor applications in [ZHA21]. The results also show that the rotor with glass-fibre sleeve has better performance than the rotor with Inconel71 sleeve in terms of higher output torque and less rotor eddy current loss. Based on a 24s/2p HSPM machine with toroidal windings, the electromagnetic design, thermal analysis, and cooling method are widely researched in [WAN09] [XIN10] [CHE11] [DON14] [DON14a] [DON14b]. A 117kW, 60krpm, 36s/2p, HSPM generator used in micro turbine generation system has been investigated in terms of thermal optimization, sleeve materials, and stator structure, i.e. slotted and slotless [LIW13] [LIW14] [ZHA16c].

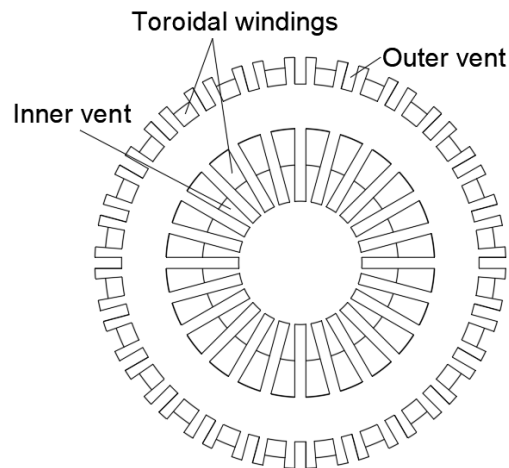


Fig. 1.11 Slotted toroidal winding structure [DON14].

2) Number of slots per pole per phase $q \leq 1$

For small-size low-power HSPM machines, the low number of slots (number of slots per pole per phase ≤ 1 and for a 2-pole machine, number of slots ≤ 6) is widely employed such as 6-slot [WAN03] [OYA03] [SHI04] [GIL15] [GIL16] [NOG05] [ZHO06] [NOG09] [WAN10a] [HON13] [KOL16] [UZH16] [IID20]; and 3-slot [HES87] [ZHU97] [EDE01] [ZHU01] [NOG05] [BIA04] [HWA14] [KRA17] [PAN14] [MAJ19] [MAJ17]. In general, the 2-pole and 4-pole are chosen to minimize the fundamental frequency and reduce the stator iron loss and converter loss.

A. Overlapping concentrated windings

Compared to large-size large-power HSPM machines with overlapping distributed windings, the small-size low-power HSPM machines often employ 6-slot stator topologies. In addition, the end-winding axial length is sensitive in small-size HSPM machines, and therefore, small-size low-power HSPM machines rarely employed overlapping distributed windings. However,

for small-size low-power HSPM machines, short-pitched windings can reduce not only the rotor loss but also the end-winding axial length. Therefore, the power density improvement based on the trade-off between winding factor and end-winding axial length has been researched in [HE21] [HE21a]. In [HE21a], the (6-slot/2-pole) 6s/2p HSPM motors with 1, 2, and 3 coil-pitch windings have been compared. It can be found that 2 coil-pitch windings can improve the torque and torque density. Two different 2 coil-pitch winding configurations have been proposed for high-speed applications in [HE21a].

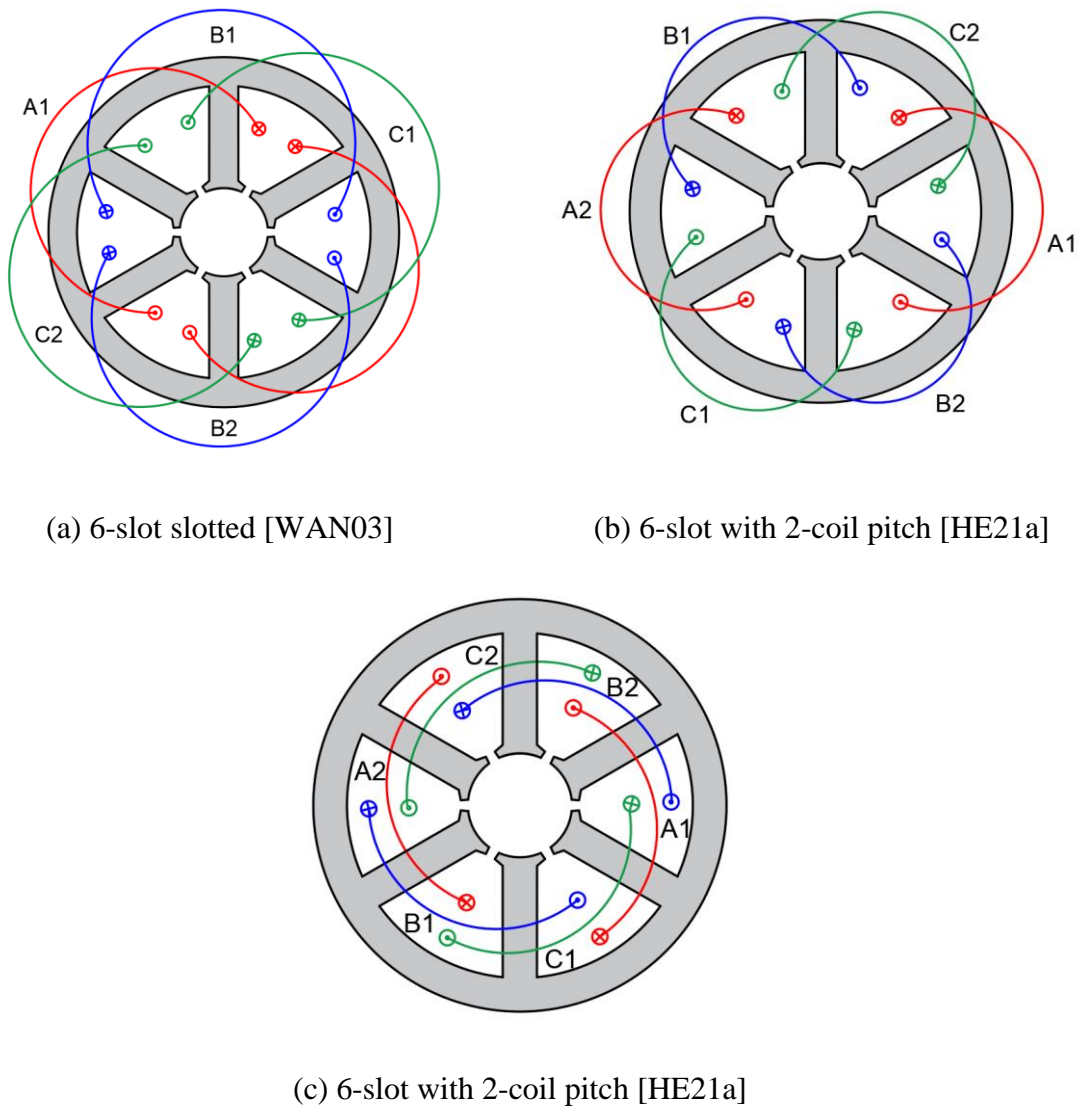


Fig. 1.12 6s/2p HSPM machines with overlapping concentrated and distributed windings.

B. Toroidal windings

An 800W, 60krpm, 2-pole, HSPM motor with 6 half-opened slot structure has been investigated to evaluate the soft magnetic core in [KOL16]. The experiment results show that this prototype has high operating efficiency and reached 90% over a wide range of torques. However, the slotted toroidal winding structure is rarely employed in HSPM machines with small number of slots, but will be researched in this thesis.

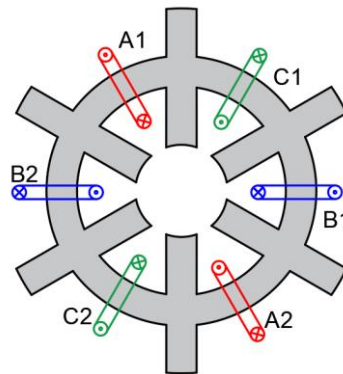


Fig. 1.13 6s/2p slotted HSPM motor with toroidal windings [XU21].

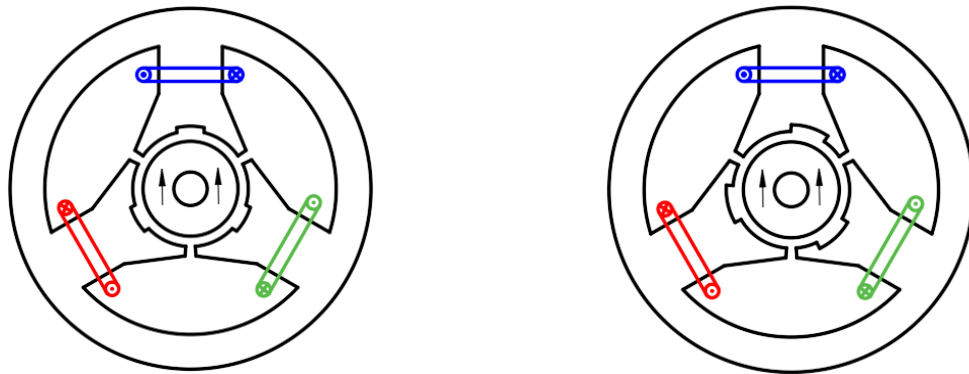
C. Non-overlapping concentrated windings

HSPM machines with non-overlapping concentrated windings have been investigated and developed for years due to short end-winding length and axial length. With a shorter rotor, the lowest flexible natural frequencies of the rotor will be higher. As a result, the machine can operate below the critical speed, enabling even higher operational speeds. In literature, 3-slot/2-pole (3s/2p) [HES87] [ZHU97] [ZHU01] [EDE01] [BIA04] [BIA05] [PAN14] [MA18] [MA19a], 6s/2p [OYA03] [SHI04] [LIM17] [ZHO06] [NOG05] [NOG09] [GII17] [GIL15] [UZH16] [JAS17] [WAN10a] and 6-slot/4-pole (6s/4p) [ZHA15h] [GIL17] [WAN18] [IID20] topologies are widely employed and investigated.

3s/2p HSPM machine with non-overlapping concentrated windings has the simplest rotor and stator topologies. A 10 W, 150 krpm, 3s/2p HSPM motor for a hand-tool application has been designed in [HES87]. In [ZHU97], the same structure has been employed for a friction welding unit which operates at 20 krpm and power of 1.3 kW. The stator iron loss also has been analysed under different stator iron flux densities and it shows that the stator iron loss should be considered in high-speed motor design. The optimization of 3s/2p HSPM motor by taking

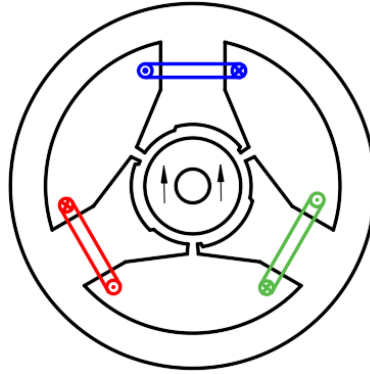
stator iron loss into consideration has been investigated in [EDE01] and the optimal goal is maximum efficiency. The potential and limits of HSPM motors are discussed in [BIA04]. 3s/2p slotted and 2-pole slotless 1 kW HSPM motors with speeds between 20-40 krpm and with non-overlapping and overlapping concentrated windings are designed, respectively. A comprehensive design and analysis of a 3s/2p HSPM machine with non-overlapping concentrated windings has been presented in [BIA04]. Further, the analysis and analytical optimization considering mechanical and thermal aspects of both motors are presented in [BIA05].

However, the diametrically asymmetric stator structure and unbalanced winding configuration of 3s/2p machine with non-overlapping concentrated windings result in inherent unbalanced magnetic force (UMF), which can cause high vibration and noise [ZHU07] [PAN14]. In order to mitigate UMF, a stator structure of extra notches in the middle of each stator tooth is proposed in [PAN14], Fig. 1.14 (a). In [MA18], the auxiliary slots in the stator tooth have been optimized to have the minimum rated on-load UMF, Fig. 1.14 (b). The result shows the proposed machine achieves almost zero UMF under rated on-load condition and slightly reduced torque compared to conventional 3s/2p HSPM machine with notches. The magnet eddy current loss has been reduced significantly by the optimized auxiliary slots in [MA19a], Fig. 1.14 (c).



(a) [PAN14]

(b) [MA18]



(c) [MA19a]

Fig. 1.14 3s/2p HSPM machine with auxiliary slots.

6s/2p structure also has been widely employed in small-size low-power HSPM machines since this slot/pole number combination has no UMF and small rotor eddy current loss. A 5kW, 240 krpm, 6s/2p HSPM motor with non-overlapping concentrated windings and its drive system have been designed in [OYA03] [SHI04]. This motor employs a straight tooth stator and ring magnet rotor with Inconel-718 sleeve. The power loss and eddy current in the rotor sleeve have been evaluated. The result shows that with the increased stator tooth width, the eddy currents and losses in the sleeve and PMs are decreased. 2 kW, 220 krpm, 3s/2p and 6s/2p HSPM motors with non-overlapping concentrated windings are designed and compared in [NGO05]. The results show that the 3-slot motor has better heat dissipation capability but large rotor eddy current loss, 6-slot motor has almost half of the power loss as 3-slot motor but low heat dissipation capability. A 5kW, 150 krpm, 6s/2p HSPM motor with non-overlapping concentrated windings has been designed for an automotive supercharger in [NOG07] [NOG09]. A straight tooth stator structure is employed due to easy manufacturing process. The optimization of stator core yoke width and tooth width to achieve high power density and high efficiency are investigated. [UZH16] presents a multidisciplinary design process which is applied to an 11 kW, 31.2 krpm, 6s/2p, HSPM generator and a 3.5 kW, 45 krpm, 6s/2p, HSPM synchronous machine for gas blower application. This design process considers the limitations of thermal, mechanical, and rotor dynamics to meet various requirements of different applications. A 4 kW, 150 krpm, 6s/2p, HSPM machine is designed for an electric turbocharger considering speed response characteristics in [LIM17].

Compared to 6s/2p structure, 6s/4p structure has the advantage of smaller copper loss due to thinner stator back iron and shorter end-winding length, which can reduce the motor axial

length and improve the rotor dynamic. But the 4-pole structure will result in larger stator iron loss and switching loss in the converter. The influence of tooth shoe shape on the electromagnetic performance especially the eddy current loss in the sleeve of a 3 kW, 80 krpm, 6s/4p HSPM generator has been investigated in [ZHA15h]. A 100kW, 30 krpm, 6s/4p HSPM machine is designed in [JAS17]. [WAN18] optimizes the split ratio of 6s/4p HSPM machine by considering stator iron loss and mechanical constraints. A 2.5 kW, 100 krpm, 6s/4p HSPM motor with non-overlapping concentrated windings is designed and compared to a conventional 6s/2p structure with overlapping concentrated winding under the same output power density in [IID20]. The motor size of 4-pole model can be reduced by 33.3% in order to keep the target output power under the same cooling, loss density condition, packing factor, and motor axial length. In [GIL17], a 4 kW, 75 krpm, 6s/4p HSPM motor with non-overlapping concentrated windings is compared to a 6-coil/2-pole slotless HSPM motor with toroidal windings. The results show that the slotless motor with toroidal windings has a lower noise level at the rated speed and lower on-load motor losses when the Litz-wires are used.

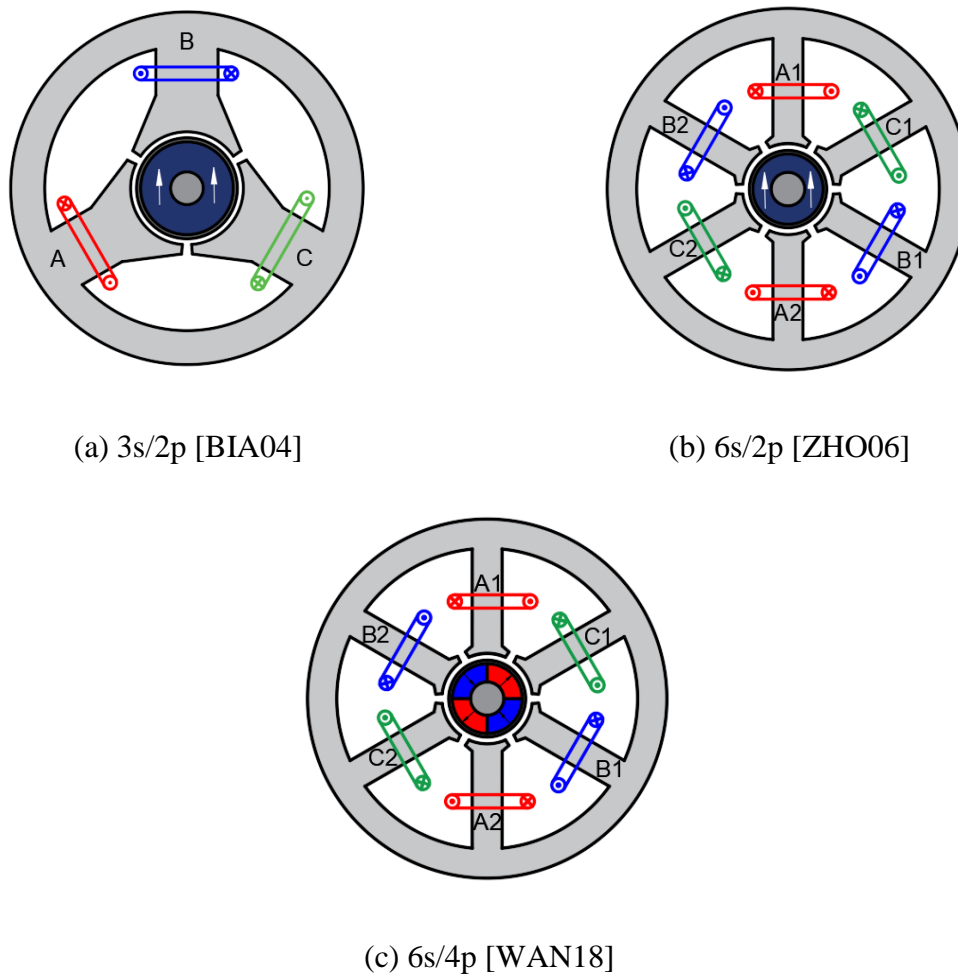


Fig. 1.15. 3- and 6-slot HSPM machines with non-overlapping concentrated windings.

In literature, different stator tooth topologies for 3- and 6-slot HSPM machines have been employed including straight tooth [OYA03] [SHI04] [NOG05] [NOG07] [NOG09] [JAS17] [GIL17], and tooth with tooth-tips [WAN10a] [UZH16] [ZHA15h] [WAN18] [IID20]. The tooth-tips can support the coil, reduce slotting effect, enhance flux focusing, and increase inductance for better PWM control and fault tolerance. The advantage of straight tooth is simple in the manufacturing process [GIL17].

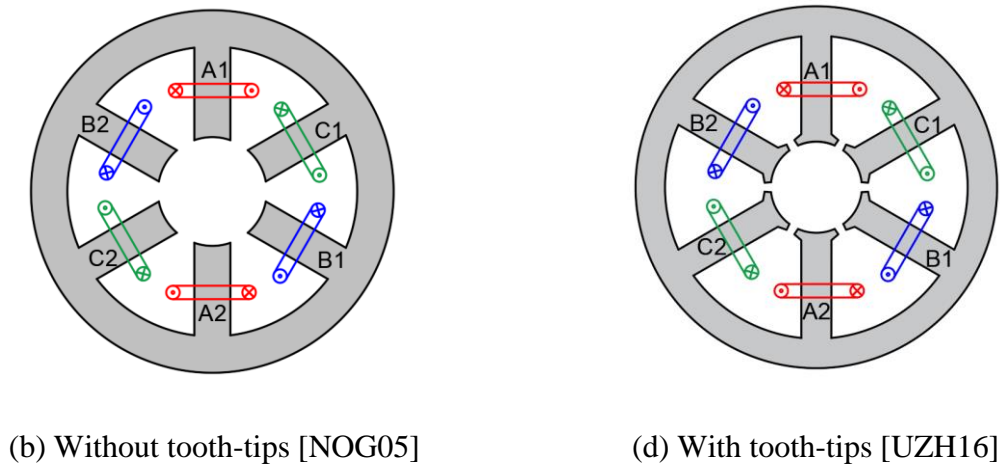


Fig. 1.16 Cross sections of six-slot HSPM machines.

1.2.3 Comparison

The comparison between slotless and slotted HSPM machines with different windings has been investigated in [BIA04] [BIA05] [GIL16] [GIL17] [ZHA16c]. [BIA04] [BIA05] design and compare a 3-coil/2-pole slotless and slotted HSPM motors. It shows that the slotless topology is preferred due to low risk of PM demagnetization and low rotor loss. [GIL16] analyses three PM machine topologies for a 15 kW, 150 krpm electrically assisted turbocharger, including a slotless topology with toroidal windings, a 6-slot straight tooth structure with non-overlapping concentrated windings, and a 6 semi-closed slots structure with non-overlapping concentrated windings. The comparison shows the slotless motor with toroidal windings has the highest efficiency but the lowest torque density. The slotted motors with non-overlapping concentrated windings have the best trade-off between efficiency and torque density, especially for the 6 semi-closed slots. In [GIL17], a 6s/4p slotted motor with non-overlapping concentrated windings and a 2-pole slotless motor with toroidal windings are compared in terms of noise and loss reduction. The results show that the slotless motor with toroidal windings has a lower noise level at the rated speed and lower on-load motor losses when using the Litz-wires. The slotted topology has the advantages of higher no-load flux density and output torque.

1.3 Rotor Topologies

For HSPM machines, rotor topology is very important since PMs suffer from the centrifugal force under high-speed operation. Generally, there are three types of rotor topologies in the HSPM machines, namely surface-mounted PM (SPM), interior PM (IPM), and solid PM rotor.

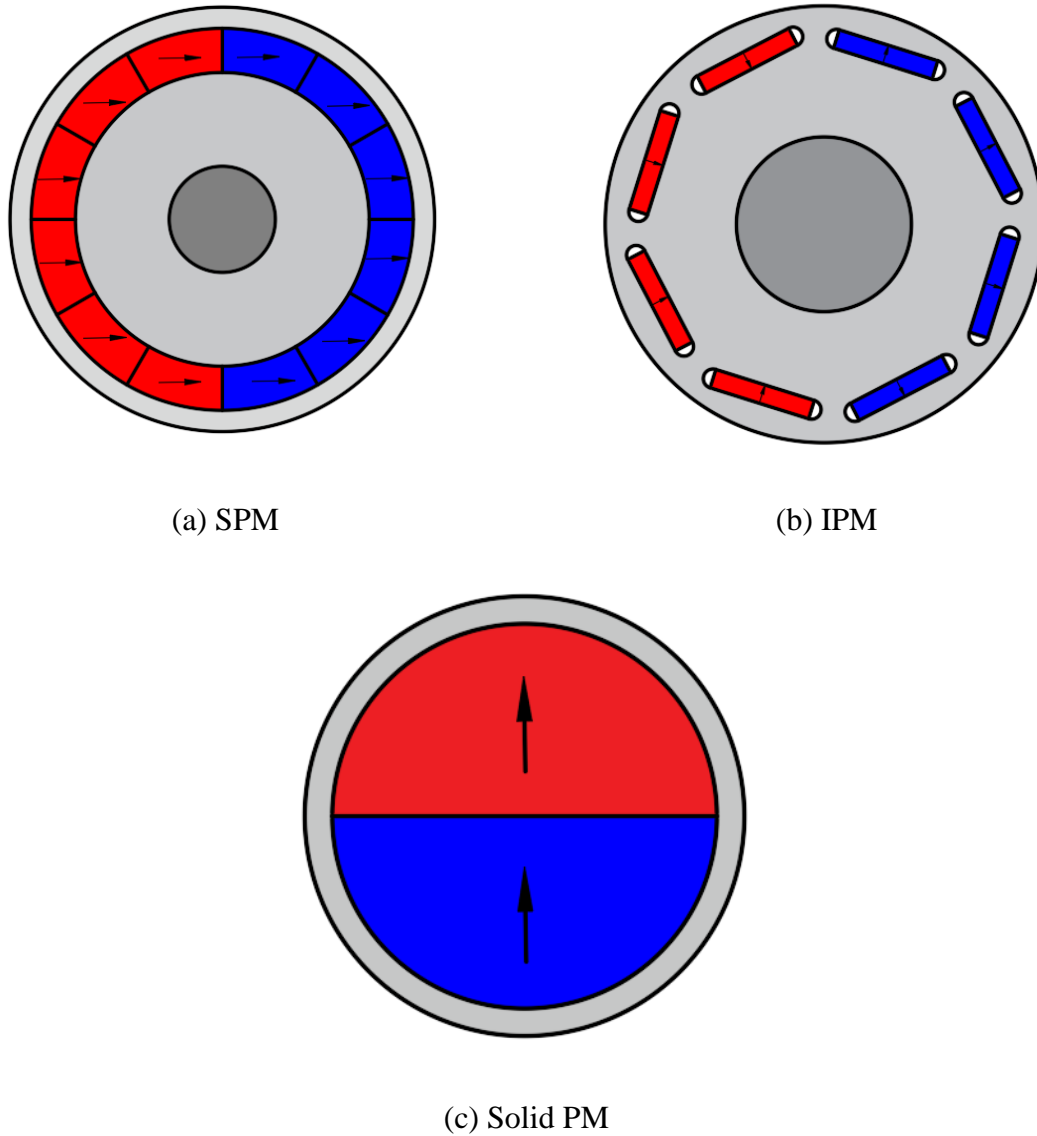


Fig. 1.17 Rotor topologies.

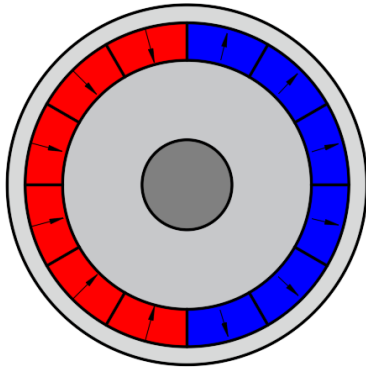
1.3.1 Surface-mounted PM (SPM)

SPM rotor topologies are widely employed in HSPM machines and typically equipped with a retaining sleeve to prevent damage to the PMs and ensure the rotor mechanical integrity since the PMs on the rotor are prone to large centrifugal force. The advantages of SPM rotor structure are high efficiency, high allowed critical speed, and easy manufactory process compared to IPM rotor structure [BIN06] [FOD14] [DON16c] [FAN17]. In literature, the design of SPM rotor structure mainly focuses on the magnet segmentation, PM pole arc to pole pitch, and sleeve design for reducing the rotor eddy current loss and improving the rotor mechanical strength [ZHO06] [SHA09] [YON12] [SHE13] [LIW14] [JUN15] [ZHA15] [WAN18] [HAN18] [AHN18]. [BIN06] presents a design process including the mechanical design of two 40kW, 40 krpm HSPM synchronous motors with SPM and IPM rotors. The mechanical behaviours are compared, and the results show SPM with carbon-fibre bandage is more suitable for high-speed application due to higher mechanical strength.

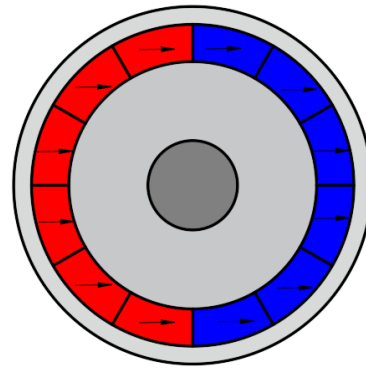
A. PM segment and magnetization

In high-speed operation, relatively large rotor eddy current loss and rotor mechanical stress will be produced. PM segmentation can reduce the rotor eddy current loss by cutting off the eddy current axial path [SHA09] [NIU12]. [ZHA16a] compares two 1.2 MW, 18krpm, 4-pole motors with 3 segments for each pole and without segment. It shows that the number of PM segments has a great impact on PM loss and PM stress. In addition, the PM segmentation can reduce the PM tangential stress but significant sleeve stress tangential concentration will occur. With the increase of segment number, this sleeve stress concentration effect is weakened whilst the PM tangential stress reduction effect is enhanced [DUG19] [WAN21]. However, the manufacturing difficulties increase with the increase of PM segment numbers, and thus, a trade-off should be made between improving the rotor characteristics, such as high mechanical stress and low rotor loss, and reducing manufacturing difficulties.

Different PM magnetizations, including parallel, radial, and Halbach, have been compared for a 36s/2p HSPM machine in [HON97]. The magnetisation directions for a Halbach magnet array in which magnets were arranged at 20 degrees intervals to realize a sinusoidal airgap field distribution with the least harmonics. The comparison shows Halbach magnetic array can reduce 30% torque pulsation and has no effect on output torque. It is worth noting that when the number of poles equals two, the parallel magnetization is the same as the Halbach array. Fig. 1.19 indicates three magnetizations of 4-pole SPM rotor.

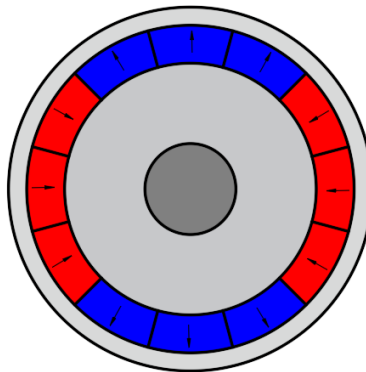


(a) Radial

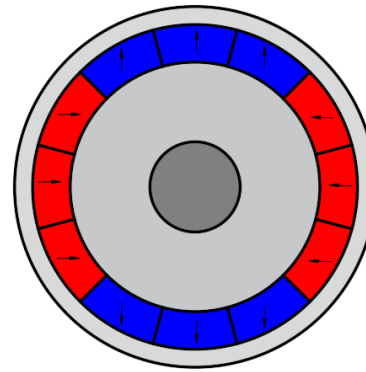


(b) Parallel

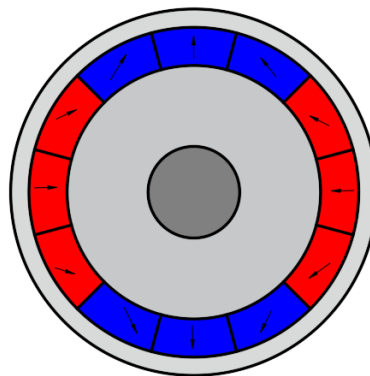
Fig. 1.18 2-pole rotor magnetization.



(a) Radial



(b) Parallel



(c) Halbach array

Fig. 1.19 4-pole rotor magnetization.

B. PM pole arc to pole pitch

For the SPM rotor with carbon-fibre sleeve, the influence of PM pole arc to pole pitch ratio is investigated by introducing the inter-pole gap, Fig. 1.11. Compared to the rotor with PMs evenly distributed along the circumference, i.e. the PM pole arc to pole pitch ratio is 1, the inter-pole gap brings additional stress in the sleeve on the edge of PMs and the bending effect may result in the rotor crush. [BIN06] suggests to fill the material with similar mechanical characteristic into the inter-pole gap to avoid the sleeve failure. The different materials inserted into the inter-pole gap has been compared in [ZHA15a], namely plastics, carbon-fibre, and Titanium alloy. The plastic fill has been selected and proved to improve the sleeve stress and rotor stiffness. The stress in the sleeves of the rotors with different materials of the inter-pole gap such as air, glass fibre, PM, and iron, have been compared in [BEN18]. The results show that the rotor with PM fill in the pole gap has the lowest stress.

The PM pole arc to pole pitch ratio (pole arc coefficient) affects not only the rotor stress but also the electromagnetic performances. For a 1.12 MW, 18krpm, 27s/4p, motor [ZHA15a] [ZHA16a], the PM eddy current loss, cogging torque, and no-load current increase with the PM pole arc to pole pitch ratio. In [ZHA17a], the same trend for back-EMF harmonics has been observed for a 150kW, 17 krpm, 36s/4p motor. Therefore, a compromise between the rotor stress and air-gap flux density/ back-EMF harmonics should be considered in selecting the PM pole arc to pole pitch ratio.

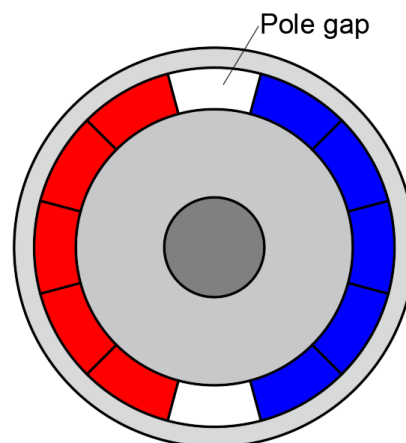
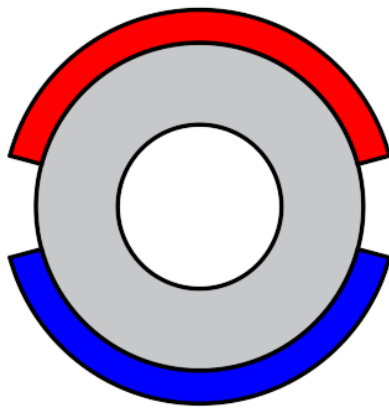


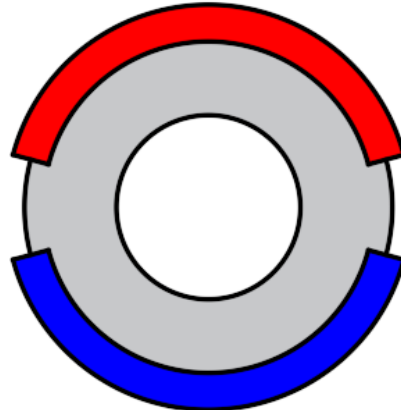
Fig. 1.20 Surface-mounted magnet with pole arc to pole pitch ratio less than 1 [BIN06].

The comparison of electromagnetic performances between the motors with conventional SPM rotor, half-insert PM rotor, and half-insert PM rotor with shaping is presented in [FOD14], Fig. 1.21. It is found that the motor with conventional SPM rotor has the highest output torque and

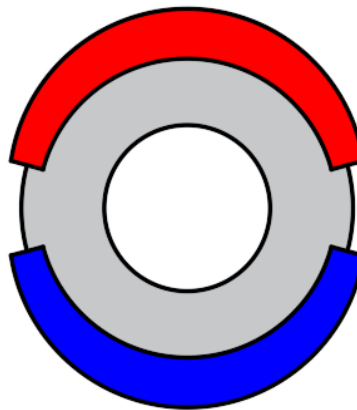
the motor with half-insert PM rotor with shaping has the lowest torque ripple. In addition, for the desired torque, the motor with conventional SPM rotor leads to the highest stator iron loss, and the motor with half-insert PM rotor has smaller stator iron loss but produces the largest rotor eddy current loss.



(a) Conventional SPM rotor



(b) Half-insert PM rotor



(c) Half-insert PM rotor with shaping

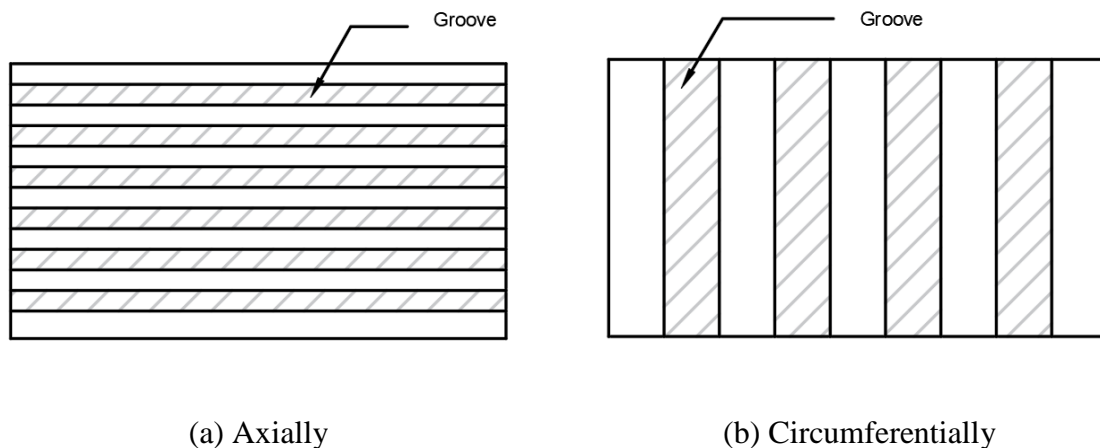
Fig. 1.21 Surface-mounted magnet rotors [FOD14].

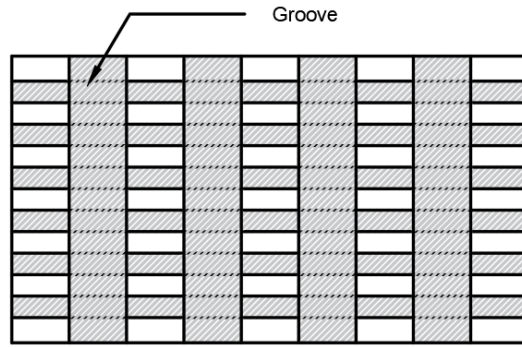
C. Sleeve design

In HSPM machines, a high-strength retaining sleeve is often employed to protect the rotor from centrifugal force and ensure the rotor integrity. Different sleeve materials and structures have been widely researched [ZHO06] [SHA09] [YON12] [SHE13] [LIW14] [JUN15] [ZHA15] [WAN18] [HAN18] [AHN18].

Generally, the materials of sleeve include carbon-fibre, stainless steel, alloy, and Titanium. The influence of sleeve materials with different relative permeabilities on the rotor eddy current loss, temperature distribution, and mechanical stress has been investigated in [ZHO06] [YON12] [LIW14] [AHN18] [ZHA15] [ZHO06]. The ideal sleeve of HSPM machine should have a degree of permeability to maximize magnetic loading, high mechanical strength, high resistivity to minimize eddy current losses, and great thermal conductivity to avoid overheat in PMs. Thus, the selection of sleeve material is important for the design of HSPM machines.

The optimization of sleeve structure and thickness has been investigated to improve the reliability of HSPM machine under high-speed operation [SHE13] [JUN15] [ZHA16a] [FAN17] [HAN18]. [SHE13] compares the circumferential, axial, and comprehensive grooves on the titanium sleeve, Fig. 1.22. It shows the circumferential grooving is the most effective to reduce the rotor eddy current loss and is simple to realize. [ZHA15a] proposes a hybrid protective sleeve consists of Ti alloy and carbon-fibre to reduce the bending stress, and the edge stress due to the inter-pole filler. The numeral results prove the hybrid protective sleeve can improve the radial and tangential stresses of PMs and sleeve at both 20°C and 150°C. [JUN15] designs a sleeve structure with skewed slits, as shown in Fig. 1.23 which reduces the eddy current loss in the sleeve. [FAN17] employs a radial multi-layer sleeve which reduces the eddy current loss in the sleeve without sacrificing the mechanical strength. This is especially suitable for the machines requiring both high-speed and large-power at the same time. [HAN18] proposed irregular-shaped rotor with laminated Titanium alloy sleeve for a 6 kW, 50 krpm, 12s/2p HSPM motor shows in Fig. 1.24. Compared to conventional cylindrical rotor with laminated Titanium sleeve and irregular-shaped rotor with Titanium sleeve, the rotor eddy current loss and rotor stress have been significantly reduced.





(c) Hybrid

Fig. 1.22 Sleeve structures with grooving [SHE13].

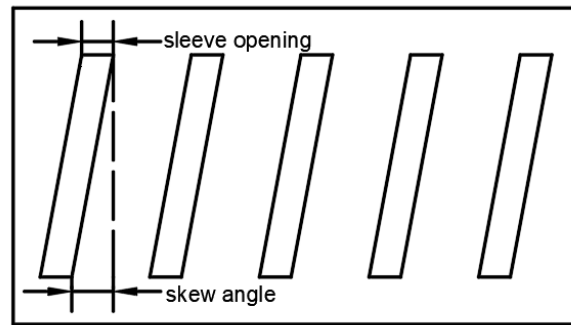


Fig. 1.23 Sleeve structure in [JUN15].

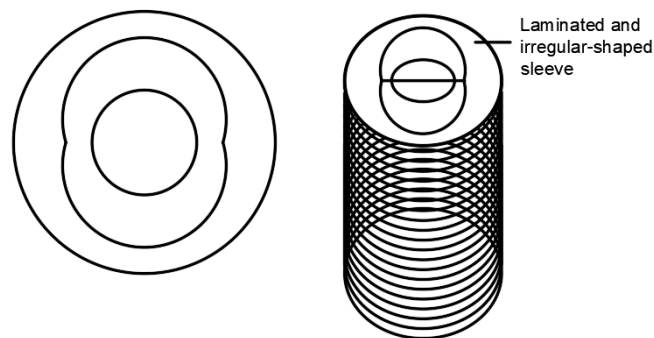


Fig. 1.24 Laminated titanium alloy sleeve with irregular-shaped [HAN18].

1.3.2 Interior PM (IPM)

With conventional IPMs, the PMs are located within the rotor iron, resulting in a conflict between the rotor flux leakage and the mechanical strength of iron bridges. In high speed operation, the iron bridge is not only subjected to its own centrifugal forces, but also to the

centrifugal force of the PM. In addition, compared to the SPM rotor the PM is not uniformly distributed in the radial direction of the rotor, resulting in localised peak stresses in the iron core at the rotor PM edges. As a result, the rotor critical speed of IPM machines is limited by mechanical stresses and is much lower than that of SPM machines with carbon-fibre sleeves.

In the dynamic analysis, since the lamination stack in the IPM rotor has a low bending stiffness while the sleeve in the SPM rotor can have some stiffening effect, the SPM rotor has higher natural frequency of the first bending mode than the IPM rotor [ZHA15d]. The electromagnetic analysis shows that spoke-type IPM and SPM rotor, Fig. 1.13, have similar back EMF amplitudes while there are more airgap flux density and back EMF harmonics in the IPM motors [DON16c]. Due to higher armature field and harmonics, the stator iron loss of the IPM motor is almost twice higher than that of the SPM motor. Meanwhile, the rotor loss of SPM rotor is lower than that of the IPM rotor [AUR16].

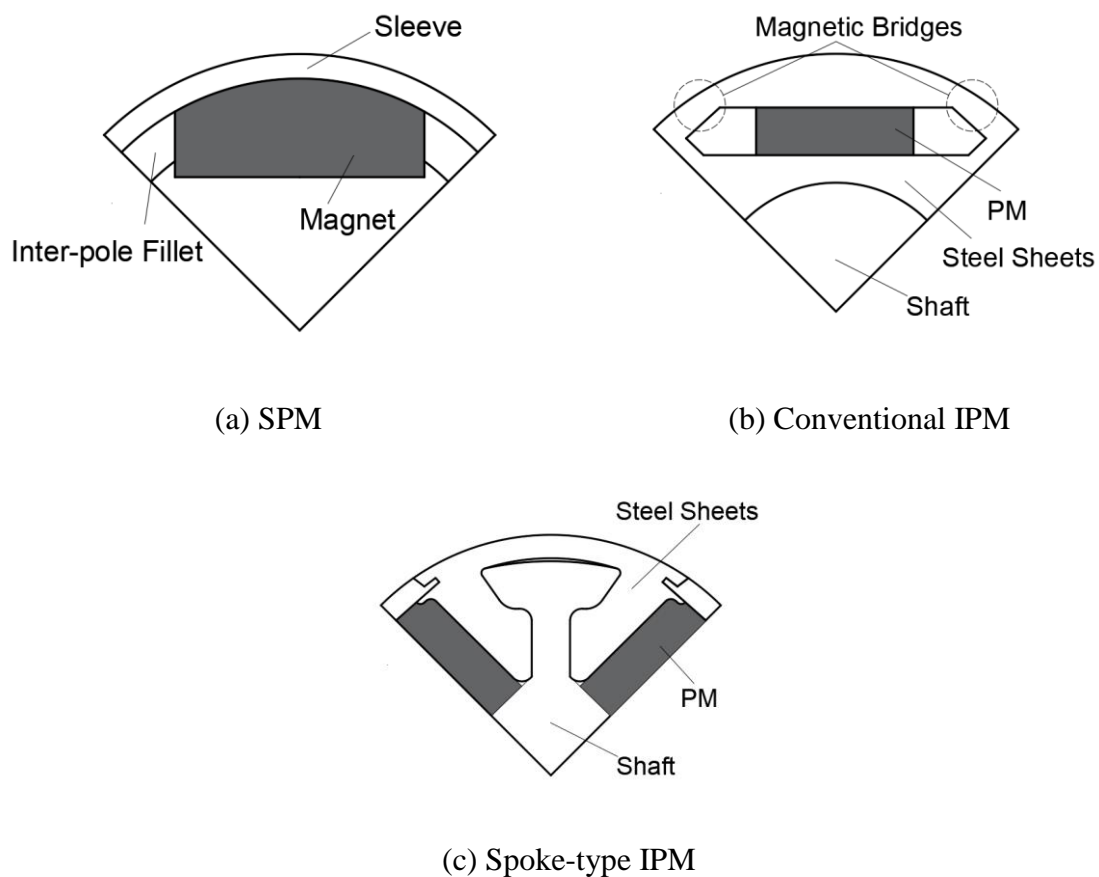


Fig. 1.25 Rotor topologies for SPM, conventional IPM, and spoke-type IPM [DON16c].

In addition, demagnetization withstand capabilities of HSPM machines with different rotor topologies also have been compared in [DON16c]. The results show that when the rotor sizes

are the same, the SPM motor with SmCo magnets and Inconel 718 sleeve have a better performance than the IPM motor with SmCo magnets. SPM motor has lower stator iron loss and lower rotor loss on load. The IPM motor has larger stator iron loss which is caused by larger and richer harmonic contents in the airgap flux density waveforms of IPM stator resulted from small equivalent air-gap and non-uniform reluctances. However, both the material costs and the processing costs of the IPM motor are much lower than those of the SPM motor. [GAL15] and [POP13] present the spoke IPM rotor structure. [GAL15] researches the effect of different PM material types on performance, which will be described in section 1.3.4, and [POP13] focuses on the proximity losses in the tooth-coil parallel paths windings. Halbach magnets have been investigated and compared with radial and parallel magnetizations in [HON97], and the 6-rib IPM structure can improve the tensile strength and yield strength of the laminations, Fig. 1.14.

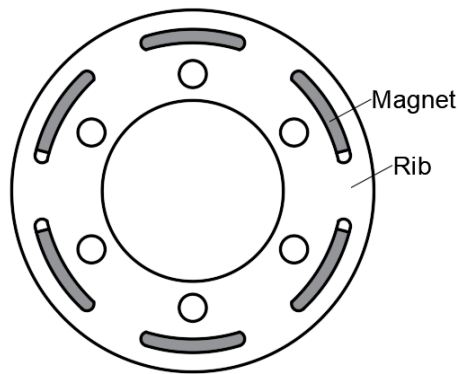
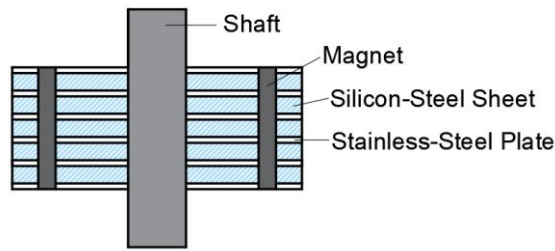


Fig. 1.26 6-rib structure.

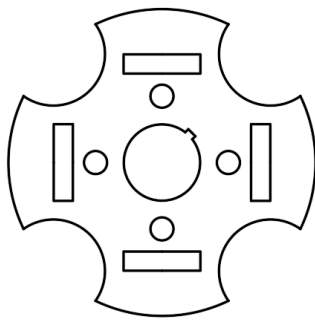
A novel IPM rotor structure has been proposed in [ZHA15d] with higher mechanical strength. The proposed rotor is inter-stacked by stainless-steel plates, in which stainless steel has much stronger mechanical properties than silicon steel, especially in tensile yield strength to withstand the centrifugal forces, as shown in Fig. 1.27. The novel rotor structure can improve the maximum operating speed by 17.4% compared with the conventional IPM rotor.

Another IPM structure with hollow shaft and PM centrally located in the shaft has been employed and developed in [ZHE05] [LIU18], Fig. 1.28. [ZHE05] designs a 2kW, 200krpm, 3-phase slotless HSPM motor for super high-speed centrifugal compressor drive application. The hollow shaft has been employed to hold the PM against the centrifugal force and improve the rotor stiffness under super high-speed operation. [HUY15] designs a 3kW, 150krpm, 24s/2p HSPM machine with a solid PM centrally located in a Titanium hollow shaft, and NdFeB is chosen since the operation is not under high temperature. In [LIU18], an amorphous rotor core

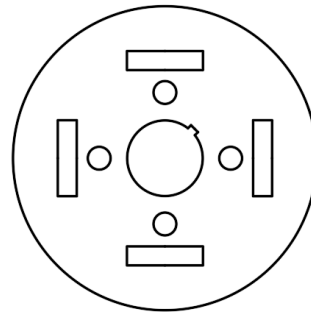
has been purposed as shown in Fig. 1.28(b). This IPM structure takes full advantage of amorphous materials and eliminates the need for sleeves. The analysis of electromagnetic, mechanical, and thermal performance indicates that this structure with hollow shaft has higher torque density, lower rotor loss, and lower rotor temperature rise but a slightly lower natural frequency compared with the motor with the silicon steel rotor core.



(a) Retaining shield rotor structure

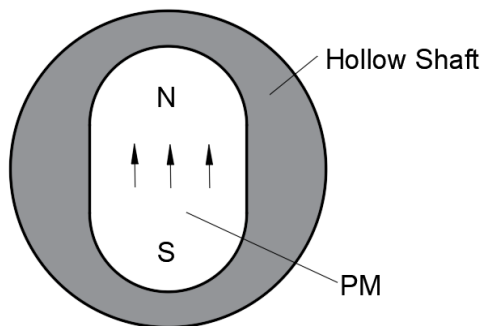


(b) Silicon steel sheet

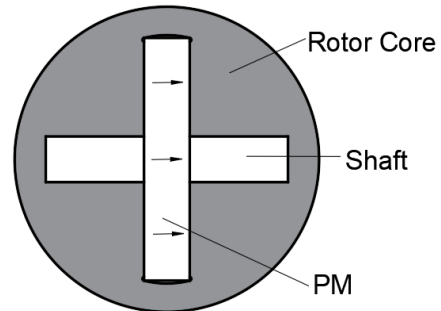


(c) Stainless-steel plate

Fig. 1.27 IPM rotor structure in [ZHA15d].



(a) Hollow shaft [ZHE05]



(b) Novel hollow shaft [LIU18]

Fig. 1.28 IPM rotor structure.

1.3.3 Solid PM

Generally, the solid PM rotor with sleeve has been widely used in HSPM machines since it has the advantage of high mechanical strength and small rotor eddy current under the same torque due to high flux density [ZWY05] [WAN09] [JUM14] [JUM15] [UZH16] [AHN17] [TUY17] [JAN18] [ISM18] [FAN19]. The PM material of solid PM rotor usually employs NdFeB due to negative thermal expansion coefficient perpendicular to the magnetization direction [UZH16] [AHN17], and $\text{Sm}_2\text{Co}_{17}$ due to its high operating temperature and appropriate energy characteristics [ZHE05] [ZWY05] [ISM18] [JAN18] [FAN19]. Different sleeve materials have been used for solid PM rotor topologies, including non-magnetic material [WAN09] [UZH16], titanium bandage [FAN19] [ZWY05] [TUY17], Inconel718 [AHN17] [AHN18], and stainless steel [JUM15]. The sleeve material comparison between non-magnetic steel and carbon-fibre employed by a 751W, 60krpm, 24s/2p HSPM machine has been investigated in [XIN10]. The high strength non-magnetic steel enclosure of the PM rotor can not only protect the PM from mechanical damage but also reduce eddy current loss in the solid PM which is beneficial to reduce the temperature of the PM. [JAN18] chooses the Titanium alloy sleeve rather than Inconel 718 for a 83kW, 12.5krpm, 24s/2p HSPM machine by considering the mechanical stresses of magnet and sleeve, and relatively low density and conductivity. The influence of different combinations of sleeve and PM materials on the mechanical stress in the PM have been investigated for a 500W, 400krpm, 6s/2p HSPM slotless machine in [AHN18]. The PM materials include NdFeB and $\text{Sm}_2\text{Co}_{17}$, while the sleeve materials include Titanium, SUS304, Inconel 718, and carbon-fibre. The combination of NdFeB magnet and Inconel718 sleeve is selected due to the high mechanical strength and the highest rotor dynamic safety factor. In order to minimize the processing difficulties of the PM and reduce the influence of PM length on magnetic performance, [CHE11] designs an axially segmented solid PM rotor. This structure has not only very good mechanical properties as the rotor one, but also very good processing properties and magnetic field distribution.

The solid PM rotor always works at high flux density zone, which can prevent the irreversible demagnetization of PMs, so that is more secure for the flux-weakening control of such PM machines [XU17]. The correlation between rotor vibration and mechanical stress in solid PM rotor structure has been investigated [AHN17]. In addition, the influence of sleeve thickness and shrink fit on the rotational vibration is researched. The experiments show that if the shrink fit is not calibrated properly, rotational vibration increases, and if the designed rotor is inappropriate, the magnet will break.

Table 1.2
Comparison of interior, surface mounted, and solid PM topologies

	SPM	IPM	Solid PM
Advantages	<ul style="list-style-type: none"> • High mechanical strength with carbon fibre sleeve • High maximum speed • Simpler manufacturing process 	<ul style="list-style-type: none"> • Low cost • Large output torque 	<ul style="list-style-type: none"> • Suitable for small size rotor • High power density • Low demagnetization risk • Ultra-high-speed application
Disadvantages	<ul style="list-style-type: none"> • High demagnetization risk 	<ul style="list-style-type: none"> • Low maximum critical speed • Low mechanical strength • Large rotor loss 	<ul style="list-style-type: none"> • Rotational vibration • Expensive

1.3.4 PM material

As mentioned before, in HSPM machines, the PM materials are mainly NdFeB and SmCo. The research of PM material for high-speed application mainly focuses on the thermal and mechanical limits. NdFeB and SmCo magnets as the most widely used permanent magnet materials have large compressive strength but low tensile strength [DON14a], which results in the necessity of sleeve protection. In addition, the Curie temperature of NdFeB is lower than that of SmCo, and thus, under high-temperature environment and rotor with the worse heat-dissipation condition, SmCo is a better choice [UZH16].

Table 1.3
Physical properties of common PM materials

	Remanence magnetism B_r (T)	Coercive field intensity H_c (kA/m)	Maximum operating temperature ($^{\circ}\text{C}$)
Ferrite	0.38-0.42	280-390	250
NdFeB	1-1.5	960-1600	180
SmCo	0.85-1.0	493-2790	250-350

In [GAL15], [DAM16], [BIA04] and [KIM16], motors with different types of NdFeB, ferrite, and SmCo are compared. Compared with NdFeB and SmCo, when the output power, rated speed, and stator active length, are the same, ferrite with lower remanence has lower magnetic loading and smaller air gap flux density, and thus, the outer diameter of the rotor with ferrite is larger and the turn number per phase is higher. In addition, large rotor outer diameter leads to mechanical issues, and large turn number leads to high copper loss and temperature rise, which are not desirable for high-speed applications.

1.4 Other Design Consideration

The design of HSPM machines needs to take other issues into consideration compared with low- and moderate-speed PM machines due to high-speed operations such as stator iron loss, AC copper loss, windage loss, sleeve mechanical stress, thermal field, and rotor dynamic characteristics. This part will introduce several important factors which needs to be considered in the design process of HSPM machines.

1.4.1 Stator iron loss

Stator iron loss is important for the design of HSPM machines due to high frequency. In general, the analytical calculation of stator iron loss is based on the Bertotti module [BER88]. The classic Bertotti module includes three losses components, i.e. hysteresis loss P_h , eddy current loss P_e , and anomalous loss P_a , as shown in 1.1 and 1.2

$$P_{fe} = P_h + P_e + P_a \quad (1.1)$$

$$P_{fe} = k_{hy}fB_{fe} + k_{ex}f^{1.5}B_{fe}^{1.5} + k_{ec}f^2B_{fe}^2 \quad (1.2)$$

where k_h , k_e , and k_a are the hysteresis, eddy current and anomalous loss coefficients, respectively. These coefficients depend on the material and are invariant with the frequency (f) and the flux density magnitude (B_m). [BER16] adds more loss components resulted from magnetic anomalies, manufacturing process, and rotational field to improve the accuracy of iron loss calculation. In addition, the influence of skin effect and rotational magnetization on the stator iron losses of HSPM machines are proposed in [DON14a] [ZHA16a]. The comparison between calculation and measurement results obtained from the Epstein test for a 75 kW, 36 krpm HSPM machine shows that the skin effect has a significant influence on the iron losses when the frequency is above 2 kHz. [ZHA16a] employs an orthogonal decomposition model with variable coefficients considering rotating magnetization to calculate the stator iron loss of a 1.12 MW, 18 krpm HSPM motor. The total iron loss calculated by decomposition model is larger than that calculated from the classical Bertotti loss model.

Generally, the stator iron material of HSPM machines is high grade steel, which has small anomalous loss coefficient, and thus the anomalous loss of Bertotti module can be neglected in HSPM machines. In addition, for reducing the stator iron loss under high-speed operation, the 0.1mm or 0.2 mm thickness electrical steel sheet is widely used for stator core [LID20]. In literature, several researches focus on the application of soft magnetic composite (SMC) for HSPM machines to reduce the stator iron loss and improve the efficiency [CHE09] [CHE15].

1.4.2 Copper loss (AC and DC)

There are two components of copper losses in HSPM machines, DC loss and AC loss.

DC loss can be simply calculated as below [GIL16] [GIL17].

$$P_{cu} = 3RI_{rms}^2 \quad (1.3)$$

where I_{rms} is the rms value of the phase current and R is the phase resistance.

In HSPM machines, the AC copper losses due to skin effect and proximity effect may increase significantly and should be considered [LIS16]. Skin effect is a tendency for alternating current (AC) to flow mostly near the outer surface of an electrical conductor. The effect becomes more and more apparent as the frequency increases. Therefore, the skin effect should be considered

in the design of HSPM machines with high frequency. To avoid the skin effect, the diameter of conductors should be less than the skin depth (δ) [UZH14], which can be calculated by

$$\delta = \sqrt{\frac{\rho}{\pi f \mu}} \quad (1.4)$$

where ρ is the resistivity of the conductor, f is the fundamental frequency, and μ is the permeability of the conductor.

Proximity effects caused by uneven distribution of current among the insulated wire strands of stator multi-strand windings, which can contribute significant bundle-level proximity losses in HSPM machines. Proximity loss is also affected by the end-winding dimensions, shape, and size [MLO15]. Parallel paths for coil conductors located at the slot top and slot bottom will experience different proximity effect since there will be different flux linkages between them due to leakage. The results show that the coils located in the slot top have higher proximity effect than that located in the slot bottom.

For slotless HSPM machines, the field caused by the PM is much larger than the field resulting from neighbouring wires. Therefore, the proximity effect is not considered but the additional eddy current losses caused by magnetic field should be calculated as a component of AC copper loss [ZWY05] [SCH17]. In the meantime, for slotted machine, and skin effect may be neglected due to the ratio of ac effective resistance to DC resistance by skin effect in the round conductor [FAN15b].

In terms of the reduction of AC copper loss, the Litz wire is widely used in slotless HSPM machines [ZWY05] [GIL17], and the current in each turn is divided into strands. In slotted HSPM machines, for reducing the AC copper loss, the small diameter wires are selected and they are located in the bottom of the slot.

1.4.3 Rotor eddy current loss

The rotor eddy current loss results from (1) stator slotting effect, (2) a non-sinusoidal stator MMF distribution, and (3) non-sinusoidal phase current waveforms, which result from six-step commutation and PWM [ZHU04]. For HSPM machines, it is important to consider the rotor eddy current loss due to the poor heat dissipation capability of rotor. Therefore, small rotor eddy current loss may result in high temperature rise and irreversible demagnetization of PMs.

Rotor eddy current losses can be estimated using either the finite element method or the analytical method [ZHU04] [BIN06]. For the analytical method, the equivalent current sheet method is usually used to take into account the effect of the armature magnetic field. The contributions of time and space harmonics are calculated analytically in [ZHU01]. A further study is completed in [ZHU01a], where the effect of eddy currents on the magnetic field is considered. An improved analytical model for eddy current losses in SPM rotors is presented in [ZHU04], which takes into account the sleeve.

The rotor eddy current loss can be reduced by (a) employing low pole number rotor [SCH97] [ZHU04]; (b) employing different winding configuration [MER15]; (c) using relatively large air-gap [TAK94]; (d) rotor shape optimization [CHA10]; (e) PM segmentation [YAM09] [HUA10] [NIU12]; and (f) employing auxiliary slots [MA19a].

1.4.4 Windage loss

The windage loss is caused by air friction and becomes larger with the increases of rotation speed. In general, the rotor will be modelled as a cylinder in the windage loss calculation, and the equation is shown in (1.5) [VRA68] [PFI10] [GIE14] [BUR17] [LIM17]

$$P_{windage} = C_f \pi \rho \omega^3 r^4 l \quad (1.5)$$

where ρ is the air density, ω is the angular speed, r and l are the rotor radius and length, respectively. C_f is the friction coefficient, which depends on the ventilation speed of air gap and rotor surface condition [ZHA17b] [HUA16]. The research shows that the windage loss increases with the roughness of the rotor surface and ventilation speed. Therefore, it is advantageous to use a smooth rotor surface and select a suitable ventilation speed to balance air friction losses and cooling condition.

1.4.5 Thermal and demagnetization

HSPM machines often suffer high temperature rise during high-speed operation, and overheat of the rotor may cause irreversible demagnetisation of PMs. Thus, it is necessary to investigate the thermal performance of HSPM machines. In [DON14a], with forced convection cooling, the temperature rise for specific parts of machine can be analysed by computational fluid dynamics (CFD) and lumped-parameter thermal network (LPTN). It is worth noting that the flow velocities are obtained by CFD and are used in the LPTN model.

According to literature, a variety of cooling systems have been designed and different calculation models are utilized. Compared to air-cooling system, water cooling system can increase the maximum current density. However, this method is restricted to less application. Air-cooling system offers higher liability but less capability. Different cooling systems are employed for different situation [ZHA13] [HUY15].

1.4.6 Rotor dynamics and vibration

Generally, vibration occurs due to the magnetic force generated between the stator and the rotor. When rotor rotating, there are two kinds of energy in the rotor, one is rotational energy, the other one is vibration energy. Under the high-speed condition, vibration will result in high noise level and rotor failure. In order to improve stability, rotor dynamic analysis is necessary during the machine design process [AHN17]. The FEM is used widely for dynamic analysis. Based on FEM, the first, second, and third bending natural frequencies should be calculated and the rated speed should be 10% larger than the first bending critical speed to keep the rotor safe [HUA16]. [EDE02] investigate the influence of design parameters on rotor dynamic characteristic, including the active length, the shaft diameter and extension, the bearings, and the material properties.

1.4.7 Optimization method (Electromagnetic/ Multiphysics)

Generally, the optimal target of the HSPM machine varies with applications, and can be efficiency [LUO09] [EDE01], torque [PFI10], and torque density [HE21]. The optimization often employs analytical or FE method.

Firstly, the FE method is the most common tool in engineering with high accuracy, while usually suffers from the long computation time, especially in the multi-physics analysis because of complicated iteration processes among different physical fields. In contrast, the analytical method could investigate the physical mechanism accounting for the influence of design parameters and eminently ease the computation burden. Therefore, the analytical method is preferred at the early design stage to reduce the number of candidates effectively. However, the FE method is necessary for further optimization and checking.

In general, for the optimization of electromagnetic performance for HSPM machines, two variables are often enough, i.e. the split ratio of inner diameter to outer diameter of the stator and the maximum stator iron flux density [ZHU97] [EDE01] [BIA05] [WAN18] [MA19b] [HE21]. Besides, other variables such as sleeve thickness for minimum rotor eddy current loss

[SHA09], notch outside the stator for improving cooling ability [ZHA15], and motor length to diameter ratio for maximum torque [HE21] are optimized for different applications of HSPM machines.

The restrictions of optimization usually are the thermal limit. However, in order to improve the reliability of HSPM machines, more loss components and constrains are considered. [EDE01] takes stator iron loss into consideration, [MA19b] takes the rotor eddy current loss into consideration, [LUO09] considers the air friction loss of the rotor. [WAN18] [LIQ15] consider the mechanical constrains, and [HE21] considers the effect of armature reaction on the stator iron loss. [HE21] restricts the allowed maximum current density. Therefore, multiphysics optimization including thermal field, mechanical strength, mechanical losses, and rotor dynamics constraints by using CFD and FE model is very popular [HUA16] [ZHA18] [DUG21]. In [HUA16], the sleeve thickness is optimized for the mechanical stress and the rotor length to diameter ratio is optimized for the rotor mechanical strength. [ZHA18] adopts global optimization method including motor structure, thermal model, and residual contact pressure for a comprehensive performance of 48s/8p HSPM machine optimization. [DUG21] sets the lowest rotor temperature, i.e. the minimum rotor eddy current loss, as the indirect optimization target, and then considers the rotor stress and output torque. [DON14] increases stator yoke width to improve the cooling capability. In addition, multi-objective optimums are required for different applications [KRA17] [ZHA18].

1.5 Scope of Research and Contributions of the Thesis

In this thesis, the electromagnetic performance of a 2-pole HSPM motor with toroidal windings for vacuum cleaner application is designed and investigated, accounting for the slot number and the slot ratio, i.e. the ratio of the inner slot area to total slot area. In addition, the influence of manufactory tolerances on electromagnetic performance is analysed. Finally, the proposed motor, slotless motor with toroidal windings, and slotted motor with tooth-coil windings are compared, respectively.

Chapter 1: Various HSPM machines are reviewed in terms of stator topologies, winding configurations, rotor topologies, and design considerations.

Chapter 2: The influence of stator slot number on electromagnetic performance of 2-pole HSPM motors with toroidal windings is investigated and compared. For small-size low-power

application, 6-slot structure has advantage of no UMF and low rotor eddy current loss. In addition, the 3s/2p HSPM motors with tooth-coil and toroidal windings are compared.

Chapter 3: The 6s/2p HSPM motor with toroidal windings is designed and optimised. One of the most important design parameters, i.e. split ratio, is optimized together with the slot ratio, i.e. the ratio of inner slot area to total slot area.

Chapter 4: The influence of stator segment gap and stator misaligned segments occurred during modular manufactory process of 6s/2p HSPM motor with toroidal windings on electromagnetic performance is investigated.

Chapter 5: The electromagnetic performance between 6s/2p slotted HSPM motor with toroidal windings and 6-coil/2-pole slotless HSPM motor with toroidal windings is compared.

Chapter 6: General conclusion and future work.

The major contributions of the thesis include:

1. It is found for the first time that the stator segment gap results in unbalanced three phase back-EMFs, not only amplitudes, but also phase angles. Further, the misaligned stator segments with gaps result in asymmetric air-gap length and winding configuration which affect the electromagnetic performance significantly.
2. It is found that the slot ratio, i.e. inner slot area and outer slot area, has great impact on the motor electromagnetic design. When the inner slot area equals to outer slot area, the output torque reaches maximum.
3. The winding factors of HSPM machines with toroidal windings are calculated and compared. In addition, it is shown that toroidal windings are not suitable for 3-slot stator structure.
4. The comparison between slotted and slotless HSPM motors with toroidal windings.

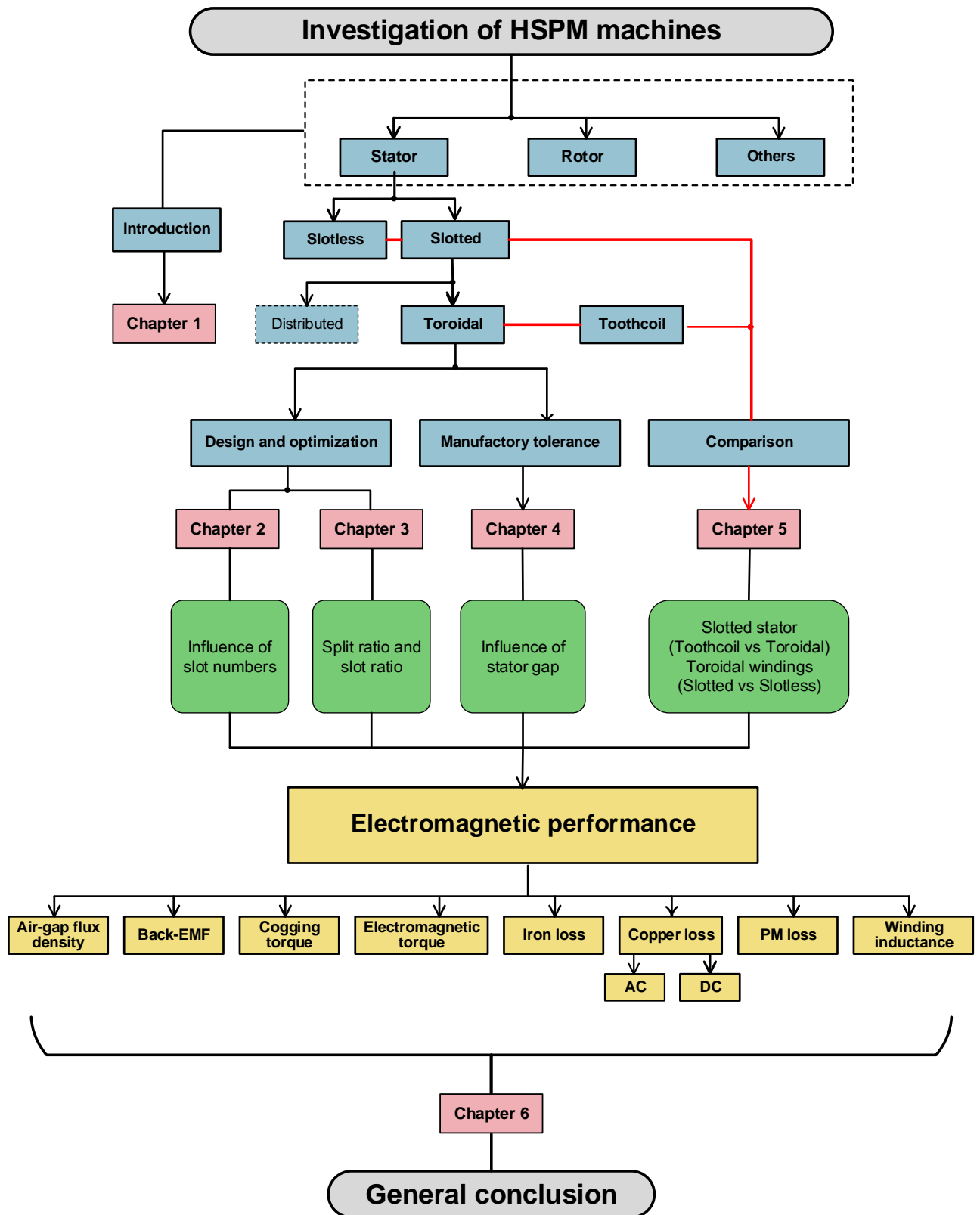


Fig. 1.29 Research scope and outline.

CHAPTER 2

INFLUENCE OF SLOT NUMBER ON ELECTROMAGNETIC PERFORMANCE OF 2-POLE HIGH-SPEED PERMANENT MAGNET MOTORS WITH TOROIDAL WINDINGS

This chapter investigates the influence of stator slot number on electromagnetic performance of 2-pole high-speed permanent magnet (HSPM) slotted motors with toroidal windings. Four 2-pole slotted motors with different slot numbers, i.e. 3, 6, 9, and 12, are globally optimised for maximum torque, and their electromagnetic performance are compared, including winding factor, air-gap flux density, back-EMF, cogging torque, electromagnetic torque, winding inductances, unbalanced magnetic force (UMF), and various loss components. It shows that the 6s/2p HSPM motor with toroidal windings is eminently suitable for high-speed applications due to no UMF and easy to realise a modular structure. In addition, toroidal and tooth-coil windings are compared in the 3s/2p motors, and the results confirm that toroidal windings are not suitable for the 3s/2p HSPM motor due to rich air-gap field harmonics. Finally, a 6s/2p prototype motor is manufactured and tested to validate the finite element (FE) predictions.

This chapter is based on the paper published in:

F. Xu, T. R. He, Z. Q. Zhu, Y. Wang, H. Bin, D. Wu, L. M. Gong, and J. T. Chen, "Influence of Slot Number on Electromagnetic Performance of 2-pole High-Speed Permanent Magnet Motors With Toroidal Windings," in *IEEE Transactions on Industry Applications*, vol. 57, no. 6, pp. 6023-6033, Nov.-Dec. 2021.

2.1 Introduction

HSPM motors have been developed over the last decades due to high power density, small size, and low weight. The toroidal windings with a short axial length are attractive for improving power density and are employed for a variety of applications. [ZWY05] designs a 100W, 500 krpm PM generator for mesoscale gas turbine, which is a promising solution for high energy and power density portable devices. [GIL16] compares different topologies of 15 kW, 150 krpm PM motors for electrically assisted turbocharger. [SCH17] presents a 160 krpm, bearingless slice motor for different applications in electrical drive systems, such as high-speed

spindles, turbo compressors, and flywheels. [BOR14] discusses three HSPM machines for different applications, including a micro-milling spindle (150W, 200 krpm), an air compressor (4.5mNm, 30~90 krpm), and a gas-turbine generator (3.7kW, 240 krpm).

In general, the structures of HSPM motors with toroidal windings can be classified as slotless and slotted. A HSPM slotless motor with toroidal windings has better heat dissipation capability due to direct contact between windings and housing [SCH17][JUM16]. In addition, the manufacturing cost of motors with toroidal windings are relatively lower compared with conventional windings due to its simple iron core structure [BOR14]. Slotless stator with toroidal windings can mitigate vibration and noise effectively since it has no slotting effect, i.e. no air-gap field slot harmonics, and thus less torque ripples. Moreover, the rotor eddy current loss may be minimized as a result of less air-gap harmonics and relatively low armature reaction [GIL17][BIA04]. However, slotless stator structures usually have relatively lower torque density due to low magnetic loading. In literature, the slotted stator/rotor structures with toroidal windings are widely employed in different low-speed and medium-speed machines, such as induction machines [JEN12][VIL13], axial-flux PM machines [MUL99], Vernier PM (VPM) machines [XUG12][TOB99][LID15], flux reversal PM (FRPM) machines [LIH20], switched flux PM (SFPM) machines [LEE06], magnetically geared machines [JUN19]. The toroidal winding has a short axial end-winding length, which is suitable for machines where the axial length is limited. In addition, compared with the concentrated winding, the toroidal winding has a larger winding factor in the machines with relatively large slot number and small pole number [LIH20].

For HSPM machines, the slotted stator structures with toroidal windings are mainly used in large power, large size, multi-slot machines, e.g. a 30kW 18s/2p [ZHA15], a 15kW 24s/2p machine [CHE11], a 75kW 24s/2p machine [DON14a][DON14b], and a 117kW 36s/2p HSPM generator [ZHA16]. Most of them focus on the calculation of various loss components and thermal analysis, since high fundamental frequency will lead to large stator iron loss and eddy current loss in magnet, which may result in high temperature rise and irreversible demagnetization of PMs. [CHE11] proposes an optimal design method considering mechanical stress, rotor dynamic characteristics, and temperature rise. However, for small size, low-power and high-speed motors with toroidal windings, the influence of various slot/pole number combinations has not been systematically discussed yet. In [XUF20], the electromagnetic performances of 3-, 6-, 9-, and 12s/2p HSPM motors with toroidal windings are investigated. As an extension to [XUF20], four 2-pole HSPM motors with different slot numbers are

optimized considering the allowed maximum stator loss, which including stator iron loss. In addition, the winding inductances, AC copper losses, and frame losses of different slot numbers are analyzed and compared. Moreover, a 6s/2p HSPM motor is manufactured and tested to verify some of the finite element (FE) predicted results.

In this chapter, the 2-pole high-speed motor topologies with toroidal windings and different slot numbers, as well as their winding factors are described in sections 2.2 and 2.3, respectively. In section 2.4, four motors are optimized analytically considering the stator thermal limitation. Section 2.5 compares the electromagnetic performance of these motors with different slot numbers. In section 2.6, one 6s/2p HSPM prototype motor with toroidal windings is manufactured and tested to validate the FE predicted results. Finally, section 2.7 is the conclusion.

2.2 Motor Topologies

The topologies of four 2-pole HSPM motors with toroidal windings and different slot numbers are shown in Fig. 2.1. In order to reduce the operating frequency, the pole number is chosen as 2 so that the electromagnetic and switching losses are minimum. The rotor is surface-mounted with a diametrically magnetized magnet ring (N45SH) and the shaft employs magnetic material (GCr15). To protect the PMs from centrifugal force, a stainless-steel sleeve is employed. The material of stator lamination is 20-JNEH1200 and the thickness is 0.2mm to reduce the stator iron loss under high frequency. The stator is also equipped with outer teeth which do not contribute to the magnetic circuit, but mainly provide the mechanical support. To ease winding, the stator employs straight teeth without tooth-tips although the influence of tooth-tips will be investigated in this chapter. Further, due to the limitation of motor size, the slot number is chosen as 3, 6, 9, and 12. It is worth noting that forced-air cooling is employed in those high-speed motors due to the applications of hairdryers and vacuum cleaners.

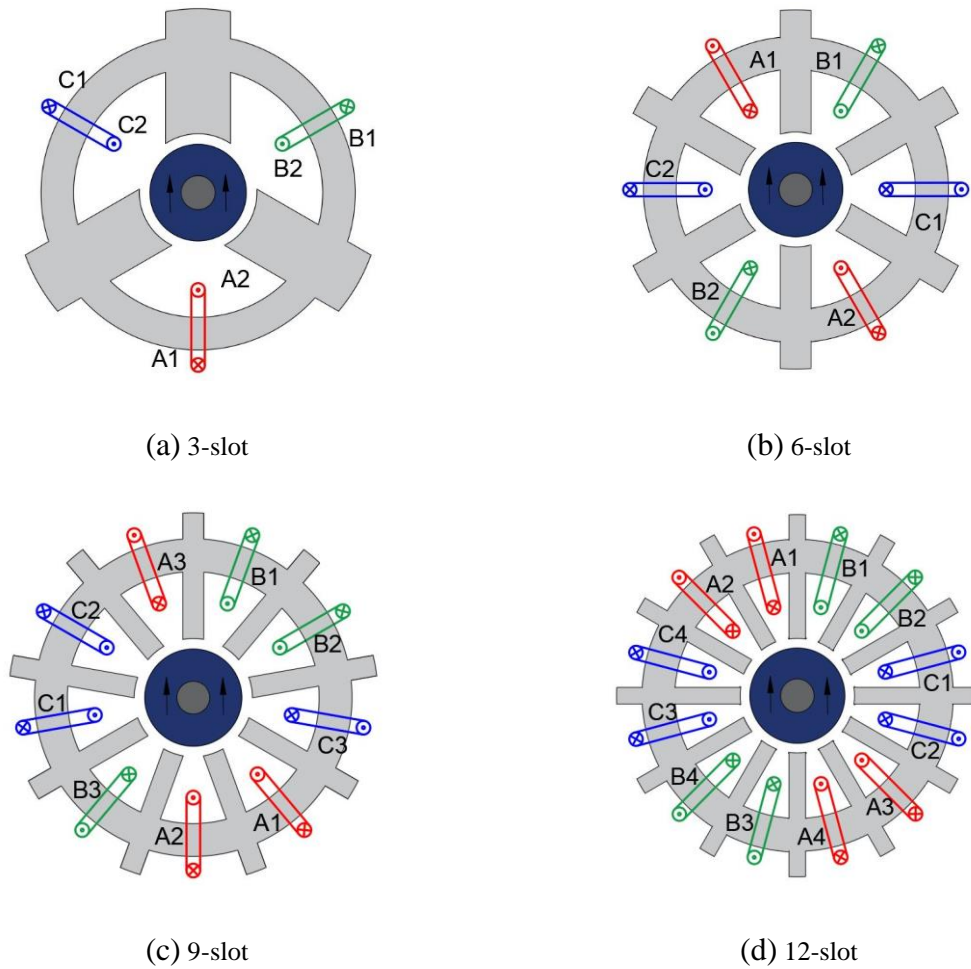
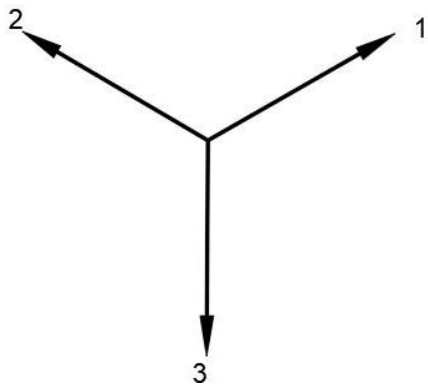


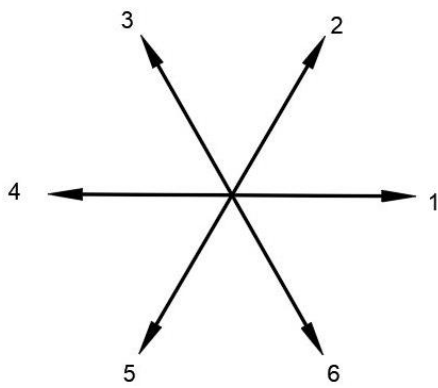
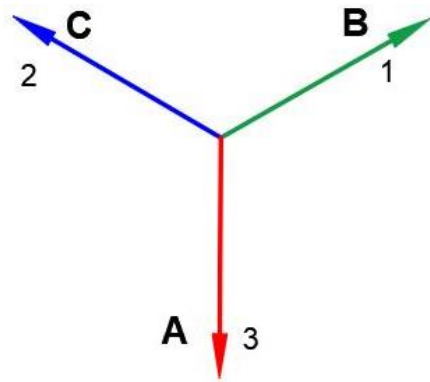
Fig. 2.1. Cross-sections of 2-pole high-speed motors with toroidal windings.

2.3 Winding Configuration and Winding Factor

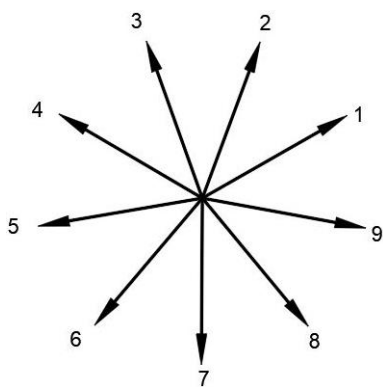
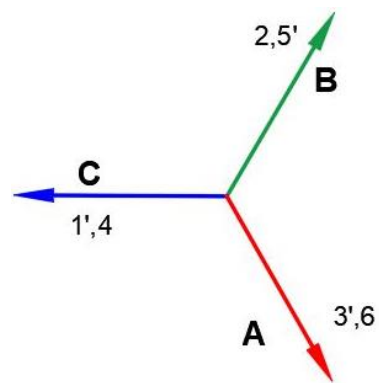
The slot/pole number combination affects winding factor (K_w) significantly. The conventional formulae of winding factor cannot be directly used in the motors with toroidal windings. In this part, Fig. 2.2 (I) shows the winding layouts of four 2-pole motors with different slot numbers. Since the coils are wound around stator core, the coil factor should be full-pitched. However, the outer side winding only formed the circuit and can be treated as end-windings, thus, the coil factor of four 2-pole motors is equivalent to only 0.5. As shown in Fig. 2.2 (II), the distribution factors of 3-slot and 6-slot motors are both equal to 1. However, the distribution factors of 9-slot and 12-slot motors should be calculated, Table 2.1. Therefore, the fundamental winding factors of 3-, 6-, 9-, 12s/2p HSPM motors with toroidal windings are 0.5, 0.5, 0.48, 0.48, respectively.



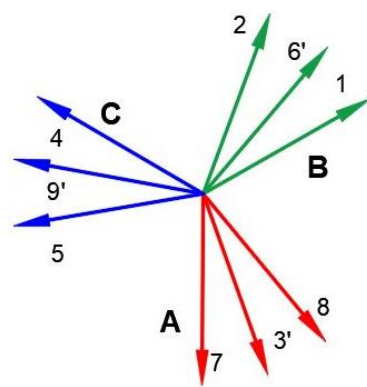
(a) 3-slot

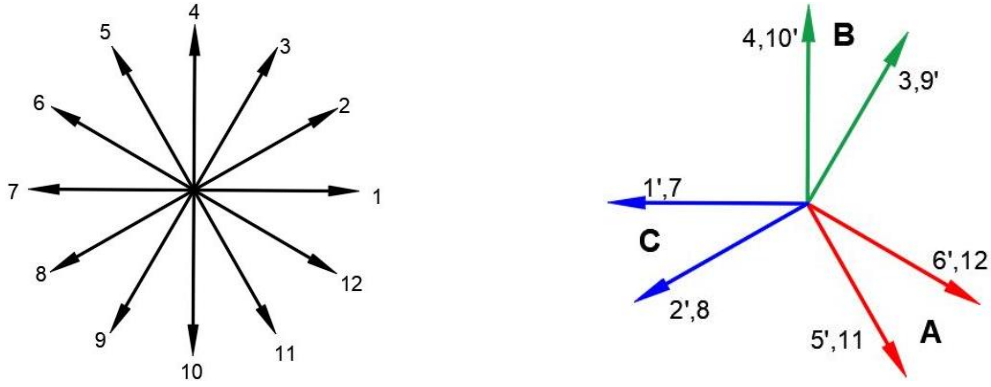


(b) 6-slot



(c) 9-slot





(d) 12-slot

(I). Winding layouts

(II). Phasors

Fig. 2.2. Winding layouts and phasors of 2-pole HSPM motors with toroidal windings.

Table 2.1
Winding Factors of 2-Pole Motors with Different Slot Numbers*

	3-slot	6-slot	9-slot	12-slot
K_p	0.5	0.5	0.5	0.5
K_d	1	1	$\frac{\sin \frac{v\pi}{6}}{3 \sin \frac{v\pi}{18}}$	$\cos \frac{v\pi}{12}$
$K_w = K_p K_d$	0.5	0.5	$\frac{\sin \frac{v\pi}{6}}{6 \sin \frac{v\pi}{18}}$	$\frac{1}{2} \cos \frac{v\pi}{12}$

*Note: where v is the harmonic order.

2.4 Optimal Design

In this section, the split ratio (λ), i.e. the ratio of stator inner diameter (D_i) to stator outer diameter (D_o), will be optimized analytically for the maximum electromagnetic torque. Small size, low power, 2-pole HSPM motors usually have large stator iron loss at high-speed operation due to high frequency [BIA04]. Therefore, a fixed current density with a limitation of stator loss including stator iron loss and copper loss will be employed in this optimization. The maximum allowable current density varies between 1 and 10 A/mm² based on experience [HAN03]. In addition, the current density in the coil windings must be limited in order to avoid local overheating, which would lead to the destruction of the winding insulation and result in a short circuit [REI13]. In high-speed motors, the insulation class is higher than the

conventional low- and medium-speed motors, and the maximum allowable current density of this thesis is provided by Midea's company as 12 A/mm².

In general, HSPM motors are designed under 120° electrical brushless operation mode. Different from tooth-coil windings, the toroidal windings need outer teeth/slot area to support the outer windings, and thus the slot area ratio, i.e. the ratio of inner to total slot area, should be considered. In this section, the slot area ratio is assumed as 0.5, and thus the inner and outer slot areas have the same area and packing factor. The influence of slot area ratio will be investigated in Chapter 3. In this thesis, the edge damage on stress is neglected.

In literature [BIA04] [BIA05], the maximum allowed stator loss depends on stator thermal limit, which can be derived as

$$P_{stator} = h v_m \pi D_o l_a \quad (2.1)$$

where h represents the overall heat transfer coefficient which is 100 W/(°Cm²) in this design due to the forced-air cooling [BIA05]. The maximum allowed temperature v_m is 120°C since the insulation class is 'E' in this design. l_a is the stator active length. In this thesis, the demagnetization is not considered. Generally, the iron loss can be calculated by the Bertotti model [ATA92]

$$P_{fe} = m_{fe} (k_{hy} f B_{fe} + k_{ex} f^{1.5} B_{fe}^{1.5} + k_{ec} f^2 B_{fe}^2) \quad (2.2)$$

where m_{fe} is the stator mass, k_{hy} , k_{ex} , and k_{ec} are the hysteresis coefficient, the eddy current coefficient, and the excess loss coefficient, respectively. f denotes the fundamental frequency and B_{fe} represents the maximum stator iron flux density.

Table 2.2
Main Parameters of 6/2 HSPM Motor without Stator Gap

Hysteresis coefficient k_{hy}	173.295	Eddy current coefficient k_{ec}	0.086
Excess loss coefficient k_{ex}	2.068		

With the rated speed and fixed fundamental frequency, the stator iron loss per unit volume only depends on the maximum stator flux density. According to Gauss' Law, the stator iron flux density is defined by the maximum air-gap flux density (B_g) resulted from PM. Since the motor employing toroidal windings, the influence of armature reaction on the stator iron loss can be neglected due to the small effect on the maximum stator flux density. Therefore, in this thesis,

the influence of armature reaction on Gauss' Law is neglected. For different slot/pole number combinations, the relationships between stator tooth width and stator yoke height are described as coefficient (k_{tw}) [PAN06]. The stator tooth width (w_t) and the stator yoke height (h_t) can be calculated by the maximum air-gap flux density and stator iron flux density

$$w_t = k_{tw} h_t = \frac{k_{tw} (D_i - l_g) B_g}{2\pi B_{fe}} \quad (2.3)$$

where l_g is the air-gap length. In literature [ZHU97], the maximum air-gap flux density can be calculated with a fixed remanence (B_r) and split ratio. According to the stator tooth width and yoke height, the cross-sectional area of one conductor (A_{cond}) can be obtained with a fixed number of turns. For toroidal winding configuration, the conductors in the outer slots are considered as the part of end-winding and thus the total end-winding length (l_e) cannot be neglected in the calculation of copper loss, which is given by

$$P_{cu} = 2I_{rms}^2 \rho_{cu} \frac{(l_a + l_e) N_s}{A_{cond}} \quad (2.4)$$

where ρ_{cu} is the resistivity of copper, N_s is the number of in series turns per phase.

The temperature rise caused by copper loss is limited by fixing current density (J_s), and the RMS phase current is given by

$$I_{rms} = J_s A_{cond} \quad (2.5)$$

Then, the electromagnetic torque is obtained as:

$$T_{em} = 2B_g (D_i - l_g) l_a N_s k_w J_s A_{cond} \quad (2.6)$$

As equations mentioned above, the electromagnetic torque is a function of the split ratio, the maximum stator iron flux density, and current density. Therefore, the stator loss should be less than the thermal limit and the torque can be rewritten as:

$$T_{em} = 2(\lambda D_o - l_g) l_a N_s k_w J_s f(\lambda, B_{fe}) \quad (2.7)$$

Fig. 2.4 indicates the variation of average torque with stator loss of four 2-pole motors with different slot numbers. It can be seen that the maximum average torques of four motors increase almost linearly with the increase of stator loss. Therefore, considering thermal limit, the

maximum torque can be achieved under an optimal combination of split ratio and maximum stator iron flux density. The parameters of four optimized designs are shown in Table 2.2.

As can be seen, four 2-pole motors with different slot numbers have almost the same optimal split ratio and maximum iron flux density, although their maximum torques are slightly different, with the highest torque in the 3- and 6-slot/2-pole HSPM motors.

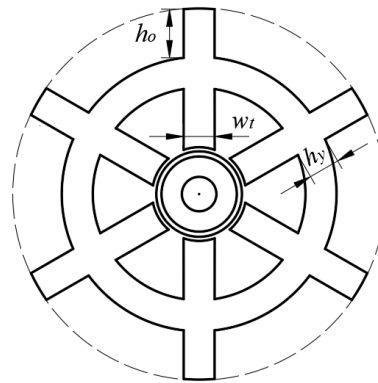


Fig. 2.3. Model of 6-slot/2-pole HSPM motor with toroidal windings.

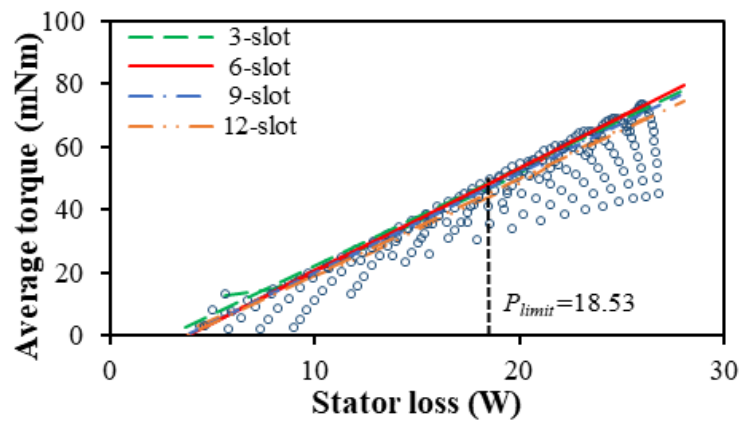


Fig. 2.4. Variation of average torque with stator loss for 2-pole HSPM motors with different slot numbers.

TABLE 2.2
Optimized Design Parameters for Four 2-Pole HSPM Motors

	3-slot	6-slot	9-slot	12-slot
Stator outer diameter D_o , mm			54	
Stator active length l_a , mm			9.1	
Air-gap length l_g , mm			1.25	
Shaft radius R_{shaft} , mm			2.5	

Sleeve thickness, mm				0.3
Number of series turns per phase, N_s				36
Outer tooth height h_o , mm				3.3
Current density, J_s , A/mm ²				12
Rated speed, krpm				110
Split ratio				0.3
Maximum stator iron flux density B_{fe} , T				1.0
Stator yoke height h_y , mm	6.3	6.3	6.3	6.1
Inner tooth width w_t , mm	12.5	6.3	4.1	3.2
Iron loss, P_{fe} W	8.17	8.17	8.09	8.16
Copper loss, P_{cu} , W	10.21	10.22	10.38	10.23
Rotor loss, W	12.69	8.74	8.16	7.97
Torque, mNm	48.72	48.72	47.53	45.81
Torque ripple, %	12.79	13.23	14.49	12.33

2.5 Analysis of Electromagnetic Performance

In this section, the influence of slot number on electromagnetic performance is investigated by FE method, including air-gap flux density, open-circuit flux linkage, back EMF, stator and rotor losses, frame losses, winding inductances, and unbalanced magnetic force (UMF).

2.5.1 Air-gap flux density

Figs. 2.4 and 2.5 show the open-circuit flux distributions and equal potential distributions of 2-pole motors with different slot numbers. It can be seen that they have the same maximum stator iron flux density, except for tooth corners due to local magnetic saturation. Fig. 2.6 shows the air-gap flux density waveforms and spectra of 2-pole motors with different slot numbers. It shows the open-circuit air-gap flux density waveforms are all sinusoidal due to 2-pole magnet with parallel magnetization. The slot number affects the harmonic contents, but does not change the fundamental amplitude since high-speed PM motors generally employ large air-gap length. The MMF generated by the 2-pole PM can be calculated as [EDE01]

$$F_{PM}(\theta, t) = F_{PM} \cos(\theta - \omega t) \quad (2.8)$$

where θ is the air-gap circumferential position.

However, due to slotting effect, there are extra slot harmonics in the air-gap magnetic field. The air-gap permeance distribution of the motor accounting for stator slotting effect can be expressed as:

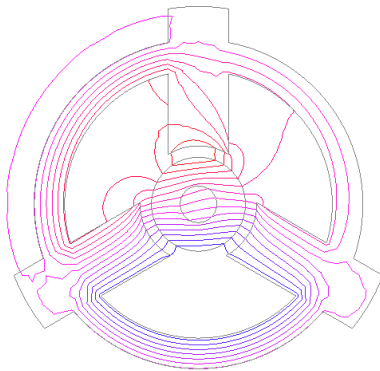
$$P(\theta) = P_0 + P_{kN_{slot}} \sum_{k=1}^{\infty} \cos(kN_{slot}(\theta - \theta_0)) \quad (2.9)$$

where P_0 is the DC component of permeance, $P_{kN_{slot}}$ is the amplitude of Fourier coefficient, N_{slot} is the stator slot number, k is the harmonics index. θ_0 represents the phase difference. According to (2.8) and (2.9), the open-circuit air-gap flux density can be expressed as

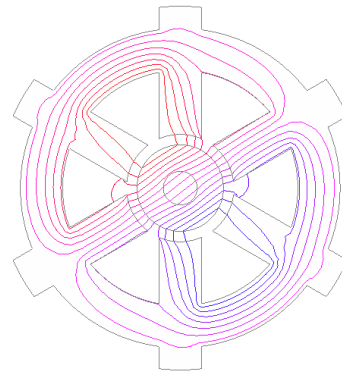
$$\begin{aligned} B_{PM}(\theta, t) &= F_{PM}(\theta, t)P(\theta) \quad (2.10) \\ &= P_0 F_{PM} \cos(\theta - \omega t) + \frac{1}{2} F_{PM} P_{kN_{slot}} \sum_{k=1}^{\infty} \cos(kN_{slot}(\theta - \theta_0)) \\ A &= (kN_{slot} + 1)\theta - kN_{slot}\theta_0 - \omega t \\ B &= (kN_{slot} - 1)\theta - kN_{slot}\theta_0 + \omega t \end{aligned}$$

Therefore, the air-gap flux density has the $(kN_s+1)^{\text{th}}$ and $(kN_s-1)^{\text{th}}$ spatial harmonics.

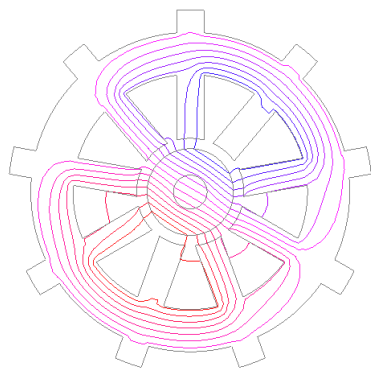
Consequently, the spatial harmonic orders in the air-gap field are 2, 4, 5, 7, ... for the 3-slot motor; 5, 7, 11, 13, ... for the 6-slot motor; 8, 10, ... for the 9-slot motor; and 11, 13, ... for the 12-slot motor. The analytical predictions agree well with the FE results, Fig. 2.6.



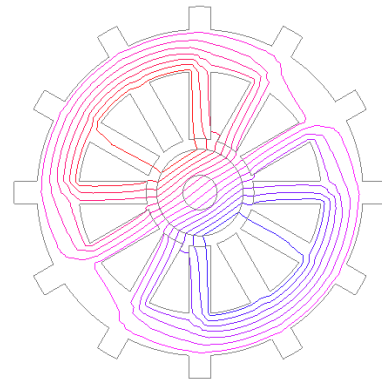
(a) 3-slot



(b) 6-slot



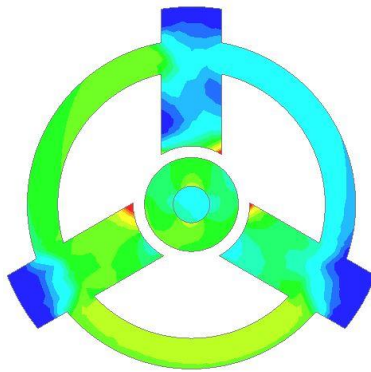
(c) 9-slot



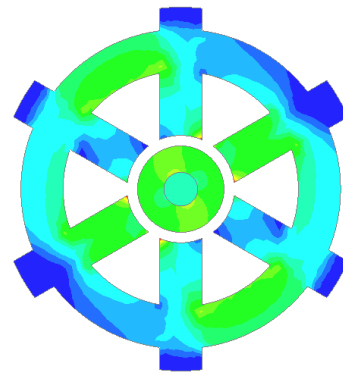
(d) 12-slot

Fig. 2.4. Open-circuit flux distributions of high-speed 2-pole motors with toroidal windings.

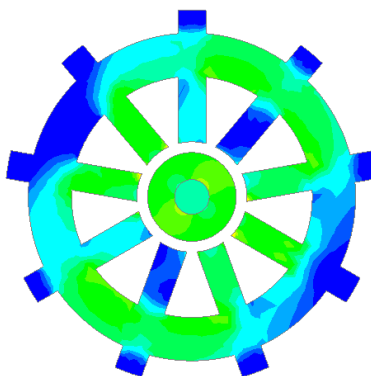
(Rotor positions are chosen for maximum core back flux)



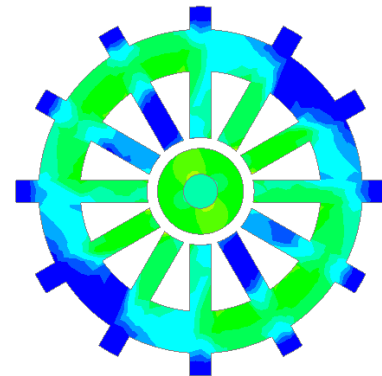
(a) 3-slot



(b) 6-slot



(c) 9-slot



(d) 12-slot

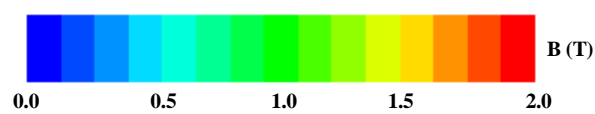
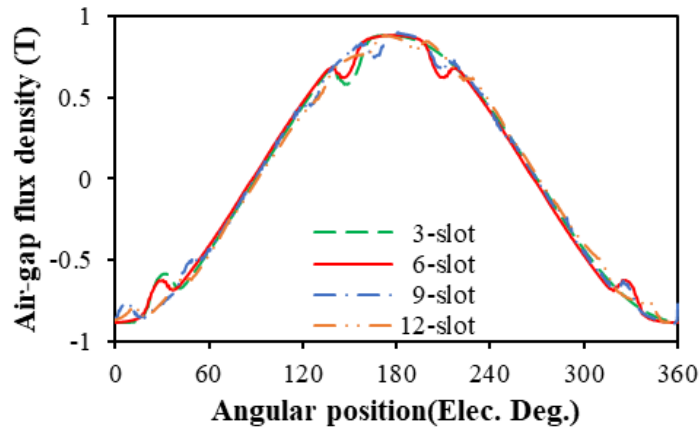
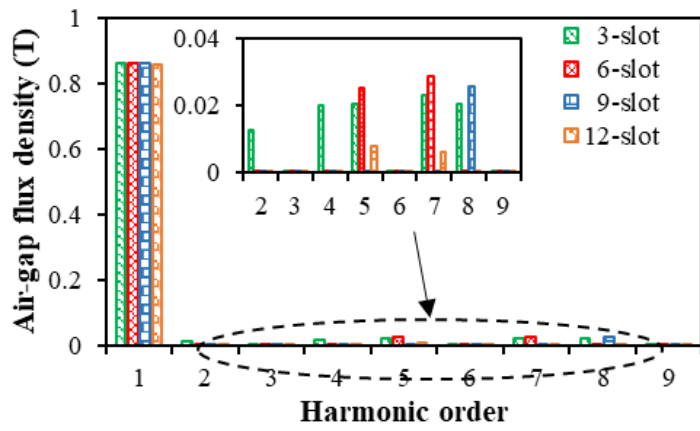


Fig. 2.5. Open-circuit equal potential of high-speed 2-pole motors with toroidal windings.



(a) Waveforms

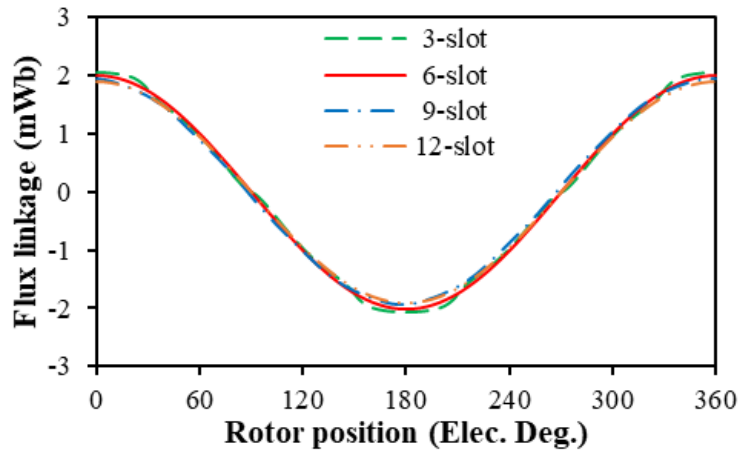


(b) Harmonics

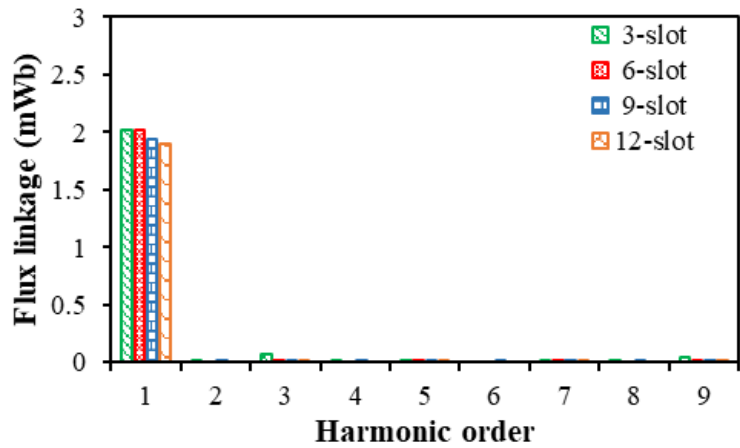
Fig. 2.6. Open-circuit air-gap flux density distributions.

2.5.2 Open-circuit flux linkage

The open-circuit flux linkage waveforms of 3-, 6-, 9- and 12-slot HSPM motors with toroidal windings are shown in Fig. 2.7. The difference in amplitudes for four motors can be mainly attributed to the different fundamental winding factors, Table 2.1, which are 0.5, 0.5, 0.48 and 0.48 for 3-, 6-, 9-, 12-slot/ 2-pole motors, respectively.



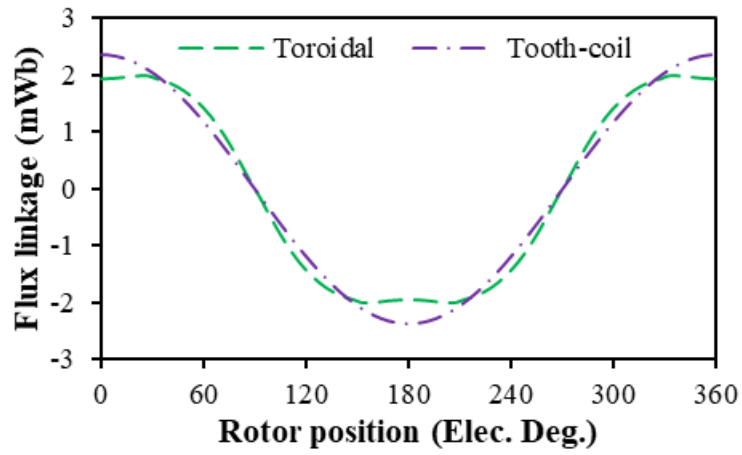
(a) Waveforms



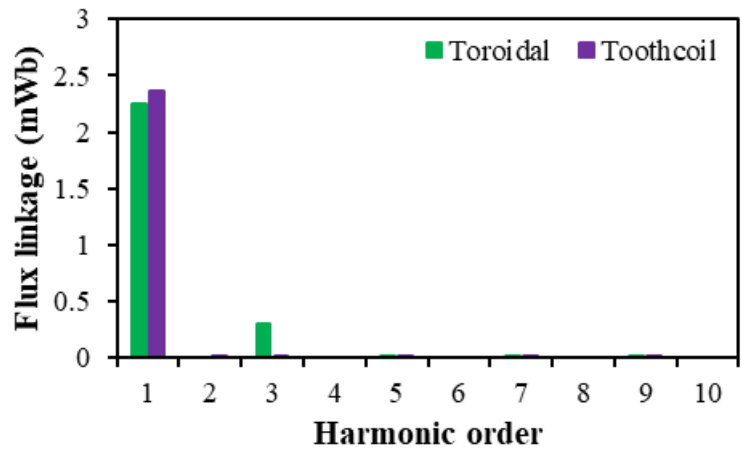
(b) Harmonics

Fig. 2.7. Flux linkages of motors with different slot numbers.

It is worth noting that only the 3-slot motor has the 3rd harmonic in the flux linkage. For toroidal windings, the conductors in outer slot cannot link the flux and thus have no flux linkage, which can be confirmed by the comparison of toroidal and tooth-coil windings. Fig. 2.8 shows different flux linkage waveforms of 3-slot motors with tooth-coil and toroidal windings. However, it still cannot explain the results clearly. Therefore, the investigation of two conductors (A1, A2) in one coil of the motors with toroidal and tooth-coil windings is necessary, Fig. 2.9. The flux linkage waveforms of A1 and A2 conductors are shown in Fig. 2.10. The 3rd harmonic of tooth-coil windings is eventually eliminated by the addition of two conductors due to the same amplitude and opposite phase angle. However, toroidal windings only have one conductor in one coil to link the flux and thus the 3rd harmonic cannot be eliminated. In addition, other topologies with different slot numbers have more than one coils per phase can link the flux and thus the 3rd harmonic can be eliminated.

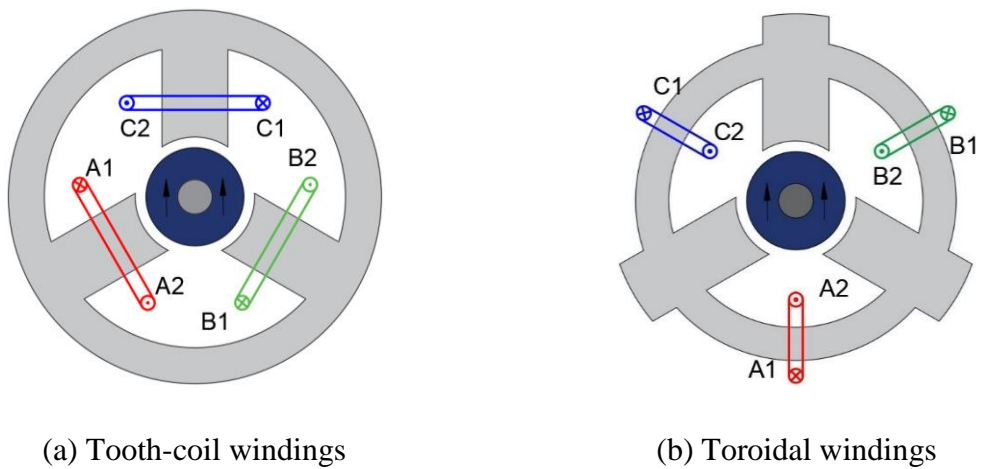


(a) Waveforms



(b) Harmonics

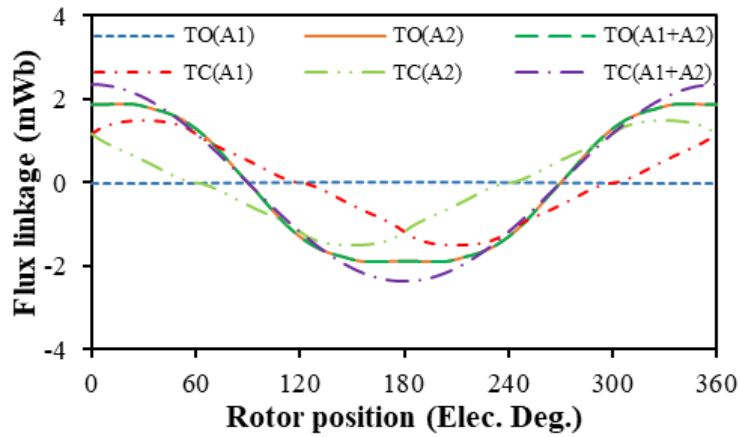
Fig. 2.8. Flux linkages of 3-slot motors with toroidal and tooth-coil windings.



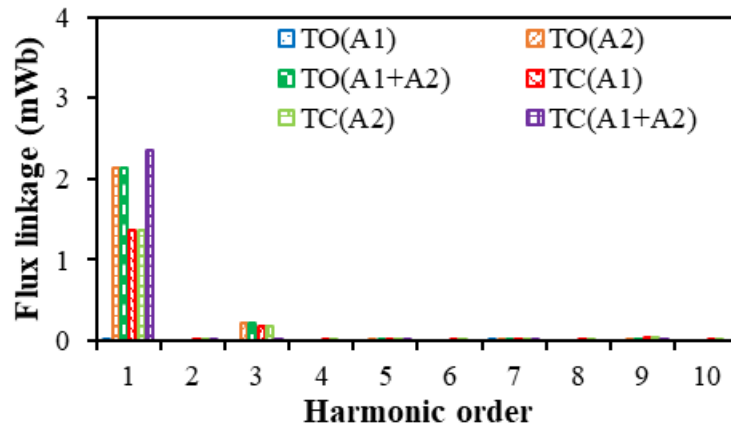
(a) Tooth-coil windings

(b) Toroidal windings

Fig. 2.9. Cross sections of 3-slot motors with tooth-coil and toroidal windings.



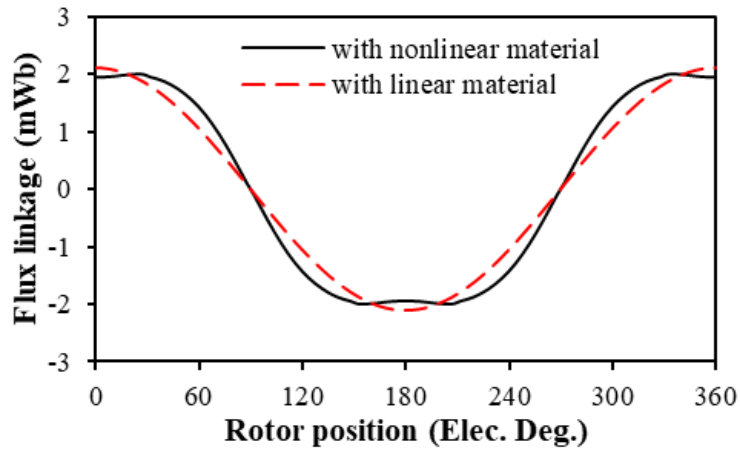
(a) Waveforms



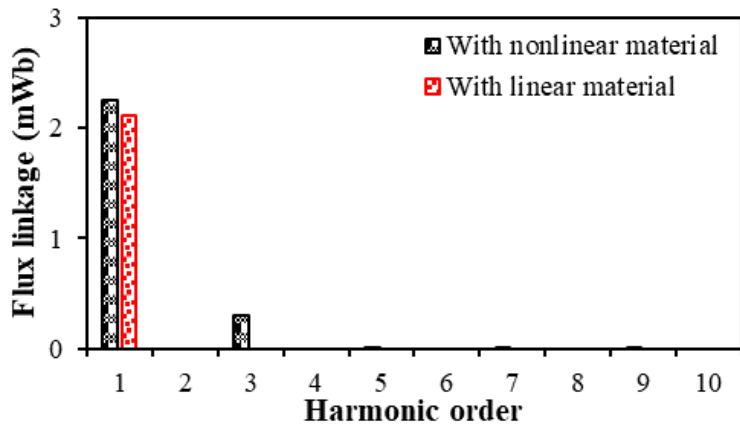
(b) Harmonics

Fig. 2.10. Flux linkages of A1 and A2 coils of 3-slot motors with toroidal (TO) and tooth-coil (TC) windings.

However, when employing linear material for stator lamination, the 3rd harmonic in the 3-slot motor with toroidal windings is disappeared, Fig. 2.11. Therefore, the main reason for the existence of the 3rd harmonic in the 3-slot motor with toroidal windings is the magnetic saturation in the stator core.



(a) Waveforms

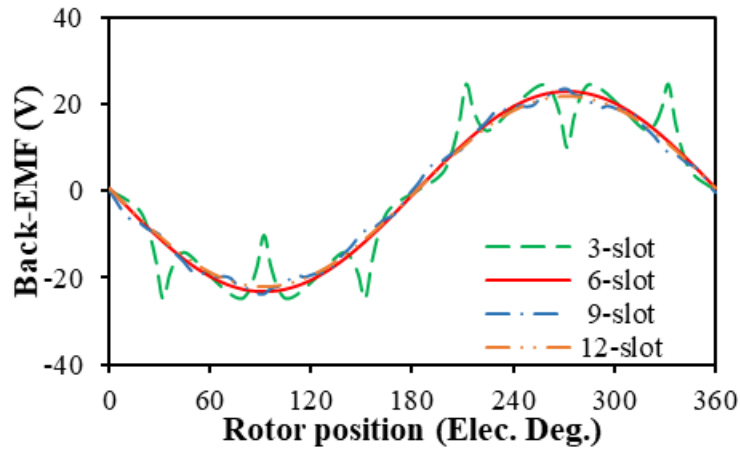


(b) Harmonics

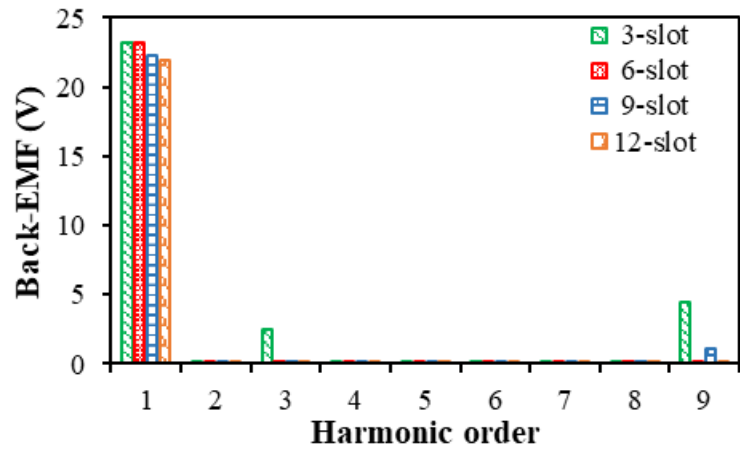
Fig. 2.11. Flux linkages of 3-slot motors employing nonlinear and linear material for stator lamination.

2.5.3 Back-EMF

The back-EMFs of four motors with different slot numbers are compared in Fig. 2.12. Since the back-EMF is proportional to the flux linkage, there are the 3rd and 9th harmonics in the phase back-EMF of the 3-slot motor with toroidal windings although it will disappear in the line back-EMF waveform and do not contribute to the torque.



(a) Waveforms



(b) Harmonics

Fig. 2.12. Back-EMFs of 2-pole motors with different slot numbers.

2.5.4 Cogging torque and electromagnetic torque

Fig.2.13 shows the cogging torque and electromagnetic torque waveforms of four 2-pole motors under ideal brushless DC drive 120-degree square wave current for idealised high-speed operation. Brushless DC drive operation is suitable since (1) the corresponding torque ripple caused by sinusoidal back-EMF waveform and square phase current waveform is less critical for high-speed operation, and (2) sinusoidal air-gap field is beneficial for reducing the iron loss which is important for high-speed operation. Cogging torques in four motors are almost zero due to sinusoidal air-gap field.

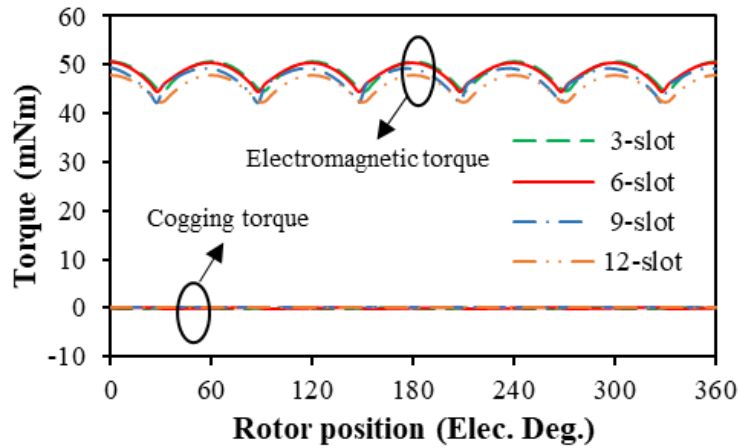
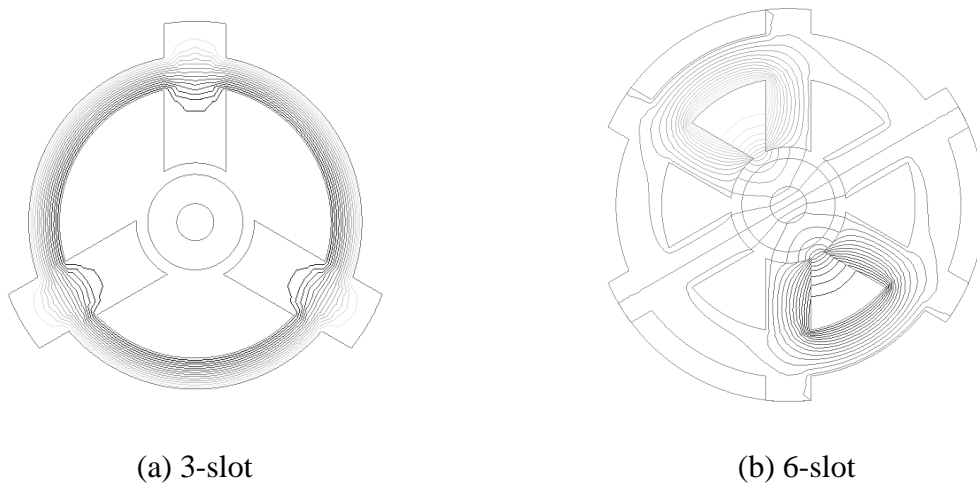


Fig. 2.13. Cogging torques and electromagnetic torques of 2-pole motors with different slot numbers.

2.5.5 Winding inductances

High speed motors normally have relatively small winding inductances for senseless control. The influence of different slot numbers on winding inductances is investigated in this part. The winding inductances are calculated by FEA when only one phase is excited ($I_a=1A$, $I_b=0A$, $I_c=0A$). Fig. 2.14 shows the magnetic field distributions when only phase A is excited. It shows that for 3-slot and 9-slot motors, almost all fluxes pass across the stator yoke, and thus the self- and mutual-inductances are significantly large and both are positive. For 6-slot and 12-slot motors, the mutual-inductance is small and negative, which leads to larger phase inductance compared with 3-slot and 9-slot motors, Table 2.3



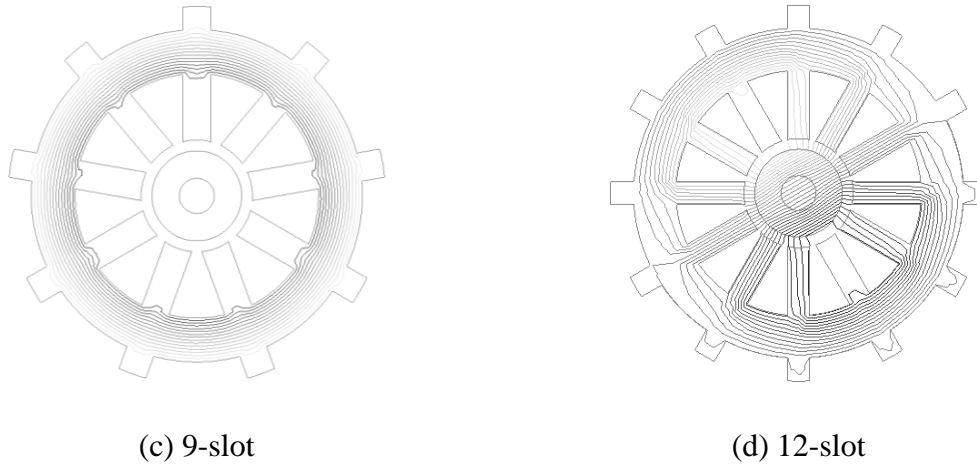


Fig. 2.14. Flux distributions when only phase A winding is excited in 2-pole motors with different slot numbers.

Table 2.3
Inductances for Four 2-Pole HSPM Motors (μH)

	3-slot	6-slot	9-slot	12-slot
Self-inductance	2027.14	17.83	720.20	17.17
Mutual-inductance	2011.48	-1.87	702.84	-2.05
Phase inductance	15.66	19.7	17.36	19.22

2.5.6 Loss analysis

Since the maximum open-circuit flux densities of four optimized motors are the same, the influence of armature reaction is small and the iron volume are similar, and the iron losses of four motors are almost the same, as shown in Fig. 2.15.

Rotor loss is important for PM motors since the generated heat is very difficult to be dissipated. Thus, the rotor temperature rise resulted from the rotor eddy current loss may lead to thermal issues and irreversible demagnetization of PMs. It is even more critical for HSPM motors due to small size and high power density. Therefore, the influence of slot number on the rotor loss of 2-pole motors should be investigated.

In this section, the rotor loss includes eddy current loss in sleeve, PMs, and shaft. Fig. 2.15 shows that the rotor losses decrease with the increase of the slot number, and the 3-slot motor has the largest eddy current losses due to the largest space harmonics. For the fundamental current, the rotor eddy current losses are significantly reduced, Fig. 2.15, since the fundamental field produced by the fundamental armature reaction is in synchronous rotation with the rotor. In another word, the time harmonics of the ideal brushless DC (BLDC) drive 120-degree square

wave current affect the magnetic field significantly, which increases the rotor eddy current loss. Meanwhile, the slot opening effect also induces rotor eddy current losses, particularly for the 3-slot motor which has relatively large slot opening, i.e. large space harmonics.

The copper loss in high-speed PM motors includes DC loss and AC loss due to skin effect and proximity effect. In this section, the skin depth at rated speed is 1.54mm [UZH14], which is larger than the conductor diameter, and thus the skin effect can be neglected. With high frequency, the magnetic field caused by PMs and phase current lead to the proximity effect. In literature [WRO10], the influence of proximity effect on the AC loss of the end-windings is smaller than that of the active length of the conductors. Therefore, the joule losses of four motors with different slot numbers under different frequencies and same phase current are shown in Table 2.4, neglecting end-winding. It shows that the ratios of AC to DC resistance in four motors are almost the same, 1.3 to 1.5, which means the AC loss caused by proximity effect should be considered.

Table 2.4
Joule Losses without End-windings (W)

	3-slot	6-slot	9-slot	12-slot
DC loss	4.81	4.81	4.81	4.81
Joule loss (50Hz)	4.93	4.84	5.46	5.98
Joule loss (1.83kHz)	7.38	7.62	7.22	7.71

The losses in the frame are taken into consideration since the toroidal windings have high external leakage caused by the outer windings, which will inevitably induce eddy currents in neighboring conductive bodies [BOR14]. The material of frame is aluminum for its electrical conductivity and cooling activity. When the frame thickness is less than 3mm, the frame eddy current loss increases sharply, while after that the frame loss remains unchanged due to the skin depth of frame is 2.1mm, Fig. 2.16. In addition, there is almost no influence of slot number on the frame loss.

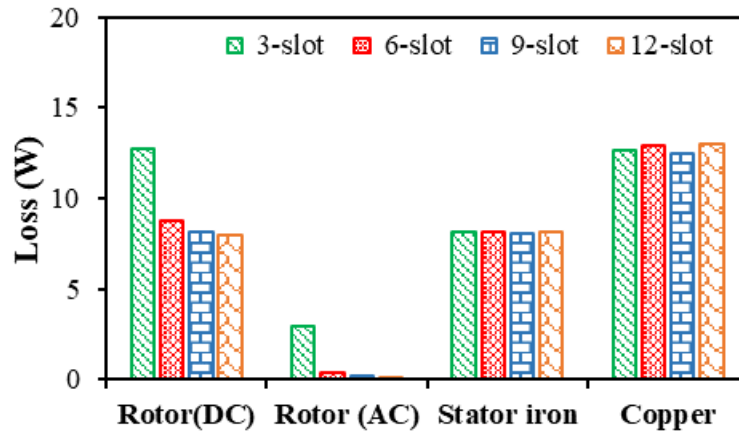


Fig. 2.15. Losses of 2-pole motors with different slot numbers and toroidal windings.

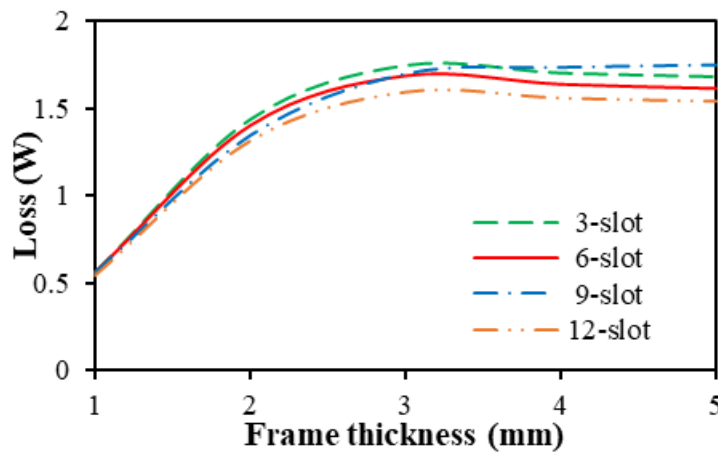


Fig. 2.16. Variation of loss with frame thickness of different slot numbers.

2.5.7 Unbalanced magnetic force

The UMF significantly affects vibration, noise level, and life of bearings, which should be considered carefully in high-speed motors. Fig. 2.17 shows the UMF of 2-pole motors with different slot numbers. It can be seen that the 3-slot motor has the largest UMF whilst the 9-slot motor has smaller UMF due to its smaller 2nd order harmonic in the armature reaction. However, 6-slot and 12-slot motors have no UMF due to the symmetrical stator topology and balanced winding distribution. Therefore, for high-speed application, 6-slot/2-pole and 12-slot/2-pole motors are preferred since they do not have UMF.

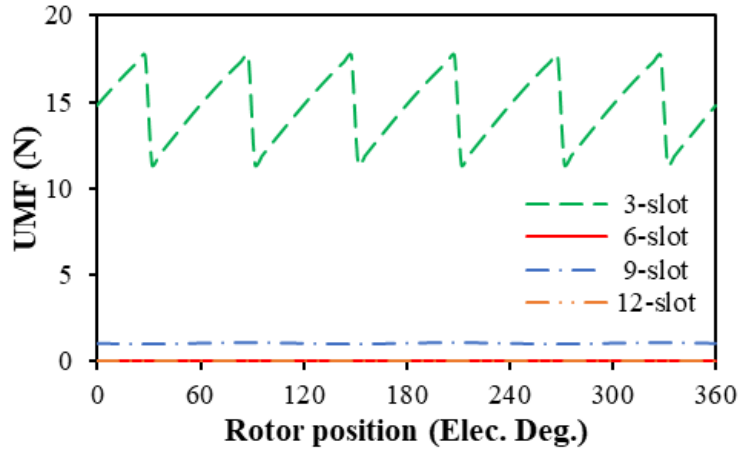


Fig. 2.17. UMF of 2-pole motors with different slot numbers.

2.6 Experimental Validation

In this section, a 6s/2p HSPM motor is manufactured by Midea and tested. Fig. 2.18 shows the prototype motor with toroidal windings, the rotor-bearing-blade system, and the house structure. The phase resistance and winding inductance of the prototype are measured by a LCR meter under 120Hz and 1000 Hz, Table 2.5. It shows that the analytical prediction of resistance is smaller than the measured results due to neglecting the influence of frequency. Under high frequency (1kHz), the measured phase resistance is significantly larger than that under low frequency (120Hz), which means the AC copper loss should be considered in toroidal windings. The FE predicted winding inductance in 2D-FE model is ideal inductance and is slightly larger than the measured inductance under 120Hz due to neglecting end-winding, Table 2.5. With the increase of frequency, the measured inductance decreases. Overall, the measured phase resistance and inductance agree well with analytical and FE predictions.

Fig. 2.19 shows a test rig for the measurement of on-load static torque [ZHU09]. With the phase currents of $I_A = -I_B = 5$ A, $I_C = 0$ A, FE predicted and measured static torques of the 6s/2p HSPM motor have a good agreement at different rotor positions, Fig. 2.20. The maximum static torque increases with the increase of phase current linearly, and the measured static torques are smaller than the FE calculations due to end effect and friction, Fig. 2.21. The comparison of the FE prediction and measurement of three phase back-EMF waveforms is shown in Fig. 2.22, and they have a good agreement. In literature, several high-speed PM motors have been manufactured and tested under high-speed operation but with no measured torque results [PFI10][ZHA16][UZH16][KAZ16][DUG20] since it is very difficult to measure the torque under the high-speed operation. In our case, the rotor shaft of the motor is directly coupled with

the blade which provides the load, as shown in Fig. 2.18(c). Hence, the direct measurement of torque is not possible. Therefore, in this Chapter, the measured back-EMF, phase current, and terminal voltage waveforms of the 6s/2p motor with toroidal windings at the rated speed of 110 krpm are provided in Fig. 2.22(a) and Fig. 2.23. The motor speed is very high so that there are only around 10 PWM waves in each electrical cycle, which makes the current ripple serious and obvious. In addition, small winding inductance will cause current ripple as well.

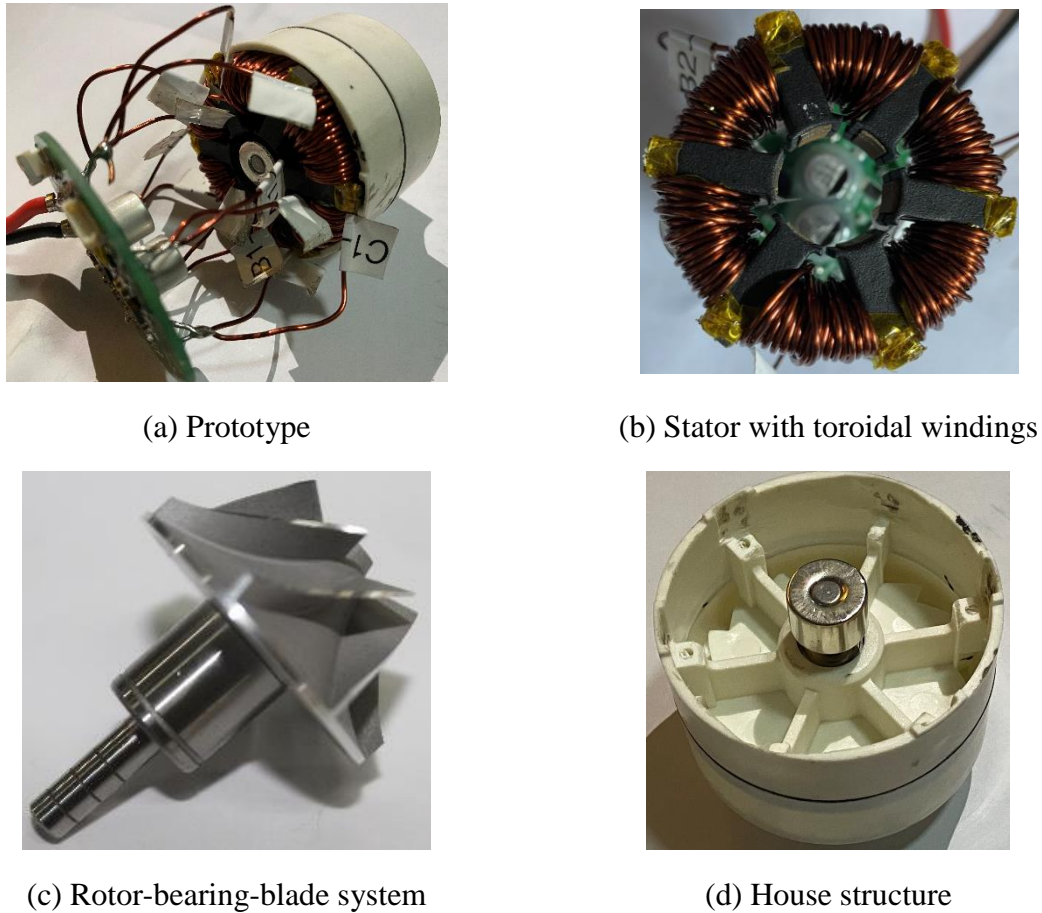


Fig. 2.18. Prototype of the 6s/2p HSPM motor with toroidal windings..

Table 2.5
Predicted and Measured Winding Resistances and Inductances

ANA	Resistance (mΩ)			Inductance (μH)		
	Measured (0Hz)	Measured (120Hz)	Measured (1kHz)	FEM	Measured (120Hz)	Measured (1kHz)
36.3	52.6	54.8	74.0	19.5	25.0	23.4

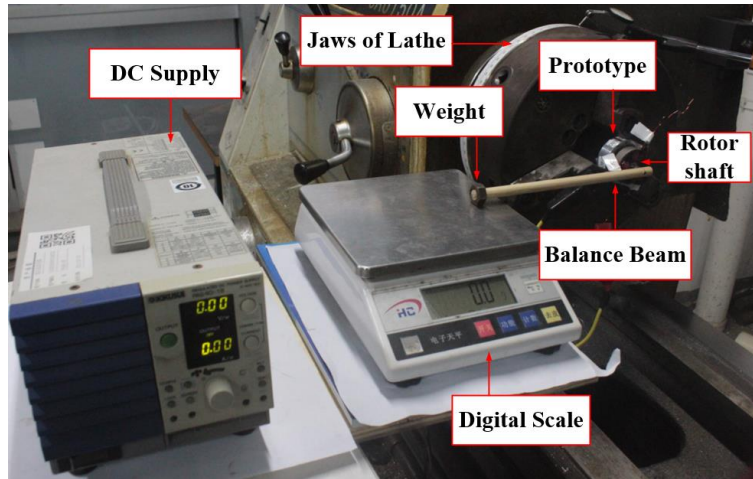


Fig. 2.19. Test rig for static torque measurement.

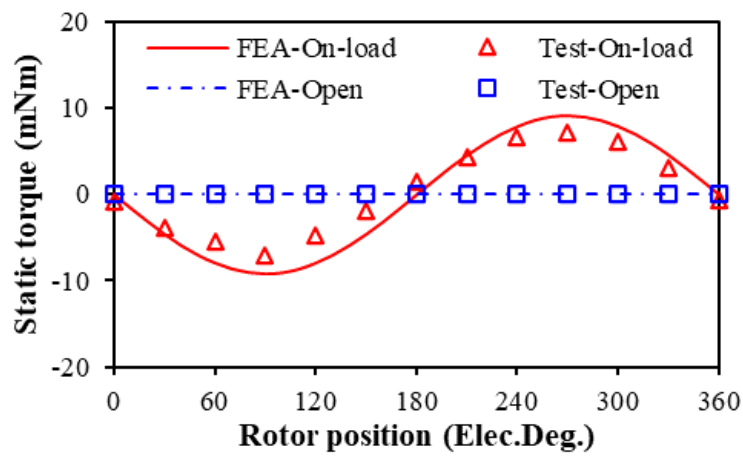


Fig. 2.20. Measured and FE predicted open-circuit and on-load static torques under the phase currents of $I_A = -I_B = 5$ A, $I_C=0$ A.

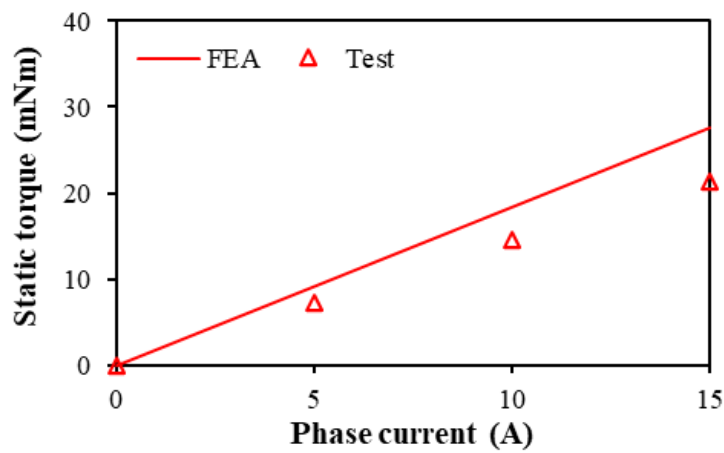
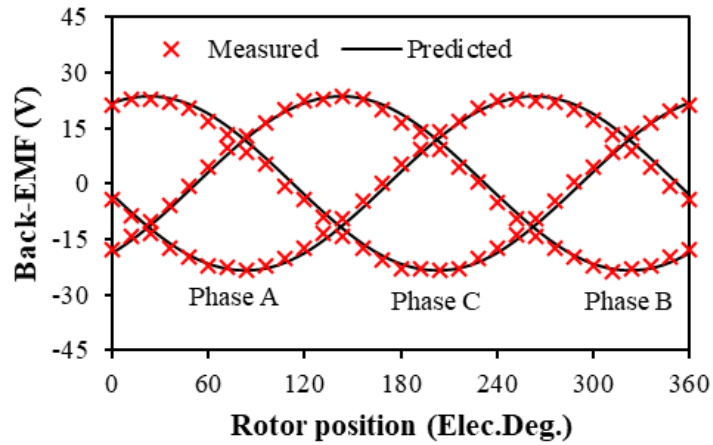
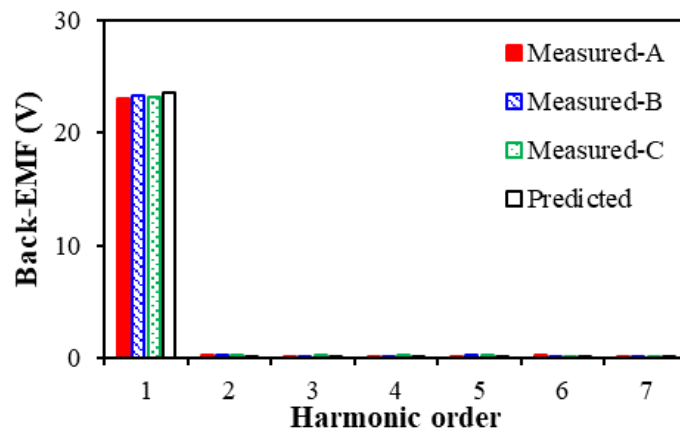


Fig. 2.21. Maximum measured and FE predicted static torques with various phase currents.



(a) Waveforms



(b) Spectra

Fig. 2.22. FE predicted and measured three phase back-EMF waveforms of the 6s/2p HSPM motor at 110 krpm.

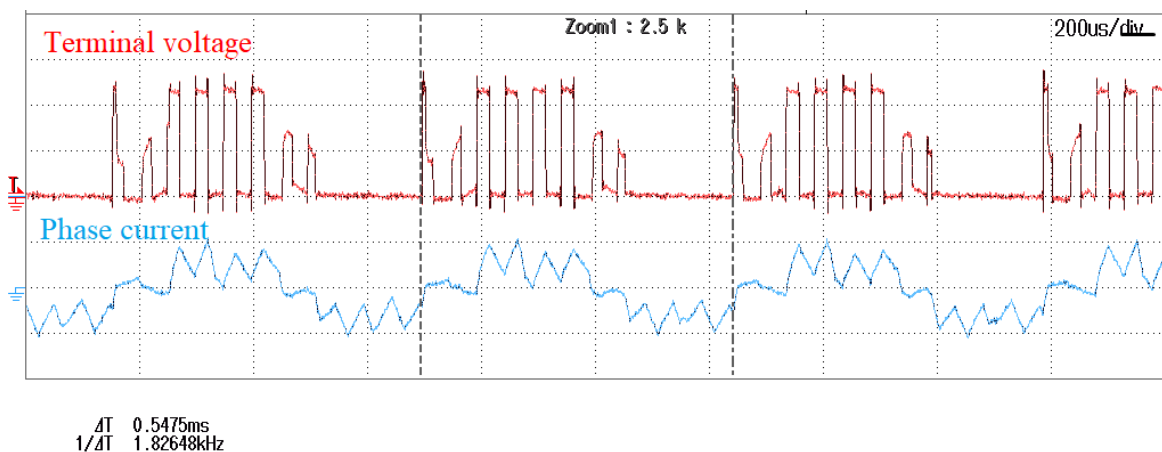


Fig. 2.23. Measured phase current and terminal voltage waveforms of the 6s/2p motor with toroidal windings at the rated speed of 110 krpm, i.e. $f=1.83\text{kHz}$, with speed control (10.0V/div; 20.0A/div; $U_{dc}=25.2\text{V}$).

2.7 Conclusion

In this chapter, the 3-/6-/9-/12-slot, 2-pole low-power small size high-speed PM motors with toroidal windings are optimized and their open-circuit and on-load electromagnetic performances are investigated and compared, including winding factor, air-gap flux density, back-EMF, cogging torque, electromagnetic torque, winding inductances, unbalanced magnetic force (UMF), and various loss components. It shows that the slot number has negligible influence on the optimal split ratio when fixing the current density and allowed maximum stator iron and copper losses. In addition, 6-slot and 12-slot motors are more suitable than 3-slot and 9-slot motors for high-speed application due to non-existence of UMF. Compared with the 12-slot motor, the 6-slot motor has less iron loss and larger torque due to larger winding factor, which is a better choice for high-speed application.

It is worth noting that the 2-pole toroidal winding motors have relatively low winding factor (≤ 0.5), which is almost the same as that of a 6s/2p tooth-coil motor (0.5), and all lower than that of a 3s/2p tooth-coil motor (0.866). However, a 3s/2p motor exhibits unbalanced magnetic force which is critical for high-speed operation, while both 6s/2p tooth-coil and toroidal winding motors have no unbalanced magnetic force.

CHAPTER 3

SPLIT RATIO OPTIMIZATION FOR 6-SLOT/2-POLE HIGH-SPEED PERMANENT MAGNET MOTOR WITH TOROIDAL WINDINGS

Split ratio, i.e. the ratio of stator inner diameter to outer diameter, has a close relationship with electromagnetic performance of permanent magnet (PM) motors. In this chapter, the toroidal windings with short end-winding axial length are employed in the 6-slot/2-pole PM motor for high-speed applications. The split ratio is optimized together with the ratio of inner slot area to total slot area, i.e. slot ratio, considering stator total loss of stator iron loss and copper loss. In addition, the influence of maximum stator iron flux density and tooth-tips on the optimal split ratio, slot ratio, and average torque is investigated. The analytical predictions show that when the slot ratio is 0.5, the maximum torque can be achieved, and the optimal split ratio increases with the decrease of slot ratio, as confirmed by the finite element (FE) analyses. Finally, some of predicted results are verified by the measured results on a 6s/2p prototype motor with 0.5 slot ratio.

3.1 Introduction

High-speed permanent magnet (HSPM) motors have advantages of high power density and high efficiency. They are widely employed in many industrial applications, such as electric turbochargers, automotive m superchargers, micro gas turbines, compressors, blowers, pumps, hybrid electric vehicles, turbo-molecular pumps, and machine tool spindle drives [BIA05] [GER14] [TEN14] [SHE18] [DUG20] [JAN11] [KOL11] [ISM18]. For domestic appliances, e.g. vacuum cleaners, small size low power HSPM motors offer advantages in high power density and high efficiency which are desirable and attractive [ZHU97]. There are different slot/pole combinations has been employed in this area, such as 3-slot/2-pole (3s/2p) PM motor with non-overlapping windings [ZHU97] [HES87], 6-slot/2-pole (6s/2p) PM motors with non-overlapping/overlapping windings [TEN14] [SHI04] [NOG05].

In literature, [HES87] designs a 3s/2p HSPM motor for hand piece tool. The rotor with a solid PM together with stainless steel shaft is designed to improve the mechanical strength for high-speed operation (150 krpm). In [ZHU97], a 20 krpm, a 3s/2p HSPM motor is designed for

friction welding unit. It shows that compared with conventional motors, a high-speed motor with high frequency results in large stator iron loss, which cannot be neglected in the optimization of high speed motor. 3s/2p PM motors with inherent unbalanced magnetic force (UMF) may lead to vibration and noise, and thus, a 6s/2p PM motor with no UMF is more attractive for high speed applications. In [SHI04], a 6s/2p HSPM motor with tooth-coil windings is designed and analyzed. The Inconel material (Inconel-718) for magnet protection covers the rotor surface and the magnets are magnetized radially. The differences between 3s/2p and 6s/2p HSPM motors with tooth-coil windings are compared in [NOG05]. The results show that the 6s/2p motor has less rotor eddy current loss since a 3-slot motor has richer spatial harmonics caused by slotting effect, which is desirable for high-speed application. However, the 6s/2p HSPM motor with non-overlapping windings has relatively low winding factor (0.5). Therefore, a 6s/2p HSPM with two slot-pitch windings is proposed to increase the output torque and torque density since it has large winding factor (0.866) and short axial length [HET21].

As another kind of non-overlapping windings, toroidal windings with short end-winding axial length can be beneficial for better rotor mechanical stiffness under high speed rotation, which have been employed for several applications, such as micro turbine, gas turbine, and air compressor [WAN03] [ZWY05] [BOR14]. [WAN03] and [ZWY05] design a 6s/2p HSPM generator for micro turbines and for mesoscale gas turbine, respectively. In [BOR14], three 6s/2p HSPM motors with different rated speeds (150 W at 200 krpm, 42 W at 90 krpm, 3.7 kW at 240 krpm) are designed. It is found that the high external leakage of the armature field of toroidal windings will lead to eddy current losses in the housing, which may account for 50% of total motor loss and should be considered. [XUF21] investigates the effect of slot number on the electromagnetic performances of 2-pole HSPM motors with toroidal windings, accounting for back electromotive forces (back-EMF), cogging torque, electromagnetic torque, different loss components including losses in the housing, winding inductance, and UMF. Overall, toroidal windings have advantages of short end-winding axial length, simple structure, easy manufacturing process, and modular design

In general, when the stator outer diameter is fixed, the design of stator inner diameter, i.e. split ratio SR, has a great effect on motor torque, power capability and overall manufacturing cost [HES87] [CHA94] [CHA00]. In literature, the optimal SR has been investigated under different design considerations and restrictions [ISM18] [EDE01] [PAN06] [WAN18] [MAJ19] [REI13]. For low- and moderate-speed PM motors with overlapping and non-overlapping windings, the optimal SR has been investigated comprehensively in [PAN06]. Moreover, the

influences of operation mode, air-gap flux density distributions, tooth-tips and end-windings on optimal SR are discussed. For HSPM motors, [ISM18] analyses the optimal SR and optimal flux density ratio by analytical method. Considering the stator iron loss, [EDE01] optimizes the SR for the highest efficiency. [WAN18] considers the stator iron loss and mechanical constraints for optimal SR in 6s/4p HSPM motor. [MAJ19] derives an analytical expression of the optimal SR accounting for both stator and rotor loss limitations in small size HSPM motors. For HSPM motors with toroidal windings, [XUF21] uses finite element (FE) method to optimize the SR for maximum torque with fixed current density and stator thermal limitation. However, the outer slots of motors with toroidal windings can be used as the cooling channels to improve the heat dissipation capability under the forced-air cooling. Therefore, different outer and inner slot areas may affect the optimal SR, which has not been investigated before. In this paper, the effect of the slot ratio, i.e. the ratio inner slot area to total slot area, on the optimal SR of the 6s/2p HSPM motor with toroidal windings (TWHSPM) will be investigated considering the stator total loss.

In section 3.2, the motor topology including end-winding model are described. The optimal SR for maximum torque with fixed stator total loss is investigated analytically in section 3.3. The influence of different design parameters on the optimal SR, including slot ratio, maximum stator iron flux density, and tooth-tips are illustrated in Section 3.4. A prototype motor is manufactured and tested in section 3.5. Section 3.6 is the conclusion.

3.2 Motor Topology

The cross section of a 6s/2p TWHSPM motor is shown in Fig. 3.1. The slot is divided into inner and outer slots by stator yoke due to toroidal winding configuration. The toroidal windings mean the winding is wound on the stator yoke, one side of the coil is located in the outer slot and the other side is located in the inner slot. It is worth noting that the connection polarities of the coils A1 and A2 for the same phase in the inner slot are opposite, Fig. 3.1. Under high-speed operation, a 2-pole ring magnet with diametric magnetization is adopted to reduce the operating frequency and also reduce the iron loss due to sinusoidal air-gap field. The rotor magnet is protected by a stainless steel sleeve, and a magnetic shaft is adopted to improve the output torque. In addition, the straight tooth without tooth-tips is employed for simplifying manufacture process. Table 3.1 shows the basic parameters of the motor.

For motor with toroidal winding, only conductors in the inner slot of winding can effectively link the flux and produce the back-EMF, the rest conductors, i.e. the conductors in the outer slot only form the current circuit loop. Therefore, the winding factor (k_w) of the 6s/2p combination is 0.5 as the winding in the outer slot can be treated as a part of end-winding [XUF21]. Fig. 3.2 shows the end-winding model includes two end parts linking the outside and inside conductors which are assumed to be semi-circular. The total end-winding length (l_e) of one coil can be calculated as

$$l_e = 2l_{er} + l_a = 2 \left[\frac{\pi}{2} \left(\frac{h_{out} + h_{in}}{2} + h_y \right) + 4l_{ex} \right] + l_a \quad (3.1)$$

where h_{out} , h_{in} and h_y depict the outer tooth height, the inner tooth heights, and the stator yoke height, respectively. l_{er} and l_a are the radial end-winding length and the stator active length, respectively. In addition, based on the manufactory process the extra part of end-winding length (l_{ex}) is variable and considered in this paper.

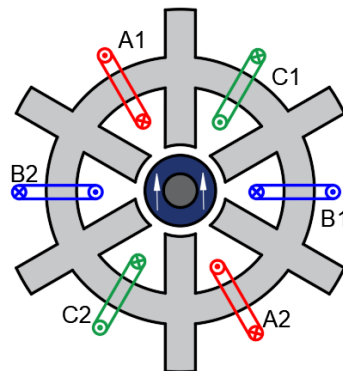
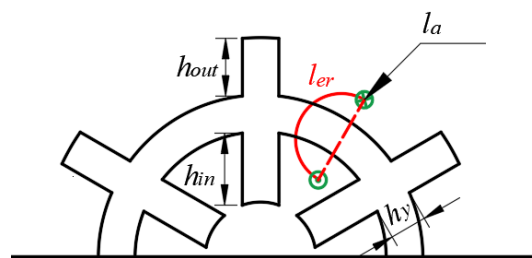
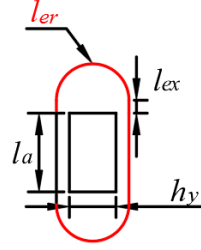


Fig. 3.1. Cross section of the 6s/2p TWHSPM motor.



(a) Model 1



(b) Model 2

Fig. 3.2. End-winding model of the motor with toroidal windings.

Table 3.1
Basic Parameters of TWHSPM Motor

Rated speed (krpm)	110	Shaft diameter (mm)	5
Stator outer radius (mm)	27	Remanence (T)	1.3
Stator active length (mm)	9.1	Magnetization	Parallel
Air-gap length (mm)	1.55	Number of series turns per phase	37

3.3 Design and Optimization

In this section, the SR of the 6s/2p TWHSPM motor is optimized for maximum average torque by analytical method. It is assumed that the inner slot area equals to outer slot area, and the outer tooth and inner tooth have the same width although the outer teeth are only used for mechanical supporting. In HSPM motors, high frequency will result in large stator iron loss. Therefore, the optimal SR of the HSPM motor takes both stator iron loss and copper loss into account. The stator iron loss are calculated by the Bertotti module [BER88]

$$P_{fe} = m_{fe} W_{fe} \quad (3.2)$$

$$W_{fe} = k_{hy} f B_{fe} + k_{ex} f^{1.5} B_{fe}^{1.5} + k_{ec} f^2 B_{fe}^2 \quad (3.3)$$

where W_{fe} represents the iron loss density, k_{hy} , k_{ex} , and k_{ec} depicts the hysteresis coefficient, the eddy current coefficient, and the excess loss coefficient. f and B_{fe} depicts the fundamental frequency and the maximum stator iron flux density. m_{fe} is the stator mass

$$m_{fe} = \rho_{fe} A_{fe} l_a = \rho_{fe} l_a \left\{ \frac{[(D_s - h_{out})^2 - (D_s - h_{out} - D_i)^2] \pi}{4} - A_{sin} \right\} \quad (3.4)$$

where ρ_{fe} and D_i depict the iron mass density and the stator inner diameter, A_{sin} is the inner slot area, A_{fe} is the stator iron area without the area of outer slot teeth since there are no flux in outer slot teeth and their iron flux densities are equal to almost zero.

In order to limit the motor operating temperature, the optimization employs a fixed stator loss, which counts for stator iron loss and copper loss. In this case, under forced-air cooling, the stator thermal limitation can be derived as [BIA05] [BIA04]

$$P_{limit} = h v_m \pi D_s l_a \quad (3.5)$$

where D_s is the stator outer diameter. h is the overall heat transfer coefficient of 100 W/(°C m²). Accounting for 'E' insulation class, the winding hotspot temperature must be lower than the maximum allowed temperature v_m of 120 degrees for slotted structure. As mentioned in section II, the coils are wound toroidally, and thus, the length of end-winding is not negligible. In general, HSPM motors are designed under 120° electrical brushless DC operation mode. Therefore, the copper loss is given by

$$P_{cu} = 2 I_a^2 \rho_{cu} \frac{(l_a + l_e) N_s}{A_{cond}} \quad (3.6)$$

where I_a , ρ_{cu} , N_s and A_{cond} depict the amplitude of phase current, the resistivity of copper; the number of series turns per phase and the cross section area of conductors, respectively. Since the copper loss equals to $(P_{limit} - P_{fe})$, the amplitude of phase current is given by

$$I_a = \sqrt{\frac{(P_{limit} - P_{fe}) A_{cond}}{2 \rho_{cu} (l_a + l_e) N_s}} \quad (3.7)$$

and the electromagnetic torque (T_{em}) is obtained as

$$T_{em} = \frac{3\sqrt{3}}{\pi} D_g l_a N_s k_w B_g I_a = \frac{3\sqrt{3}}{\pi} B_g (D_i - l_g) l_a N_s k_w \sqrt{\frac{(P_{limit} - P_{fe}) A_{cond}}{2 \rho_{cu} (l_a + l_e) N_s}} \quad (3.8)$$

where l_g and B_g depict the air-gap length and the maximum air-gap flux density. D_g is the diameter of middle of the equivalent air-gap. B_g can be calculated by (3.9)

$$B_g = \frac{B_r \left[1 - \frac{R_r^2}{R_m^2} \right] \left[\frac{R_m^2}{R_i^2} - \frac{R_m^2}{(R_i^2 - \frac{l_g}{2})^2} \right]}{\left[1 + \frac{R_m^2}{R_r^2} \right] \left[1 - \frac{R_r^2}{R_m^2} \right] + \mu_r \left[1 - \frac{R_m^2}{R_r^2} \right] \left[1 + \frac{R_r^2}{R_m^2} \right]} \quad (3.9)$$

where B_r and μ_r are the remanence and relative recoil permeability of the magnet. R_i , R_m , and R_r denote the stator inner radius, the rotor outer radius, and the shaft outer radius, respectively.

As mentioned before, equation (3.3), the frequency and B_{fe} , are the main factors to the calculation of the stator iron loss. According to equation (3.2), stator iron loss also depends on stator core volume, which can be calculated by

$$B_g A_g = B_m A_m \quad (3.10)$$

$$B_m A_m = B_{fe} A_{fe} \quad (3.11)$$

where A_g and A_m are the air-gap area and the permanent magnet area, respectively.

For the 6s/2p PM motor, the stator tooth width is the same as the stator yoke height [PAN06]. Therefore, the stator tooth width (w_t) and the stator yoke height (h_t) can be calculated by B_g and B_{fe} according to (3.10) and (3.11)

$$w_t = h_t = \frac{(R_i - \frac{l_g}{2}) B_g}{\pi B_{fe}} \quad (3.12)$$

Then, with a fixed packing factor and the same inner and outer slot areas, the cross section area of conductors (A_{cond}) can be calculated. Therefore, the electromagnetic torque can be presented as a function of the split ratio (λ) and B_{fe} , and equation (3.8) can be rewritten by

$$T_{em} = 2l_a N_s k_w \sqrt{\frac{1}{2\rho_{cu} N_s}} f(\lambda, B_{fe}) \quad (3.13)$$

where

$$f(\lambda, B_{fe}) = (\lambda D_s - l_g) B_g(\lambda) \sqrt{\frac{A_{cond}(\lambda, B_{fe})}{l_a + l_e(\lambda, B_{fe})}} \sqrt{P_{limit} - P_{fe}(\lambda, B_{fe})} \quad (3.14)$$

For a given B_{fe} , the optimal SR for the maximum average torque can be obtained by

$$\frac{\partial f(\lambda)}{\partial(\lambda)} = 0 \quad (3.15)$$

Fig. 3.3 depicts the effects of SR and B_{fe} on the average torque. It can be observed that for each B_{fe} , the torque increases at first and then drops with the increase of SR. The same trend can be observed for the relationship between the maximum average torque and B_{fe} . Therefore, with an optimal combination of SR and B_{fe} , the maximum average torque can be achieved. Fig. 3.4 shows the variations of FE and analytically predicted average torques with SR under the optimal B_{fe} (1.2T). The results predicted by FE and analytical methods have a good agreement in optimal SR and only a slight difference exhibited in the average torque.

As mentioned before, the stator iron loss is considerably large due to high frequency, and thus the effects of the considered stator iron loss on the optimal SR is analyzed in this section. Fig. 3.5 depicts the effect on average torque with SR by considering and neglecting stator iron loss. It is clear that compared with considering copper loss only, the considered stator iron loss decreases not only the optimal SR but also the maximum average torque. With the fixed stator loss, the considered stator iron loss leads to the reduced copper loss, thus the reduced electric loading and maximum average torque. In addition, the influence of stator iron loss on the optimal SR can also be verified by FE method, Fig. 3.4, and the analytical and FE predicted torques have a good agreement. Table 3.2 shows the optimized design of the 6s/2p TWHSPM motor.

Table 3.2
Optimized Parameters of Motor with Toroidal Windings

Optimal split ratio	0.3	Inner tooth width (mm)	5.4
Maximum iron flux density (T)	1.2	Inner tooth height (mm)	10
Stator inner radius (mm)	8.1	Stator yoke height (mm)	5.4
Magnet thickness (mm)	4.1	Average torque (mNm)	50.9

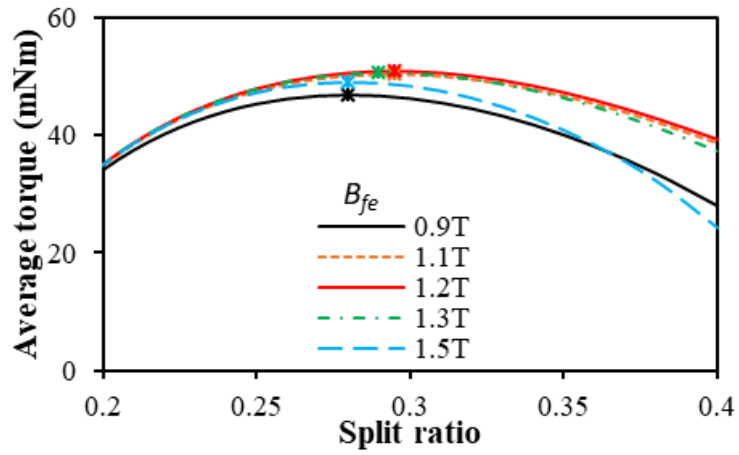


Fig. 3.3. Relationship between average torque and SR with different B_{fe} .

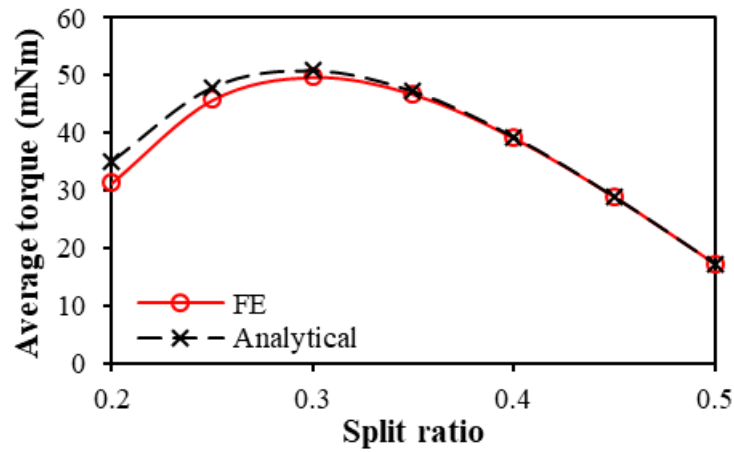


Fig. 3.4. Variation of FE and analytically predicted average torques with SR ($B_{fe}=1.2T$).

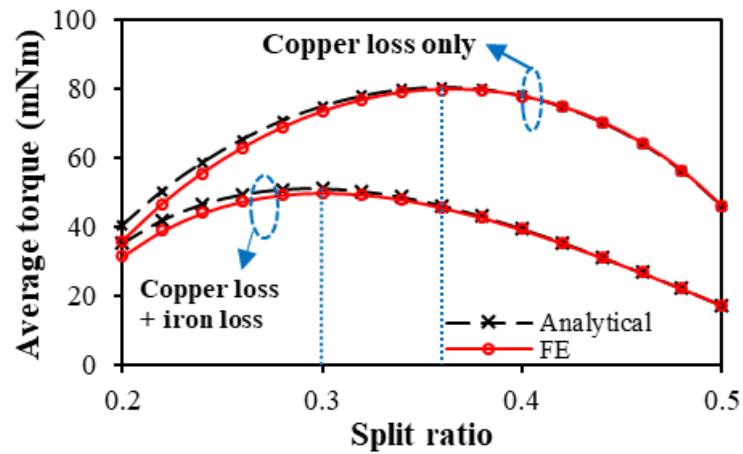


Fig. 3.5. Variation of average torque with SR by analytical and FE methods ($B_{fe}=1.2T$).

3.4 Influence of Design Parameters on Optimal Split Ratio

3.4.1 Influence of slot ratio

In section 3.3, the inner and outer slot areas are assumed to be the same. However, the outer slot area usually is designed to be larger than the inner slot area for the forced-air cooling requirement. Thus, the slot ratio (K_a), i.e. the ratio inner slot to total slot is introduced to determine the influence of the unequal inner and outer slot areas on the optimal SR, Fig. 3.6. It should be noted that during the variation of the slot ratio, different inner and outer slot areas lead to different packing factors. Since the packing factor in the smaller slot area is larger than that in the larger slot area, the required packing factor is employed in the slot with smaller area and the packing factor in the slot with larger area can subsequently be calculated.

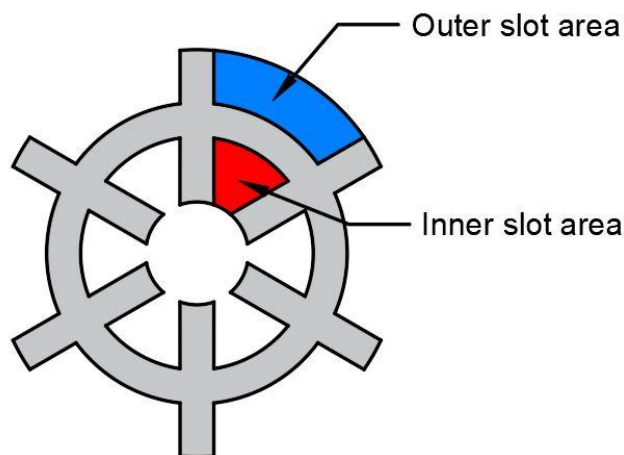


Fig. 3.6. Inner and outer slot areas of 6s/2p TWHSPM motor.

Slot ratio should be taken into consideration since it affects the stator iron volume, which will influence the calculation of stator iron loss. Although different slot ratios lead to different end-winding radial lengths, the influence of the copper loss of end-winding radial lengths on the optimal SR is very small considering stator iron loss. Therefore, the torque calculation can be rewritten as

$$T_{em} = \frac{3\sqrt{3}}{\pi} l_a N_s k_w \sqrt{\frac{1}{2\rho_{cu} N_s}} f(\lambda, B_{fe}, K_a) \quad (3.16)$$

where

$$f(\lambda, B_{fe}, K_a) = (\lambda D_i - l_g) B_g(\lambda) \sqrt{\frac{A_{cond}(\lambda, B_{fe}, K_a)}{l_a + l_e(\lambda, B_{fe})}} \sqrt{P_{limit} - P_{fe}(\lambda, B_{fe}, K_a)} \quad (3.17)$$

and

$$A_{cond} = \begin{cases} A_{sin} k_p & (K_a \leq 0.5) \\ A_{sout} k_p & (K_a > 0.5) \end{cases} \quad (3.18)$$

With the given B_{fe} and K_a , the optimal SR can be obtained by

$$\frac{\partial f(\lambda)}{\partial(\lambda)} = 0 \quad (3.19)$$

It is assumed that the B_{fe} is fixed as 1.2T, which is the optimal value when the slot ratio is 0.5. Fig. 3.7 shows the variation of average torque with SR under different slot ratios. It can be seen that for each given slot ratio, the average torque increase at first and then drops with the SR increases, which means the optimal SR for maximum torque can be achieved. Fig. 3.8 depicts the effect of slot ratio on the maximum average torque and optimal SR. It shows that with a fixed B_{fe} , the increased slot ratio decreases the optimal SR linearly and the maximum average torque can be achieved when the slot ratio is 0.5. The results can be explained by the active slot area, as shown in Figs. 3.9 and 3.10. The motor with $K_a=0.5$ has the largest active slot area and thus it has the largest average torque, Fig. 3.9. For the optimal SR, the differentials of active slot area curves against SR are shown in the Fig. 3.10. It depicts that the differential values increase when the slot ratio increases, and thus the motor with larger slot ratio has smaller optimal SR. It must be noted that the slot ratio also affects the total slot area, which leads to the different active slot areas between $K_a=0.1/0.9$, $0.3/0.7$, Fig. 3.11.

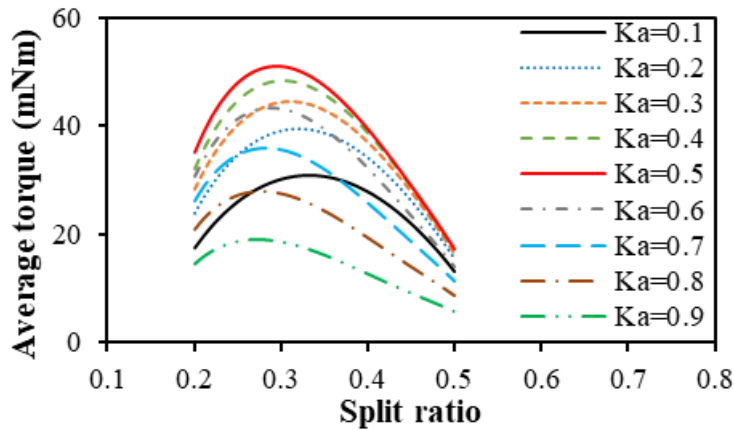


Fig. 3.7. Relationship between average torque and SR under different slot ratios ($B_{fe} = 1.2T$).

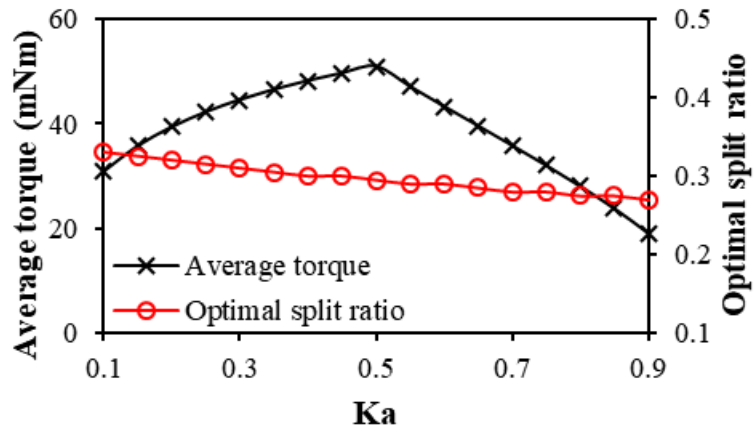


Fig. 3.8. Relationship between average torque and optimal SR with slot ratio Ka ($B_{fe} = 1.2T$).

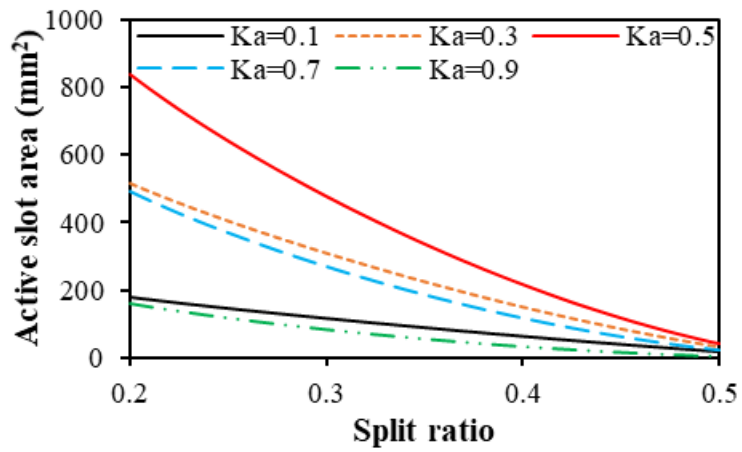


Fig. 3.9. Influence of SR on active slot area under different slot ratio Ka. ($B_{fe} = 1.2T$).

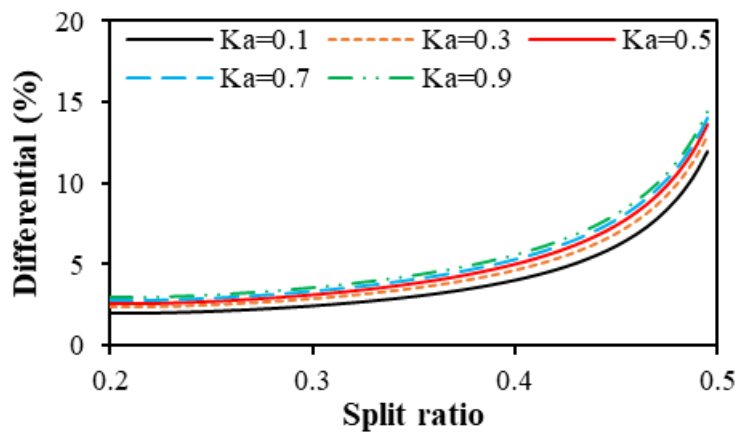


Fig. 3.10. Variation of differential active slot area curves against SR under different Ka ($B_{fe} = 1.2T$).

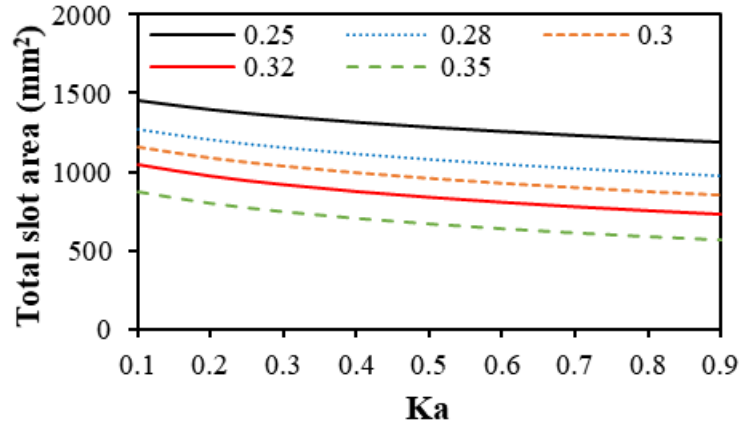


Fig. 3.11. Variation of total slot area with slot ratio Ka under different SR ($B_{fe} = 1.2T$).

3.4.2 Influence of maximum stator iron flux density

As stated in Section 3.3, the maximum stator iron flux density B_{fe} has important influence on the stator iron loss, which affects the optimal SR with fixed stator loss. In order to investigate the effect of B_{fe} on the relationship between optimal SR and slot ratio, different B_{fe} are selected. Figs. 3.12 and 3.13 show the variation of average torque with SR under different slot ratios when B_{fe} is 0.9 T and 1.5T, respectively. It is clear that the maximum average torque can also be achieved when the slot ratio is 0.5. Fig. 3.14 depicts the influence of B_{fe} and slot ratio on optimal SR. It shows that for any given B_{fe} , the optimal SR drops with the increase of slot ratio. When B_{fe} is larger than 1, the influence of K_a on the optimal SR is significantly large, i.e. large variation range of optimal SR. When B_{fe} is less than 1, the influence of K_a on the optimal SR is relatively small, i.e. small variation range of optimal SR, Fig. 3.14. Therefore, the optimal SR of the case of B_{fe} larger than 1 is sensitive to the slot ratio, and that of the case of B_{fe} less than 1 is relatively insensitive. Fig. 3.15 depicts the relationship between maximum average torque and slot ratio under different B_{fe} . It indicates that for any given B_{fe} , the peak value of the maximum torque can be achieved when the slot ratio is 0.5. In addition, the maximum torque difference between different B_{fe} decreases with the increase of slot ratio, when it is larger than 0.5. However, when the slot ratio is smaller than 0.5, the optimal B_{fe} for the maximum torque rises with the decreases of slot ratio. Therefore, considering the design of forced-air cooling channel, i.e. the slot ratio less than 0.5, the relatively large B_{fe} can be selected for enhancing the torque capacity.

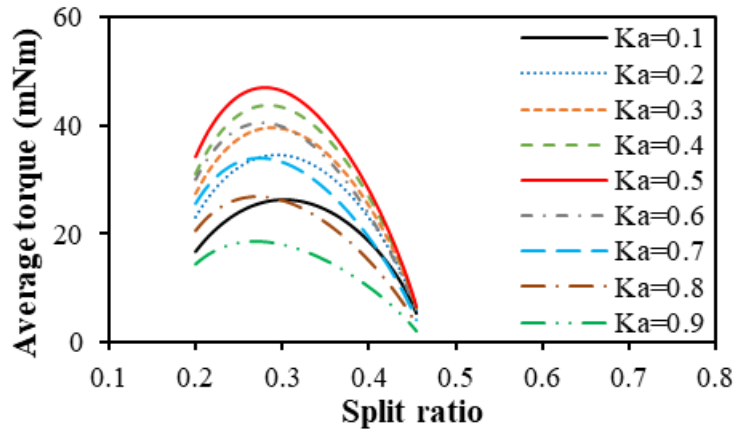


Fig. 3.12. Relationship between average torque and SR ($B_{fe}=0.9T$).

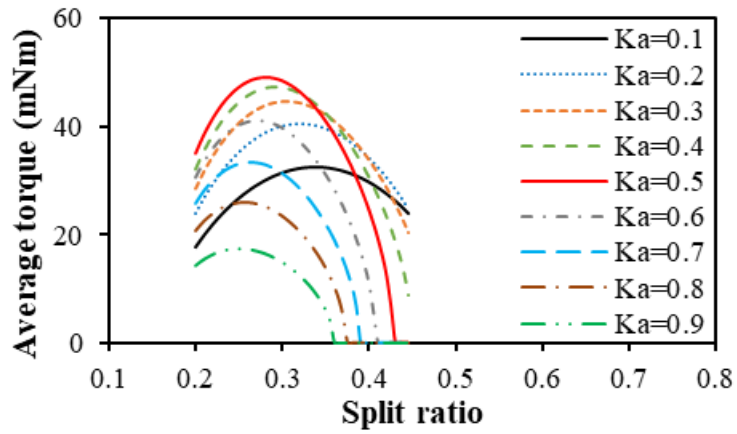


Fig. 3.13. Relationship between average torque and SR ($B_{fe}=1.5T$).

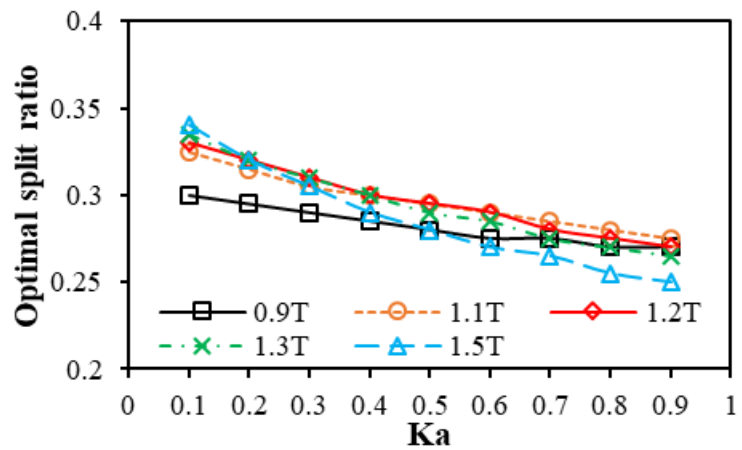


Fig. 3.14. Influence of K_a on optimal SR under different B_{fe} .

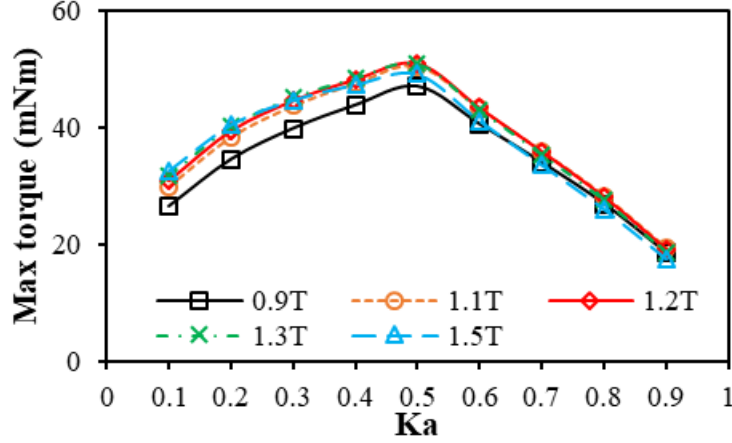


Fig. 3.15. Relationship between K_a and maximum average torque with different B_{fe} .

3.4.3 Influence of tooth-tips

In the foregoing analyses, the motor employs straight tooth without tooth-tips for simplifying manufacturing process. However, the tooth-tips can reduce the leakage flux and increase the phase inductance. Therefore, in this section, the influence of tooth-tips on the maximum torque and optimal SR will be investigated. The cross section of the 6s/2p TWHSPM motor with tooth-tips is illustrated in Fig. 3.15. The active slot area considering the tooth-tips can be given by

$$A_{sin} = \pi \left[\begin{array}{l} h_{out}^2 + h_t^2 + 2h_{out}h_t - (D_s + \frac{N_s w_t}{\pi})h_{out} - (D_s + \frac{N_s w_t}{\pi})h_t \\ -h_t^2 - 2\pi h_t - \frac{N_s w_t}{\pi} \frac{D_s}{2} (1 - \lambda) + \frac{N_s w_t}{\pi} h_t \end{array} \right] \quad (3.20)$$

where h_t is the tooth-tip height.

Fig. 3.17 depicts when the slot ratio is 0.5, the effect of SR under different B_{fe} with 1mm tooth-tip thickness on average torque. The analytical and FE-predicted torques with and without tooth-tips have a good agreement, Fig. 3.18. For a given B_{fe} , tooth-tips have almost no influence on the variations of maximum torque and optimal SR with slot ratio, as shown in Figs. 3.19 and 3.20.

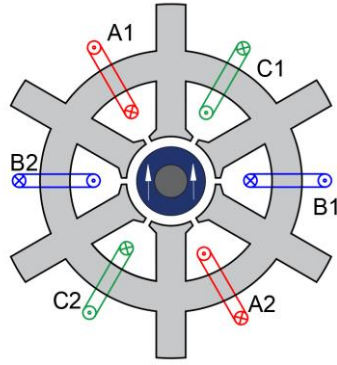


Fig. 3.16. Cross section of 6s/2p TWHSPM motor with tooth-tips.

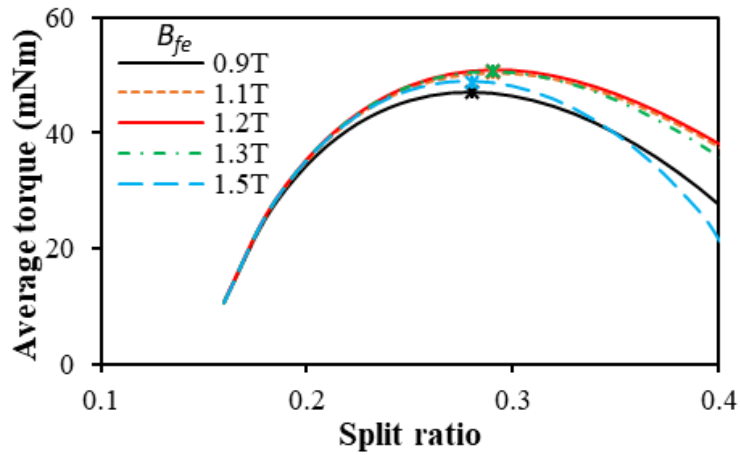


Fig. 3.17. Variation of average torque with SR and B_{fe} with tooth-tip ($K_a=0.5$, $h_{tt}=1\text{mm}$).

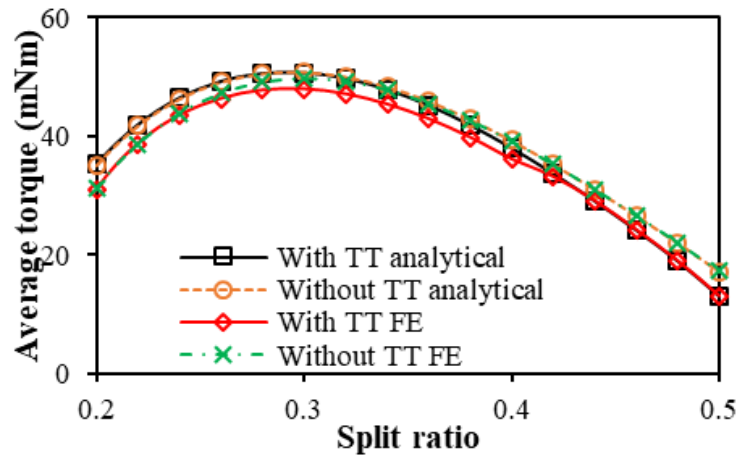


Fig. 3.18. Variation of FE and analytically predicted average torques with SR ($B_{fe}=1.2\text{T}$).

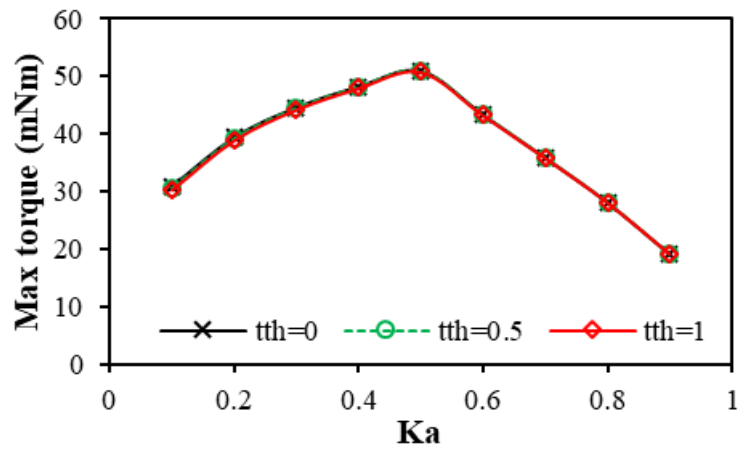


Fig. 3.19. Influence of K_a and tooth-tip thickness on maximum average torque ($B_{fe}=1.2T$).

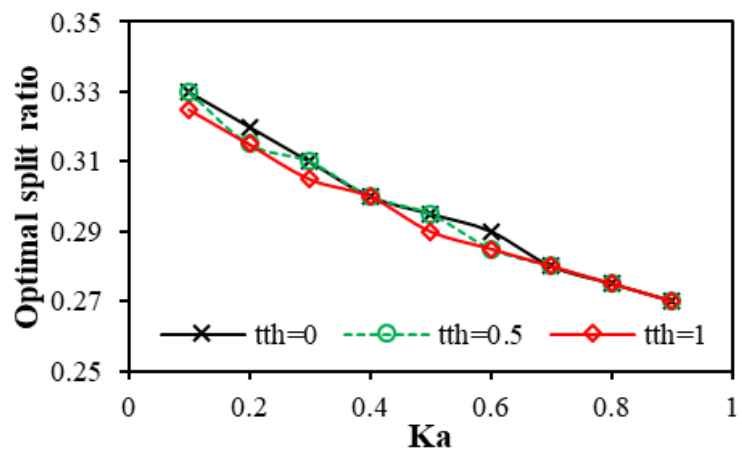


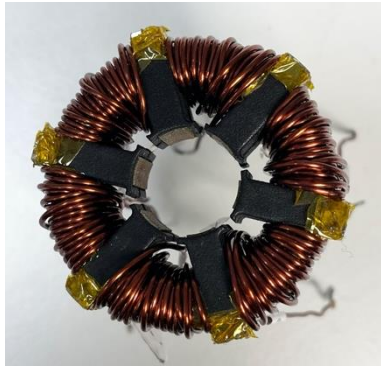
Fig. 3.20. Influence of K_a and tooth-tip thickness optimal SR ($B_{fe}=1.2T$).

3.5 Experimental Validation

In this section, some of predicted results are verified by the measured results on a 6s/2p TWHSPM prototype motor with 0.5 slot ratio manufactured by Midea. Fig. 3.21 indicates the stator structure of the prototype motor, the shaft-bearing-blade system, the forced-air cooling system, and the house structure.

Table 3.3 provides the values of phase resistance and winding inductance of the prototype, which are measured by a LCR meter. Due to manual winding, the extra end-winding length (l_{ex}) is set to be 1.5mm, the analytically predicted resistance has good agreement with the measured result (1Hz). It should be noted that the measured resistance under high frequency (1833Hz) is substantially larger than that under low frequency (1Hz), this means the AC copper loss of toroidal windings is large under high frequency. However, it can be avoided by using Litz-wires and is ignored in the previous analysis. In Table 3.3, since the 2D-FE model provides an ideal winding inductance which neglects end-winding inductance, the FE predicted winding inductance is smaller than the measured result. Due to skin effect, the measured inductance drops when the frequency increases due to skin effect.

Fig. 3.22 shows the analytically predicted, FE computed, and measured back-EMFs of phase A in the prototype motor at 11 krpm. It can be seen that the FE predicted and measured results have a good agreement but the analytical prediction is slightly larger due to neglecting the flux leakage caused by straight tooth without tooth-tips. The static torque is measured by a test rig in this paper since it is difficult to measure the torque under high speed operation in general [ZHU09], Fig. 3.23. The test results show that the measured open-circuit static torque, i.e. cogging torque, is almost zero, which is the same as the predicted result. The measured on-load static torque has a good agreement with the FE predicted result, Fig. 3.24. With the phase current rises, the maximum static torque increases linearly, and the measured maximum static torques have an excellent agreement with the FE calculations, Fig. 3.25. The measured phase current and terminal voltage waveforms of the prototype motor at 110 krpm are shown in Fig. 3.26. In addition, Fig. 3.27 shows the prototype motor operates at 120 krpm which is above the rated speed.



(a) Stator



(b) Shaft-bearing-blade system



(c) Forced air cooling system

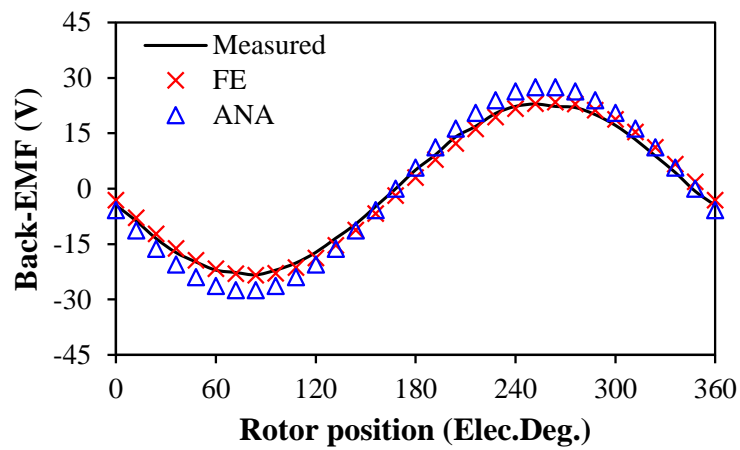


(d) House

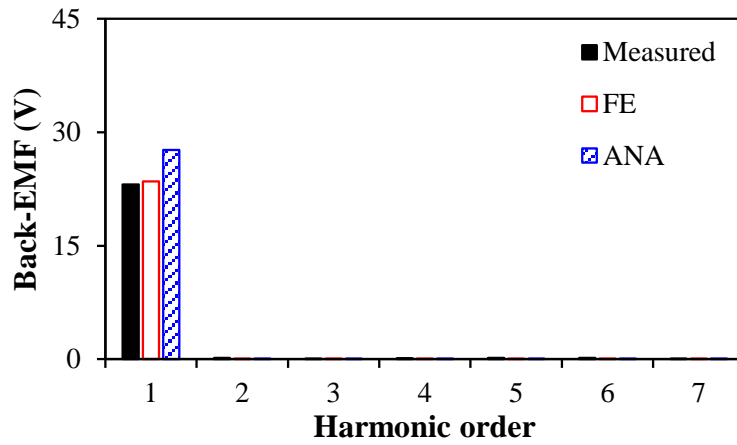
Fig. 3.21. Prototype of the 6s/2p TWHSPM motor.

Table 3.3
Predicted and Measured Winding Resistances and Inductances

Resistance (mΩ)			Inductance (μH)		
Predicted	Measured (1Hz)	Measured (1.83 kHz)	Predicted	Measured (1Hz)	Measured (1.83kHz)
40.05	44.16	72.80	19.5	26.32	23.16



(a) Waveforms



(b) Spectra

Fig. 3.22. Back-EMF of phase A of FE calculated, analytically predicted, and measured in the 6s/2p TWHSPM motor at 110 krpm.

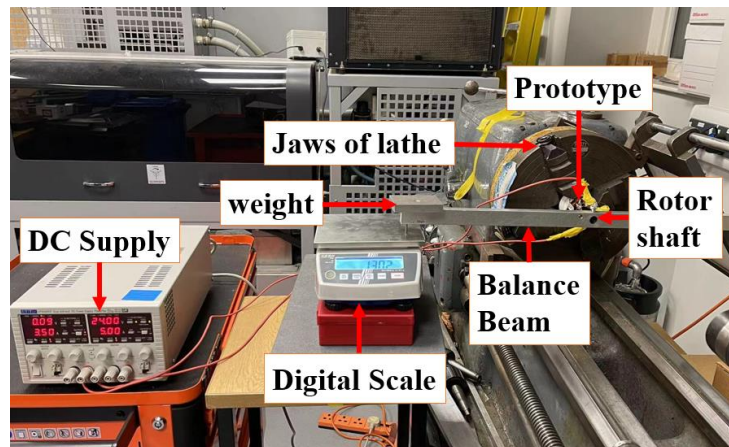


Fig. 3.23. Static torque test rig.

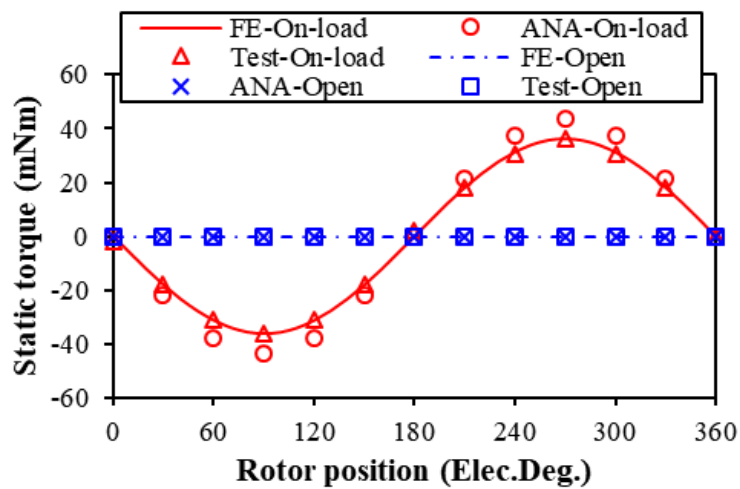


Fig. 3.24. Measurement and FE predicted open-circuit and on-load static torques under the phase currents of $I_A = -I_B = 5$ A, $I_C = 0$ A.

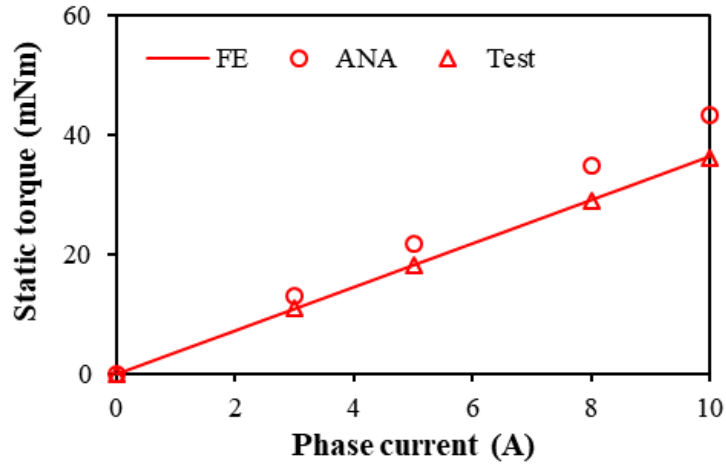


Fig. 3.25. Maximum measurement and FE predicted static torques with various phase currents.

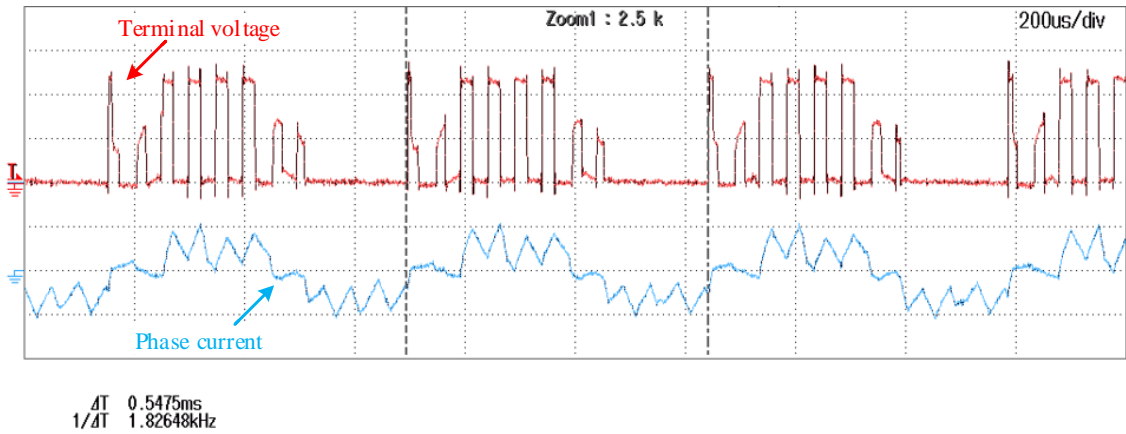


Fig. 3.26. Measured phase current and terminal voltage waveforms of the 6s/2p TWHSPM motor at 110 krpm, i.e. $f=1.83$ kHz, with speed control (10.0V/div; 20.0A/div; $U_{dc}=25.2$ V).

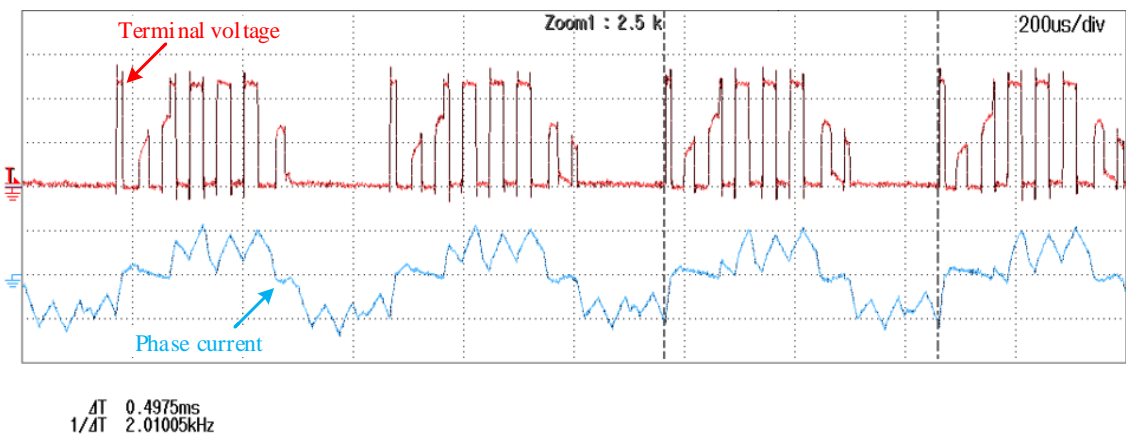


Fig. 3.27. Measured phase current and terminal voltage waveforms of the 6s/2p TWHSPM motor at 120 krpm, i.e. $f=2.00$ kHz, with speed control (10.0V/div; 20.0A/div; $U_{dc}=25.2$ V).

3.6 Conclusion

In this paper, the optimal split ratio of the 6s/2p TWHSPM motor has been investigated by analytical method considering stator copper loss and iron loss, and validated by FE method. Meanwhile, the influences of slot ratio, B_{fe} , and tooth-tips on optimal SR are investigated. It depicts that the maximum torque can be achieved when the inner slot area is equal to the outer slot area, i.e. slot ratio is 0.5. When the slot ratio increases the optimal SR decreases, and the results are affected by B_{fe} . Some of the analytical predictions have been validated by FE method and experiments.

CHAPTER 4

INFLUENCE OF STATOR GAP ON ELECTROMAGNETIC PERFORMANCE OF 6- SLOT/2-POLE MODULAR PERMANENT MAGNET MOTOR WITH TOROIDAL WINDINGS

The 6-slot/2-pole (6s/2p) permanent magnet motors with a diametrically magnetized PM rotor are popular for high-speed application. Meanwhile, toroidal winding can not only reduce end-winding length but also eliminate unbalanced magnetic force for short axial length motors. Therefore, the electromagnetic performance of a 6s/2p HSPM motor with toroidal windings is firstly analyzed, including air-gap flux density, flux linkage, back-EMF, cogging torque and electromagnetic torque. Then, considering modular design for auto-manufacturing, the influence of stator gap and misalignment on the electromagnetic performance is investigated. It shows that the stator gap results in unbalanced three phase back-EMFs, not only amplitudes, but also phase angles. The stator gap increases the equivalent air-gap length and PM flux leakage, which leads to lower air-gap flux density, back-EMF, and average torque. Moreover, the stator gap results in asymmetric air-gap length, which results in large cogging torque. Further, it shows that the misalignment of two stator parts mainly affects the uneven equivalent air-gap length and symmetry of winding configuration, which leads to unbalanced three phase back-EMFs, especially phase angles, and self-/mutual-inductances, as well as rotor PM loss. Experimental results of a prototype motor with/without stator gap and/or misalignment are given to validate the finite element predicted analyses.

This chapter is based on the paper published in:

F. Xu, Z. Q. Zhu, T. R. He, Y. Wang, H. Bin, D. Wu, L. M. Gong, and J. T. Chen, "Influence of stator gap on electromagnetic performance of 6-slot/2-pole modular high-speed permanent magnet motors with toroidal windings," in *IEEE Access*, vol. 9, no. 6, pp. 94470-94494, 2021.

4.1 Introduction

Permanent magnet (PM) motors have been widely used and become more and more popular in recent years. For small size, high-speed application, 6s/2p HSPM motors with concentrated tooth coil windings are employed widely due to short end-winding length and no unbalanced

magnetic force [NOG05]. In high-speed operation, high aspect ratio due to long motor axial length normally leads to a rotor dynamic issue and may cause the damage of the rotor [EDE01]. Hence, besides the tooth coil with short end-winding length, the toroidal winding also becomes a popular design alternative for high speed application which demands a short motor axial length [NOG05] [ZWY05] [GIL16] [SCH17]. They are widely adopted in low-power application whilst the operating speed normally exceeds 100krpm. In [ZWY05], a 100W, 500 krpm PM slotless machine with toroidal winding for gas turbines was designed and tested. The slotless toroidal winding is adopted to eliminate the rotor eddy-current loss due to no slotting effect. Such combination of slotless stator and toroidal winding can also be found in [GIL16]. In [GIL16], the 6s/2p HSPM motor with slotted tooth-coil winding and the 6s/2p HSPM slotless motor with toroidal winding were compared. It shows that slotless motor with toroidal winding has the highest efficiency and torque density when operating at 150 000 rpm. In addition, this paper shows that the slotted motor has higher thermal capability and larger heat transfer coefficient. A 160 000 rpm millimeter-scale slotless bearingless motor is presented in [SCH17] to overcome the limitation of conventional ball bearings for high-speed spindle applications.

Besides, compared with conventional distributed windings, toroidal windings are widely adopted to shorten end-winding and motor total axial length for high-power high-speed application [CHE11] [WAN09] [DON14] [ZHA16]. Another merit of such toroidal windings is higher thermal dissipation capability due to the presence of extra air-duct.

On the other hand, the modular design is widely employed for manufacture automation. For tooth-coil windings, there are several modular designs have been researched. The influence on electromagnetic performance of modular stator has been investigated in [ZHU06] [ZHU18] such as stator tooth segments and back-iron segments. Different segmented stator core and manufacturing methods of motors with concentrated windings have been investigated in [LIB06]. [CHE95] [SPO96] [SPO96a] [SPO98] have proposed a modular flux concentrating machine with segmented stator and rotor. In [ZHU18], the modularity techniques in PM machines with tooth-coil winding were comprehensively reviewed. In [LIG14] [LIG15] [ZHU12], the influence of modularity on the machine performance has been investigated and analyzed. Although several modularity techniques can be employed in toroidally-wound motors, the influence of modular design on the performance of motors with toroidal windings has never been investigated in literature and will be analyzed in this chapter.

In this chapter, the motor topology, winding factor and end-winding model of the 6s/2p HSPM motor with toroidal windings are illustrated in section 4.2. In section 4.3, the electromagnetic performances of the motor without stator gap are analyzed, including air-gap flux density, flux linkage, back-EMF, cogging torque and electromagnetic torque. Section 4.4 investigates the influence of the stator gap on the performance of the 6s/2p HSPM toroidally-wound motor. Sections 4.5 and 4.6 further investigate the influence of misalignment, as well as mixed stator gap and misalignment. Section 4.7 illustrates the potential influence of tooth tip. Section 4.8 provides extensive experimental results for a prototype motor with/without stator gap and/or misalignment to validate the finite element predicted results. Finally, the conclusion is given in section 4.9.

4.2 Topologies of HSPM Motors with Toroidal Windings

The cross-sections of 6s/2p HSPM toroidally-wound motors without and with stator gap are presented in Fig. 4.1. The stator gap is located between the windings of phase A and phase C, which divides stator into two halves which can ease the automated winding. To simplify the production, this 6-slot motor with straight teeth has no tooth tip, whose influence will also be investigated later in this chapter. It is assumed that the sum of split teeth width in Fig. 4.1 (b) is the same as that of one un-split tooth. The 2-pole rotor consists of two parts including N45SH parallel magnetized magnet ring (or cylinder) and SUS430 magnetic shaft. The main parameters of 6s/2p HSPM motors without stator gap are given in Table 4.1.

Table 4.1
Main Parameters of 6/2 HSPM Motor without Stator Gap

Rated current density (A/mm^2)	10	Air-gap length (mm)	1.55
Rated speed (krpm)	180	Rotor outer radius (mm)	5.25
Stator outer radius (mm)	27	Magnet thickness (mm)	2.75
Stator active length (mm)	8.6	Remanence (T)	1.3
Stator inner radius (mm)	6.8	Magnetization	Parallel
Stator yoke height (mm)	4.6	Number of turns per phase	32

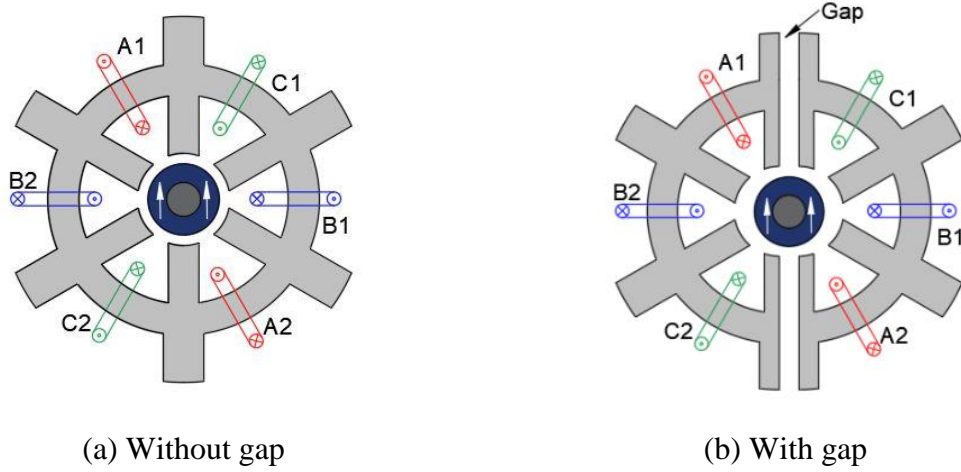


Fig. 4.1. 6s/2p HSPM toroidal motors without and with stator gap.

4.2.1 Winding factor

For the toroidal winding, the calculation of winding factor is different from the conventional formulae for tooth-wound winding. The winding factor of a 6s/2p PM motor with toroidal windings is only 0.5, which results from the product of pitch factor ($=0.5$) and distribution factor ($=1$) [XUF21]. Both 6s/2p PM motors with tooth-wound and toroidal windings have no unbalanced magnetic force and the same winding factor (0.5), which is lower than that of 3s/2p tooth-wound windings (0.866) which has significant unbalanced magnetic force.

4.2.2 End-winding

The end-winding of the toroidally-wound motor is special. The outside conductors form the current loop, and can be treated as a part of end-winding length. In addition, the end-winding length also includes the axial part links the outside and inside conductors. In this chapter, a semi-circular end-winding model is employed, Fig. 4.2. The total end-winding length (l_e) of one coil can be calculated by [PAN06].

$$l_e = 2 \left[\frac{\pi}{2} \left(\frac{h_{out} + h_{in}}{2} + h_y \right) \right] + l_a \quad (4.1)$$

where h_{out} and h_{in} mean the outer and inner tooth heights, respectively. h_y is the yoke height. l_a is the stator active length.

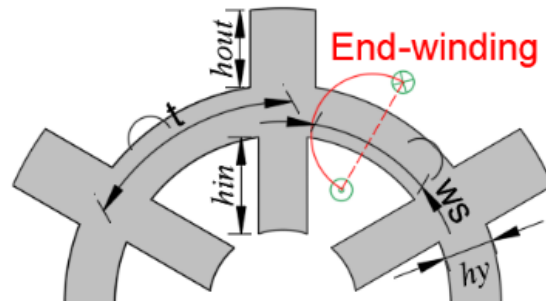


Fig.4.2. End-winding model.

4.3 Electromagnetic Performance without Stator Gap

In this section, the electromagnetic performances of the 6s/2p motor without stator gap are analyzed, including air-gap flux density, flux linkage, back-EMF, cogging torque and electromagnetic torque. Fig. 4.3 shows the equal potential and flux density distributions of the motor without stator gap by the finite element analysis (FEA). It can be seen that there is almost no flux linking with the outside conductors (and this is why this part of conductors can be treated as a part of the end windings). Fig. 4.4 shows the air-gap flux density waveform and spectrum. The air-gap flux density of the motor without stator gap is essentially sinusoidal due to diametrically magnetized PM. Meanwhile, the air-gap flux density also exists the 5th, 7th, 11th, 13th,... order harmonics due to slotting effect. The flux linkage and back-EMF of the motor without stator gap are shown in Fig. 4.5 and Fig. 4.6. The waveforms are all sinusoidal and have negligible harmonics. Due to opposite connection polarities of the inside parts of coil A1 and coil A2, the harmonics are almost eliminated.

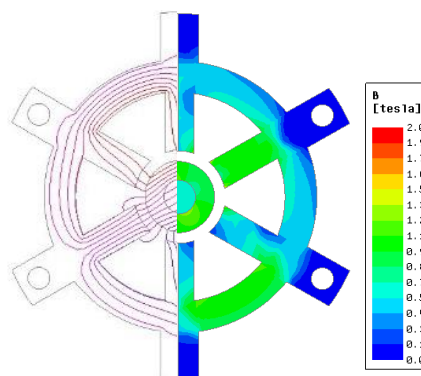
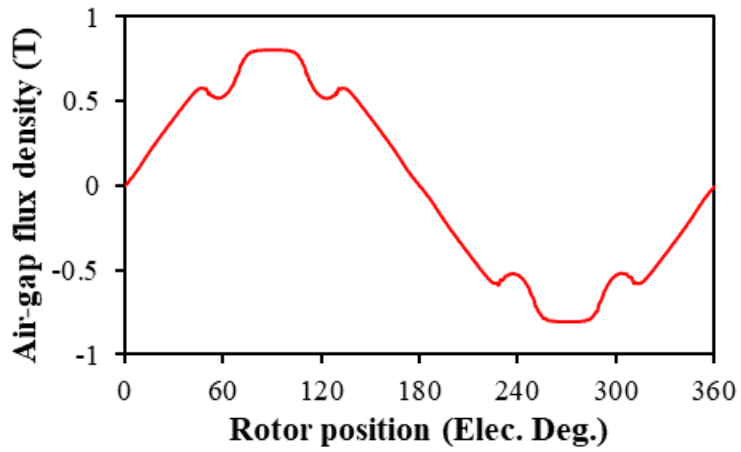
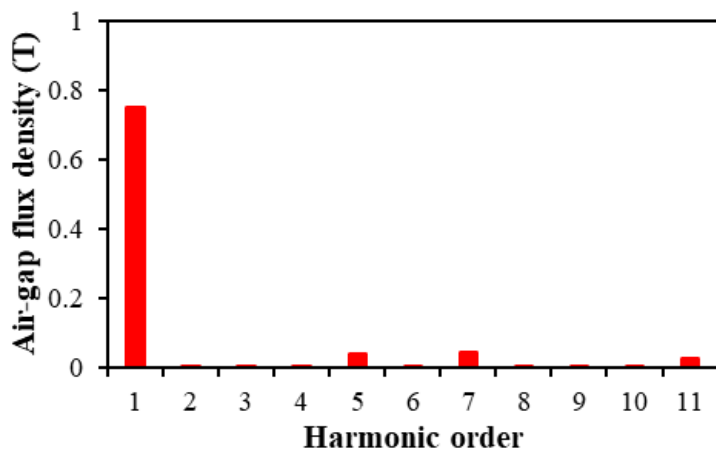


Fig. 4.3 Flux distribution and equal potential of the 6s/2p HSPM toroidal motor without stator gap.

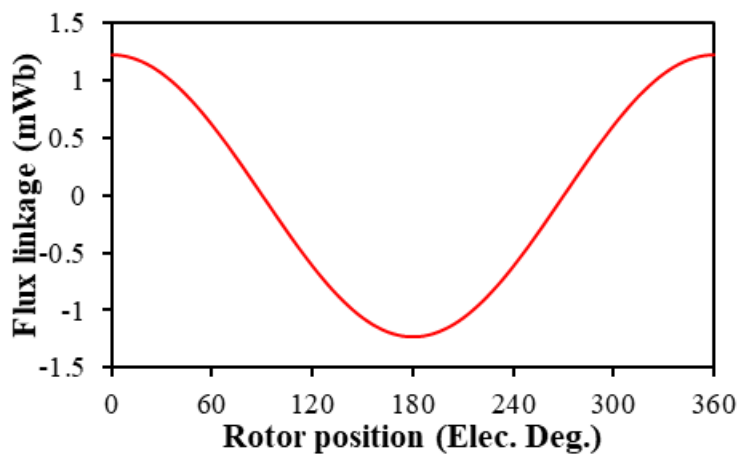


(a) Waveform

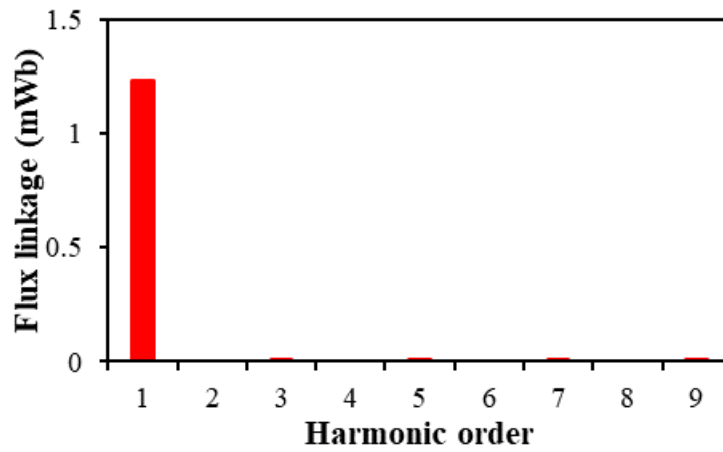


(b) Harmonics

Fig. 4.4. Open-circuit air-gap flux density of the motor without stator gap.

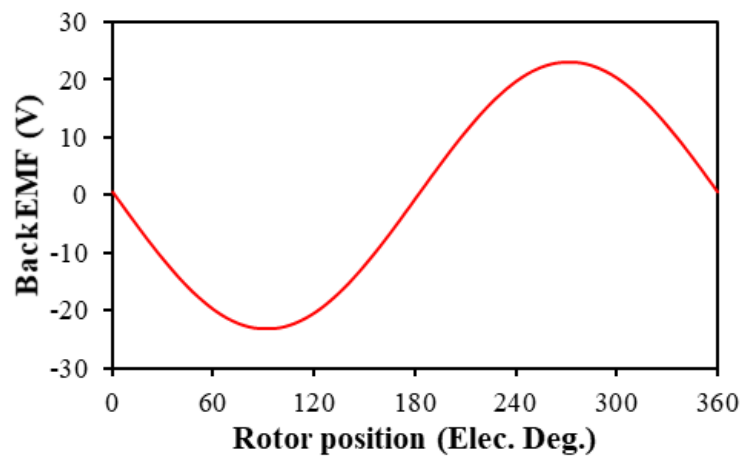


(a) Waveform

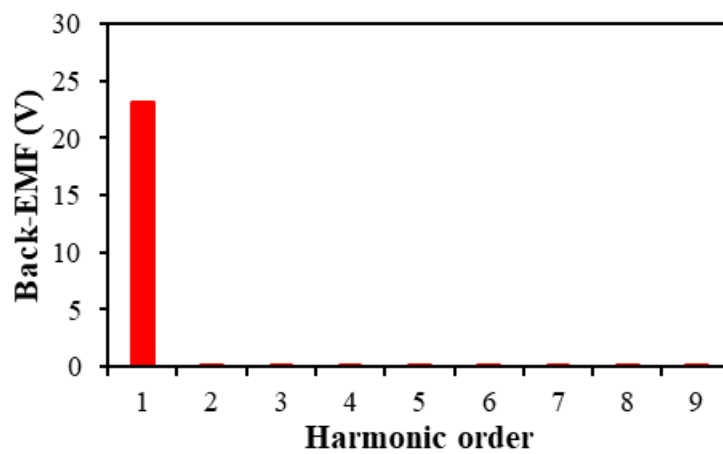


(b) Harmonics

Fig. 4.5. Flux linkage of phase A of the motor without stator gap.

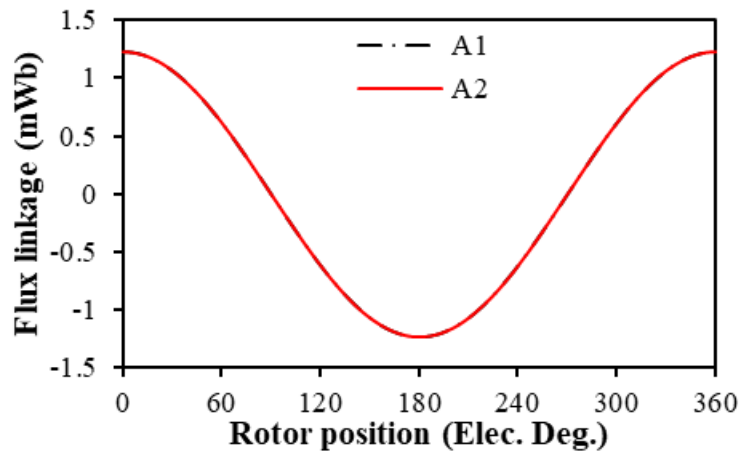


(a) Waveform

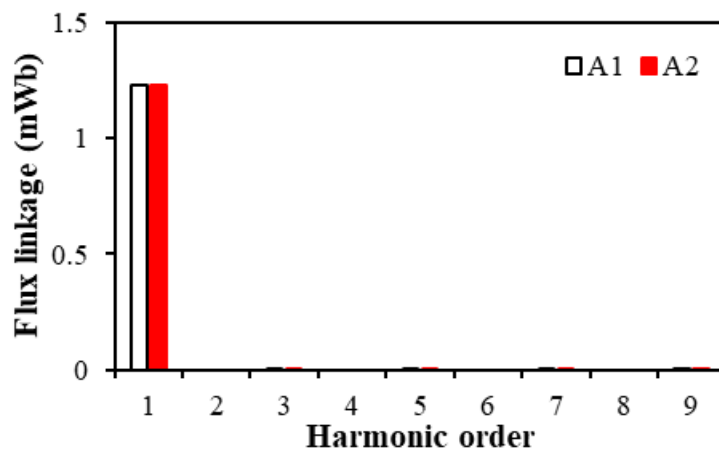


(b) Harmonics

Fig. 4.6. Back-EMF of phase A of the motor without stator gap.

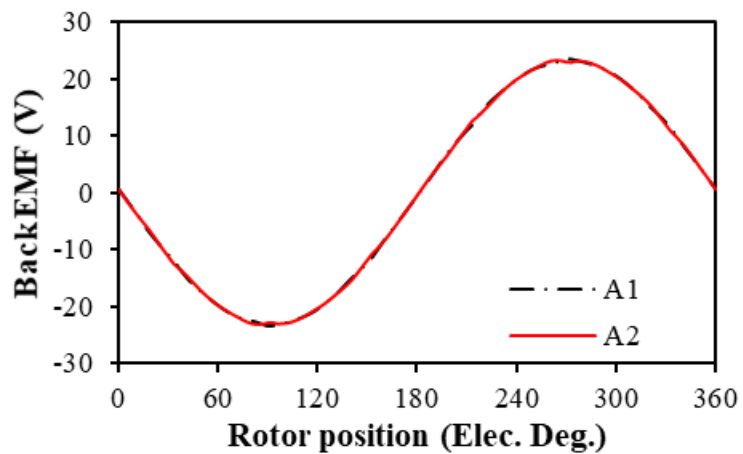


(a) Waveforms

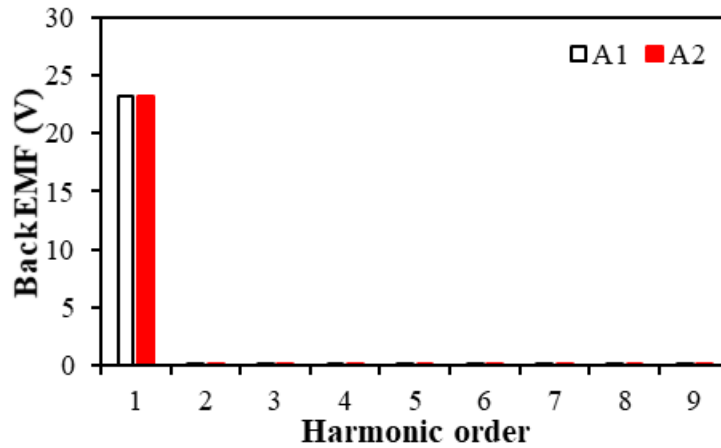


(b) Harmonics

Fig. 4.7. Flux linkages of coil A1 and coil A2 of the motor without stator gap.



(a) Waveforms



(b) Harmonics

Fig. 4.8. Back-EMFs of coil A1 and coil A2 of the motor without stator gap.

Under brushless direct current (BLDC) operation which is common for high speed operation, the ideal square BLDC current waveforms with the rated current density of 10 A/mm^2 are illustrated in Fig. 4.9. Meanwhile, the electromagnetic torque and cogging torque waveforms are presented in Fig. 4.10. The results show that the motor without stator gap has almost no cogging torque, but has relatively large torque ripple, which results from the product of square BLDC currents and almost sinusoidal back-EMF waveforms.

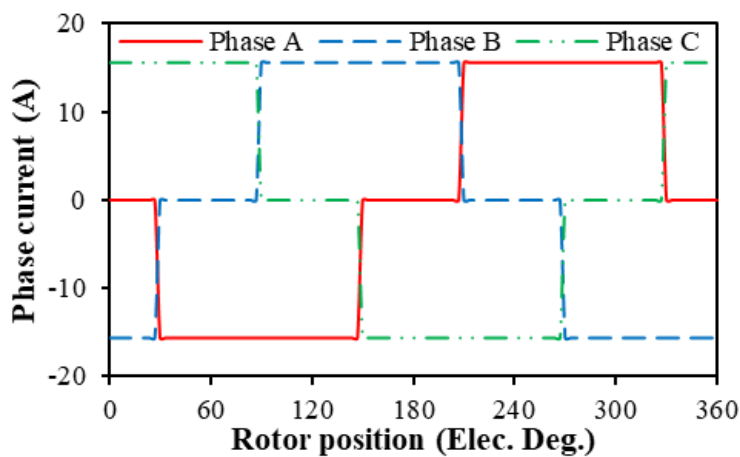
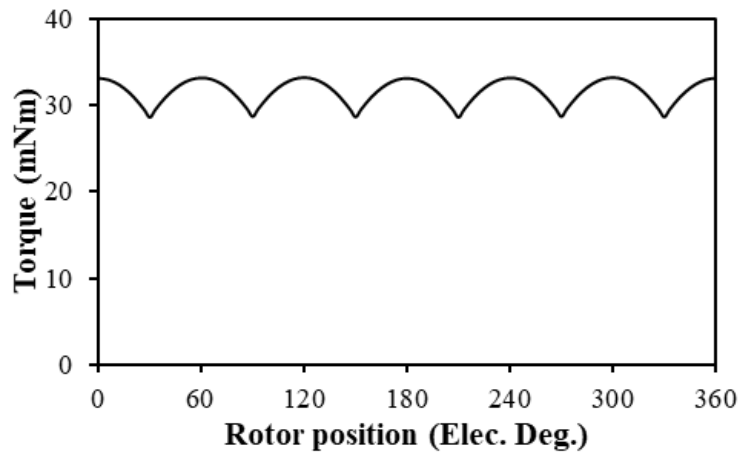
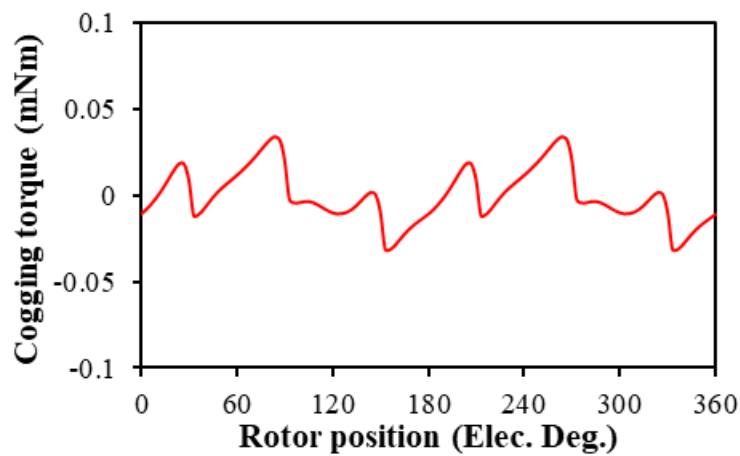


Fig. 4.9. Ideal square phase current waveforms.



(a) Electromagnetic torque



(b) Cogging torque

Fig. 4.10. Torque of the motor without stator gap.

4.4 Electromagnetic Performance with Stator Gap

To realize the modularity for automated winding, the stator is split into two parts. However, the modular design inevitably introduces the gaps in the stator, in Fig. 4.1(b). Generally, the presence of air-gap in the stator teeth increases the equivalent air-gap length of the motor thus making an impact on the electromagnetic performance. On the other hand, the actual slot number changes from six to eight due to the presence of two extra air gaps. The stator can be treated as a virtually whole stator with eight slot with uneven teeth and slot openings. Correspondingly, the stator slotting effect on the electromagnetic performance such as EMF and cogging torque may be significantly changed. Therefore, the influence of the stator gap on the electromagnetic performances will be comprehensively investigated in this section.

4.4.1 Air-gap flux density

The gap between split stators not only enlarges the equivalent air-gap but also results in uniform air-gap distribution of motor. Fig. 4.11 shows the open-circuit equal potential distributions of the motors with different stator gaps, i.e. 0, 1, 2, and 3 mm, although the stator gap is a bit exaggerated in order to reveal and appreciate its influence. Fig. 4.12 shows that the fundamental amplitude of air-gap flux density decreases with the increase of stator gap. This results from the increased average stator reluctance with the enlarged stator gaps. Meanwhile, amplitudes of the 5th, 7th, 11th, 13th order harmonics due to slotting effect decrease with the stator gap, as shown in Fig. 4.12. The stator gap changes the slot number from 6 to 8, which means the field harmonics of the order $(mp \pm 8)$ occur, e.g., the 3rd, 9th, etc., as shown in Fig. 4.12(b).

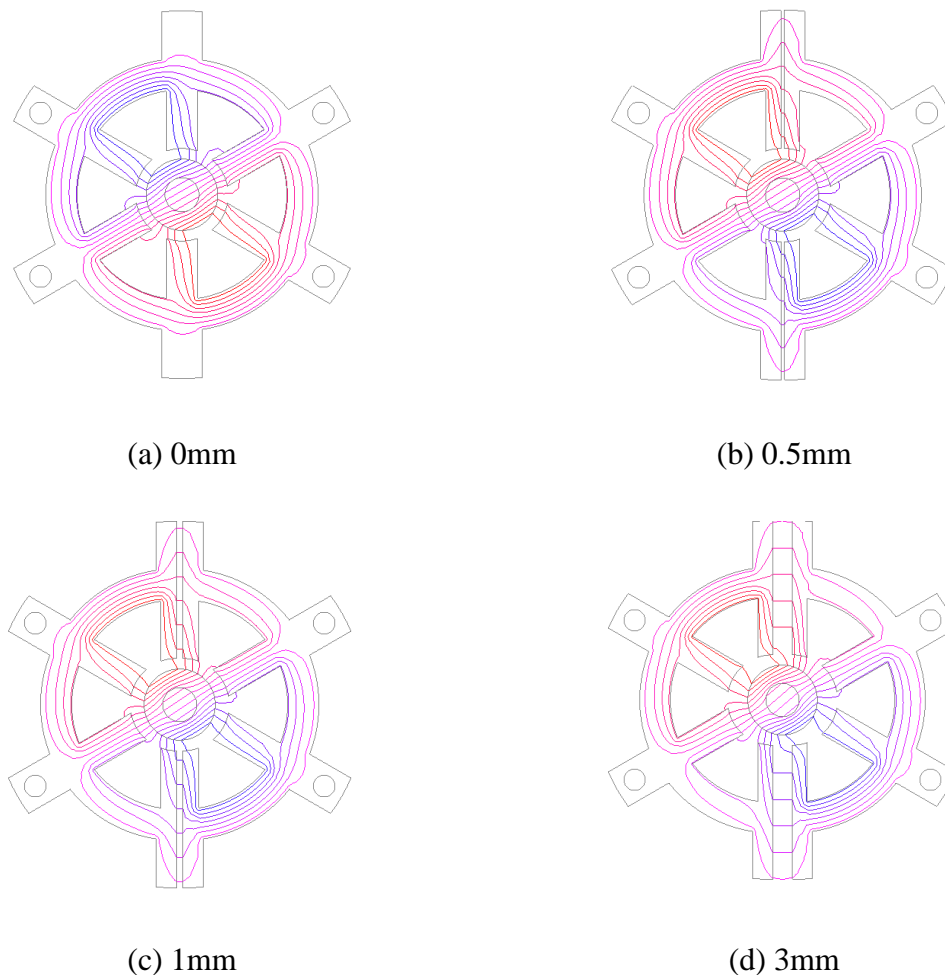
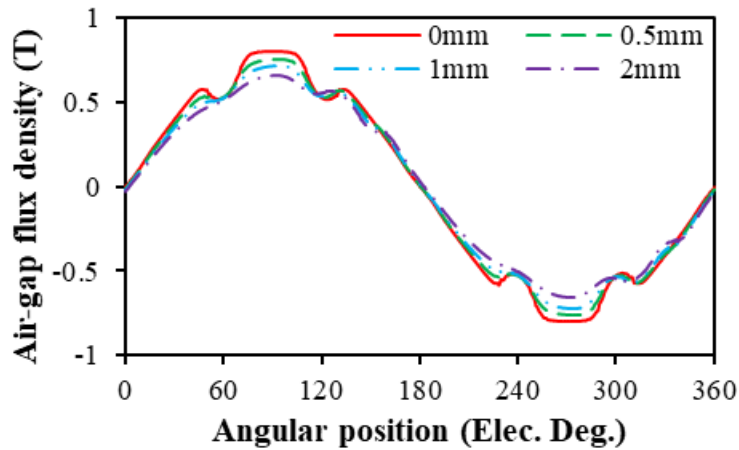
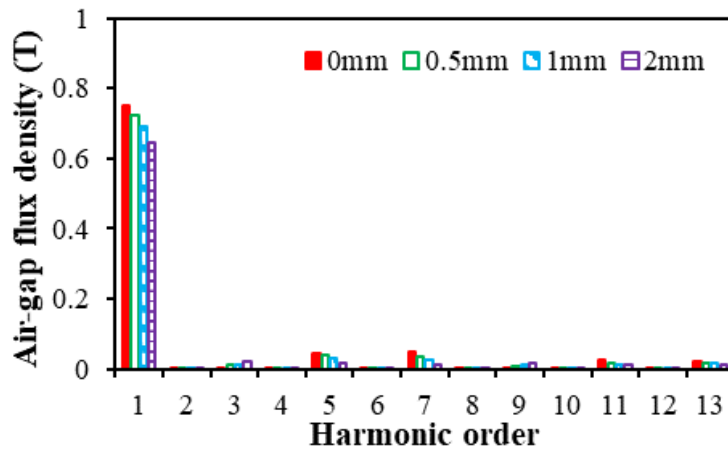


Fig. 4.11. Open-circuit equal potential distributions of 6s/2p HSPM toroidal wound motors with different stator gap.



(a) Waveforms



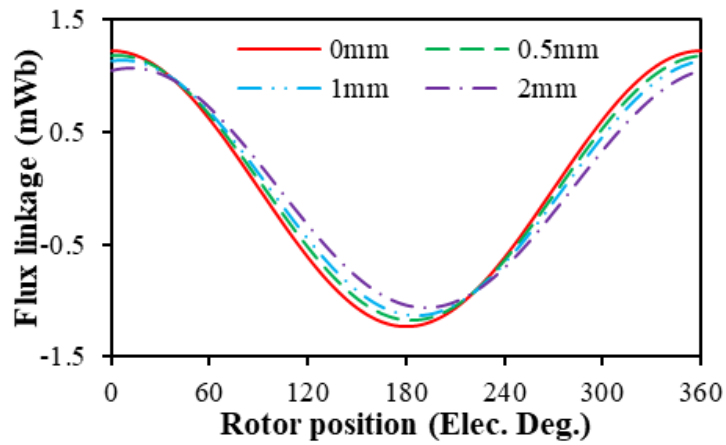
(b) Harmonics

Fig. 4.12. Air-gap flux density distributions of the motor with different stator gaps on circular path away from rotor by 0.775 mm.

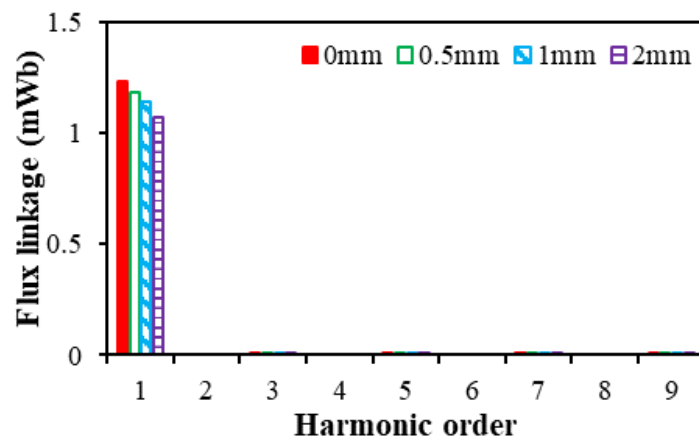
4.4.2 Flux linkage

As mentioned in section 4.2, the stator gap increases the leakage flux due to the increase of equivalent air-gap length. Therefore, the fundamental amplitude of flux linkage decreases with the increase length of stator gap. The introduction of stator gaps introduces almost no extra harmonics in the flux linkage, although the rotor positions where the amplitudes of flux linkage reach maximum and minimum are significantly altered, Fig. 4.13. Fig. 4.14 indicates equal potential distribution of the motor with 1mm stator gap at the specific rotor position when the flux linkage of phase A or phase C reaches the maximum. Phase angle of phase A is retarded and that for phase C is leaded. Fig. 4.15 illustrates the variation of phase angle of flux linkage with the increase of stator gap. The phase angle of phase B remains the same when the stator gap increases. The reason is that the stator gap is located between phase A and phase C, and both

coils of phase B are symmetrical. The variations of phase angles for phase A and phase C are opposite.

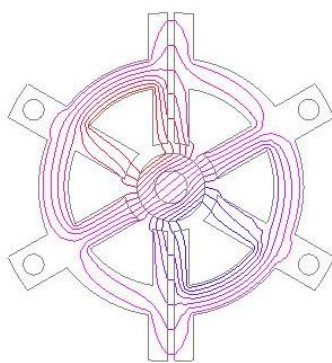


(a) Waveforms

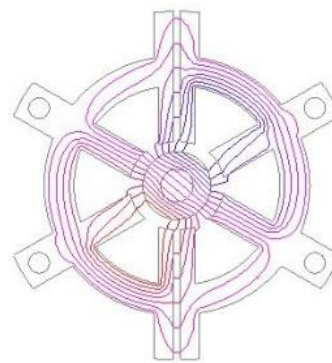


(b) Harmonics

Fig. 4.13. Flux linkage of phase A with different stator gaps.

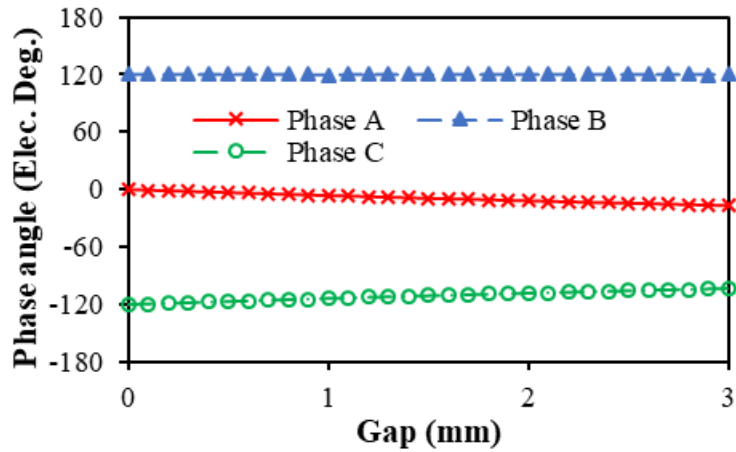


(a) Phase A

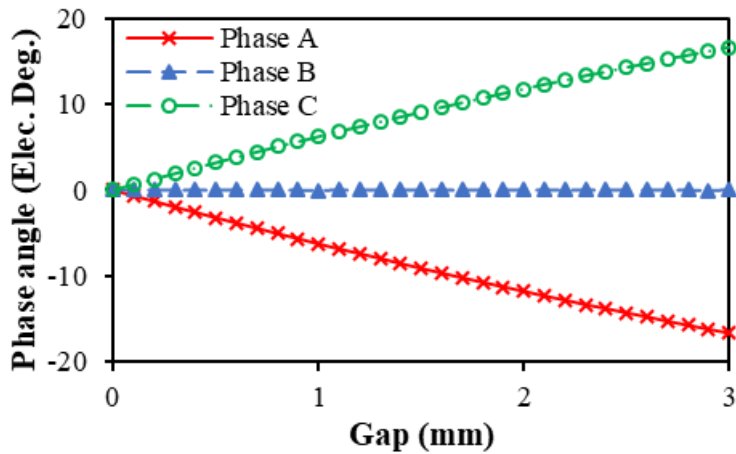


(b) Phase C

Fig. 4.14. Equal flux potential distributions with the specific rotor positions for maximum flux linkage. (Stator gap=1mm).



(a) Phase angle

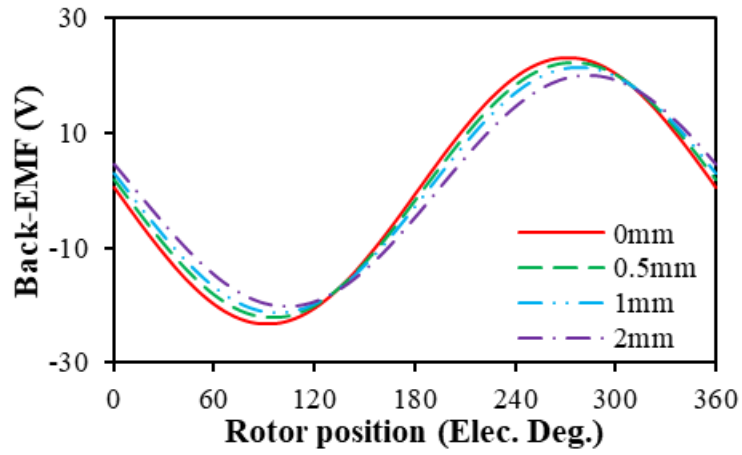


(b) Offset phase angle

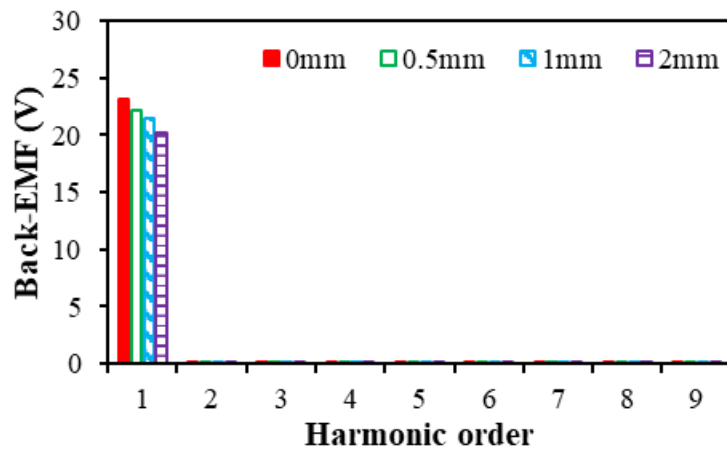
Fig. 4.15. Influence of stator gap on phase angle of flux linkage.

4.4.3 Back-EMF

The back-EMF exhibits a similar trend with the flux linkage. As shown in Fig. 4.16, the stator gap decreases the amplitude of fundamental back-EMF, but does not introduce extra harmonic contents. More importantly, the stator gap affects the phase angle of three phase back-EMFs, which leads to the unbalanced three phase back-EMFs. In Fig. 4.17, when the stator gap is 3 mm, the phase angles of three phase back-EMFs do not differ by 120 electrical degrees. Compared with the motor without stator gap, phase A and phase C of the motor with stator gap have the lead and retard angles, but phase B keeps the same phase angle due to the stator gap location between phase A and phase C. Fig. 4.17 shows the influence of stator gap on the phase lead and retard angles. As mentioned before, the variation trends of back EMFs of phase A and phase C are opposite but the offset value remains the same.

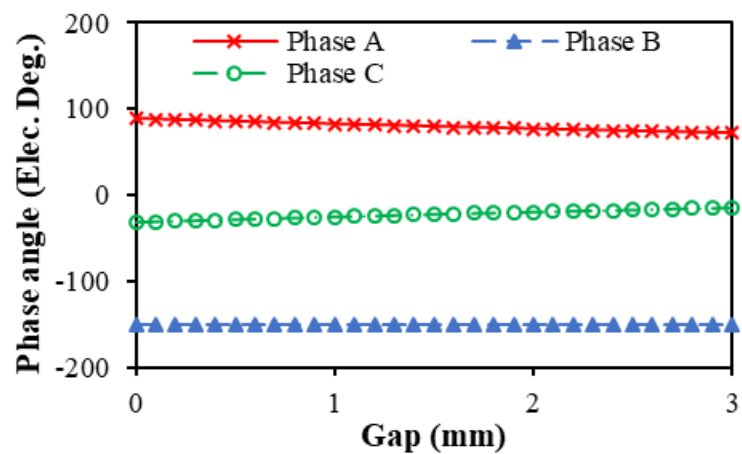


(a) Waveforms

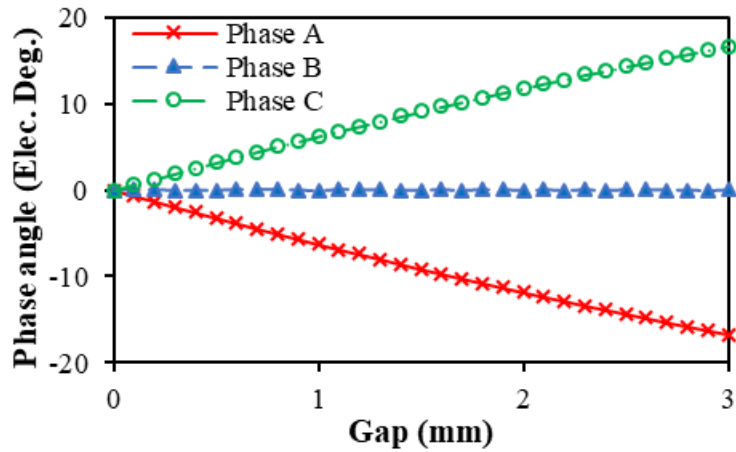


(b) Harmonics

Fig. 4.16. Back-EMFs of phase A with different stator gaps.



(a) Phase angle

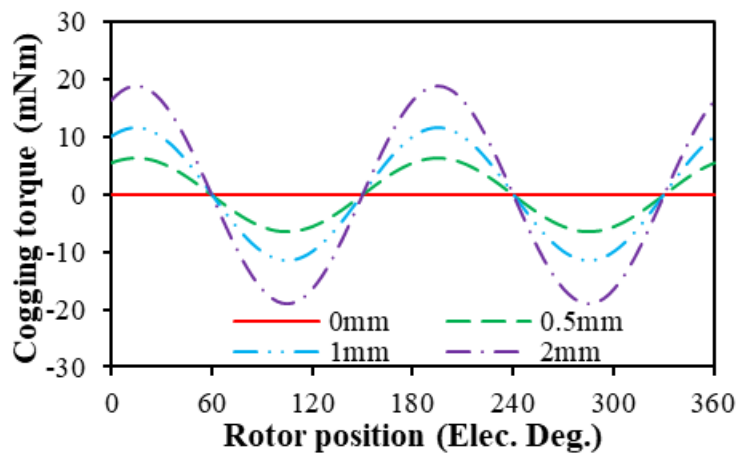


(b) Offset phase angle

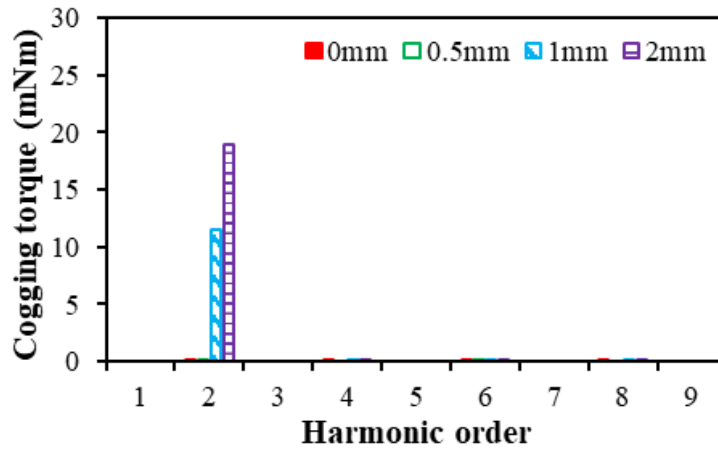
Fig. 4.17. Influence of stator gap on phase angle of back EMF.

4.4.4 Cogging torque

Cogging torque is generated from the interaction between stator slots and rotor PM poles. Generally, the 6s/2p PM motor with parallel magnetized rotor should have negligible cogging torque. Significant cogging torque is produced due to the presence of stator gap. Fig. 4.18 and Fig. 4.19 show that the peak cogging torque rises with the increase of stator gap before reaching the maximum value and then drops afterwards. The maximum peak cogging torque can be achieved when the stator gap is 4.8 mm.



(a) Waveforms



(b) Harmonics

Fig. 4.18. Cogging torque of the motor with different stator gaps.

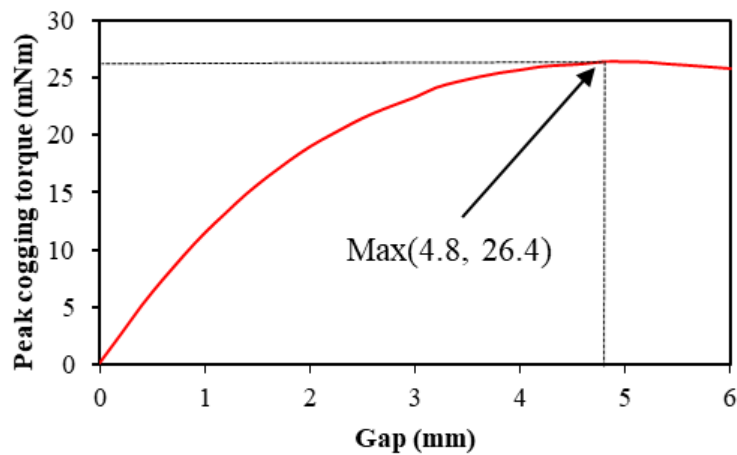
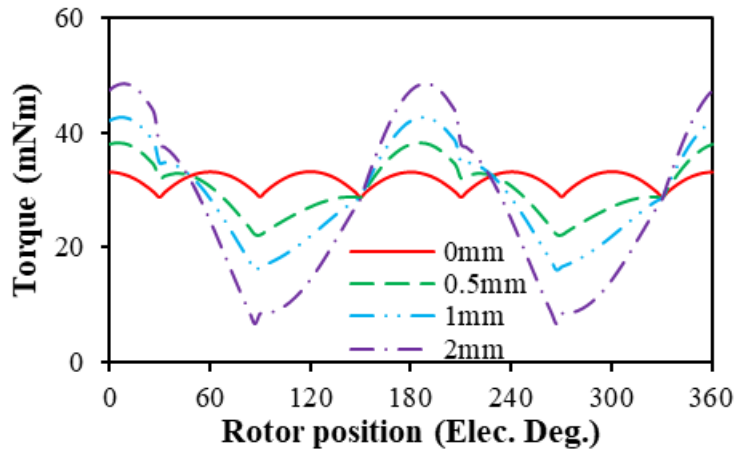


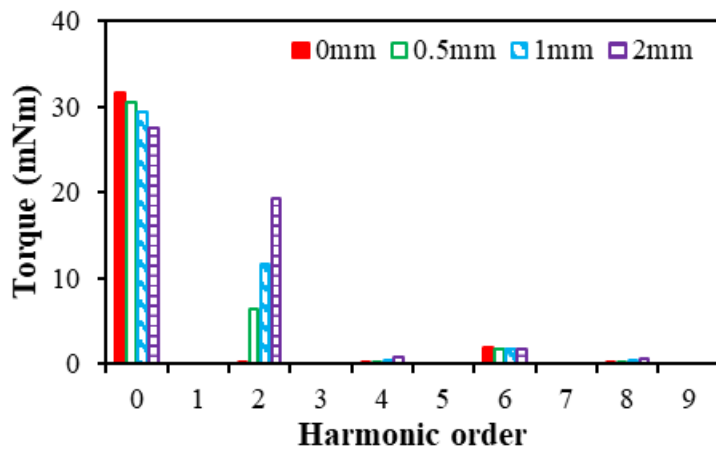
Fig. 4.19. Influence of the stator gap on the peak cogging torque.

4.4.5 On-load torque

The influence of different stator gaps on the on-load torque of the motor with rated current density ($10\text{A}/\text{mm}^2$), Fig. 4.20. It can be seen that the torque ripples increase significantly with the increase of the stator gap due to the increase of cogging torque. When the stator gap is larger than 3 mm, the on-load torque has negative values at several rotor positions, as shown in Figs. 4.20 and 4.21. Fig. 4.21 shows that when the stator gap is 3mm, the cogging torques are negative at several rotor positions, and the amplitudes of the negative cogging torque are larger than the electromagnetic torque at the same rotor position, which results in negative on-load torque. It is assumed that the influence of on-load condition on cogging torque is neglected. In addition, the stator gap affects not only the harmonic amplitudes, but also the harmonic contents, especially the 2nd harmonic which due to cogging torque, as shown in Fig. 4.20(b).



(a) Waveforms



(b) Harmonics

Fig. 4.20. Torque of the motor with different stator gaps ($J = 10A/mm^2$).

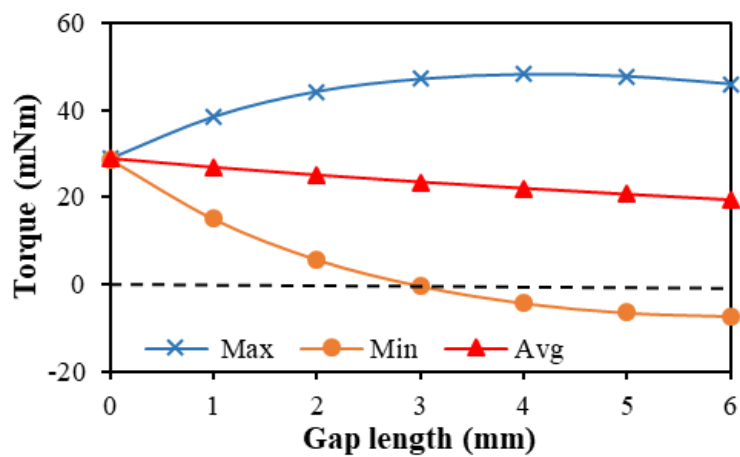


Fig. 4.21. Influence of stator gap on average torque.

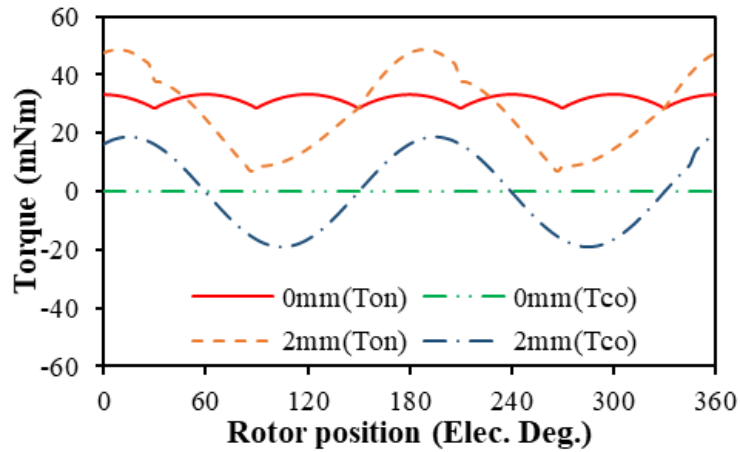
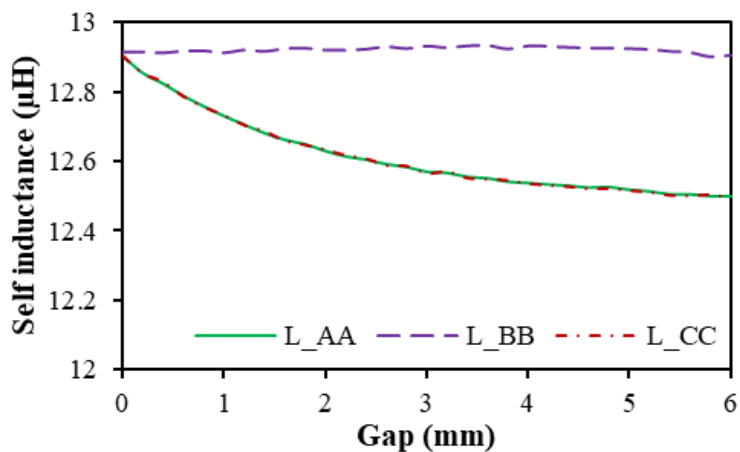


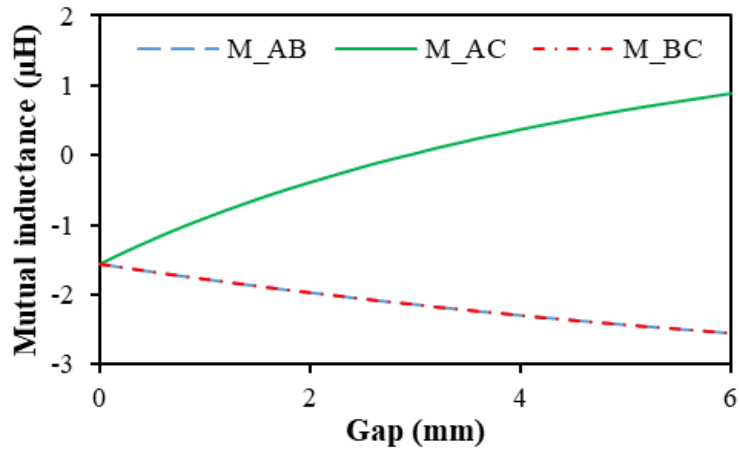
Fig. 4.22. Relationship between cogging torque and on-load torque of the motor with 2mm stator gap.

4.4.6 Inductance

High speed motors normally have small winding inductances. Even though there is a slight change of inductance due to the stator gap, the influence could be significant. The inductance is calculated by FEA, when only one phase excited ($I_a=1A$, $I_b=0A$, $I_c=0A$). Since the stator gap is located between phase A and phase C, the self-inductance of phase B remains the same with the stator gap, but the self-inductances of phase A and phase C decrease, as shown in Fig. 4.23. The mutual-inductances between phase B, phase A and C decrease when the stator gap increases. However, the mutual-inductances of phase A to phase C increases.



(a) Self-inductance



(b) Mutual-inductance

Fig. 4.23. Inductances of the motor with different stator gaps.

4.4.7 Losses

Stator iron loss will be affected due to non-uniformed air-gap because of the gap between the stator. In this section, the current density is fixed and the ac effect on the copper loss is neglected. In high speed motor, due to the poor thermal dissipation capability, the rotor temperature rise caused by the rotor eddy current loss should be considered. High rotor temperature may result in irreversible demagnetization and damage the rotor bearing system. With the increase of stator gap, dc copper loss keeps the same, the stator iron loss decreases and the rotor PM loss increases, Fig. 4.24. It can conclude that the stator gap below 1mm has almost no effect on the losses.

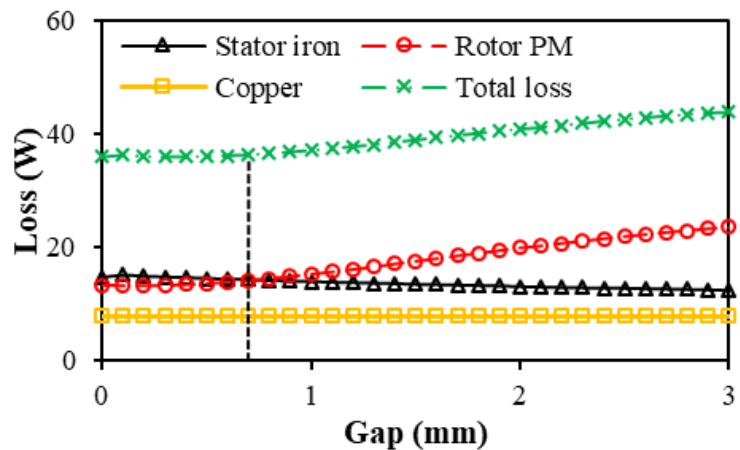


Fig. 4.24. Loss of the motor with different stator gaps ($J=10A/mm^2$, 180krpm).

1). Stator Iron Loss

Generally, the iron loss can be calculated using the Bertotti model [BER88] [ATA92]:

$$P_{fe} = m_{fe} (k_{hy} f B_{fe} + k_{ex} f^{1.5} B_{fe}^2 e + k_{ec} f^2 B_{fe}^2) \quad (4.2)$$

where m_{fe} is the stator mass, k_{hy} , k_{ex} and k_{ec} are the hysteresis coefficient, eddy current coefficient and excess loss coefficient respectively. f denotes the fundamental frequency and B_{fe} represents the peak value of the stator iron flux density.

Fig. 4.25 compares the no-load and on-load stator iron losses of the motors with different stator gaps. It can be seen that the no-load and on-load stator iron losses all decrease with the increase of gap, and the on-load stator iron loss is larger than no-load stator iron loss for each gap. Therefore, the influence of armature reaction on the stator iron loss cannot be neglected.

Fig. 4.26 shows the stator iron loss distributions of the motors with different gaps. It can be clearly observed that the stator iron losses in the split stator teeth are increased and in other parts are decreased with stator gap. For further investigation, by way of example as shown in Fig. 4.27, point A is chosen in the middle of yoke between two teeth, and point B is chosen in the middle of the tooth to compare the variation of stator iron flux density with different gaps [MAJ17].

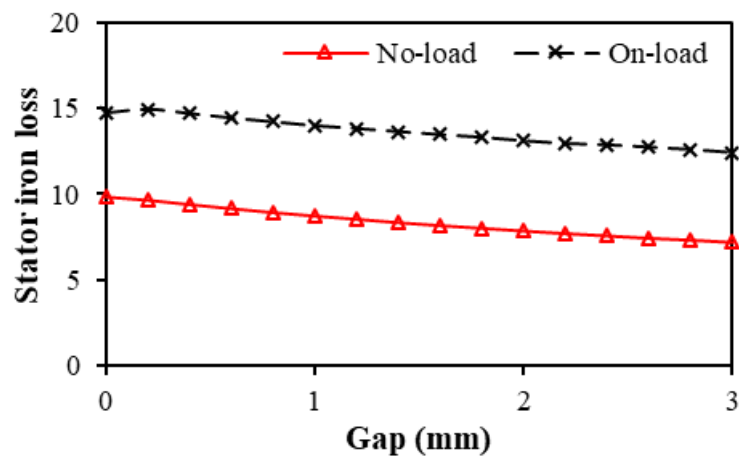
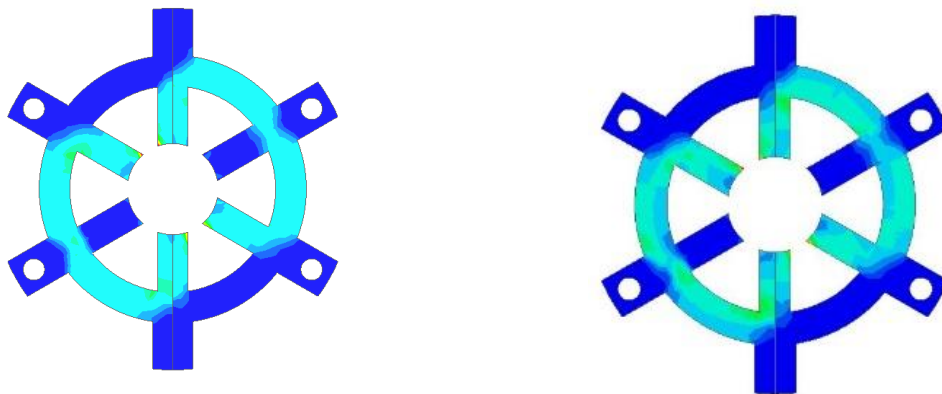
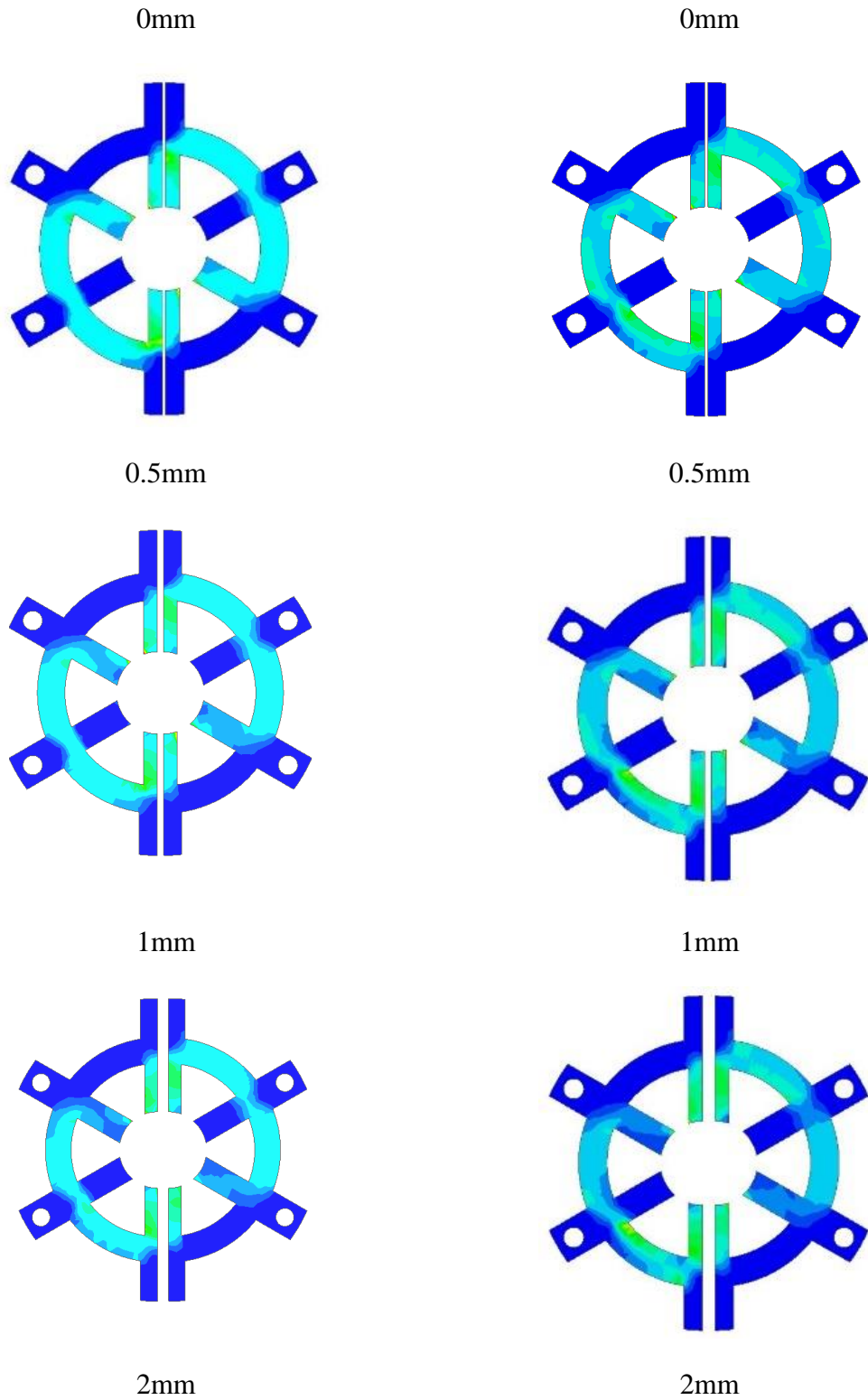


Fig. 4.25. Comparison of stator iron losses under no-load and on-load condition with variation of stator gap.





(a) Open-circuit

(b) On-load (J=10A/mm², 180krpm)

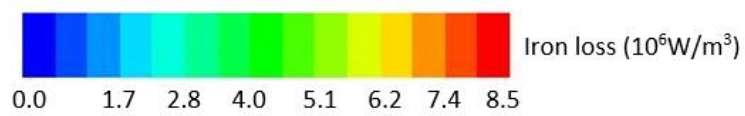


Fig. 4.26. Stator iron loss distributions with different stator gap.

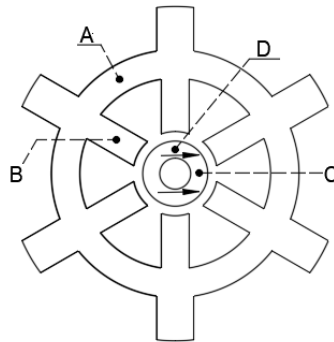
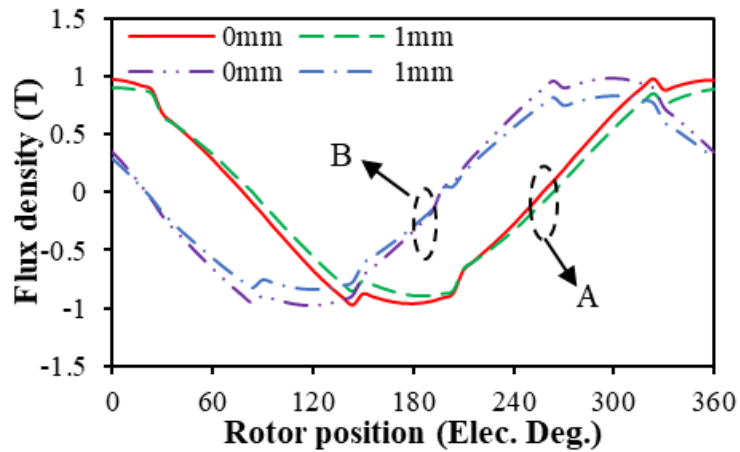
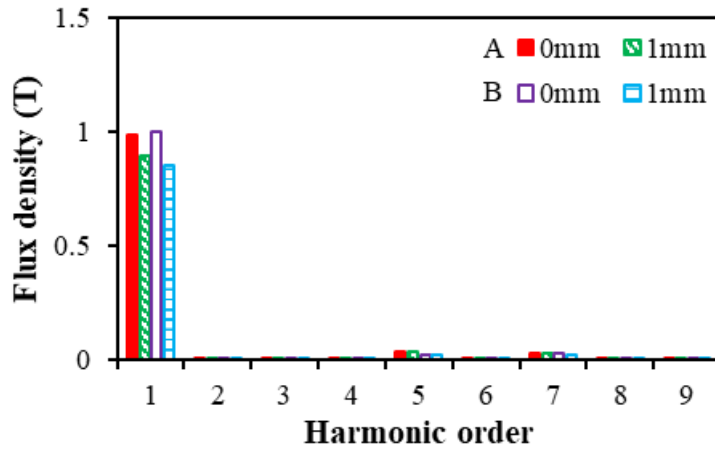


Fig. 4.27. Point A (middle of yoke), B (middle of tooth), C (middle of North pole), D (middle between north and south poles).

The flux densities of points A and B of the motors with 0mm and 1mm stator gaps are compared under on-load condition, as shown in Fig. 4.28. It can be seen that compared with 0mm stator gap, the points A and B of the motor with 1mm stator gap have smaller amplitudes of fundamental flux densities. The amplitudes of fundamental flux density of points A and B decrease linearly when the stator gap increases, Fig. 4.29, which results in the decreased stator iron loss.



(a) Waveforms



(b) Harmonics

Fig. 4.28. Comparison of flux densities at points A and B with 1mm and without stator gap ($J=10\text{A}/\text{mm}^2$, 180krpm).

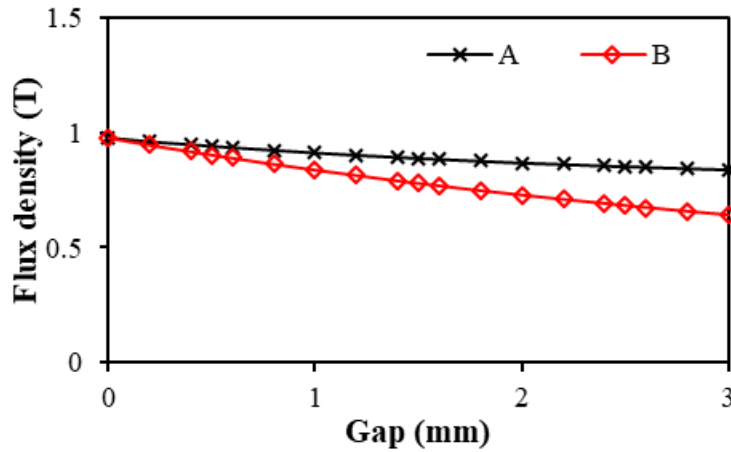


Fig. 4.29. Variation of fundamental value of stator flux density of the motor with 1mm and without stator gap ($J=10\text{A}/\text{mm}^2$, 180krpm).

2). Rotor Loss

The effect of stator gap mainly reflects on the non-uniformed air-gap. This will result in more harmonics of air-gap flux density. The variation of shaft and PM eddy current losses, in addition the variation of rotor total loss with the gap is shown in Fig. 4.30. Due to the shielding effect of PM, the shaft loss is small. Fig. 4.31 shows the rotor loss distributions of the motors with different stator gaps, including magnet ring and shaft. The eddy current loss of the magnet ring increases when the stator gap increased. The shaft of this motor employs magnetic material, i.e. SUS430.

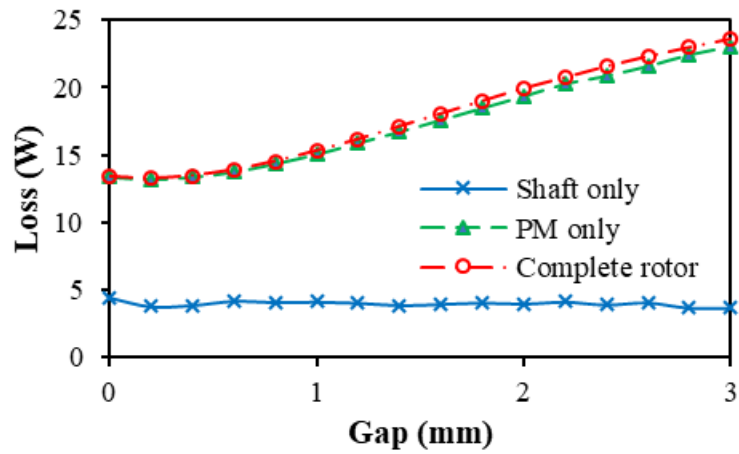


Fig. 4.30. Loss of the motor with different stator gaps ($J=10\text{A}/\text{mm}^2$, 180krpm).

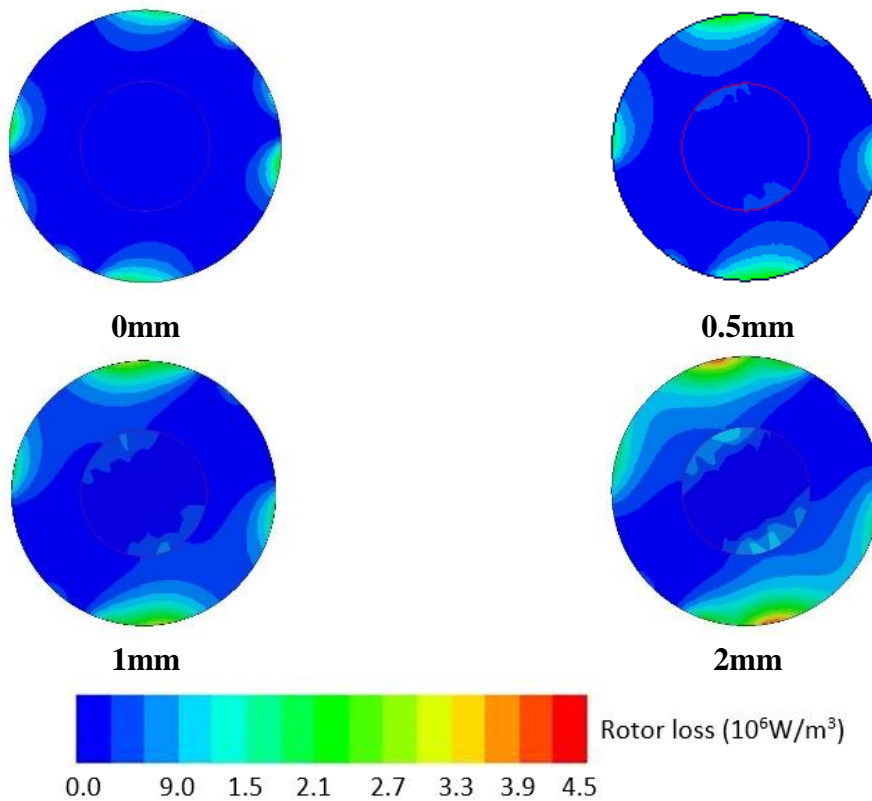
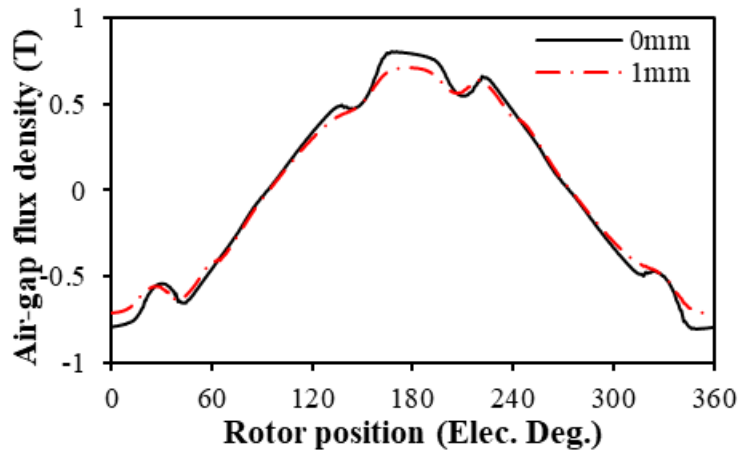
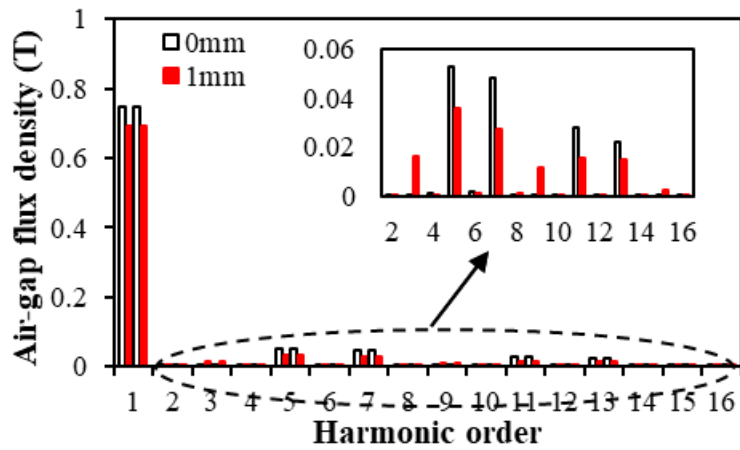


Fig. 4.31. Rotor loss distributions with different stator gap ($J=10\text{A}/\text{mm}^2$, 180krpm).

In order to verify that the increase of magnet eddy current loss is due to the increase of spatial harmonics, the on-load air-gap flux density distributions of the motors with 0mm and 1mm stator gap are shown in Fig. 4.32. The variation of each harmonic is shown in Fig. 4.33. Under on-load condition, with the increased stator gap, the 3rd and 9th harmonics are appeared and increased, while the 5th and 7th harmonics are decreased.



(a) Waveforms



(b) Harmonics

Fig. 4.32. Air-gap flux densities of the motor with 1mm stator gap and no stator gap ($J=10\text{A}/\text{mm}^2$, 180krpm).

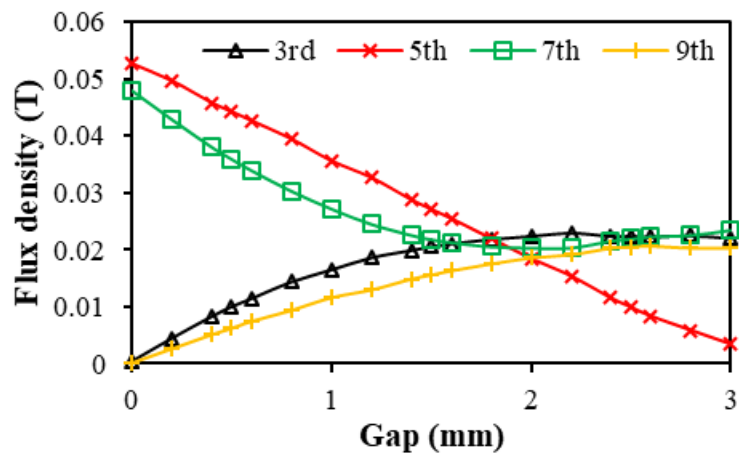


Fig. 4.33. Variation of harmonics of air-gap flux density with stator gap ($J=10\text{A}/\text{mm}^2$, 180krpm).

For further investigation, Fig. 4.34 shows the variation of magnet eddy current loss due to armature reaction only and PM only with stator gap. It can be seen that the rotor PM loss due to armature reaction only is significantly larger than that due to PM only. In addition, with the increase of stator gap, the rotor PM loss due to armature reaction only decreases, but that due to PM only increases significantly. Fig. 4.35 shows the influence of stator gap on the air-gap field due to armature reaction only. It shows that the stator gap decreases the amplitudes of fundamental, 5th, 7th, and 11th order harmonics caused by armature reaction. Fig. 4.12 shows the influence of stator gap on the air-gap field due to PM only.

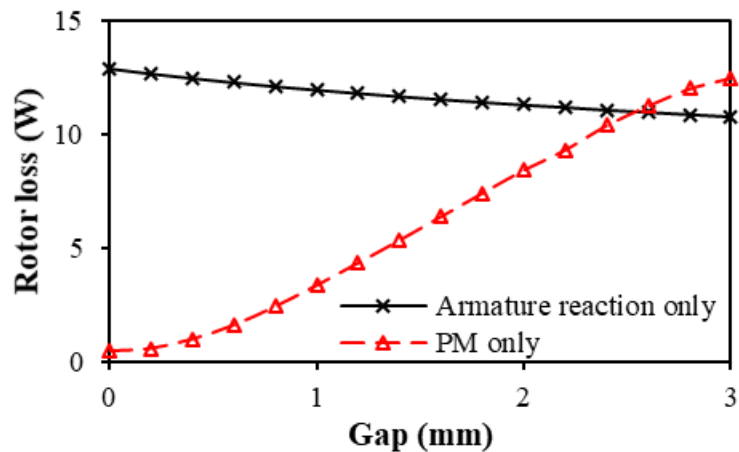
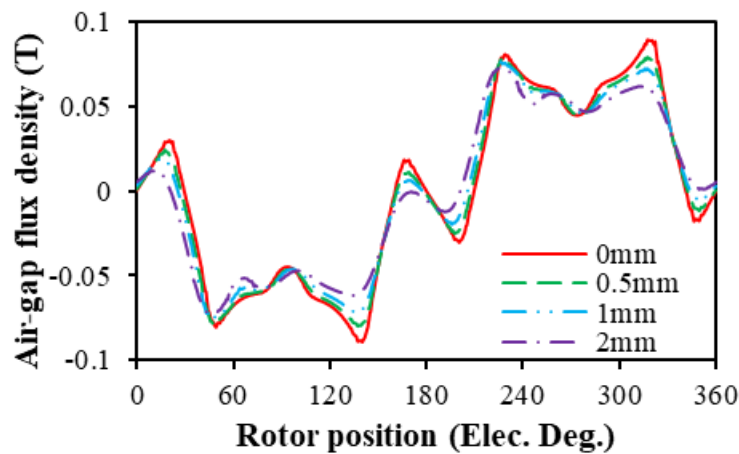
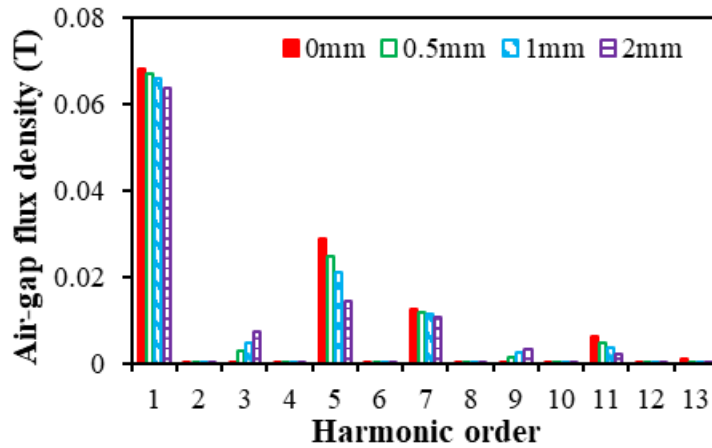


Fig. 4.34. Variation of rotor total loss due to PM only and armature reaction only ($J=10A/mm^2$, 180krpm).



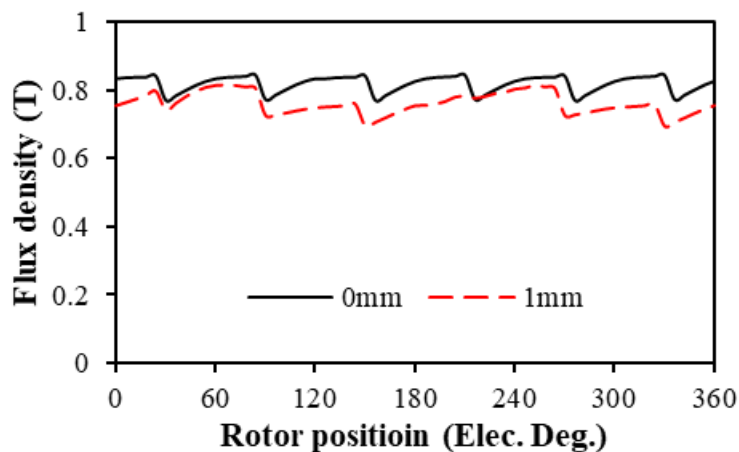
(a) Waveforms



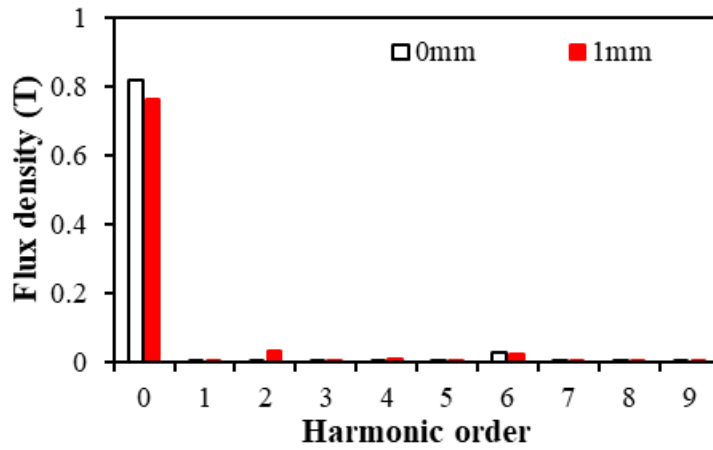
(b) Harmonics

Fig. 4.35. Air-gap flux density due to armature reaction only ($J=10A/mm^2$, 180krpm).

Since the PM eddy current loss has direct relationship with the flux density produced by the magnet, the influence of stator gap on the flux density of magnet will be investigated in this part. Point C is chosen in the middle of north pole and point D is chosen in the middle between south and north pole, as shown in Fig. 4.27. Figs. 4.36 and 4.37 compare the flux densities at point C with 0mm and 1mm stator gap under on-load and no-load conditions, respectively. The amplitude of the 2nd order harmonic increases with the increase of stator gap no matter what is the condition, which results in the increase of the PM eddy current loss. Figs. 4.38 and 4.39 show almost the same results for point D. It is worth noting that under no-load condition, the flux density of point D exists the 4th order harmonic.

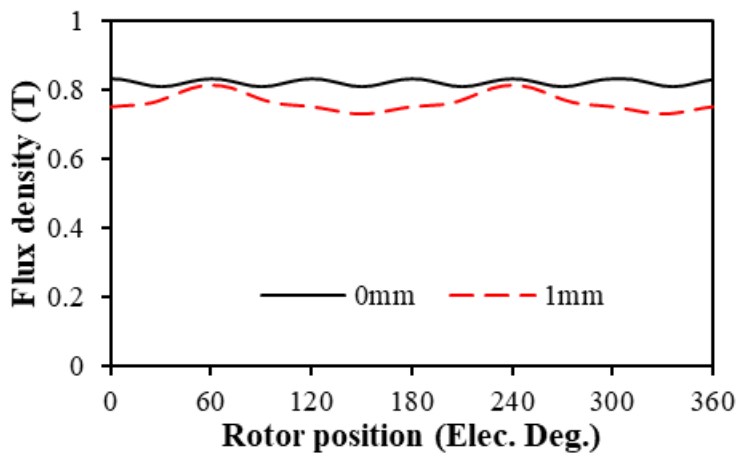


(a) Waveforms

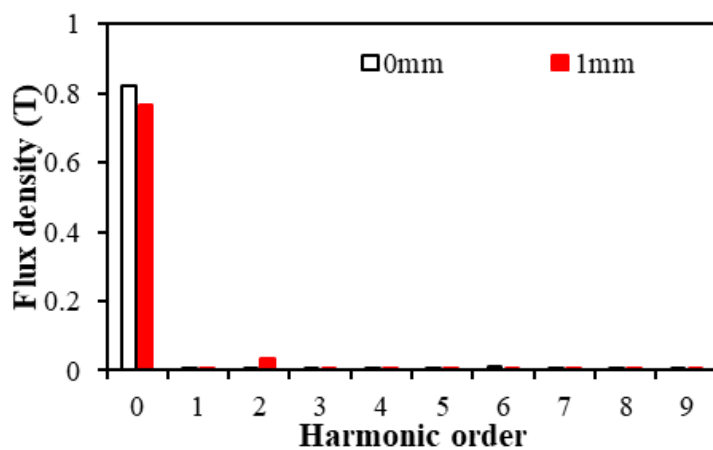


(b) Harmonics

Fig. 4.36. Flux density of Point C with different stator gaps under on-load condition.

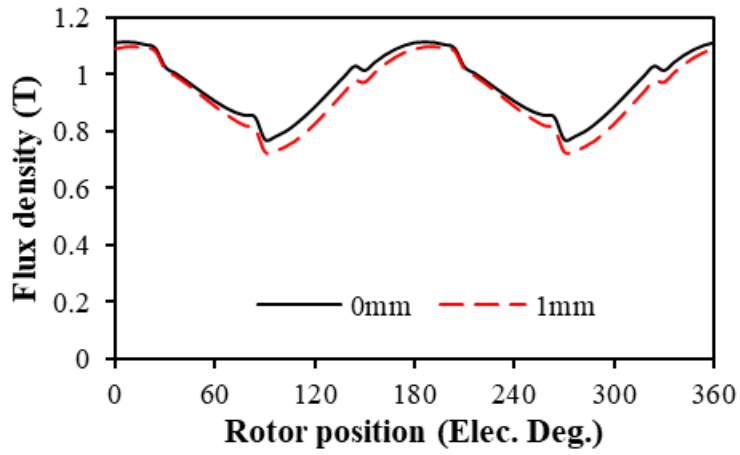


(a) Waveforms

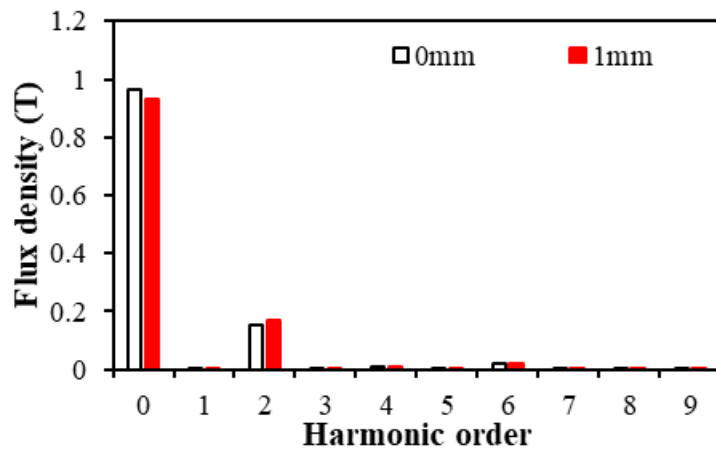


(b) Harmonics

Fig. 4.37. Flux density of Point C with different stator gaps under no-load condition.

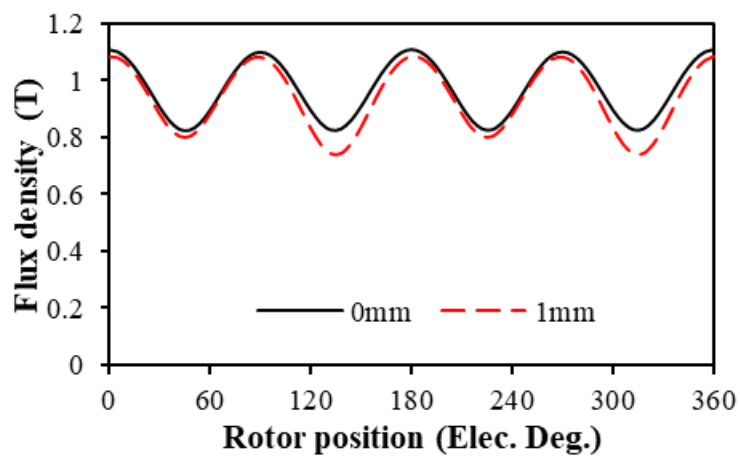


(a) Waveforms

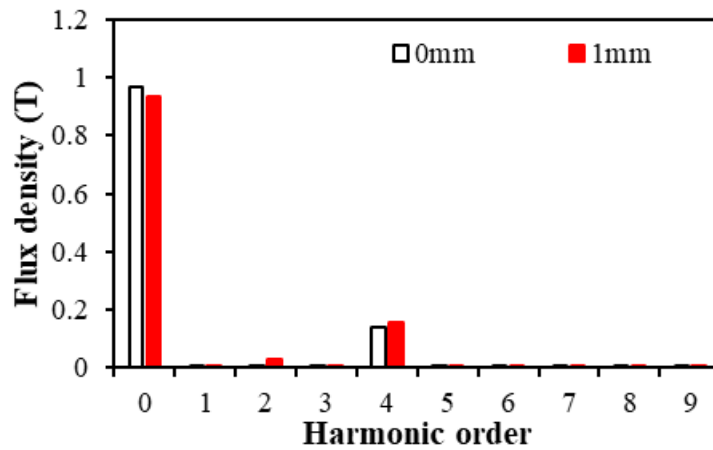


(b) Harmonics

Fig. 4.38. Flux density of Point D with different stator gaps under on-load condition.



(a) Waveforms



(b) Harmonics

Fig. 4.39. Flux density of Point D with different stator gaps under no-load condition.

4.5 Electromagnetic Performance with Misaligned Stator Structure

Another potential manufacturing tolerance of the completed assembly is shown in Fig. 4.40. For simplicity, assuming one stator split part is assembled with uniform air-gap distribution but the other part is assembled with unbalanced air-gap distribution. The offset value is defined as m in Fig. 4.40. In this section, the influence of the misaligned stator structure on the electromagnetic performance is investigated, including air-gap field, back-EMF, cogging torque, torque, and various loss components.

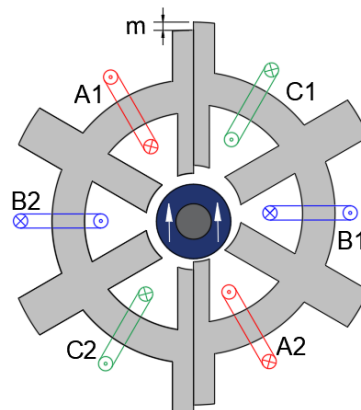


Fig. 4.40 6s/2p HSPM toroidal motor with misaligned stator structure.

4.5.1 Air-gap flux density

The open-circuit equal potential distributions of motors with different offset values, i.e. 0, 0.5 and 0.7 mm are presented in Fig. 4.41. Fig. 4.42 shows that there exists a pulsation in the air-gap

flux density waveform due to the sudden change of the equivalent air-gap, and the magnitude of pulsation increases with the increase of offset value. The spectra show that the misaligned assembly leads to the 2nd, 3rd, and 4th order harmonics of air-gap flux density, and the magnitudes of those additional harmonics increase with the increased offset value. However, the misaligned assembly has almost no influence on the fundamental amplitude of air-gap flux density.

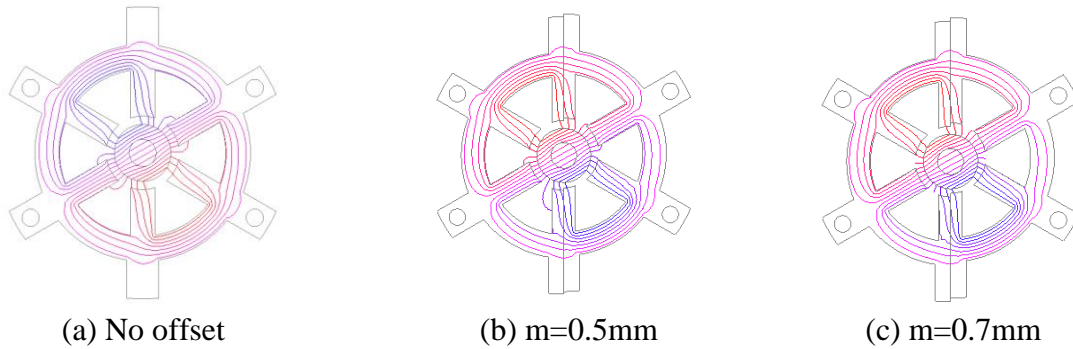


Fig. 4.41. Equal potential distributions of motors with misaligned assembly.

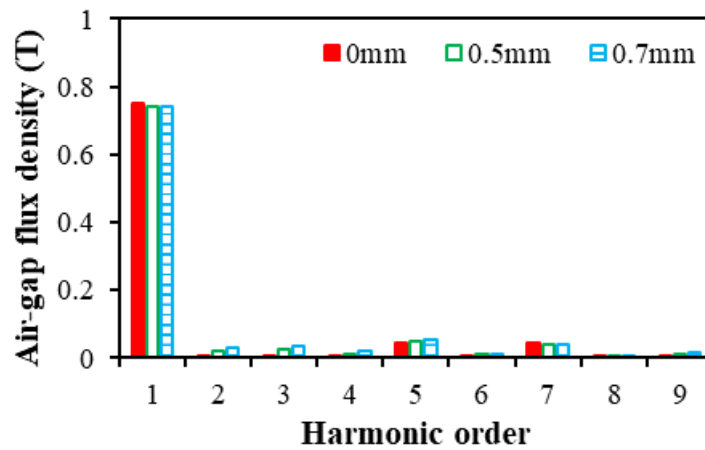
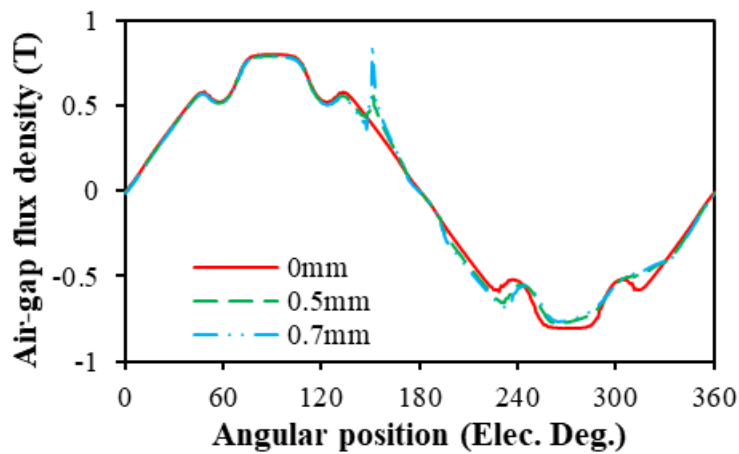
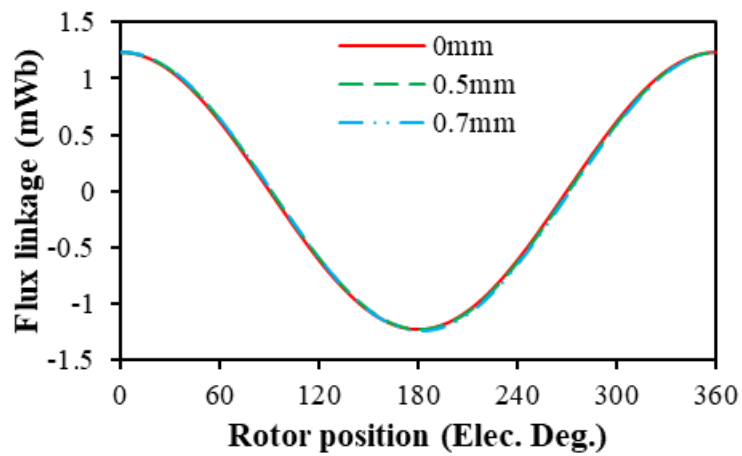


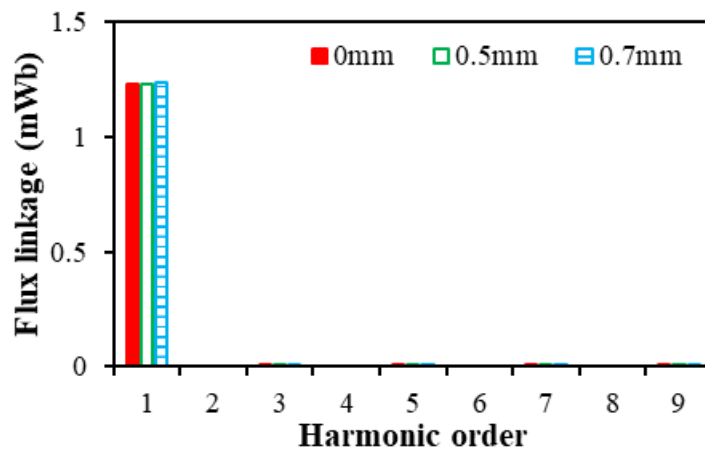
Fig. 4.42. Air-gap flux density distributions of the motor with different offset values on circular path away from rotor by 0.775 mm.

4.5.2 Flux linkage

Fig. 4.43 shows the influence of misaligned assembly on the flux linkage. In terms of phase angle, phase B is retarded, and the offset phase angle of the flux linkage in phase B increases with the increase of offset value. The variation of winding B1 has the biggest change, Fig. 4.44. This is because of the asymmetric position of phase B. Besides, phase A and phase C have not much influence as Phase B.



(a) Waveforms



(b) Harmonics

Fig. 4.43. Flux linkage of phase A with different offset values.

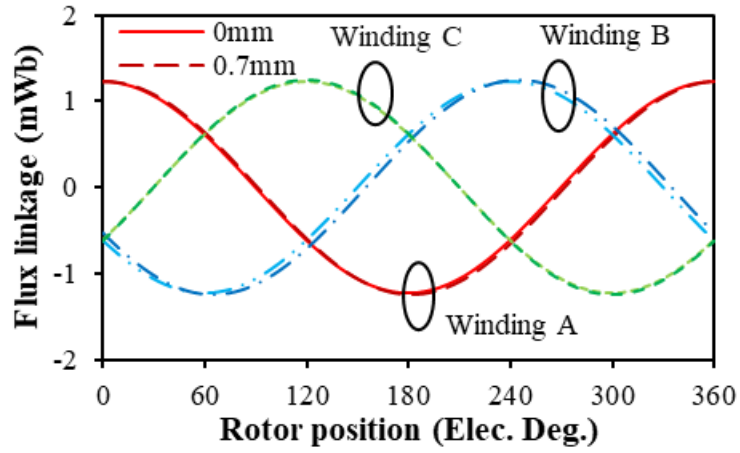
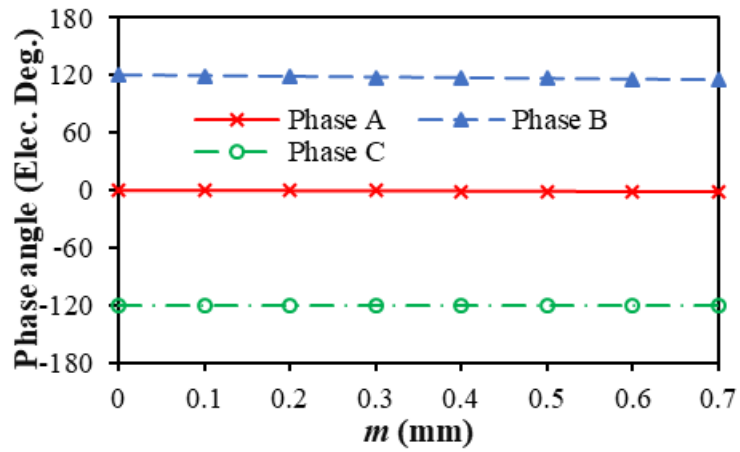
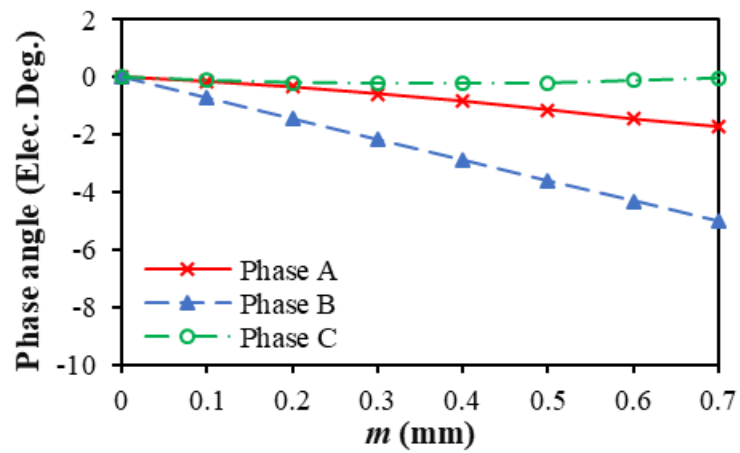


Fig. 4.44. Flux linkage waveforms of motor with 0 and 0.7mm offset values.

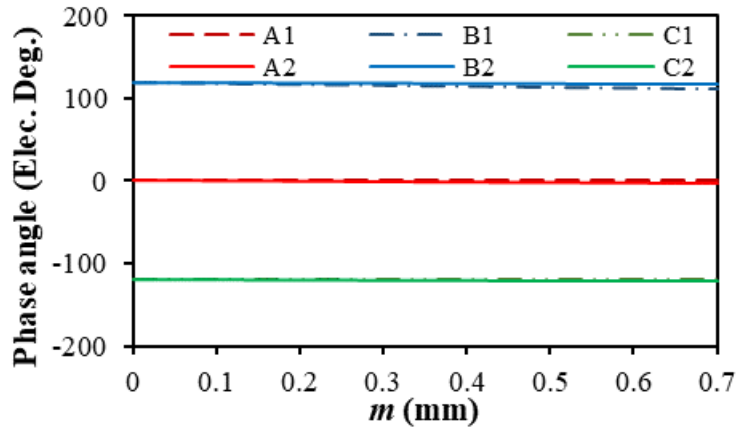


(a) Phase angle

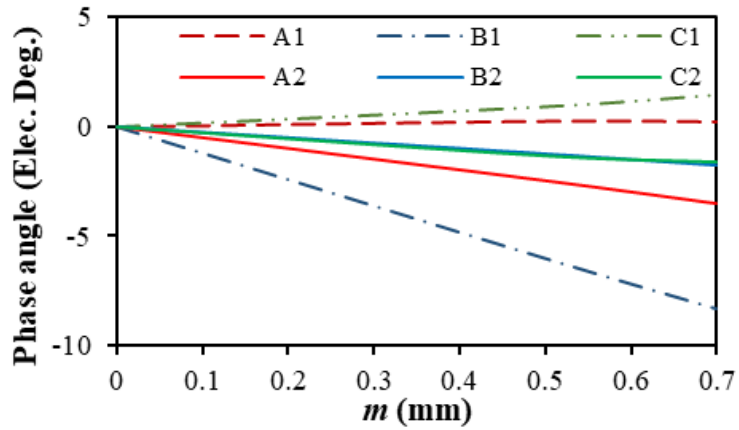


(b) Offset phase angle

Fig. 4.45. Influence of misaligned offset value on phase angle of flux linkage.



(a) Phase angle



(b) Offset phase angle.

Fig. 4.46. Influence of misaligned offset value on winding angle of flux linkage.

4.5.3 Back-EMF

Fig. 4.47 shows that the increased misaligned offset value has almost no effect on the amplitude of fundamental back-EMF and does not change the harmonic contents. With the same result of flux linkage, the misaligned offset value affects the phase angle of three phase back-EMFs, which leads to the unbalanced three phase back-EMFs. Fig. 4.48 shows the variation of the phase angles and offset phase angles of three phase back-EMFs with misaligned offset value. It can be seen that the offset phase angles of phase A and Phase B increases with the offset value, but phase C remains the same. Since the misaligned assembly is located between phase A and phase C, phase B suffers most serious asymmetric and thus has the largest offset phase angle.

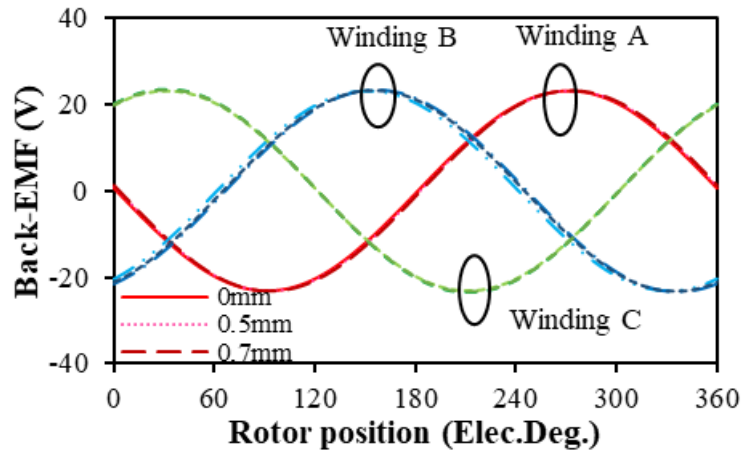


Fig. 4.47. Back EMF waveforms of motors with different offset values.

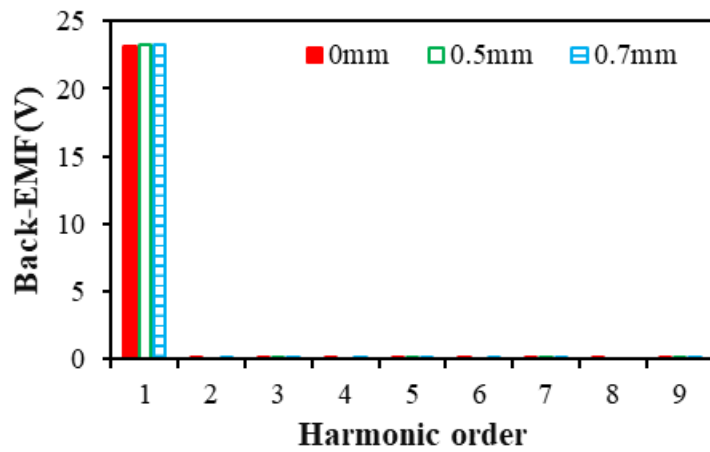
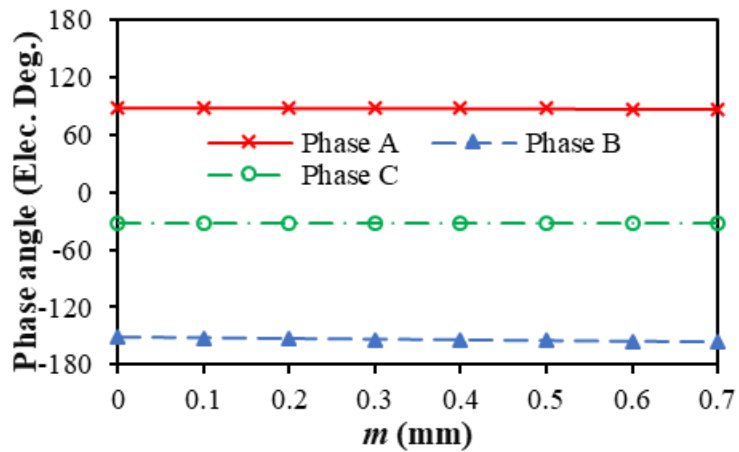
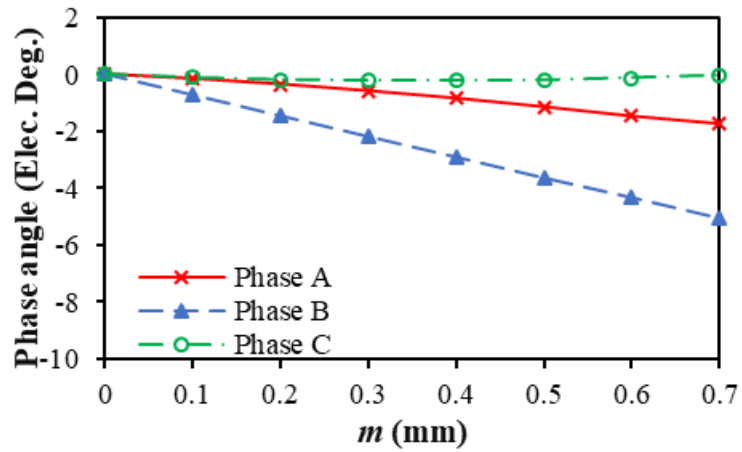


Fig. 4.48. Back EMF harmonics of Phase A with different offset values.



(a) Phase angle

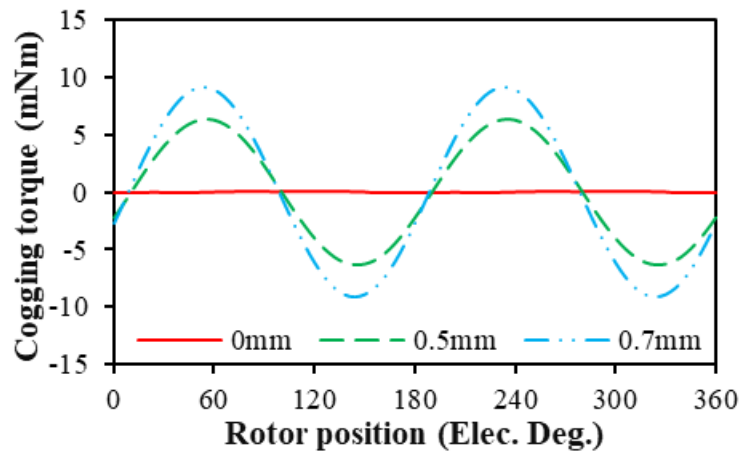


(b) Offset phase angle

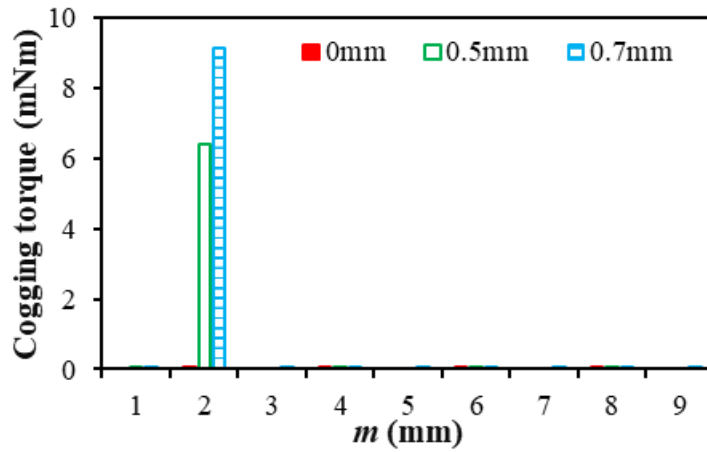
Fig. 4.49. Influence of misaligned offset value on phase angle of back EMF.

4.5.4 Cogging torque

Generally, the 6s/2p PM motor with diametrically-magnetized magnet has negligible cogging torque. Significant cogging torque is produced due to the misaligned assembly. Figs. 4.50 and 4.51 show that the peak cogging torque rises with the increase of misaligned offset values.



(a) Waveforms



(b) Harmonics

Fig. 4.50. Cogging torque of the motors with different misaligned offset value.

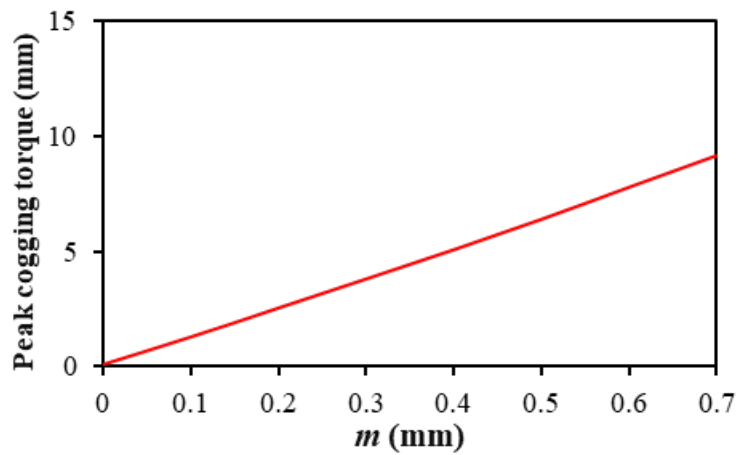
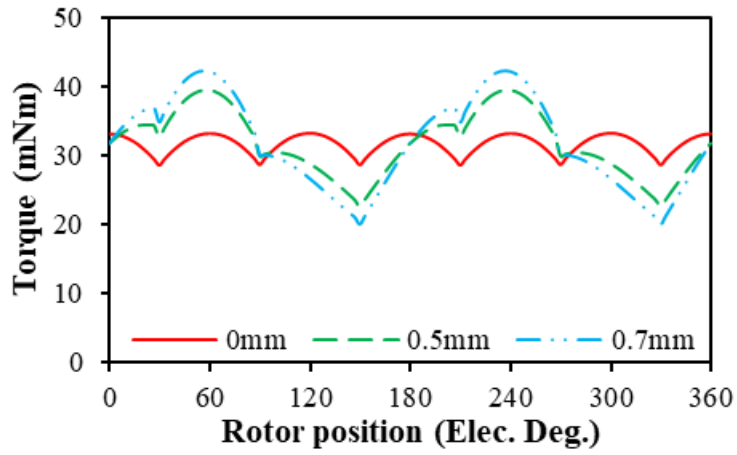


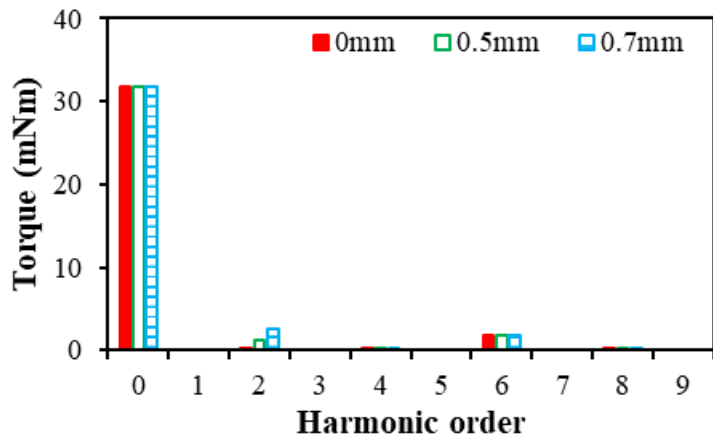
Fig. 4.51. Influence of misaligned offset values on peak cogging torque.

4.5.5 Electromagnetic torque

The influence of different misaligned offset values on the electromagnetic torque is shown in Fig. 4.52. It can be seen that the torque ripples rise with the increase of the misaligned offset value due to the increase of peak cogging torque. The spectra show that the misaligned assembly does not change the magnitudes of the fundamental and the 6th order harmonic, but leads to the 2nd order harmonic, which results from the cogging torque. It is assumed that the influence of on-load condition on cogging torque is neglected. Fig. 4.53 shows that the misaligned assembly has negligible influence on the average torque.



(a) Waveforms



(b) Harmonics

Fig. 4.52. Torque of motors with different misaligned offset value ($J=10A/mm^2$).

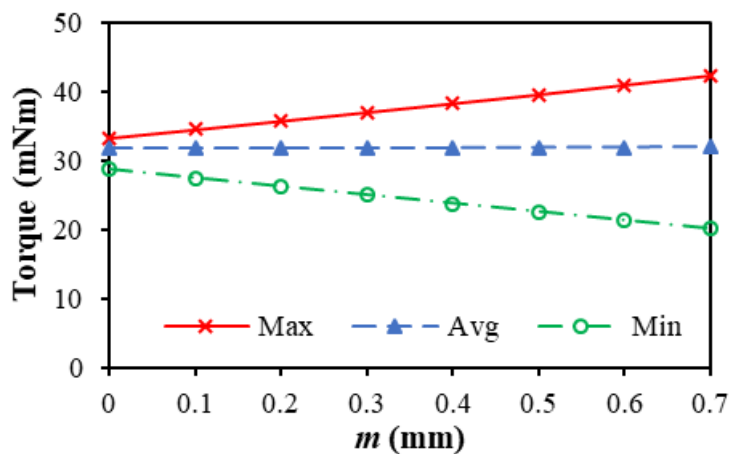
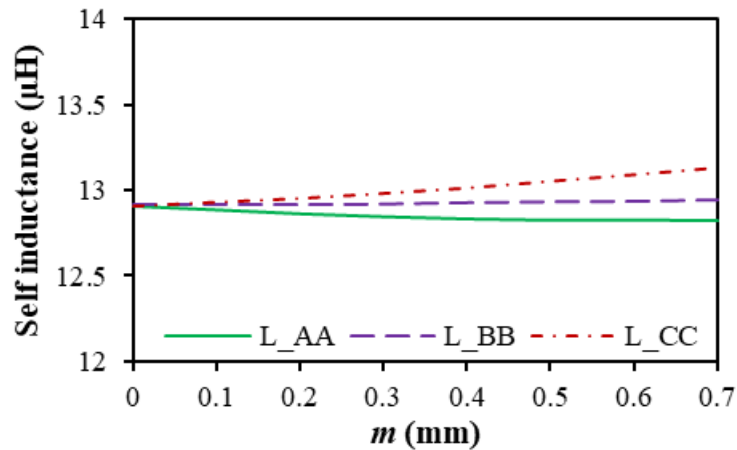


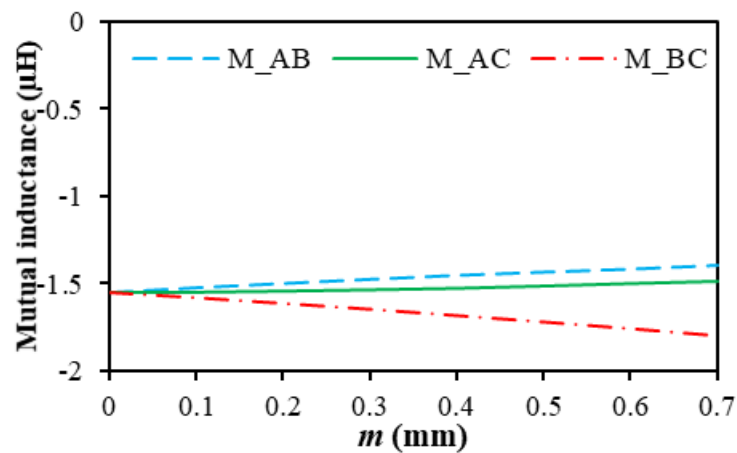
Fig. 4.53. Influence of misaligned offset value on output torque.

4.5.6 Inductance

High speed motors normally have small winding inductances. Even though there is a slight change of inductance due to the stator misaligned, the influence could be significant. The inductance is calculated by FEA, when only one phase excited ($I_a=1A$, $I_b=0A$, $I_c=0A$). Fig. 4.54 shows that the influence of misaligned assembly has small influence on the self- and mutual-inductances.



(a) Self-inductance



(b) Mutual-inductance.

Fig. 4.54. Inductances of the motors with different misaligned offset values.

4.5.7 Loss

As mentioned before, the gap between the stator segments affects the stator iron loss due to the spatial harmonics in MMF. The misaligned assembly has negligible influence on MMF, and thus the stator iron loss remains unchanged with the offset values, Fig. 4.55. In this part, the ac effect on the copper loss is again neglected. Thus, only dc copper loss is considered and it remains unchanged with the misaligned offset value. Misaligned assembly leads to non-uniformed air-

gap and thus increases the rotor PM loss, as shown in Fig. 4.55. In summary, with the increase of misaligned offset value, the total motor losses increase due to the increased rotor PM loss.

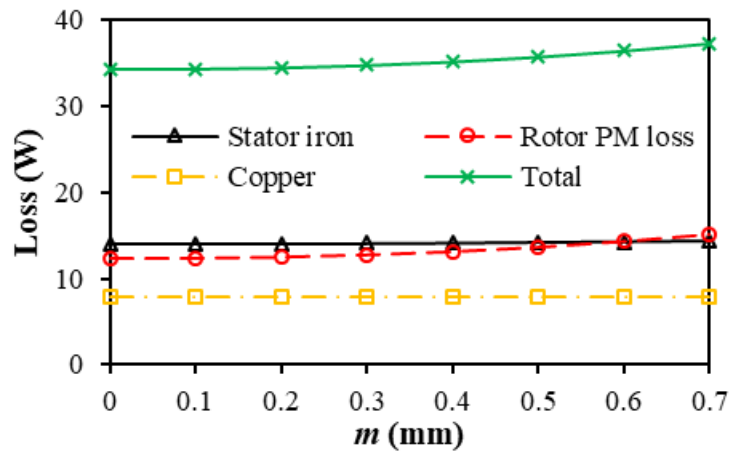


Fig. 4.55. Variation of various loss components of the motors with different misaligned offset values ($J=10A/mm^2$, 180krpm).

4.6 Influence of Both Gap and Misalignment

Fig. 4.56 shows the cross-sections of 6s/2p HSPM toroidally-wound motors with stator gap and misaligned assembly. The stator gap is located between the windings of phase A and phase C, which divides the stator into two halves. The misaligned assembly also occurs between the windings of phase A and phase C.

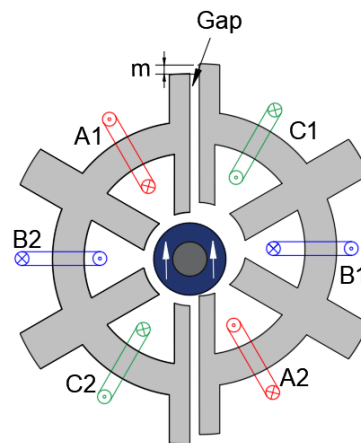


Fig. 4.56. 6s/2p HSPM toroidal motors with stator gap and misaligned assembly.

4.6.1 Air-gap flux density

Fig. 4.57 compares open-circuit equal potential distributions of motors with both gap of 0.5 mm and offset values of 0.5 mm. Fig. 4.58 shows that there exists a pulsation in the air-gap flux

density waveform due to the sudden change of the equivalent air-gap length, and the magnitude of pulsation increases with the increase of offset value. The spectra show the misaligned assembly leads to the 2nd, 3rd, and 4th order harmonics of air-gap flux density, and the magnitudes of those additional harmonics increase with the increased offset value. However, the misaligned assembly has almost no influence on the fundamental amplitude of air-gap flux density.

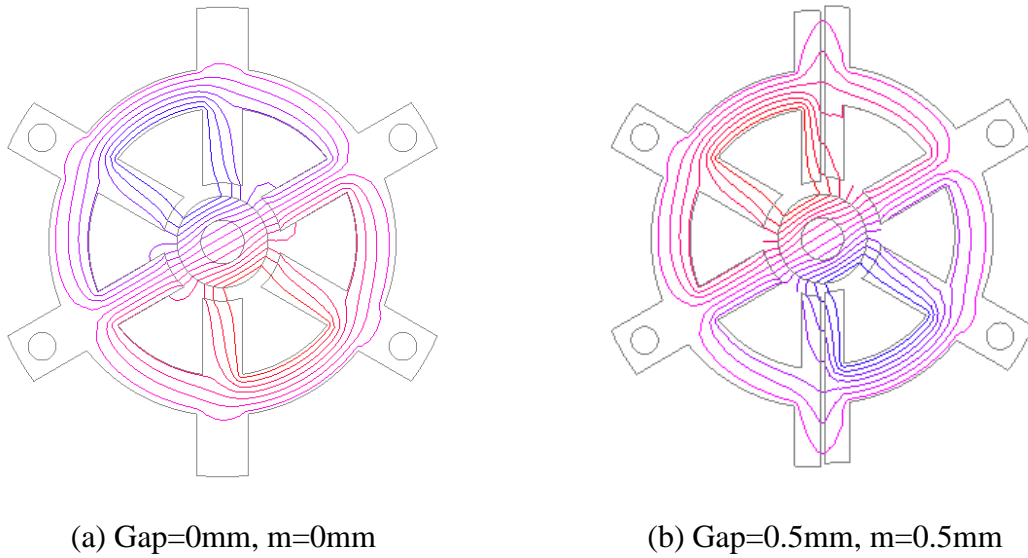
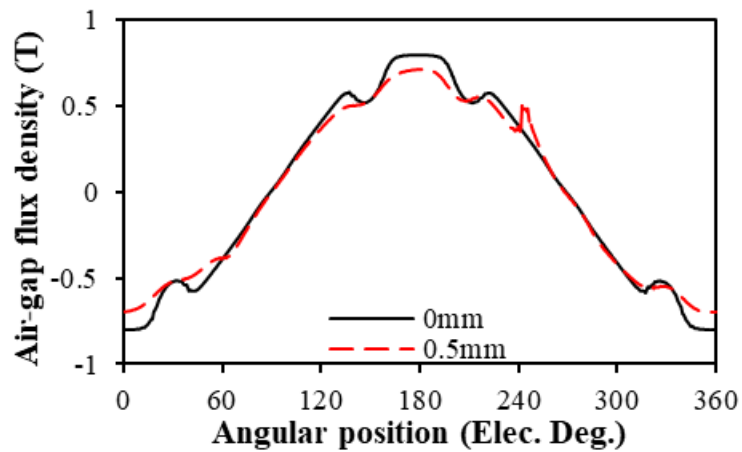
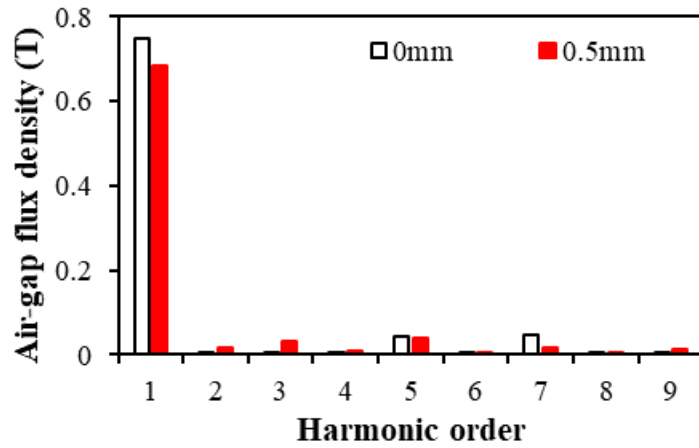


Fig. 4.57. Equal potential distributions of 6s/2p HSPM toroidal motors.



(a) Waveforms

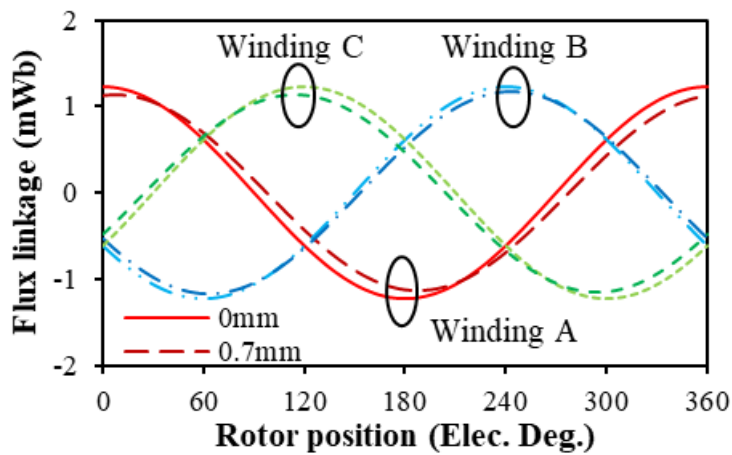


(b) Harmonics

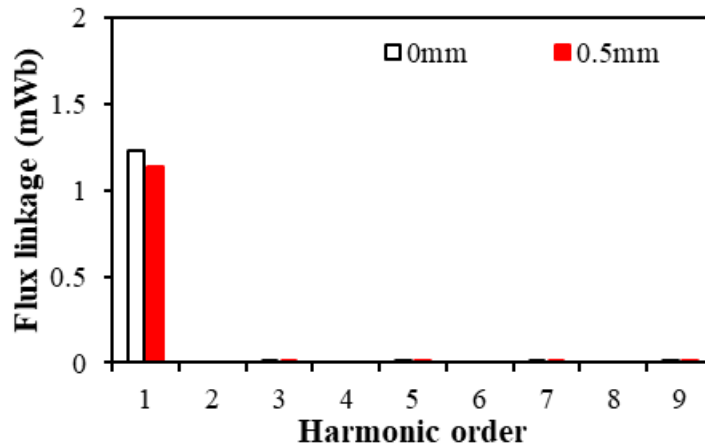
Fig. 4.58. Comparison of air-gap flux density distributions of the motor with gap=0mm, m=0mm and the motor with gap=0.5mm, m=0.5mm on circular path away from rotor by 0.775 mm.

4.6.2 Flux linkage

Fig. 4.59 shows the influence of misaligned assembly on the flux linkage. It can be seen that misaligned mainly affect the phase angle of phase B. Gap affects both the amplitudes of fundamental and phase angles of phase A and phase C.



(a) Waveform

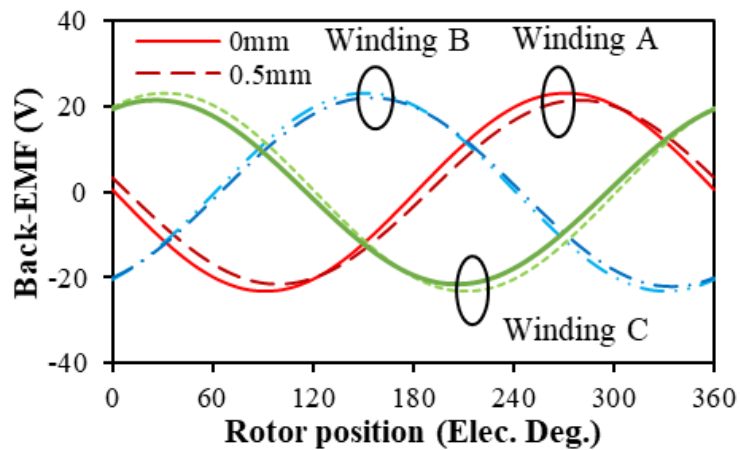


(b) Harmonics

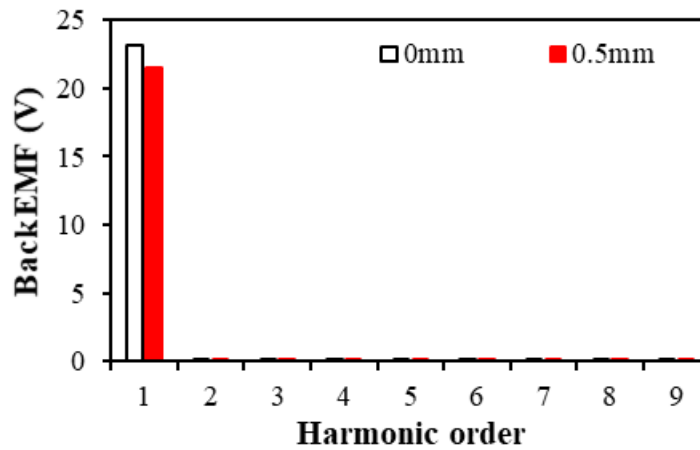
Fig. 4.59. Comparison of flux linkages of the motor with gap=0mm, m=0mm and the motor with gap=0.5mm, m=0.5mm of phase A.

4.6.3 Back-EMF

The comparison of no gap and misaligned with 0.5mm gap and misaligned off-set value is shown in Fig. 4.60. It can be seen that both the amplitude of fundamental back-EMF and the harmonic contents changed. With the same result of flux linkage, the misaligned offset value affects the phase angles of three phase back-EMFs, which leads to the unbalanced three phase back-EMFs.



(a) Waveforms

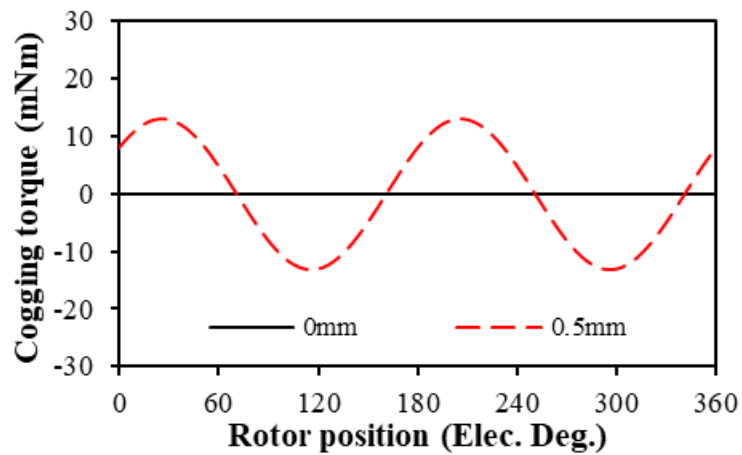


(b) Harmonics

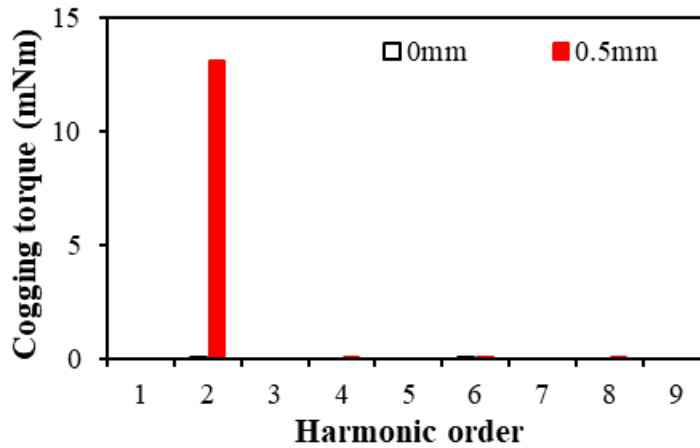
Fig. 4.60. Comparison of flux linkages of the motor with gap=0mm, m=0mm and the motor with gap=0.5mm, m=0.5mm of phase A.

4.6.4 Cogging torque

Cogging torque has been affected significantly by either gap or misalignment. Fig. 4.61 shows with 0.5mm gap and misaligned off-set value, cogging torque is significantly changed due to asymmetric and non-uniform structure.



(a) Waveforms

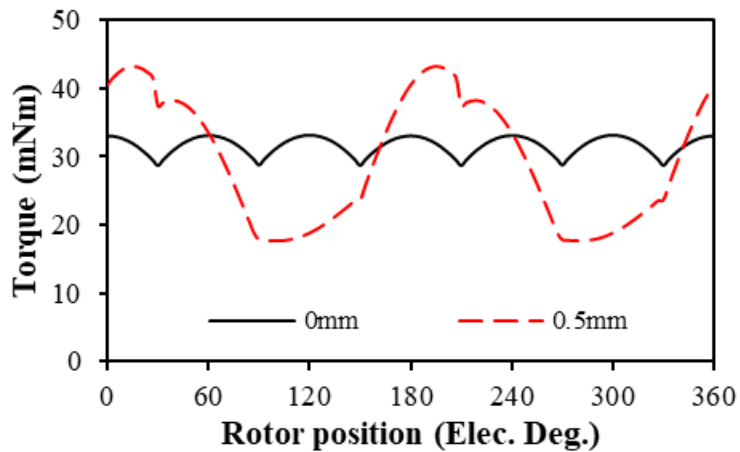


(b) Harmonics

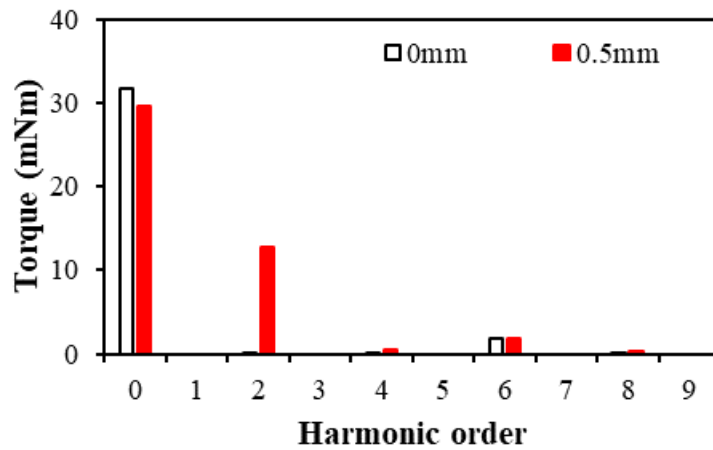
Fig. 4.61. Comparison of cogging torques of the motor with gap=0mm, m=0mm and the motor with gap=0.5mm, m=0.5mm.

4.6.5 Electromagnetic torque

Comparison of the motor with no gap and misalignment and the motor with 0.5mm gap length and misaligned off-set value is shown in Fig. 4.62. It can be seen that the torque ripples rise when the misaligned offset value increases due to the increase of peak cogging torque. The spectra show that the misaligned assembly does not change the magnitudes of the fundamental and the 6th order harmonic, but leads to the 2nd order harmonic, which is resulted from the cogging torque.



(a) Waveforms



(b) Harmonics

Fig. 4.62. Comparison of on-load torques of the motor with gap=0mm, m=0mm and the motor with gap=0.5mm, m=0.5mm ($J=10\text{A}/\text{mm}^2$).

4.6.6 Inductance

The inductance is calculated by FEA when only one phase excited ($I_a=1\text{A}$, $I_b=0\text{A}$, $I_c=0\text{A}$). Fig. 4.63 shows that the influence of misaligned assembly has negligible influence on the self- and mutual- inductances.

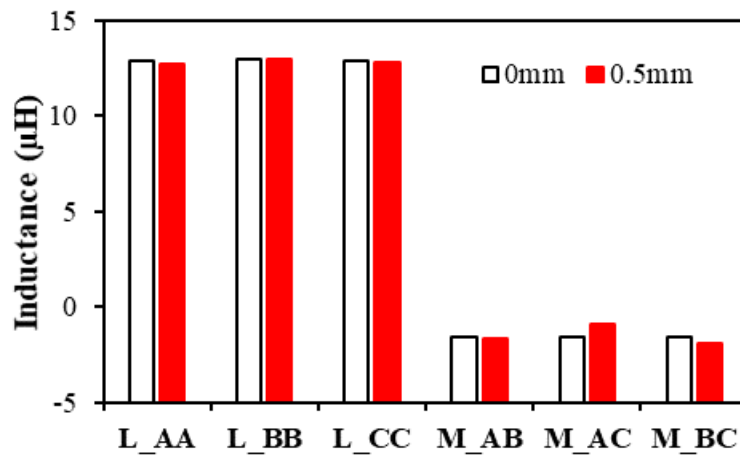


Fig. 4.63. Comparison of inductances of the motor with gap=0mm, m=0mm and the motor with gap=0.5mm, m=0.5mm.

4.6.7 Losses

As mentioned in section 4.4, the gap between the stator segments affects the stator iron loss due to spatial harmonics in MMF. The misaligned assembly has small influence on MMF, and thus the stator iron loss remains unchanged when the offset values increases, in Fig. 4.55. In this part, the ac effect on the copper loss is again neglected. Thus, only dc copper loss is considered and it

remains unchanged with either the gap or the misaligned offset value. Misaligned assembly leads to non-uniformed air-gap and thus increases the rotor PM loss, as shown in Fig. 4.64. In summary, compared with the motor without gap and misalignment, the stator iron loss is reduced, the rotor PM loss is increased, and total loss is increased.

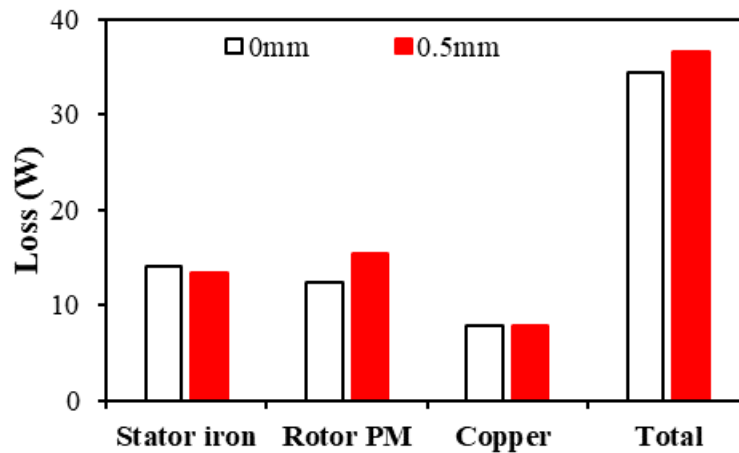
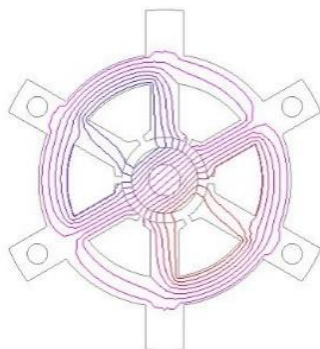


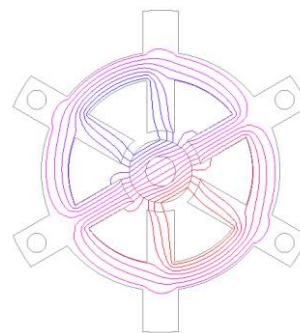
Fig. 4.64. Comparison of losses of the motor with gap=0mm, m=0mm and motor with gap=0.5mm, m=0.5mm.

4.7 Influence of Tooth Tip

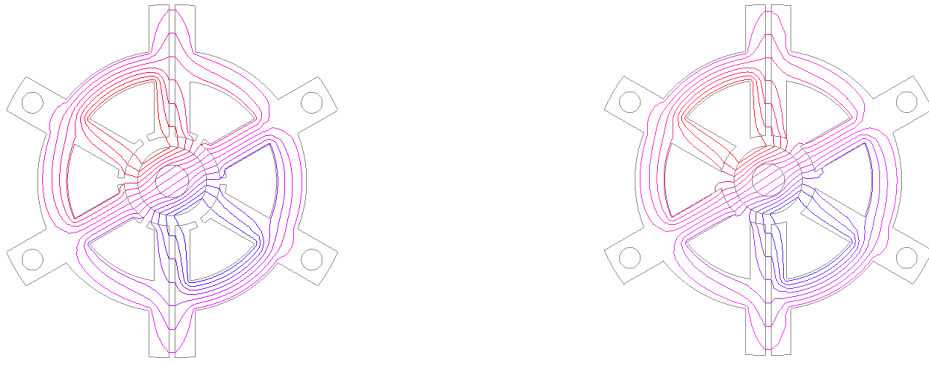
The influence of tooth tip is investigated in this section. Fig. 4.65 shows the influence of tooth tip on the equal potential distribution of the motor with 0mm and 1mm stator gap length. The slot opening of the motor with tooth tip is 1mm compared with 2.5mm of motor without tooth tip. Compared with motor without tooth tip, the motor with tooth tip has similar flux distribution. Fig. 4.66 shows the motor with tooth tip and 0mm gap has the highest fundamental amplitude and less harmonic contents of air-gap flux density than the motor without tooth tip.



(a) Gap=0mm with tooth tip



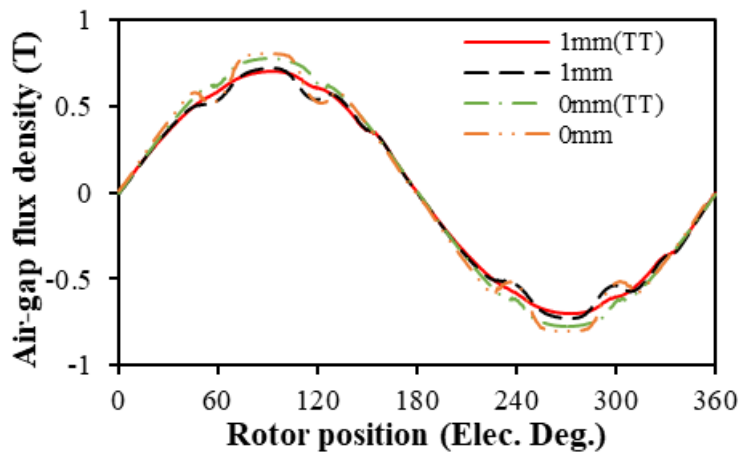
(b) Gap=0mm without tooth tip



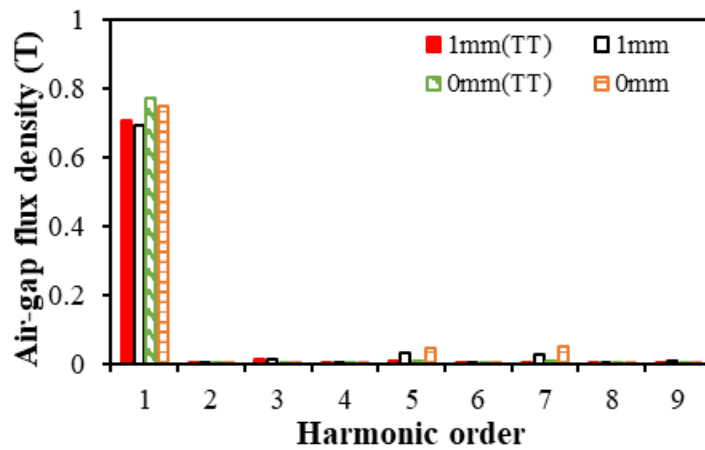
(c) Gap=1mm with tooth tip and 1mm gap

(d) Gap=1mm without tooth tip

Fig. 4.65. Equal potential distributions of 6s/2p HSPM toroidal motors.



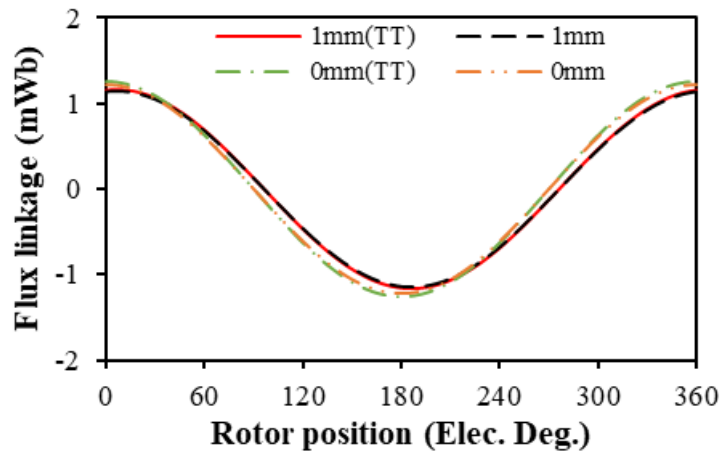
(a) Waveforms



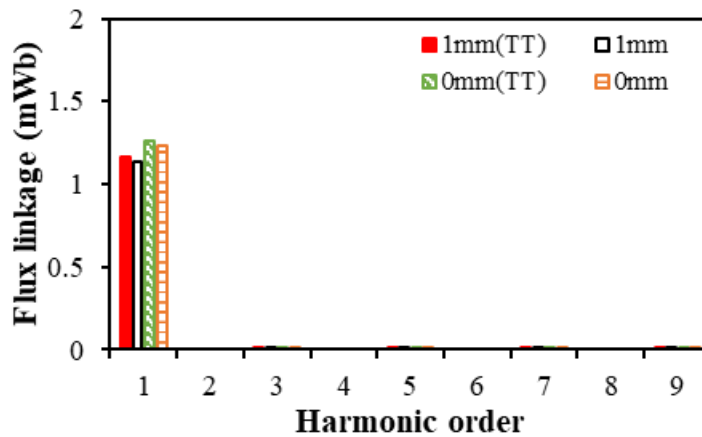
(b) Harmonics

Fig. 4.66. Comparison of air-gap flux density distributions of the motor with gap=0mm and gap=1mm with and without tooth tip (TT) on circular path away from rotor by 0.775 mm.

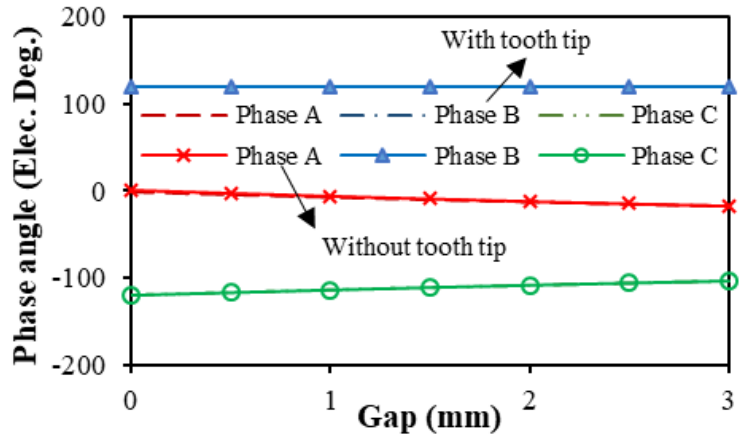
Fig. 4.67 and Fig. 4.68 show the influence of tooth tip on the flux linkage and back EMF of the motor with 0mm and 1mm stator gap, respectively. It can be seen that the tooth tip has small influence on the flux linkage and back EMF. In addition, the influence of stator gap length on phase angles of motor with tooth tip has the same trend as the motor without tooth tip. Fig. 4.69 shows the cogging torque waveforms of the 0mm and 1mm stator gap motors with and without tooth tip. It shows the tooth tip has almost no influence on the cogging torque of the motor with 1mm stator gap. Therefore, for 6s/2p HSPM motor with 1mm stator gap length, the tooth tip only affects the air-gap flux density, and it reduces the fundamental amplitude and harmonic contents.



(a) Waveforms

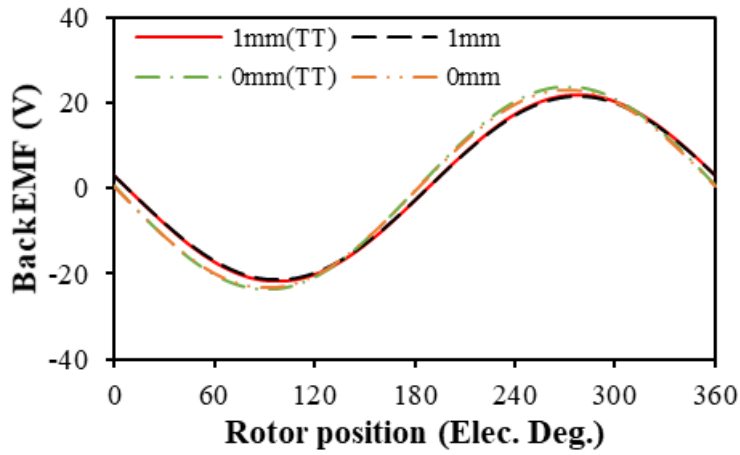


(b) Harmonics

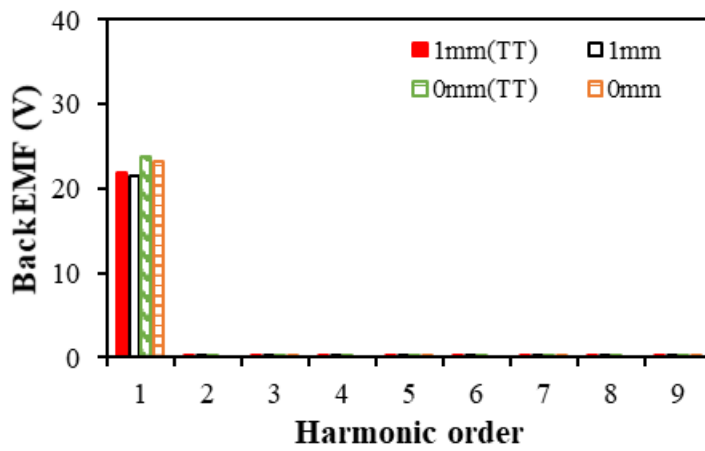


(c) Phase angles

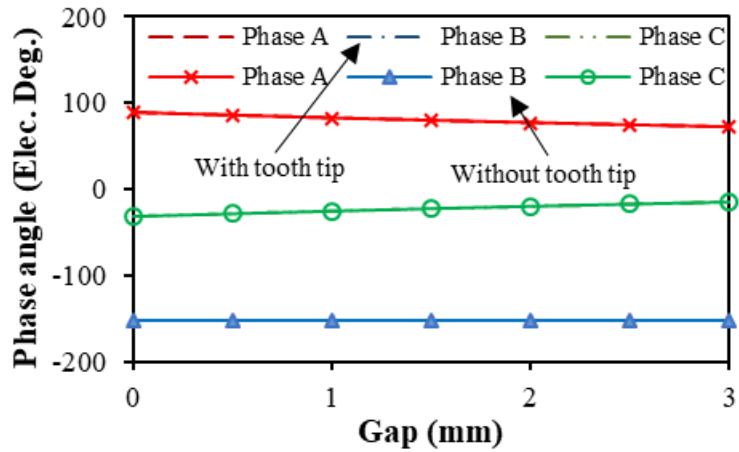
Fig. 4.67. Flux linkage of motor with gap=0mm and gap=1mm with and without tooth tip (TT).



(a) Waveforms



(b) Harmonics



(c) Phase angles

Fig. 4.68. Back EMF of motor with gap=0mm and gap=1mm with and without tooth tip (TT).

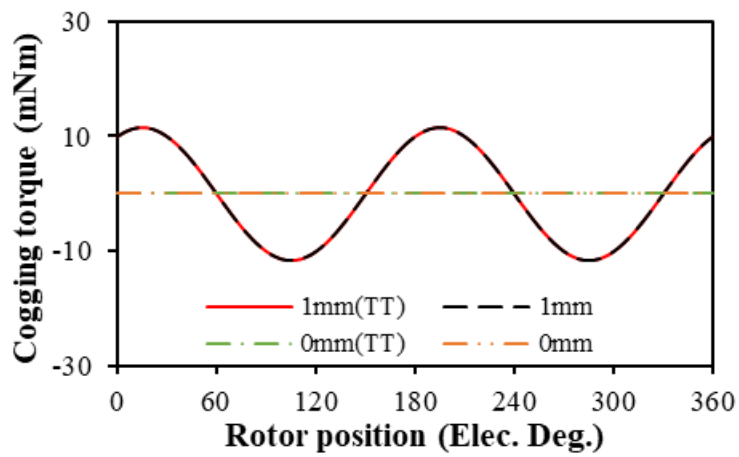


Fig. 4.69. Cogging torque of motor with gap=0mm and gap=1mm with and without tooth tip (TT).

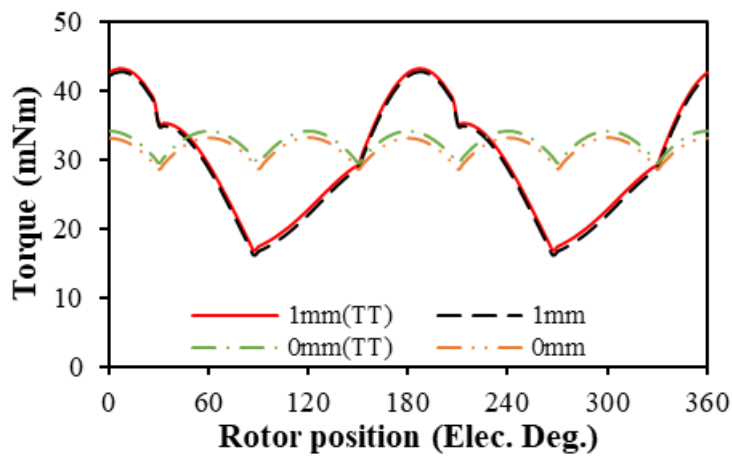


Fig. 4.70. On-load torque of the motor with gap=0mm and gap=1mm with and without tooth tip (TT). ($J=10\text{A}/\text{mm}^2$, 180krpm).

Fig. 4.71 shows the influence of tooth tip on the inductance of the motor with 0mm and 1mm stator gap. The inductances are calculated by FEA. It shows that the tooth tip has large influence on the self-inductance of the motor with and without stator gap. The reason is that tooth tip can increase flux leakage in the slot opening significantly.

Fig. 4.72 compares the loss of motor with and without tooth tip with 0mm and 1mm stator gap when the current density is 10 A/mm² at the speed of 180 krpm. It shows that tooth tip results in larger iron loss but lower rotor PM loss. With the increased gap, the rotor loss is decreased.

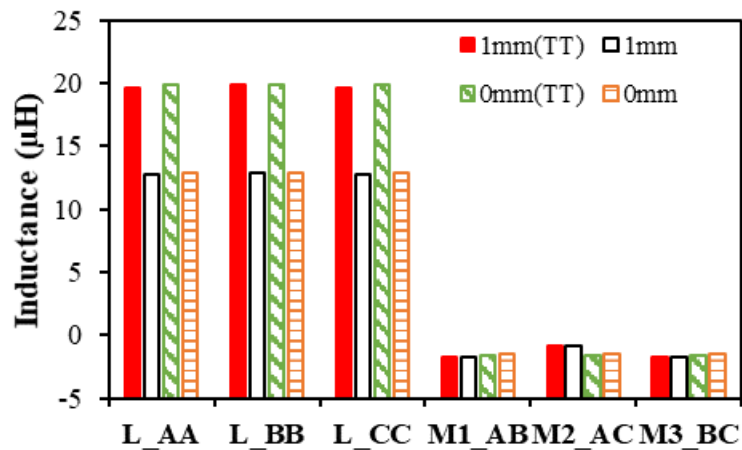


Fig. 4.71. Comparison of inductances of motor with gap=0mm and gap=1mm with and without tooth tip (TT).

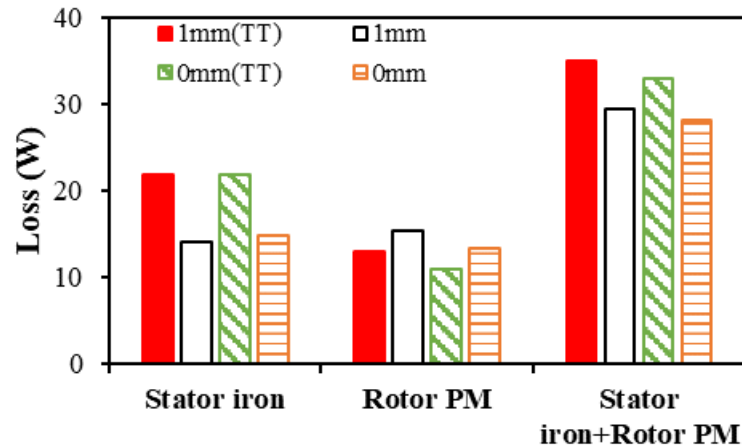
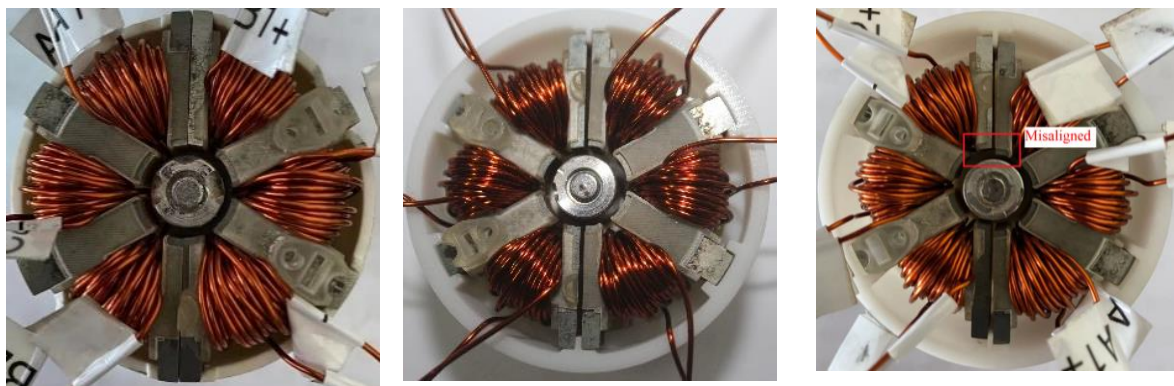


Fig. 4.72. Comparison of losses of motor with gap=0mm and gap=1mm with and without tooth tip (TT) ($J=10\text{A/mm}^2$, 180krpm).

4.8 Experimental Validation

In this section, the back-EMF and on-load static torque waveforms of 6-slot/2-slot PM motors with and without stator gap are measured to validate the FE predictions. Fig. 4.73 shows the prototypes of the 6s/2p HSPM motors without and with stator gap and misalignment. Fig. 4.74 shows the modular stator lamination structure, the rotor-bearing system, and the frame structures without and with 1mm stator gap. For supporting the modular stator structure with 1mm stator gap, a special frame is designed and manufactured by 3D printing. The frame has two teeth with 1mm thickness to form a 1mm stator gap. In addition, there are four slots to fix four outer teeth and support the stator structure, Figs. 4.74 (c) and (d).

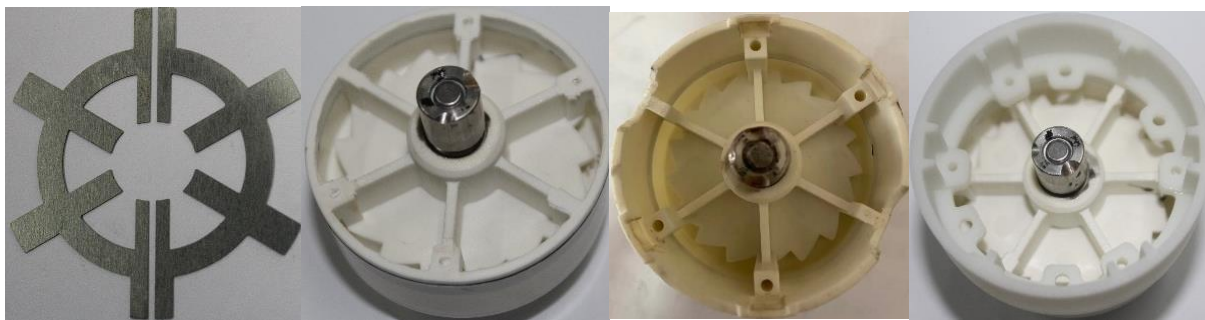


(a) No stator gap & no misalignment

(b) 1mm stator gap & no misalignment

(c) 1mm stator gap & 1mm misalignment

Fig. 4.73. Prototypes of the 6s/2p HSPM motor.



(a) Modular stator lamination

(b) Rotor-bearing system

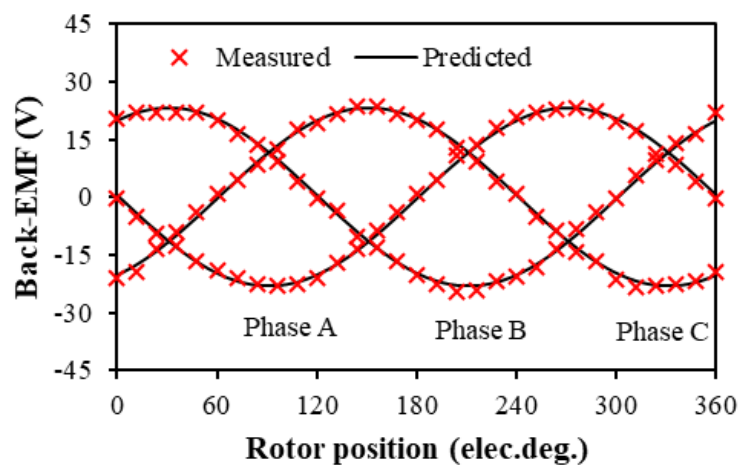
(c) Frame structure without stator gap

(d) Frame structure with 1 mm stator gap

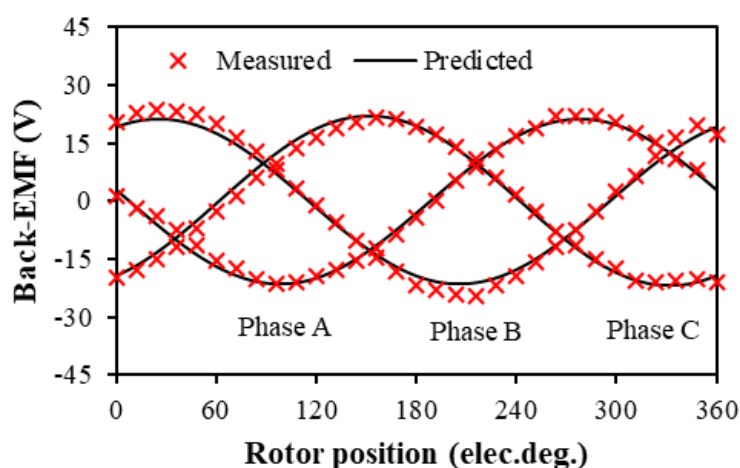
Fig. 4.74. Stator lamination and frame structure.

4.8.1 Back-EMF

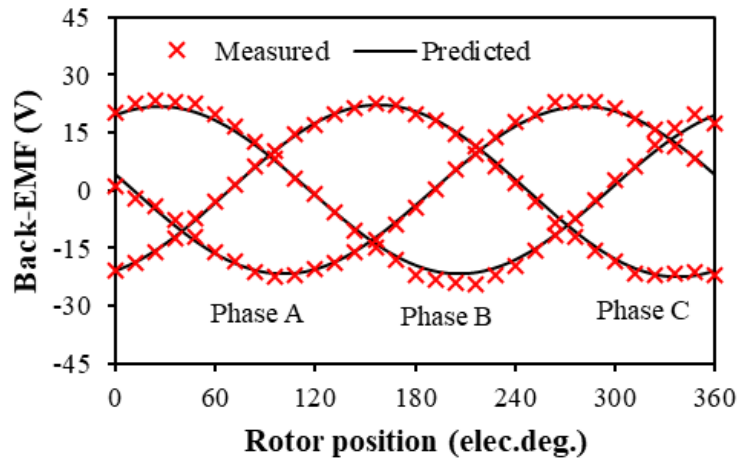
Fig. 4.75 (I) shows the FE predicted and measured three phase back-EMF waveforms of 6s/2p motor with toroidal windings having no stator gap and misalignment. It can be seen that the measured results agree well with the FE predictions. For the motor with 1mm stator gap and no misalignment, the FE predicted three phase back-EMF waveforms are slightly smaller than the measured results, Fig. 4.75 (II). In addition, the stator gap changes the phase angles of three phase back-EMF waveforms, Fig. 4.75 (II-c). Fig. 4.75 (III) shows that when the stator gap is 1mm and the misaligned offset is 1mm, the test results are in good agreement with FE prediction, including the fundamental magnitudes and phase angles of three phase back-EMFs. Overall, the influence of stator gap and misalignment on the back-EMF is verified by the measured results.



(I) No stator gap & no misalignment

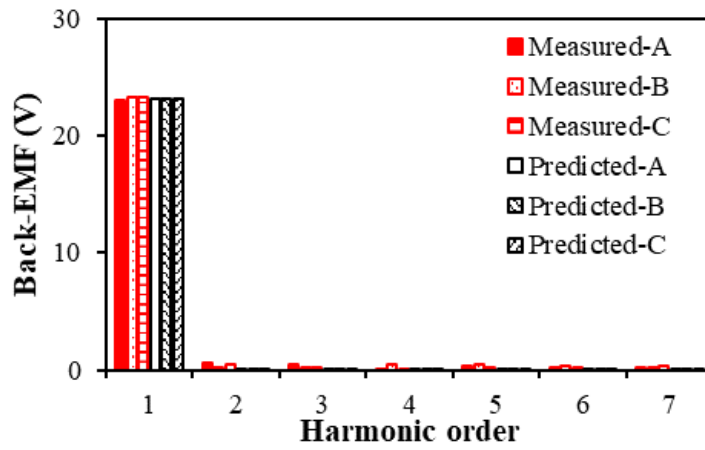


(II) 1mm stator gap & no misalignment

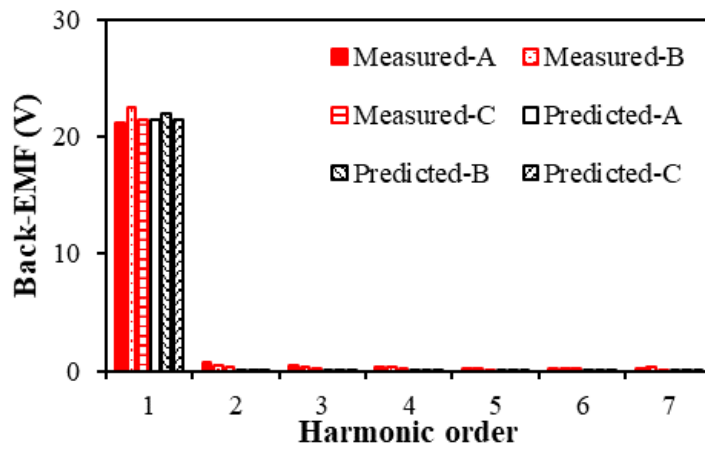


(III) 1mm stator gap & 1mm misalignment

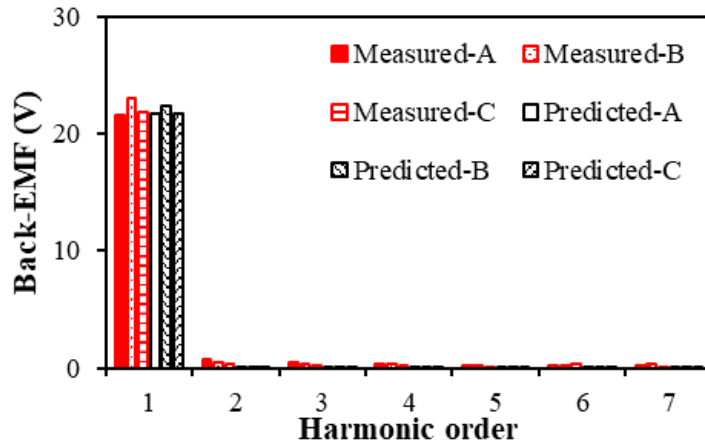
(a) Waveforms



(I) No stator gap & no misalignment

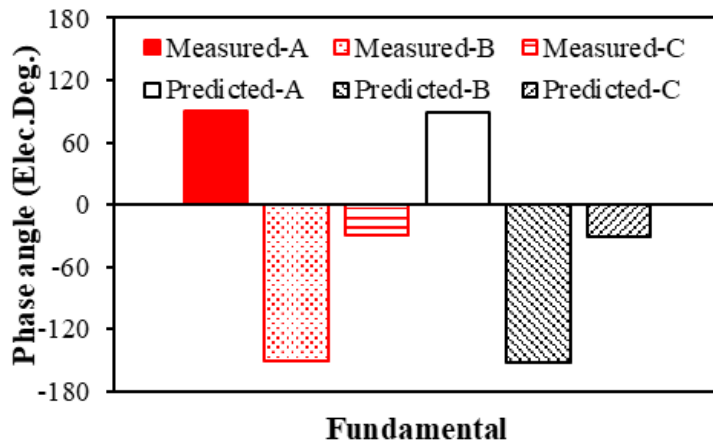


(II) 1mm stator gap & no misalignment

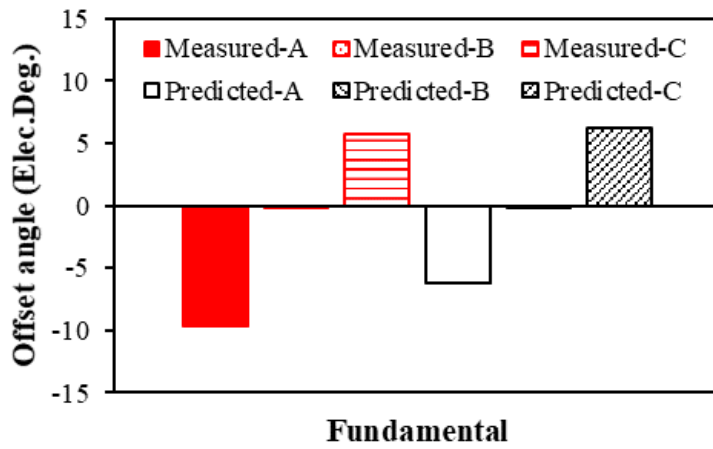


(III) 1mm stator gap & 1mm misalignment

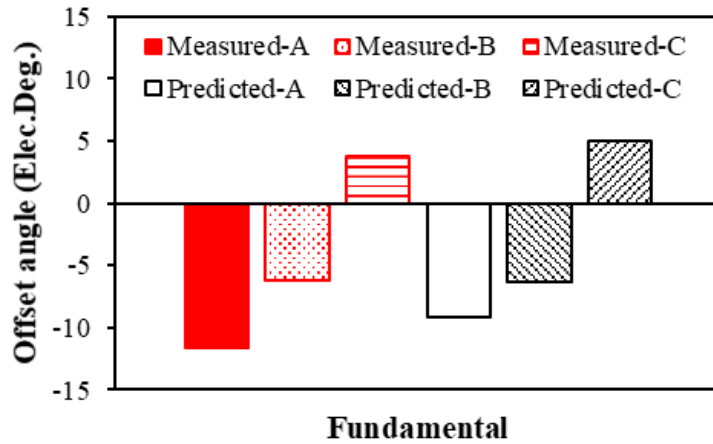
(b) Spectra



(I) No stator gap & no misalignment



(II) 1mm stator gap & no misalignment



(III) 1mm stator gap & 1mm misalignment

(c) Phase angle

Fig. 4.75. FE predicted and measured three phase back-EMF waveforms of 6s/2p motors without and with stator gap and misalignment. (b) Spectra

4.8.2 Phase resistance and winding inductance

The phase resistance and winding inductances are measured by a LCR meter under 0 Hz, 120Hz and 1000 Hz, Table 4.2 and 4.3. Since the analytical prediction is DC resistance and neglecting the influence of frequency, the measured phase resistance by an ohmmeter is almost the same as the prediction. Under 120Hz, the measured result is larger than the analytical result. The measured phase resistance under high frequency (1kHz) are significantly larger than that under low frequency (120Hz).

For winding inductance, the FE predictions are ideal winding inductances and neglecting the influence of frequency, and thus the measured inductances are larger than the predicted results by FEA due to neglecting end-winding in 2D-FE model. With the increase of frequency, the measured inductance decreases. It is worth noting that the stator gap increases the inductance of phase B since the gap occurs between phases A and C.

Table 4.2
Winding Resistances (mΩ)

ANA	Measured (0 Hz)	Measured (120Hz)	Measured (1000Hz)
24.3	25.1	25.5	36.5

Table 4.3
Winding Inductances(μH)

		2-D FE	Measured (120Hz)	Measured (1000Hz)
No stator gap	A	14.45	24.1	23.47
	B	14.45	24.1	23.47
	C	14.45	24.1	23.47
Stator gap=1mm	A	14.50	35.93	35.40
	B	14.68	39.60	38.08
	C	14.50	35.93	35.40

4.8.3 Static torque

In literature [XUF20], a test rig is designed to measure the on-load static torque, Fig. 4.76. The cogging torque can be measured under open-circuit condition, and with the armature currents of $I_A = -I_B = 5\text{A}$, $I_C = 0\text{A}$, the on-load static torques of the 6s/2p motor at different rotor positions can be measured. Without and with stator gap and misalignment, the FE predicted and measured cogging torques and on-load static torques have a good agreement, Figs. 4.77, 4.78, and 4.79. Fig. 4.80 shows that with the increase of phase current, the measured maximum static torques are in good agreement with FE predictions of 6s/2p motor without and with stator gap and misalignment.

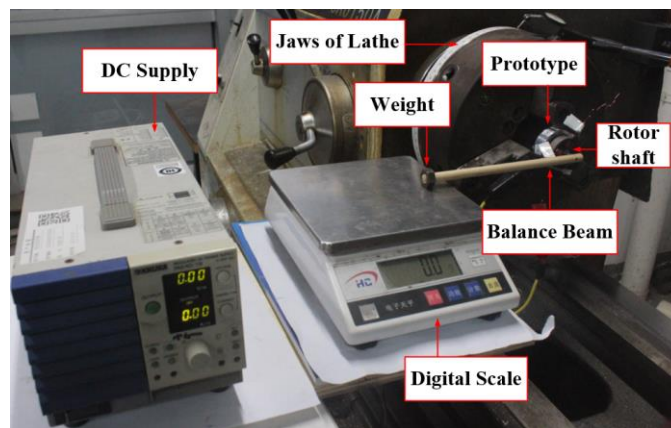
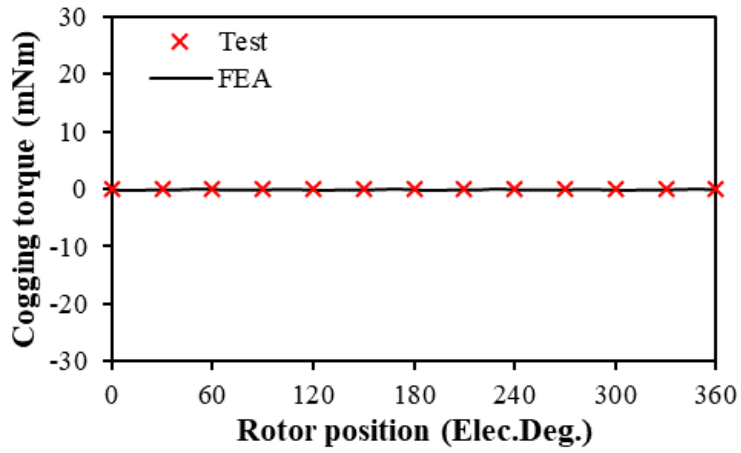
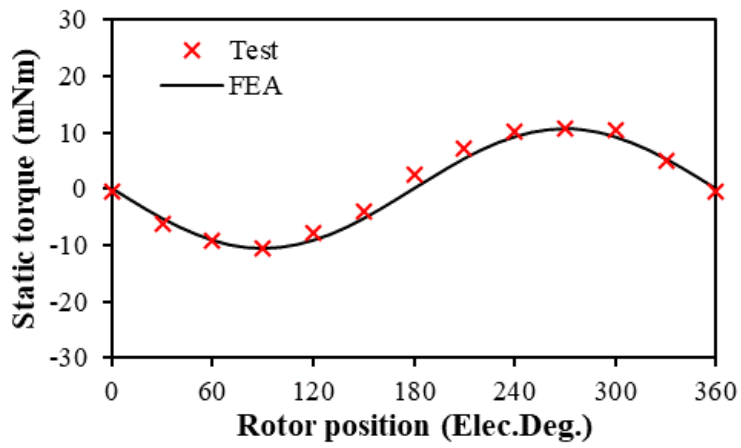


Fig. 4.76. Test rig for static torque measurement.

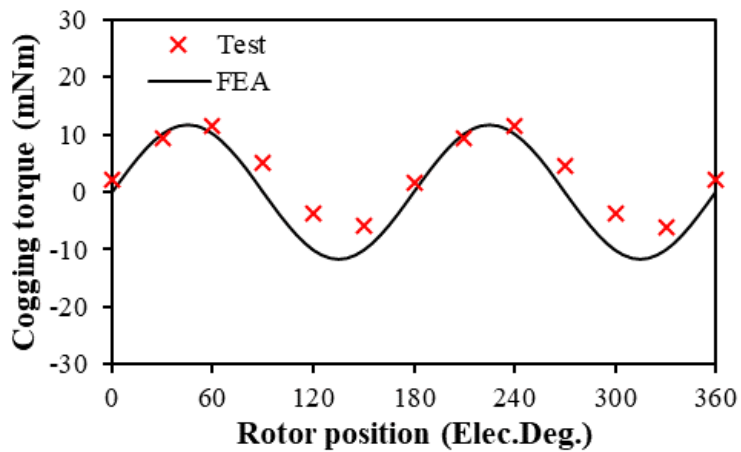


(a) Cogging torque

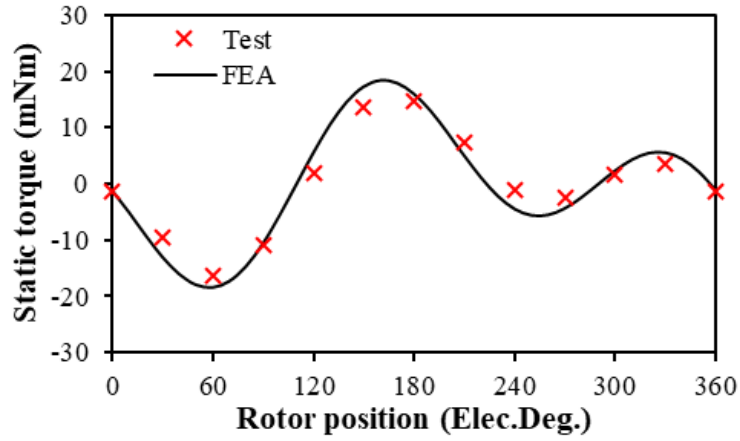


(b) Static torque

Fig. 4.77. FE predicted and measured cogging torques and static torques, No stator gap, no misalignment.

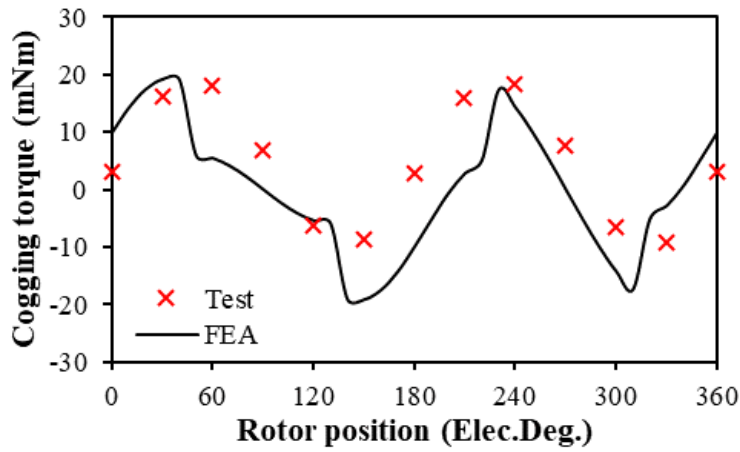


(a) Cogging torque

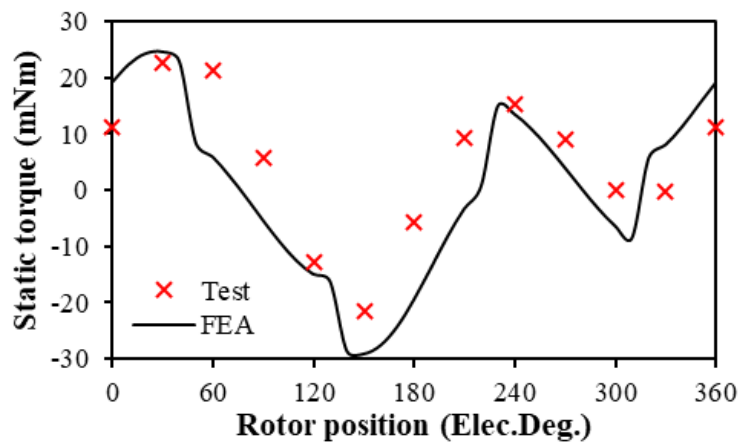


(b) Static torque

Fig. 4.78. FE predicted and measured cogging torques and static torques, 1 mm stator gap and no misalignment.



(a) Cogging torque



(b) Static torque

Fig. 4.79. FE predicted and measured cogging torques and static torques, 1 mm stator gap and 1 mm misalignment.

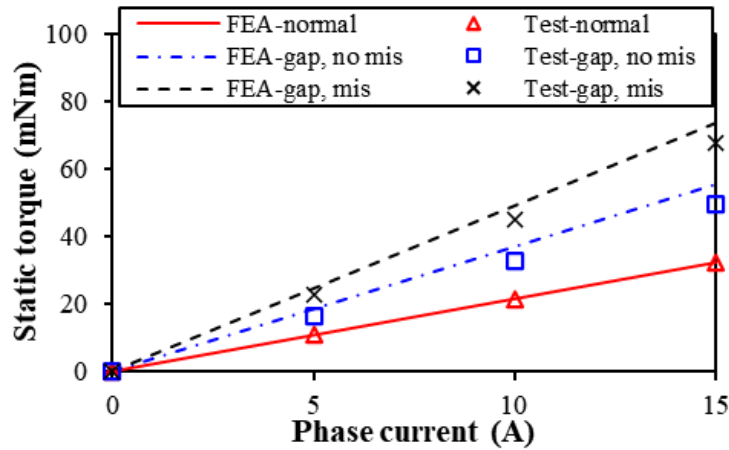


Fig. 4.80. Variation of FE predicted and measured peak static torques with phase current, without and with 1 mm stator gap (gap) and 1 mm misalignment (mis).

4.9. Conclusion

The influence of stator gap and misalignment due to manufacturing tolerances on the electromagnetic performance of 6s/2p HSPM motor with toroidal winding and diametrically magnetized PM rotor has been analyzed and experimentally validated.

It can be seen that the stator gap mainly affects the equivalent air-gap length and magnetic reluctance, which decreases the fundamental magnitude of air-gap flux density, flux linkage, back-EMF and average on-load torque. Meanwhile, the stator gap changes the equivalent combination of slot and pole number, which increases the harmonic contents of air-gap flux density and peak cogging torque significantly. Due to the uneven equivalent air-gap distribution, stator gap leads to unbalanced three phase back-EMFs (both amplitudes and phase angles) and self- and mutual-inductances. In addition, the stator gap increases the total motor loss due to the increase of rotor PM loss. The results also show that the influence on total loss is small when the stator gap less than 1mm. The tooth tip mainly affects the self-inductance of the motor with 1mm stator gap.

The influence of another manufacturing tolerance, i.e. misalignment of two split parts, on the electromagnetic performance of 6s/2p HSPM motor with toroidal winding and diametrically magnetized PM rotor has also been analyzed. It shows that the misalign of two stator parts mainly affects the uneven equivalent air-gap and symmetry of winding configuration, which leads to unbalanced three phase back-EMFs, especially phase angles, and self- and mutual-inductances. In addition, the misalignment increases the total motor loss due to the increase of rotor PM loss and has negligible influence on stator iron loss.

CHAPTER 5

COMPARISON OF 2-POLE HIGH-SPEED PERMANENT MAGNET MOTOR WITH DIFFERENT STATOR STRUCTURES AND WINDING CONFIGURATIONS

This chapter compares the electromagnetic performance of 2-pole slotted and slotless high-speed permanent magnet (HSPM) motors with toroidal and tooth-coil windings, together with the influence of the tooth-tip. All HSPM motors are optimized for maximum torque by the global algorithm employing finite element method (FEM). It found that the slotless motor with 6 coils toroidal windings has advantages of low stator iron loss and rotor eddy current loss due to no slotting effect, but has significantly high AC copper loss. Although slotted and slotless HSPM motors with toroidal windings have the same winding factor, the slotted motor with 6 slots has higher torque, higher PM utilization, lower AC copper loss, and larger winding inductance. The comparison between slotted HSPM motor with toroidal and tooth-coil windings indicates the toroidal windings has the advantage of relatively large torque due to small stator iron loss under the thermal limitation.

5.1 Introduction

High-speed permanent magnet (HSPM) motors have been developed for decades to meet requirements from various applications, for example, hand tools, compressors, vacuum cleaners, automotive superchargers, and micro gas turbines due to their advantages of high efficiency and high power density [HES87] [ZHU97] [ZWY05] [NOG05] [GER14] [HON18] [SHE18] [HET22]. In general, small size low power HSPM motor requires short end-winding to improve the rotor mechanical strength [UZH16], therefore the non-overlapping configurations are widely employed, such as tooth-coil [SHI04] [BIA05] [HON13] and toroidal windings [ZWY05] [ISM18] [BOR14].

Toroidal windings, which are also named gramme-ring windings [EVA83] [SPO91], as a kind of non-overlapping windings have advantages of high rotor mechanical stiffness due to short axial end-winding length [BOR14] [GIL16], and good cooling capability due to outside cooling

ducts under forced-air cooling. Therefore, toroidal windings are widely employed in slotted and slotless HSPM motors.

Generally, for slotted motors, toroidal windings are mainly used in multiple-slot high-power large-size HSPM motors, such as a 24s/2p motor with 75kW at 60krpm [WAN09] [XIN10], a 24s/2p motor with 15kW at 30krpm [CHE11], a 24s/2p motor with 75 kW at 36krpm [DON14], a 36s/2p motor with 117kW at 60krpm [LIW13]. [XIN10] compares the rotor loss of slotless, 6-, 12-, 18-, and 24s/2p HSPM motors. It shows that the 24-slot motor has the lowest rotor loss compared to the other slotted motors. For minimal-slot low-power small-size motors, toroidal windings are rarely researched in literature. In [XUF21a], the influence of slot number on electromagnetic performance is investigated for 2-pole HSPM motors with toroidal windings. The results show the 6s/2p is attractive for high-speed operation due to no unbalanced magnetic force and relatively high torque.

Slotless stator structure is very popular in low-power small-size HSPM motors because of its elimination of slotting effect and negligible cogging torque [CHE97]. In addition, without the slotting effect, the eddy current loss in rotor and stator iron would be reduced [ATA98] [CHE09]. For slotless HSPM motors, toroidal winding has been widely employed and investigated [EVA83] [SPO91] [ZWY05] [KOL13] [BOR14] [JUM14] [GIL16] [GIL17] [LEE17] [ISM18] [SNE18]. A 100W, 500 krpm slotless HSPM generator with toroidal windings is designed for mesoscale gas turbines in [ZWY05]. [KOL13] employs amorphous soft magnetic stator material for a 1kW 70 krpm slotless HSPM motor with toroidal windings. [BOR14] designs three slotless HSPM motors with toroidal windings: 1) A 150 W, 200 krpm micro-milling spindle motor; 2) A air compressor with 4.5 mNm torque and 30-50 krpm speed range; 3) A 3.7 kW, 240 krpm gas turbine generator. [JUM14] analyses rotor eddy current loss of 50 W, 100 krpm slotless motors with toroidal, concentrated, and helical windings. The results show that under the same torque, the slotless motor with concentrated windings (3 coils) has the highest rotor eddy current loss, and the motors with toroidal and helical windings have almost the same low rotor eddy current loss. [ISM18] designed a 123 W, 1.2 million rpm slotless motor with toroidal windings and Litz wires. It shows that under ultra-high-speed operation, the aerodynamic losses are dominated, which takes a large proportion in total motor losses, almost 84%. [GIL16] analyses three PM machine topologies for a 15 kW, 150 krpm electrically assisted turbocharger (EAT), including a slotless structure with toroidal windings, a 6-slot straight teeth structure with concentrated windings, and a 6 semi-closed slots structure with concentrated windings. The comparison shows the slotless motor with toroidal windings

has the highest efficiency but the lowest torque density. The slotted motor with concentrated windings has the best trade-off between efficiency and torque density, especially for the 6 semi-closed slots structure. In [GIL17], a 6s/4p slotted motor with concentrated windings and a 2-pole slotless motor with toroidal windings are compared in terms of noise and loss reduction. The results show that the slotless motor with toroidal windings has a lower noise level at the rated speed and lower on-load motor losses. It is worth noting that all the slotted motors in comparison use concentrated windings and the comparison between slotted and slotless HSPM motors with toroidal windings has not been mentioned, which will be investigated in this chapter.

Tooth-coil windings are used widely in slotted HSPM motors [NOG05] [MAJ19b] [HON13], especially for 3s/2p and 6s/2p HSPM motors. Although 3s/2p PM motors with tooth-coil windings have relatively large winding factor (0.866) and high torque, the inherent unbalanced magnetic force (UMF) and high rotor eddy current loss are undesirable for high-speed applications. 6s/2p HSPM motors with tooth-coil windings have no UMF and low rotor loss, which also have the same winding factor as motors with toroidal windings. However, the comparison between those two different winding configurations in 6s/2p HSPM motors has not been investigated before, which will be researched in this chapter.

This chapter is organized as follows. In section 5.2, firstly, the motor topologies of 2-pole slotted and slotless HSPM motors with toroidal windings are described. Secondly, two HSPM motors are optimized for maximum torque by the finite element method (FEM). Thirdly, the electromagnetic performances of the optimized slotted and slotless HSPM motors with toroidal windings are compared. In section 5.3, the comparison of the electromagnetic performances between 6s/2p HSPM motors with toroidal and tooth-coil are described. Section 5.4 is the conclusion.

5.2 Comparison of Slotted and Slotless Motors with Toroidal Windings

5.2.1 Toroidal winding motor topologies

Fig. 5.1 shows the cross-sections of 2-pole HSPM toroidally-wound motors with 6-slot slotted and 6-coil slotless structures. For toroidal windings, coils are wound around the stator yoke and two opposite coils belong to the same phase. For the slotted motor, six coils are separated by stator teeth, which have no tooth-tip to ease manufacturing processes, Fig. 5.1(a). According

to [XUF21b], the influence of tooth-tip was found to be negligible, except for rotor loss and winding inductances, and thus the slotted motor with tooth-tip will be researched for these two items. In general, the width of outer tooth in the slotted motor for mechanical support may be different from the inner tooth width. However, they have been assumed to be the same for simplicity in this chapter. For the slotless motor without stator teeth, six coils span over the 60 elec. Deg., Fig. 5.1 (b), and the similar outer teeth for mechanical support are neglected in this investigation [ZWY05] [JUM15] [GIL16] [GIL17]. The rotor consists of a diametrically magnetized magnet ring, a magnetic shaft, and a stainless steel sleeve. The magnetic shaft can improve the output torque and the sleeve can protect the PM from centrifugal force. The main parameters of 2-pole slotted and slotless HSPM motors with toroidal windings are given in Table 5.1.

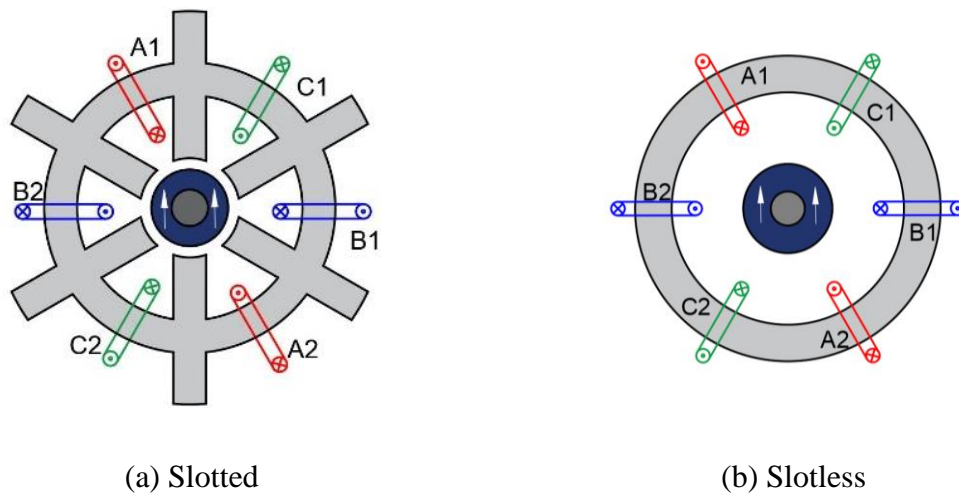


Fig. 5.1. Cross-sections of two 2-pole HSPM toroidal motors.

Table 5.1
Main Parameters of 2-Pole HSPM Motors

Rated speed (krpm)	110	Sleeve thickness (mm)	0.3
Stator outer diameter (mm)	54	Shaft diameter (mm)	5
Stator active length (mm)	9.1	Remanence (T)	1.3
Air-gap length (mm)	1.55	Number of turns per phase	37

5.2.2 Optimal designs

In this section, 2-pole slotted and slotless HSPM motors with toroidal windings are optimized for maximum electromagnetic torque (T_{em}) by FEM. Meanwhile, the maximum stator loss (stator iron loss and copper loss) [BIA04] and the maximum current density [REI13] [HET21]

must be limited in order to avoid global and local overheating, respectively, which would lead to the destruction of the winding insulation and short circuit.

According to [BIA04], the maximum allowed stator loss depends on stator thermal limit (P_{limit}), which can be derived as

$$P_{limit} = h w_m \pi D_s l_a \quad (5.1)$$

where l_a is the stator active length, h represents the overall heat transfer coefficient, which is $100 \text{ W}/(^{\circ}\text{Cm}^2)$ for the slotted motor and $50 \text{ W}/(^{\circ}\text{Cm}^2)$ for the slotless motor [BIA04] with forced-air cooling. The maximum allowed temperature (v_m) is 120°C since the insulation class is 'E'. In general, the maximum allowed current density of high-speed motors is higher than that of conventional low- and medium-speed motors, and it is $12 \text{ A}/\text{mm}^2$ for both slotted and slotless HSPM motors in this chapter.

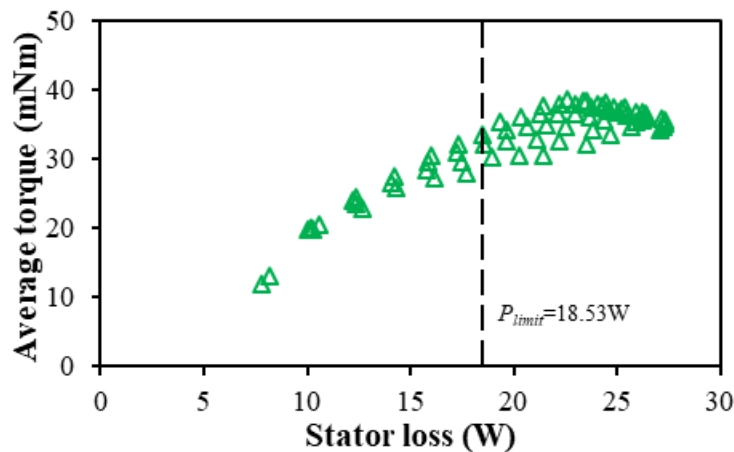
In this optimization, the shaft diameter is fixed by the manufacturing requirement, which depends on the standard bearing size. In addition, the stator outer diameter, air-gap length, and sleeve thickness are fixed. According to [PAN06a], 6s/2p PM motors have the same stator tooth width (w_t) and stator yoke height (h_y), Fig. 2. In addition, for the slotted motor, the inner and outer stator tooth widths are the same. It is worth noting that the inner winding areas are equal to the outer winding areas for maximum torque and thus the inner winding height can be calculated by geometric relationship. Therefore, only two variables are considered, i.e. outer winding height (h_o) and stator yoke height (h_y). With different combinations of outer winding height and stator yoke height, the stator loss and electromagnetic torque are computed by fixing current density. Then, the design with maximum torque is selected when its stator loss is under the maximum allowed stator loss.



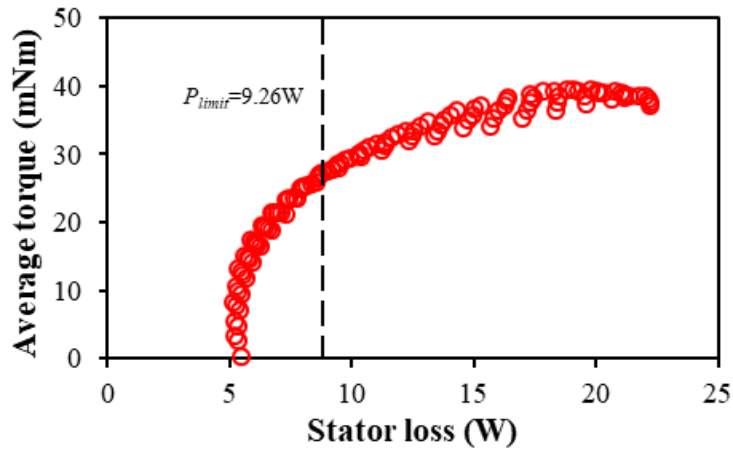
Fig. 5.2. Models of two 2-pole HSPM toroidal motors. (a) Slotted. (b) Slotless.

Fig. 5.3 indicates the variation of average torque with stator loss. It can be seen that the average torques of 2-pole slotted and slotless HSPM motors increase with the increase of stator loss. Therefore, considering thermal limit, the maximum torque can be achieved at the maximum

stator loss and the slotted motor has higher average torque than the slotless motor. The variation of PM utilization, i.e. the average torque per PM volume, with the stator loss is shown in Fig. 5.4. The PM utilization decreases with the increase of stator loss, which has the opposite trend to the average torque. The variations of maximum average torque with stator loss in slotted and slotless motors for different stator losses are shown in Fig. 5.5. It shows that without thermal limit, the slotless motor has higher torque than the slotted motor for each stator loss since the winding area of the slotless motor is larger than that of the slotted motor. However, considering thermal limit, the corresponding slotted motor has 16% higher maximum torque than the allowed slotless motor, Fig. 5.5. The variations of the maximum PM utilization with stator loss in slotless and slotted motors for different stator losses are shown in Fig. 5.6. It can be seen that the PM utilization in the slotted motor is more sensitive to stator loss than that in the slotless motor, and the corresponding slotted motor has 65% higher maximum PM utilization than the allowed slotless motor. Therefore, considering thermal limit, the optimized slotted motor has advantages of high torque and high PM utilization compared to the optimized slotless motor. The results of two optimized slotted and slotless motors are shown in Table II.

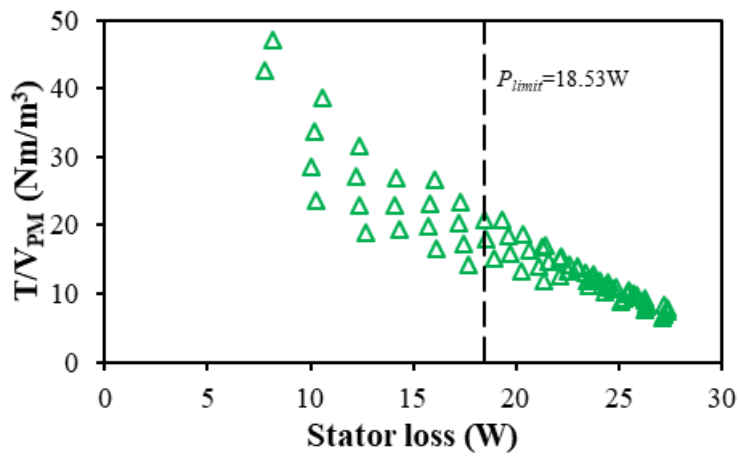


(a) Slotted

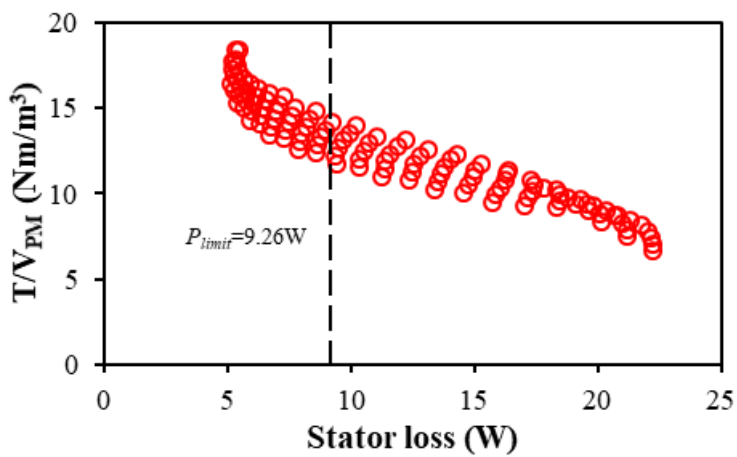


(b) Slotless

Fig. 5.3. Variation of average torque with stator loss.



(a) Slotted



(b) Slotless.

Fig. 5.4. Variation of average torque per PM volume with stator loss.

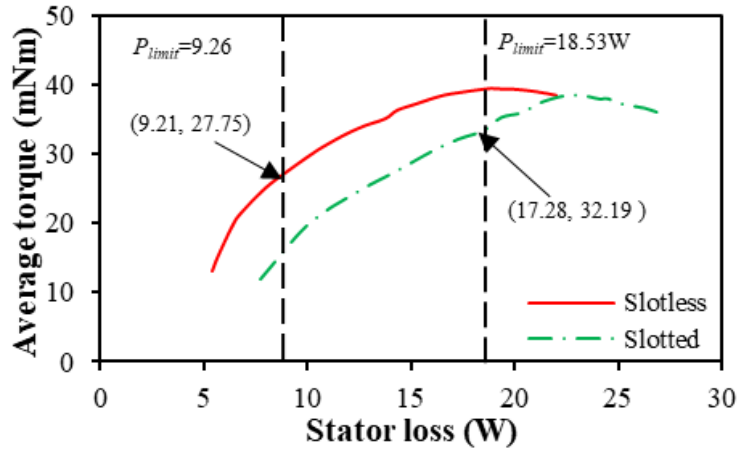


Fig. 5.5. Variation of maximum average torque with stator loss.

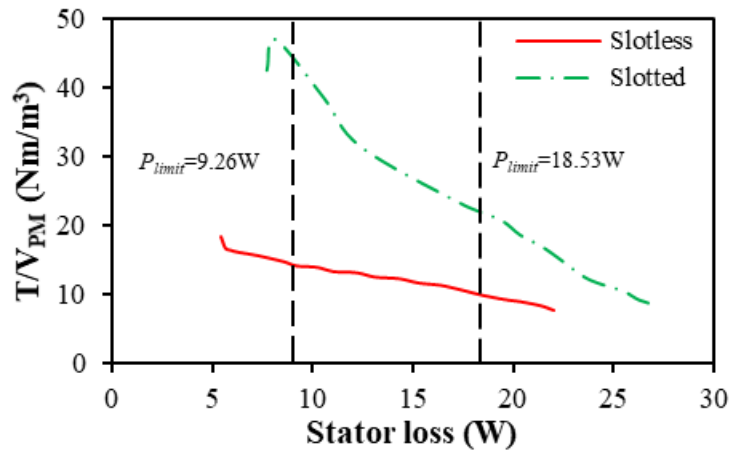


Fig. 5.6. Variation of maximum average torque per PM volume with stator loss.

Table 5.2
Optimized Design Parameters for Two 2-Pole HSPM Motors

	Slotted	Slotless
Rated speed (krpm)		110
Stator active length, l_a (mm)		9.1
Stator outer diameter, D_o (mm)		54
Stator inner diameter D_i , mm	8.9	10.2
Outer winding height h_o , mm	4.4	4.6
Stator yoke height h_y , mm	4.2	4.2
PM thickness, mm	4.90	6.15
Limited stator loss, W	18.53	9.26
Stator iron loss, P_{fe} W	13.91	5.18
DC copper loss, P_{cu} , W	3.37	4.02
Rotor loss, W	15.59	1.73
Torque, mNm	32.19	27.75
Torque/PM volume, Nm/m ³	23.42	14.16

5.2.3 Electromagnetic performance

In this section, the comparison of electromagnetic performances between 2-pole slotted and slotless HSPM motors are investigated by FEM, including air-gap flux density, back electromotive force (back-EMF), cogging torque and electromagnetic torque, motor losses, winding inductances, and mechanical stress.

1) Open-circuit air-gap flux density

Fig. 5.7 shows the equal potential and air-gap flux density distributions of 2-pole slotted and slotless HSPM motors. It can be seen that the maximum stator iron flux densities of the slotted and slotless motors are 1.2T and 1.0T, respectively. Due to diametrically-magnetized, the air-gap flux density waveform of the slotless motor is sinusoidal and there are no harmonic components due to no slotting effect, Fig. 5.8(a). For the slotted motor without tooth-tip and large slot opening, the air-gap flux density waveform is almost sinusoidal and the 5th and 7th order harmonics exist due to slotting effect, Fig. 5.8(b). Although no harmonic components, the slotless motor has a smaller fundamental magnitude than the slotted motor due to larger leakage flux.

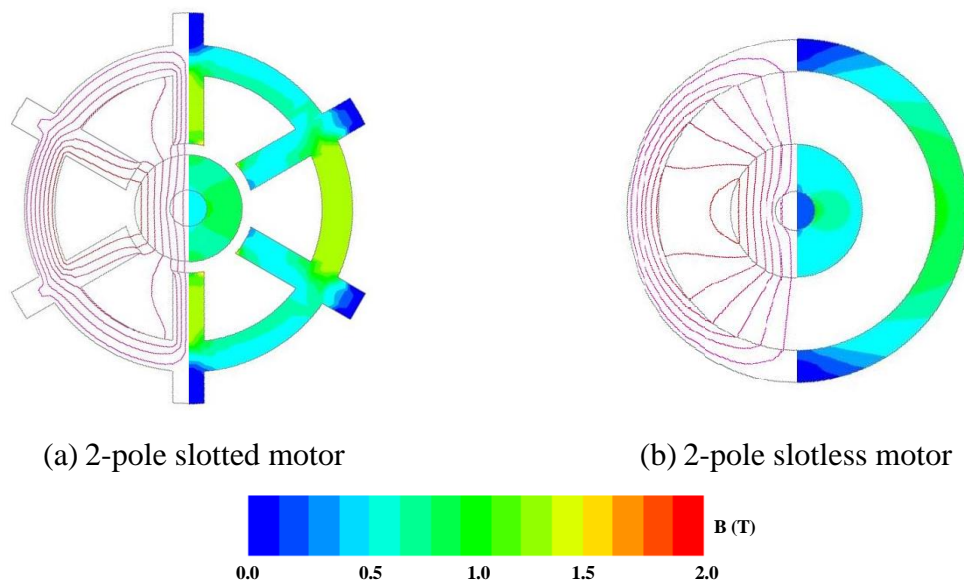
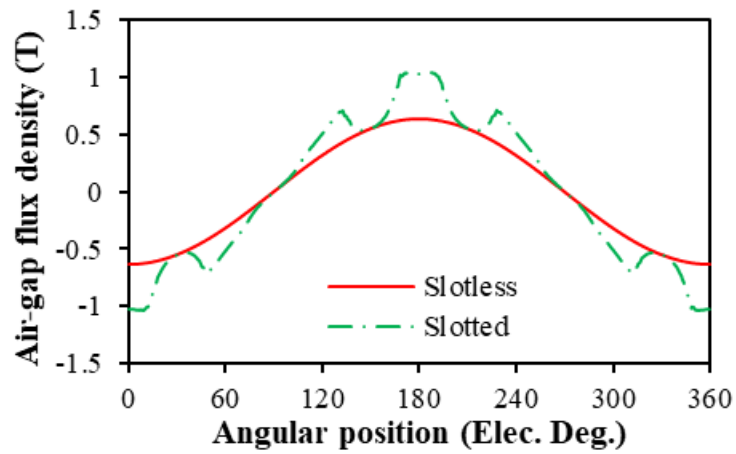
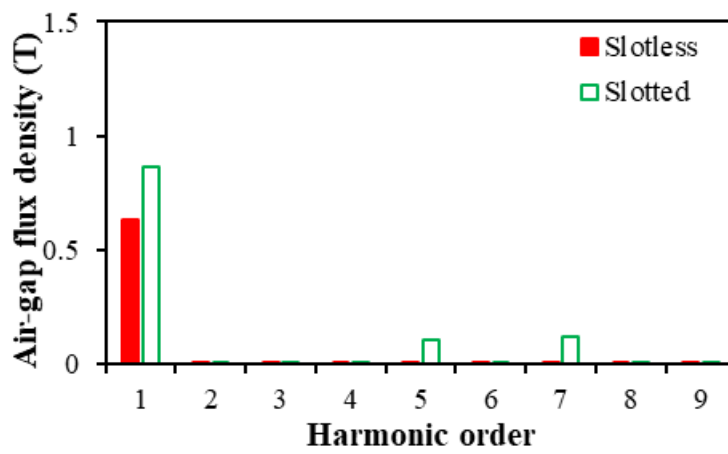


Fig. 5.7. Open-circuit equal potential and air-gap flux density distributions of two HSPM motors.



(a) Waveforms

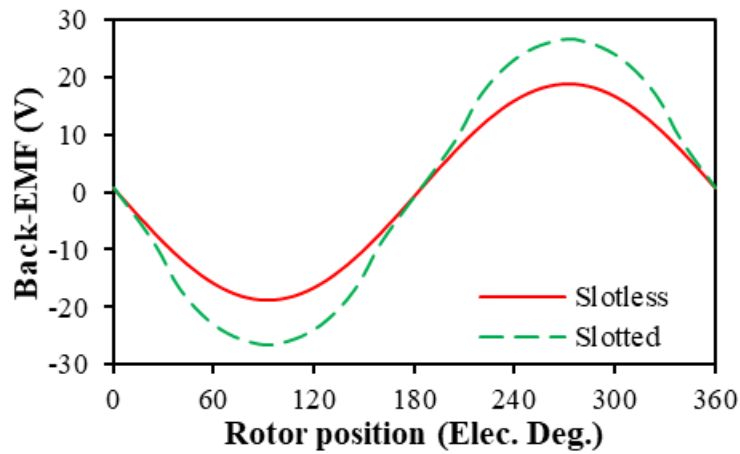


(b) Harmonics

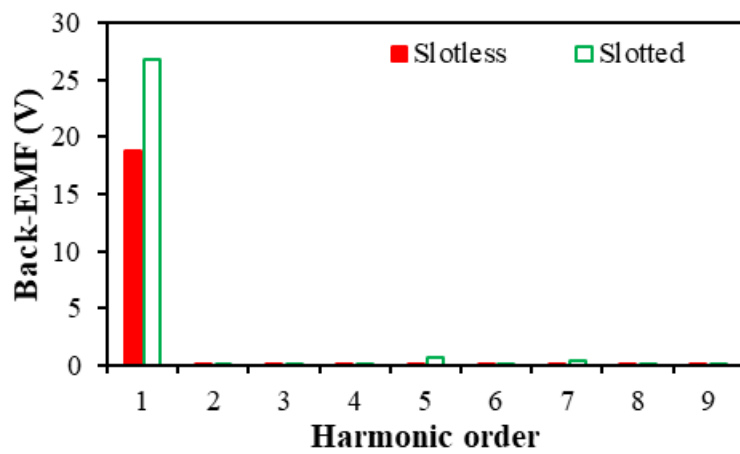
Fig. 5.8. Open-circuit air-gap flux densities of 2-pole slotted and slotless motors.

2) Back-EMF

The back-EMFs of 2-pole slotted and slotless HSPM motors are compared in Fig. 5.9. The back-EMF waveforms of phase A of two motors are sinusoidal and the slotted motor has a larger fundamental magnitude of back-EMF than the slotless motor, which is the same as the air-gap flux density.



(a) Waveforms



(b) Harmonics

Fig. 5.9. Comparison of back-EMFs of phase A between slotted and slotless motors.

3) Cogging torque and electromagnetic torque

Fig. 5.10 shows the cogging torque and electromagnetic torque waveforms for slotted and slotless motors under ideal brushless DC drive 120-degree square wave current for high-speed operation, Fig. 5.11. It can be seen that the cogging torque of the slotted motor is larger than the slotless motor due to the large slot opening [ZHU92]. Compared to the slotless motor, the slotted motor carrying smaller phase currents has a higher electromagnetic torque.

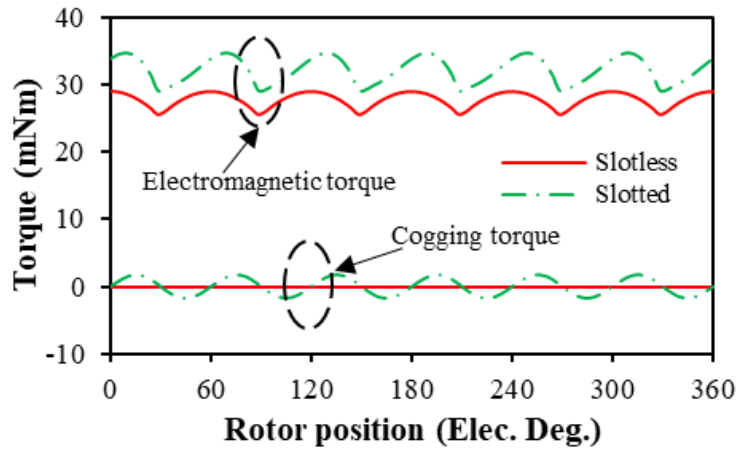


Fig. 5.10. Cogging torques and electromagnetic torques of 2-pole slotless and slotted motors.
($J_s=12A/mm^2$)

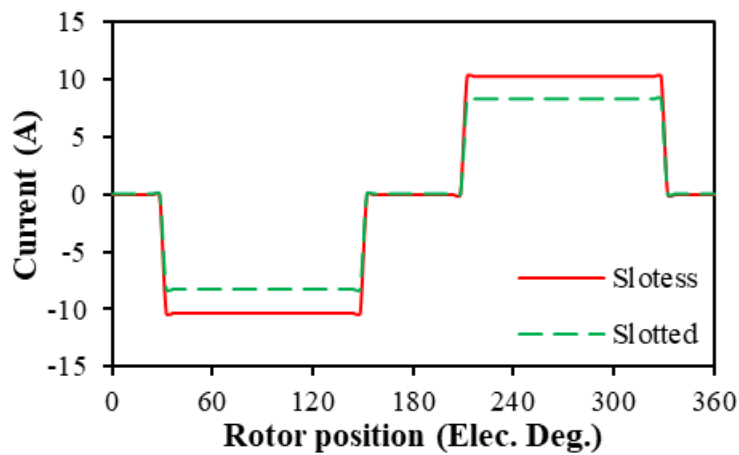


Fig. 5.11. Phase currents of 2-pole slotless and slotted motors under the same current density, phase A.

4) Loss analysis

A. Stator iron loss

The no-load and on-load stator iron losses of slotted and slotless motors are calculated by FEM, Fig. 5.12. It can be seen that the armature reaction has negligible influence on the stator iron loss, the no-load and on-load stator iron losses are nearly the same. However, the slotted motor has larger stator iron loss than the slotless motor due to higher maximum stator iron flux density and larger stator iron volume, Fig. 5.7. The on-load stator iron loss distributions of slotted and slotless motors are shown in Fig. 5.13.

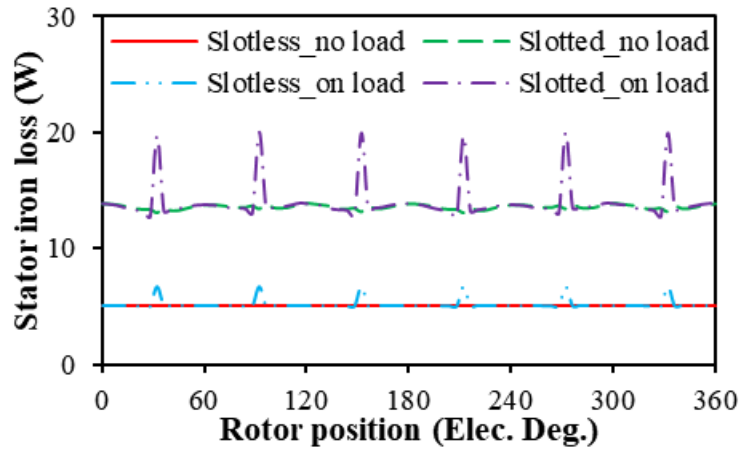


Fig. 5.12. Stator iron losses of slotted and slotless motors.

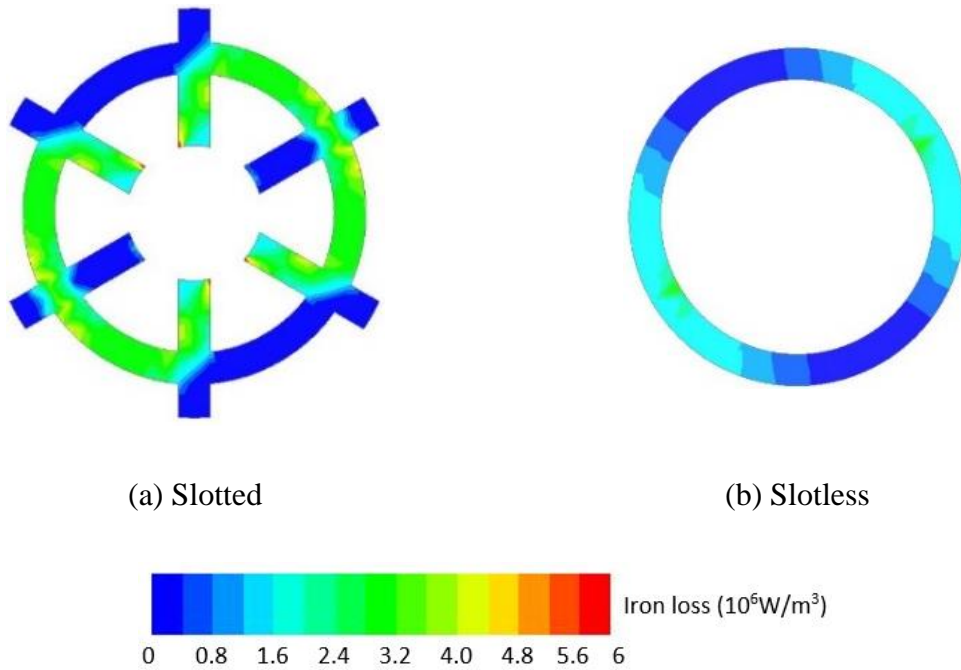


Fig. 5.13. On-load stator iron loss distributions of slotted and slotless motors.

B. Copper loss

Generally, the copper loss consists of two parts, i.e. DC and AC copper losses. In high-speed motors, the AC copper losses due to skin effect and proximity effect may increase significantly and should be considered [LIS16]. To avoid the skin effect, the diameter of conductors should be less than the skin depth (δ) [UZH14], which can be calculated by

$$\delta = \sqrt{\frac{\rho}{\pi f \mu_c}} \quad (5.2)$$

where ρ is the resistivity of the conductor, f is the fundamental frequency, and μ is the permeability of the conductor. In this chapter, the skin depth is 1.6mm, and thus the skin effect can be neglected when the diameters of conductors in slotted and slotless motors are 0.48mm and 0.52mm, respectively.

Fig. 5.14 and Table 5.3 show the no-load and on-load Joule losses of two motors neglecting short end-winding. It can be seen that the slotted motor has relatively small AC loss but the slotless motor has significantly large AC loss, even under the no-load condition. For the slotted motor, the rotating magnetic field only affects the conductors near the slot opening but has negligible influence on the conductors at the bottom of the slot, Fig. 5.15(a). Therefore, the AC loss of the slotted motor mainly results from the proximity effect. For the slotless motor, the rotating magnetic field affects almost all the inner conductors, and the maximum flux density in conductors of the slotless motor is twice that of the slotted motor, Fig. 5.15(b). Therefore, the AC loss of the slotless motor mainly results from the field caused by the permanent magnet, and the proximity effect can be neglected since the inner conductors are all in the air-gap [ZWY05]. In general, for high-speed motors, the Litz wires are essential in order to avoid large AC copper loss [GIL17].

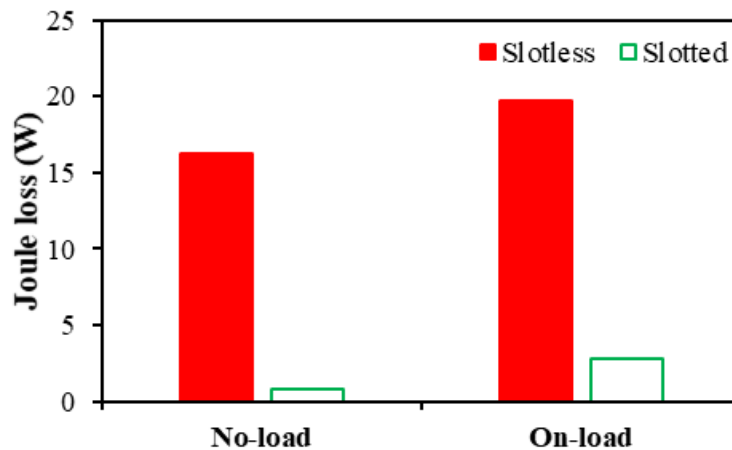


Fig. 5.14. Comparison of Joule losses of slotted and slotless motors under no-load and on-load conditions.

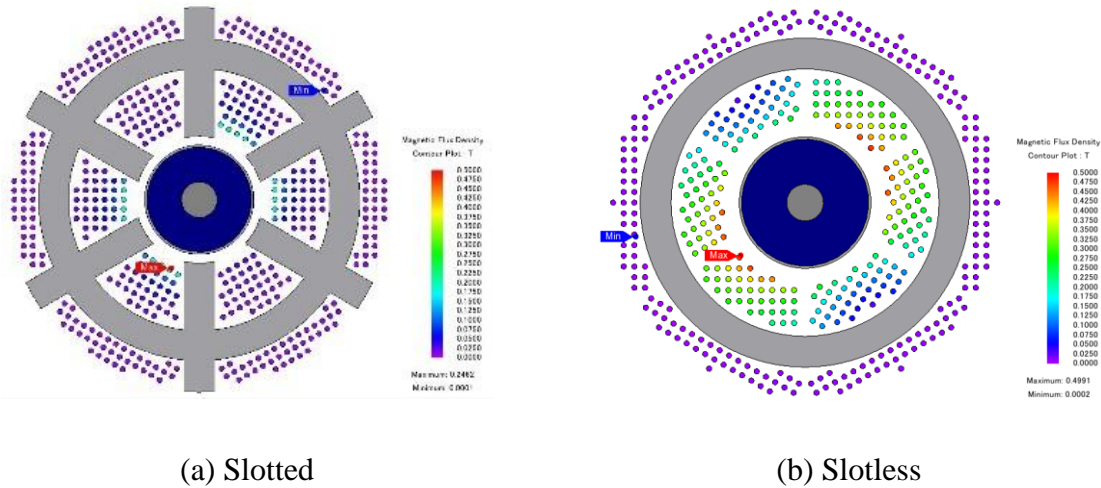


Fig. 5.15. On-load flux density distributions of conductors in two motors.

Table 5.3
Joule Losses without End-winding (W)

	Slotless		Slotted	
	No-load	On-load	No-load	On-load
Joule losses	16.22	19.72	0.80	2.82
DC loss	-	1.43	-	1.15
AC loss	16.22	18.29	0.80	1.67
AC/Joule, %	-	92.7	-	59.2

C. Rotor loss

A stainless-steel sleeve is employed to retain the PMs from centrifugal force, and thus the rotor loss includes eddy current losses in sleeve, PMs, and shaft. Those eddy current loss not only affects the motor efficiency but also may result in irreversible demagnetization of PMs due to overheating [EDE01]. In general, the rotor eddy current loss is caused by the spatial harmonics as well as the time harmonics. Therefore, the slotted motor without tooth-tip (5mm slot-opening) has higher rotor loss than the slotless motor mainly due to the slotting effect, Fig. 5.16. However, the slotted motor with tooth-tip (1.5mm slot-opening), Fig. 5.17, has almost the same rotor loss as the slotless motor. Fig. 5.18 shows the rotor loss distributions of slotted and slotless motors.

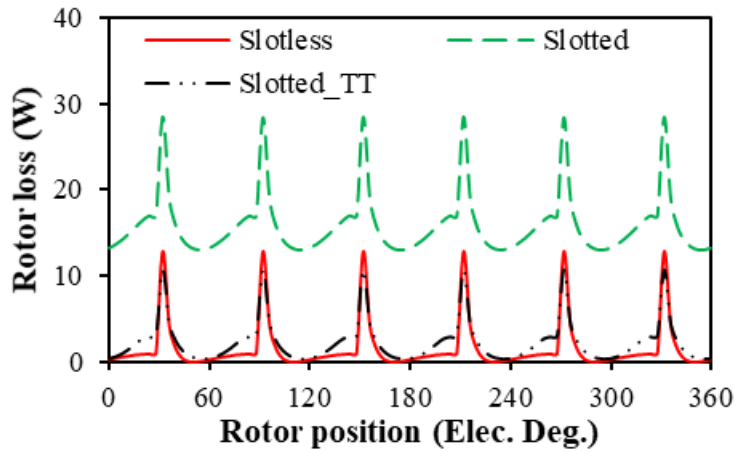


Fig. 5.16. Comparison of rotor losses between slotted and slotless motors.

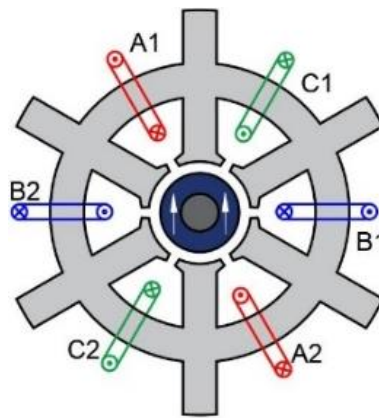


Fig. 5.17. 2-pole slotted motor with tooth-tip.

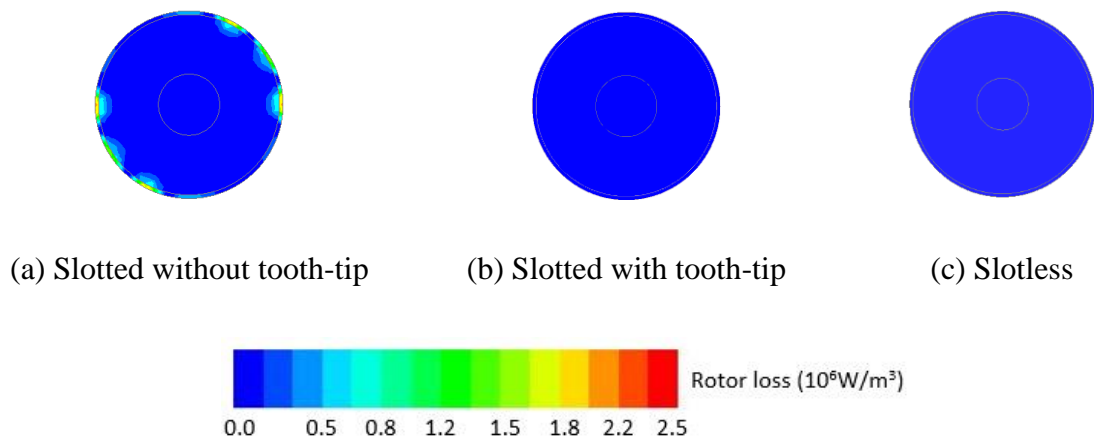


Fig. 5.18. On-load rotor loss distribution of slotted and slotless motors.

D. Frame loss

The losses in the frame are taken into consideration since the toroidal windings have high external leakage caused by the outer windings, which will inevitably induce eddy currents in neighbouring conductive bodies [PAN06b] [BOR14]. The material of the frame is Aluminium

for its electrical conductivity and cooling activity. When the frame thickness is less than 1mm, the frame eddy current loss increases sharply, while after that the frame loss remains unchanged since the skin depth of the frame is 1.2 mm, Fig. 5.19. Figs. 5.20 and 5.21 show the eddy current density and eddy current loss distributions of the frames (1mm) in the slotted and slotless motors. In addition, the slotless motor has a larger frame loss than the slotted motor since the slotless motor has a larger rated phase current, Fig. 5.11. Overall, compared to other loss components, the frame loss is very small and can be neglected.

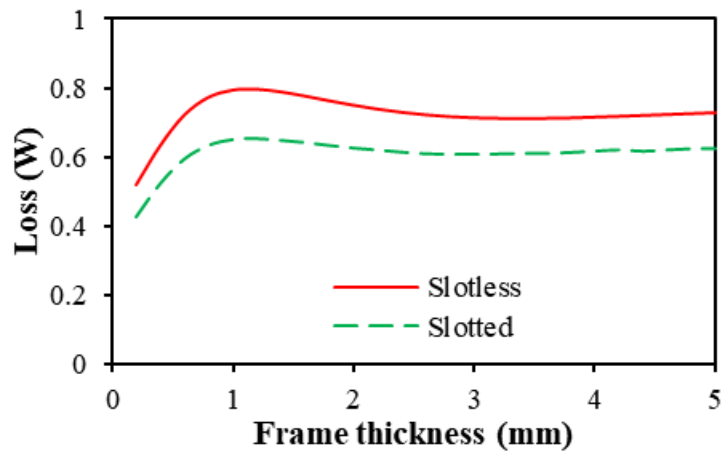


Fig. 5.19. Variation of frame losses with frame thickness of slotted and slotless motors.

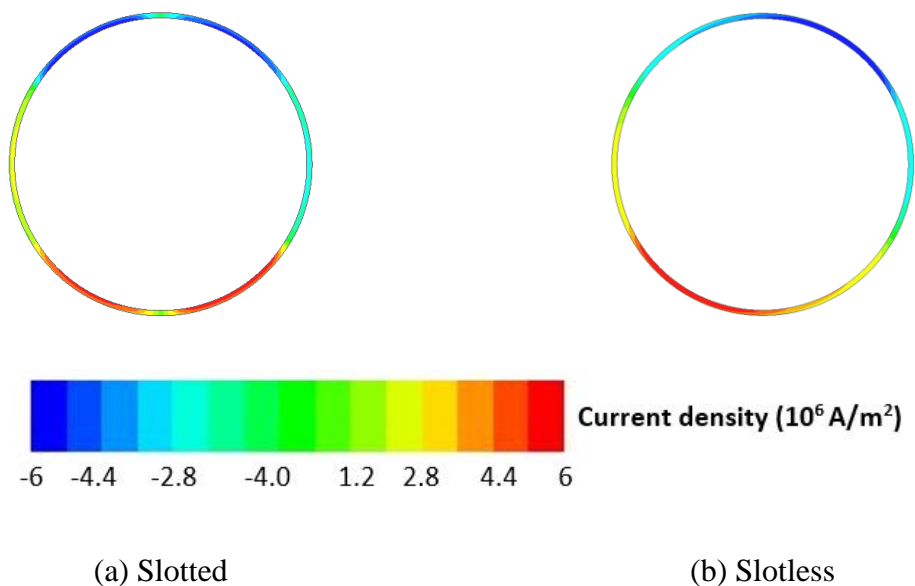


Fig. 5.20. Eddy current density distributions of the frames (1mm) in slotted and slotless motors.

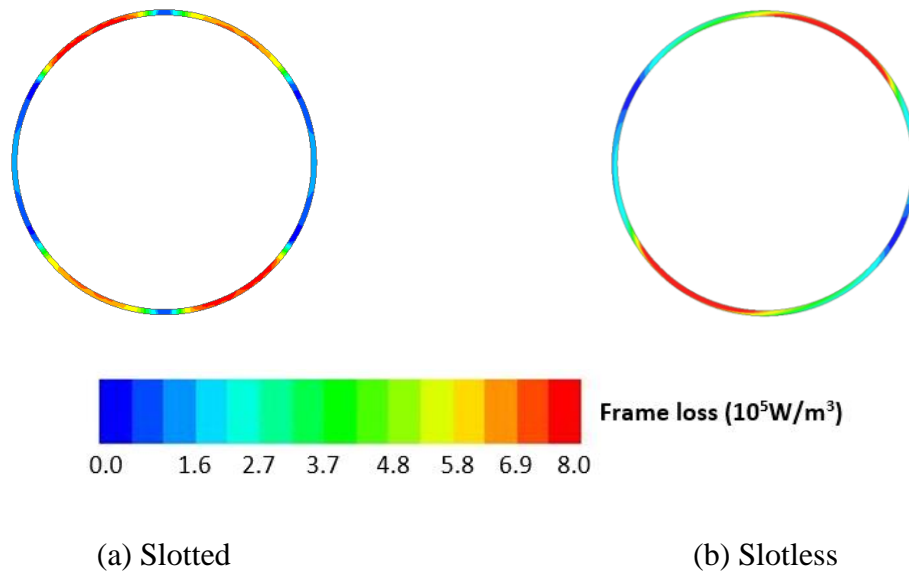


Fig. 5.21. Eddy current loss distributions of the frames (1mm) in slotted and slotless motors.

5). Winding inductances

In high-speed motors, winding inductances normally have a profound influence on sensorless control [ZHU01]. The winding inductances of slotted without tooth-tip, slotted with tooth-tip, and slotless motors are compared. The winding inductances are calculated by FEM when only phase A is excited ($I_a=1A, I_b=0A, I_c=0A$). Fig. 5.22 shows the flux distributions of three motors when only phase A is excited. It can be seen that the slotless motor has small leakage of armature field, and thus the phase inductance of the slotless motor is smaller than that of two slotted motor, Table 5.4. Since the tooth-tip can increase flux leakage significantly, Fig. 5.22 (b), and reduce the slot effect, the winding inductances of the slotted motor with tooth-tip are the largest. It is worth noting that the end-winding inductance is neglected in this chapter due to short end-winding. In any case, the end-winding inductances in both slotted and slotless machines are similar.

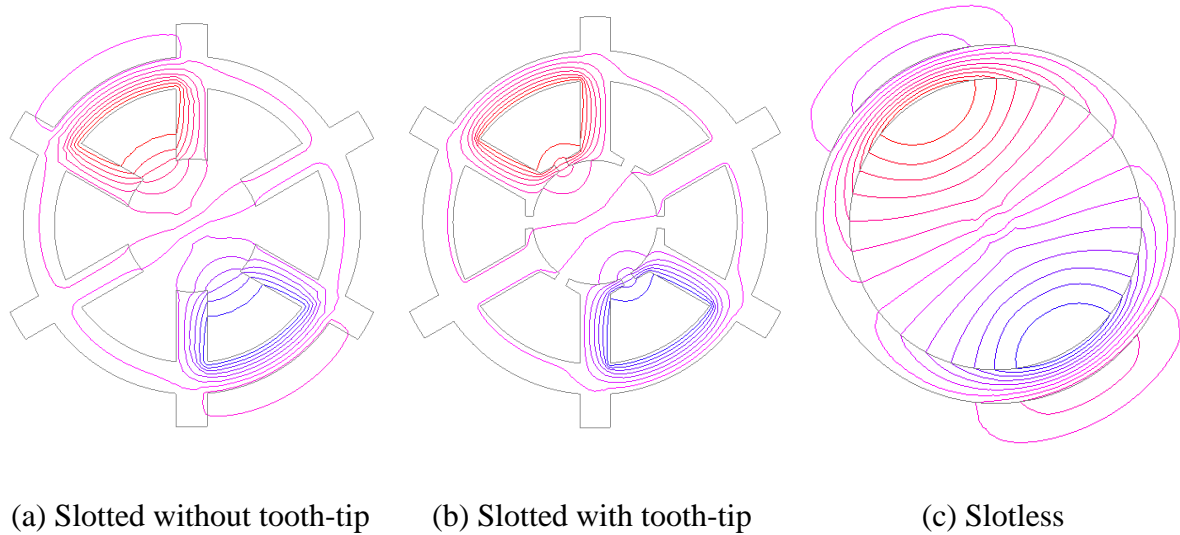


Fig. 5.22. Flux distributions of slotted and slotless motors when only phase A is excited ($I_A=1A, I_B=I_C=0A$).

Table 5.4
Winding Inductances for HSPM Motors (μH)

	Slotted	Slotted with tooth-tip	Slotless
Self-inductance	12.66	22.80	4.75
Mutual-inductance	-1.80	-1.97	-1.57
Phase inductance	14.46	24.77	6.32

5.3 Comparison of Slotted Motor with Toroidal and Tooth-coil Windings

5.3.1 Motor topologies

The cross-sections of 6s/2p HSPM motor with toroidal and tooth-coil windings are shown in Fig. 5.23. The coils are wound around the stator yoke and separated by stator teeth for the toroidal windings. As for tooth-coil windings, the coils are wound around the stator teeth. The stators of both motors employ the stator teeth with tooth-tips to reduce the slotting effect, and the slot opening of each motor is 1.5 mm. The main parameters of both slotted motors are the same as that in Table 5.1. The tooth-coil windings have the same winding factor as toroidal windings [XUF21a]. In order to have the better electromagnetic performance the inner and outer slot areas are set to be the same for the toroidal windings as shown in chapter 3.

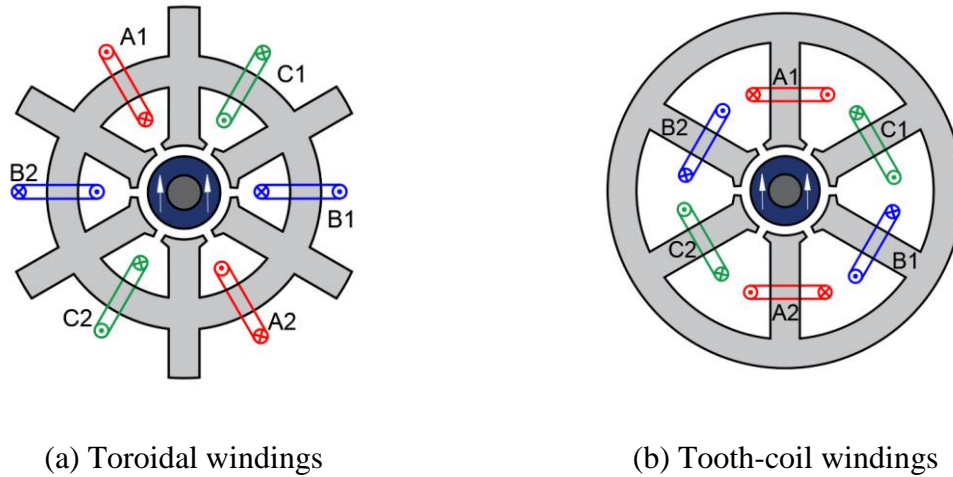


Fig. 5.23. Cross-sections of two 2-pole HSPM motor with different windings.

5.3.2 Optimal designs

In this section, 6s/2p HSPM motors with toroidal and tooth-coil winding are optimized for maximum electromagnetic torque (T_{em}) using the same method stated in 5.2.2. The shaft diameter, stator outer diameter, tooth-tip thickness, air-gap length, and sleeve thickness are fixed in this optimization. Since both motors have slotted stator structures, the overall heat transfer coefficient is $100 \text{ W}/(^{\circ}\text{Cm}^2)$. The maximum allowed current densities for both toroidal and tooth-coil motors are $12 \text{ A}/\text{mm}^2$ in this chapter.

For 6s/2p HSPM motor with tooth-coil windings, the stator tooth width (w_t) is the same as stator yoke height (h_y) [PAN06]. Therefore, only two variables are considered in the optimization: stator yoke height (h_t) and stator inner radius (R_i), Fig. 5.24(b). With different combinations of variables, outer winding height (h_o) and stator yoke height (h_t) for toroidal windings, and stator yoke height (h_t) and stator inner radius (R_i) for tooth-coil windings, the stator loss and electromagnetic torque are computed by fixing current density. Then, the design with maximum torque is selected when its stator loss is under the maximum allowed stator loss.

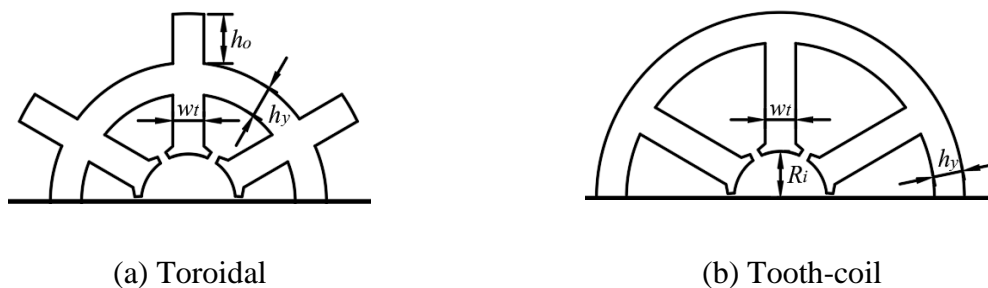
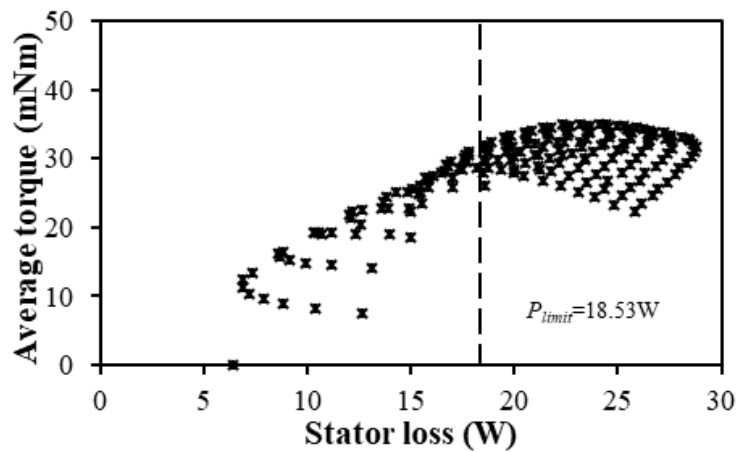
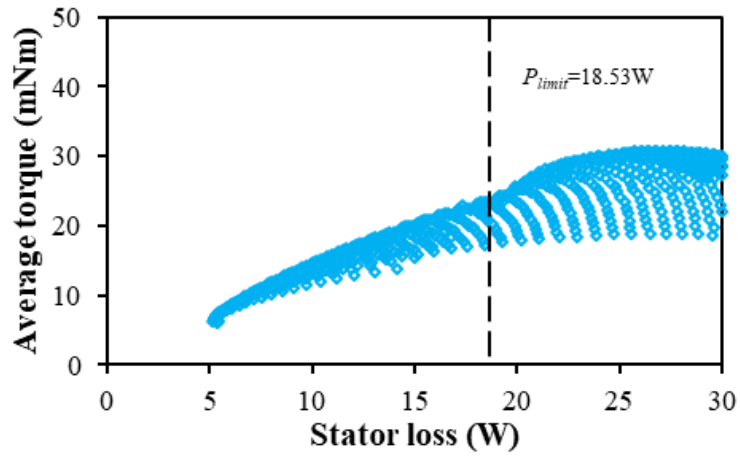


Fig. 5.24. Models of two 6s/2p HSPM motors with different windings.

Fig. 5.25 indicates the variation of average torque with stator loss. It can be seen that the average torques of 6s/2p HSPM motors with toroidal and tooth-coil windings increase with the increase of stator loss. Therefore, considering thermal limit, the maximum torque can be achieved at the maximum stator loss and the motor with toroidal windings has higher average torque than the motor with tooth-coil windings. The variation of PM utilization, i.e. the average torque per PM volume, with the stator loss is shown in Fig. 5.26. It is worth noting that the PM utilization of the motor with tooth-coil windings increases at first and then decreases with the increase of stator loss. The variations of maximum average torque with stator loss in toroidal and tooth-coil motors for different stator losses are shown in Fig. 5.27. It shows that the motor with toroidal windings has 26.1% higher torque than the motor with tooth-coil windings for different stator losses since the motor with tooth-coil windings has no outer slot area, and it has larger stator core than the motor with toroidal windings. The variations of the maximum PM utilization with stator loss in motors with toroidal and tooth-coil windings for different stator losses are shown in Fig. 5.28. When the thermal limitation is larger than almost 10W, the motor with tooth-coil windings higher maximum PM utilization than the motor with toroidal windings. It is worth noting that the maximum torque and maximum PM utilization cannot be achieved simultaneously. Therefore, considering thermal limit, the optimized motor with toroidal windings has advantages of high torque and large PM utilization compared to the optimized motor with tooth-coil windings. The results of two optimized motors are shown in Table 5.5.

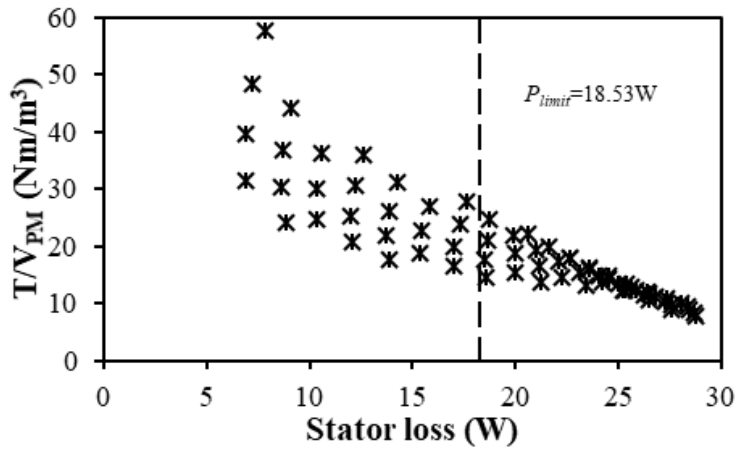


(a) Toroidal

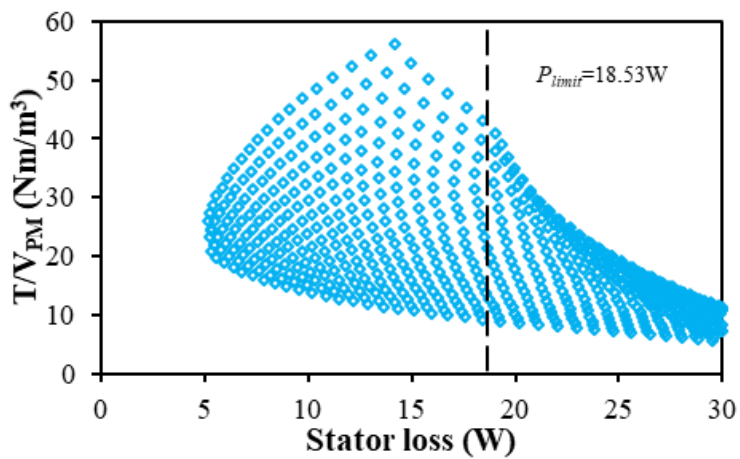


(b) Tooth-coil

Fig. 5.25. Variation of average torque with stator loss.



(a) Toroidal



(b) Tooth-coil

Fig. 5.26. Variation of average torque per PM volume with stator loss.

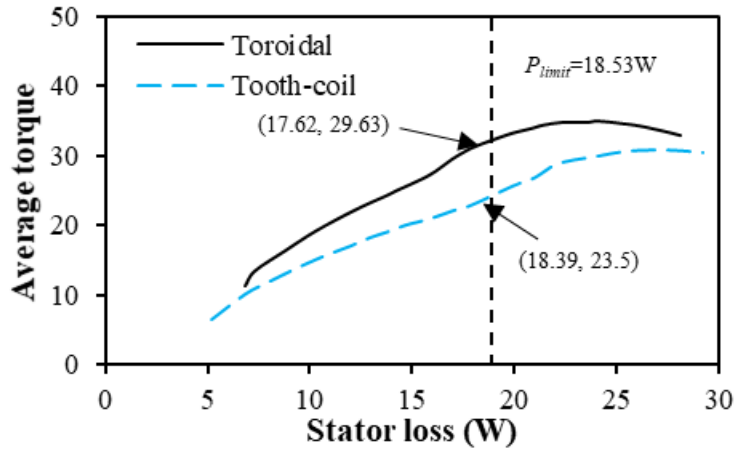


Fig. 5.27. Variation of maximum average torque with stator loss.

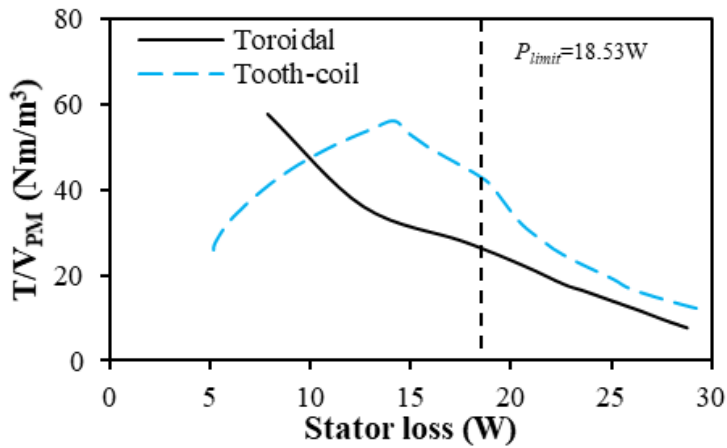


Fig. 5.28. Variation of maximum average torque per PM volume with stator loss.

Table 5.5
Optimized Design Parameters for Two 2-Pole HSPM Motors

	Toroidal	Tooth-coil
Rated speed (krpm)		110
Stator active length, l_a (mm)		9.1
Stator outer diameter, D_o (mm)		54
Stator inner diameter D_i , mm	16.4	15.6
Outer winding height h_o , mm	4.4	-
Stator yoke height h_y , mm	4.0	4.4
PM thickness, mm	4.08	3.75
Limited stator loss, W	18.53	18.53
Stator iron loss, P_{fe} W	14.32	15.64
DC copper loss, P_{cu} , W	3.31	2.74
Rotor loss, W	3.24	2.28
Torque, mNm	29.63	23.5
Torque/PM volume, Nm/m ³	27.92	25.05

5.3.3 Electromagnetic performances

In this section, the comparison of electromagnetic performances between HSPM motors with toroidal windings and tooth-coil windings are investigated by FEM, including air-gap flux density, back electromotive force (back-EMF), cogging torque and electromagnetic torque, motor losses and winding inductances.

1) Open-circuit Air-gap Flux Density

Fig. 5.29 shows the equal potential and air-gap flux density distributions of HSPM motors with toroidal and tooth-coil windings. It can be seen that the optimized motors with toroidal and tooth-coil windings have almost the same maximum stator iron flux density, 1.5T. The air-gap flux density waveforms of both motors are almost sinusoidal due to diametrically-magnetized Fig. 5.30(a). However, with the slotting effect, the 5th and 7th order harmonics existed, Fig. 5.30(b).

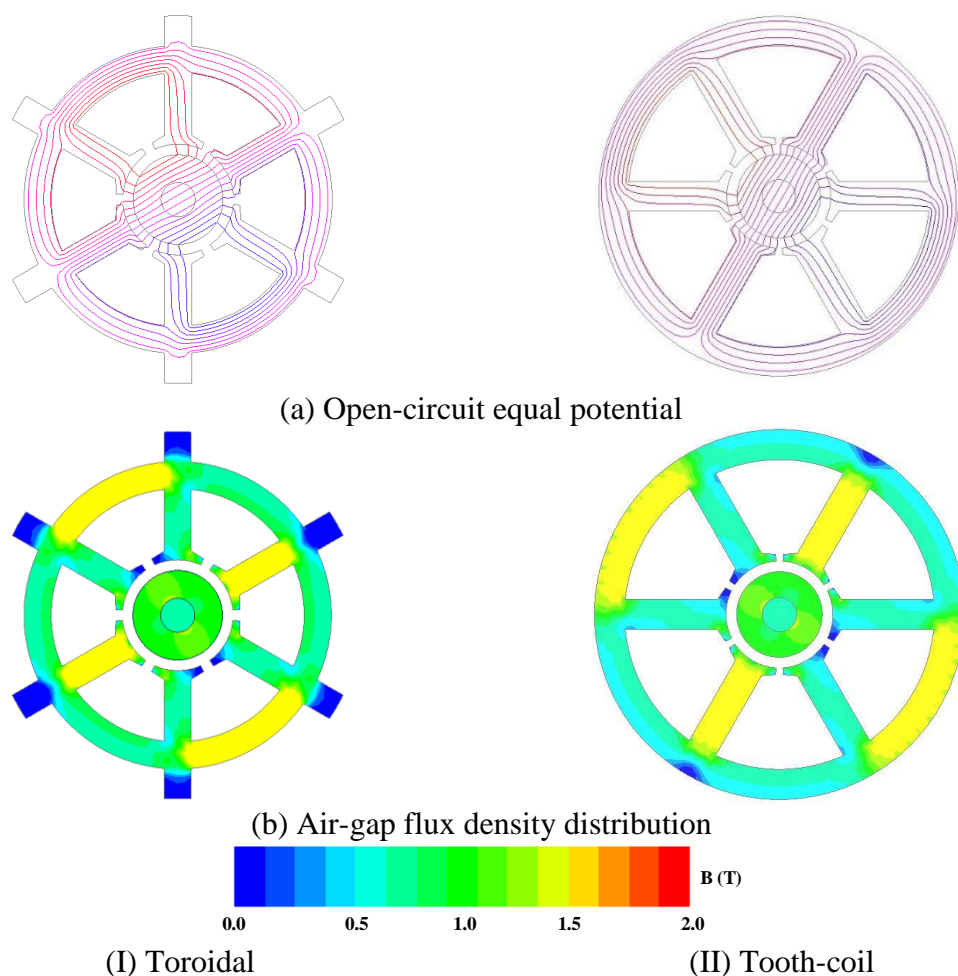
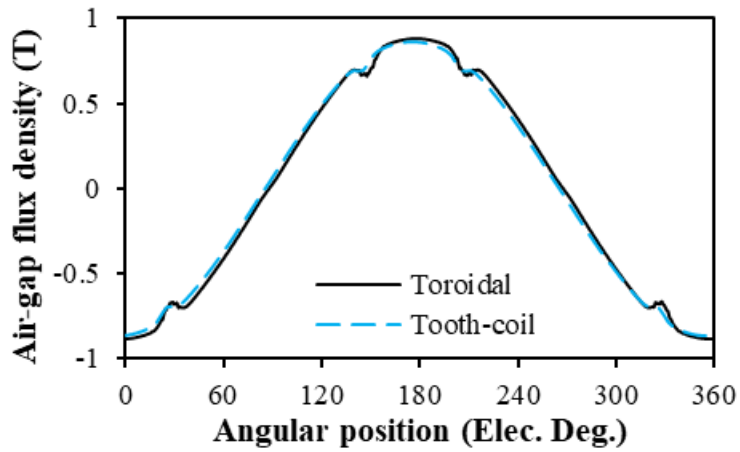
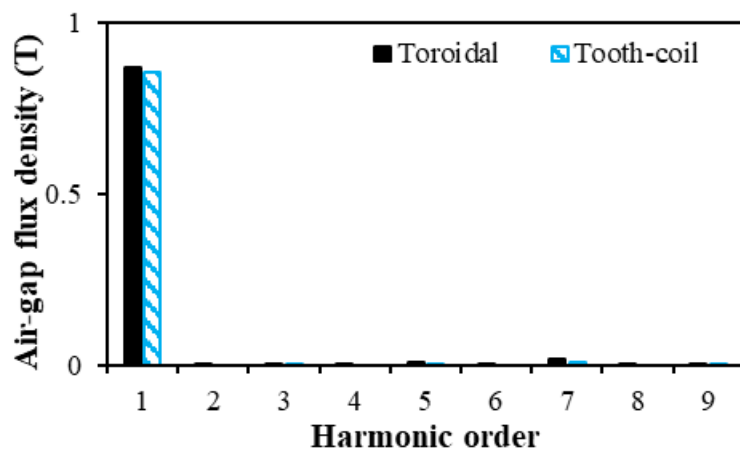


Fig. 5.29. Open-circuit equal potential and air-gap flux density distributions of two HSPM motors.



(a) Waveforms

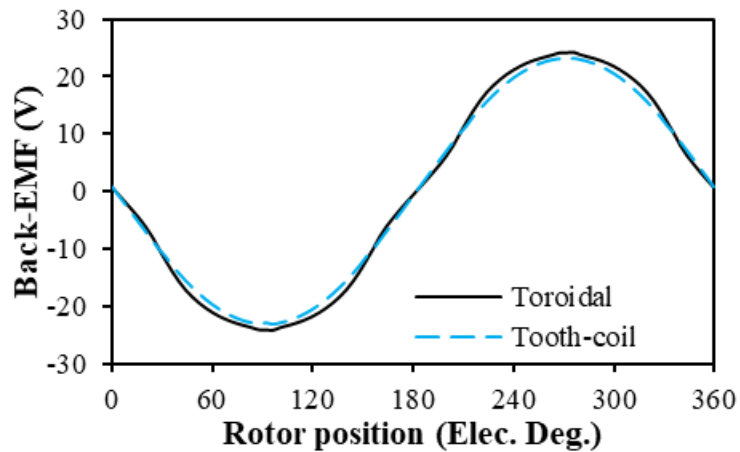


(b) Harmonics

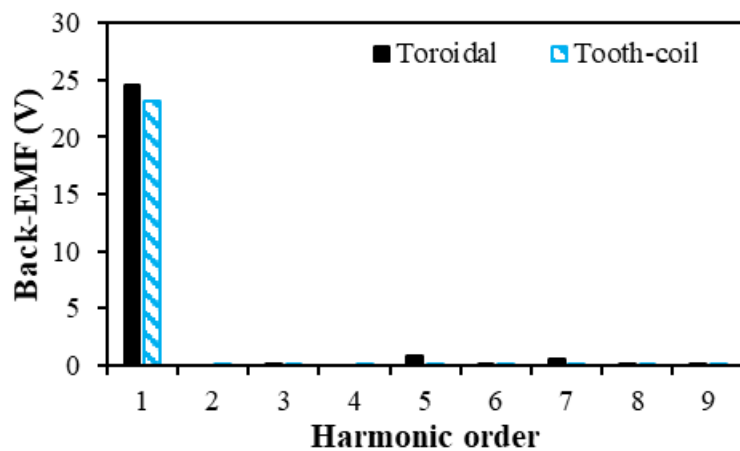
Fig. 5.30. Open-circuit air-gap flux densities of HSPM motors with toroidal and tooth-coil windings.

2) Back-EMF

The back-EMFs of 6s/2p HSPM motors with toroidal windings and tooth-coil windings are compared in Fig. 5.31. The back-EMF waveforms of phase A of two motors are sinusoidal and the motor with toroidal windings has a slightly larger fundamental magnitude of back-EMF than the motor with tooth-coil windings, which is the same result as the air-gap flux density.



(a) Waveforms



(b) Harmonics

Fig. 5.31. Comparison of back-EMFs of phase A between HSPM motors with toroidal and tooth-coil windings.

3) Cogging Torque and Electromagnetic Torque

Fig. 5.32 shows the cogging torque and electromagnetic torque waveforms for HSPM motors with toroidal and tooth-coil windings under ideal brushless DC drive 120-degree square wave current for high-speed operation, Fig. 5.33. It can be seen that the cogging torques of both motors with toroidal and tooth-coil windings are almost zero and the motor with toroidal windings has larger electromagnetic torque.

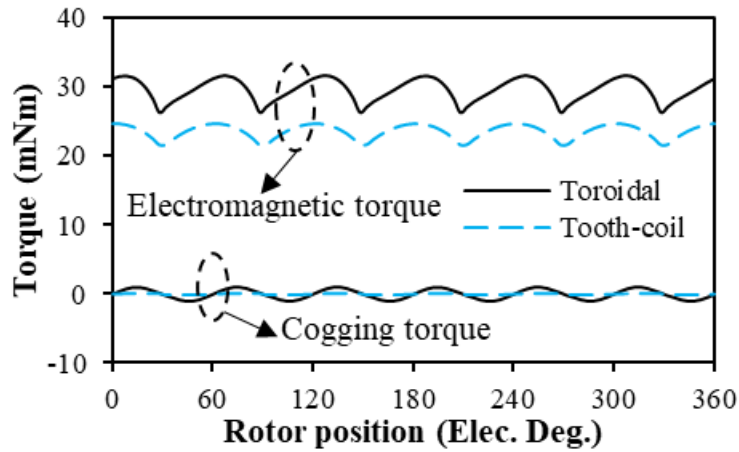


Fig. 5.32. Cogging torques and electromagnetic torques of HSPM motors with toroidal and tooth-coil windings.

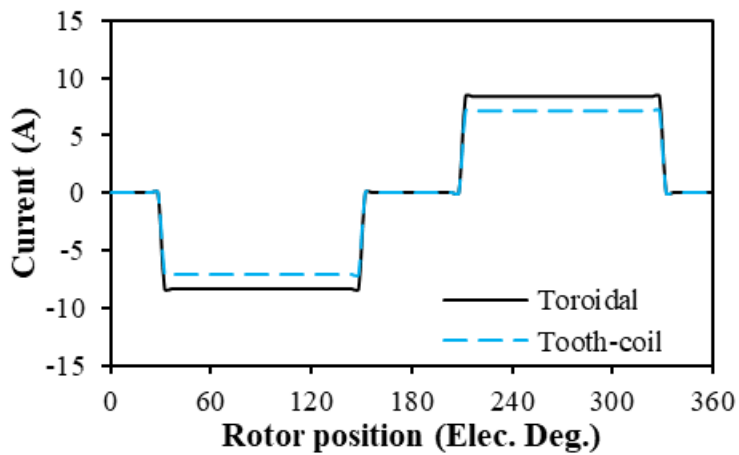


Fig. 5.33. Phase currents of HSPM motors with toroidal and tooth-coil windings under the same current density, phase A.

4) Loss Analysis

In this section, the on-load losses of two optimized motors are calculated by FEM with the fixed current density, including stator iron loss, copper loss, rotor loss, Fig. 5.34. Overall, the motors with toroidal and tooth-coil windings have almost the same total loss.

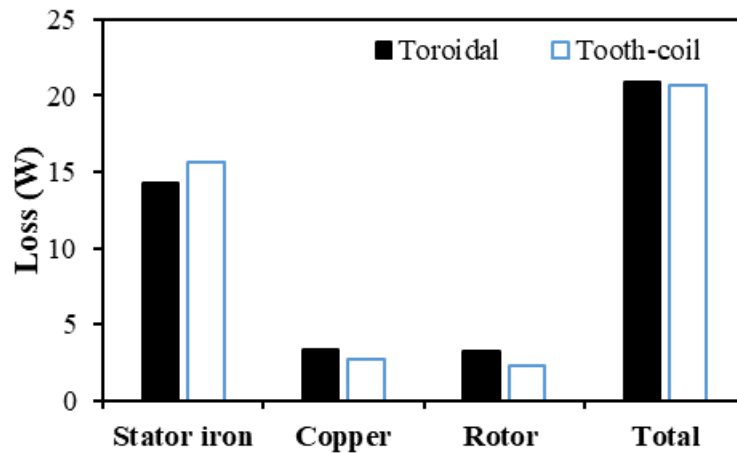


Fig. 5.34. Losses of HSPM motors with toroidal and tooth-coil windings.

A. Stator iron loss

The stator iron losses motors with toroidal and tooth-coil windings are calculated by FEM, Fig. 5.35. The armature reaction increases the stator iron loss, Fig. 5.35, and the toroidal wound motor has lower stator iron loss than the tooth-coil wound motor due to smaller stator active iron volume, which can be seen in Fig. 5.36. It is apparent that there is negligible iron loss in the outside tooth of toroidal wound motor.

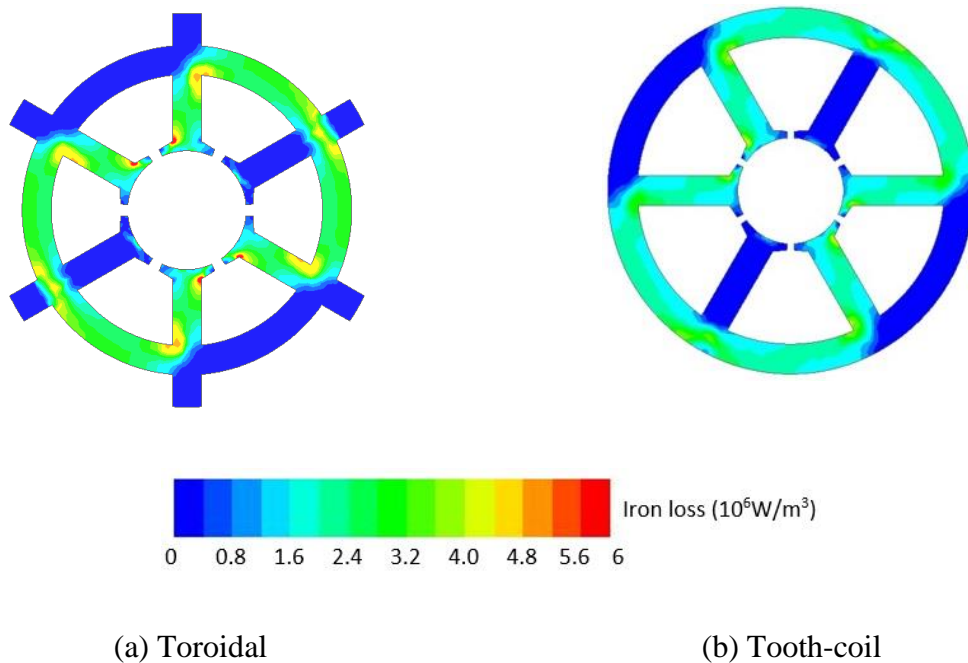
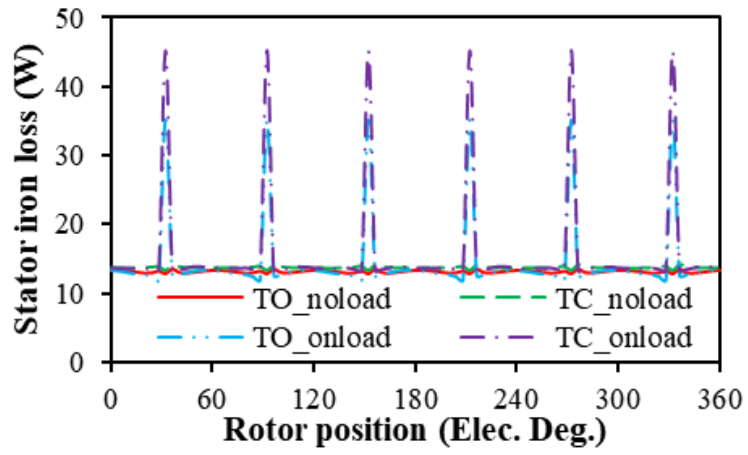
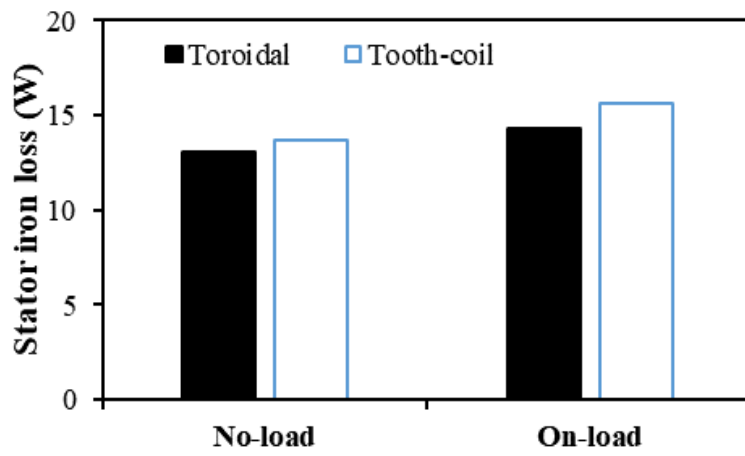


Fig. 5.35. On-load stator iron loss distributions of motors with toroidal and tooth-coil windings.



(a) Waveforms



(b) Harmonics

Fig. 5.36. Stator iron losses in toroidal and tooth-coil wound HSPM motors.

B. Copper loss

As mentioned in Section 5.2.3, the AC loss due to skin effect are negligible for slotted motor and it is essential for HSPM motor to use Litz wires in order to avoid large AC loss. Therefore, only DC copper loss are compared in this section. Although the motor with toroidal windings has smaller resistance due to the small cooper wire diameter, it still has larger DC copper loss due to the larger current, Fig. 5.34.

C. Rotor loss

A stainless-steel sleeve is employed to retain the PMs from centrifugal force, and thus the rotor loss includes eddy current losses in sleeve, PMs, and shaft. Those eddy current loss not only affects the motor efficiency but also may result in irreversible demagnetization of PMs due to overheating [EDE01]. In general, the rotor eddy current loss is caused by the spatial harmonics as well as the time harmonics. Since both motors with toroidal and tooth-coil windings are employed the stator structure with tooth-tip, the rotor losses are almost the same. Fig. 5.36 shows the rotor loss distributions of motor with toroidal and tooth-coil windings.

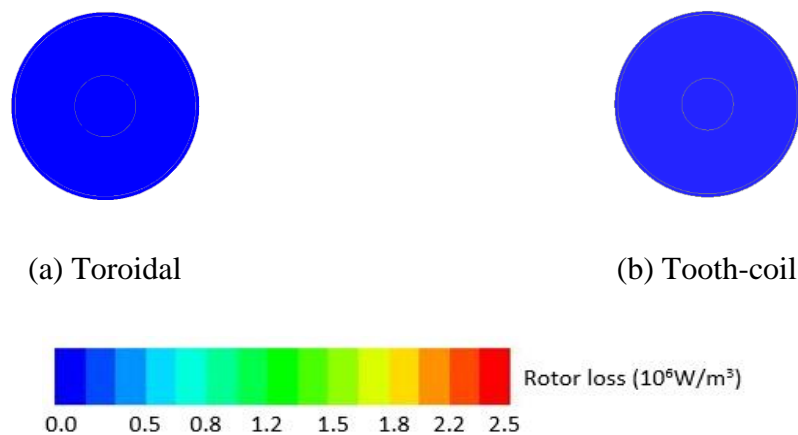


Fig. 5.36. On-load rotor loss distributions of motors with toroidal and tooth-coil windings.

D. Frame loss

As stated in 5.2.3, the losses in the frame of the motor with toroidal windings are taken into consideration since the toroidal windings have high external leakage caused by the outer windings. The frame loss of the motor with tooth-coil windings are almost zero, Fig. 5.37. However, for the motor with toroidal windings, same as the result in 5.2.3, when the frame thickness is less than 1mm, the frame eddy current loss increases sharply, while after that the frame loss remains unchanged since the skin depth of the frame is 1.2 mm, Fig. 5.37. Overall, compared to other loss components, the frame loss is very small and can be neglected.

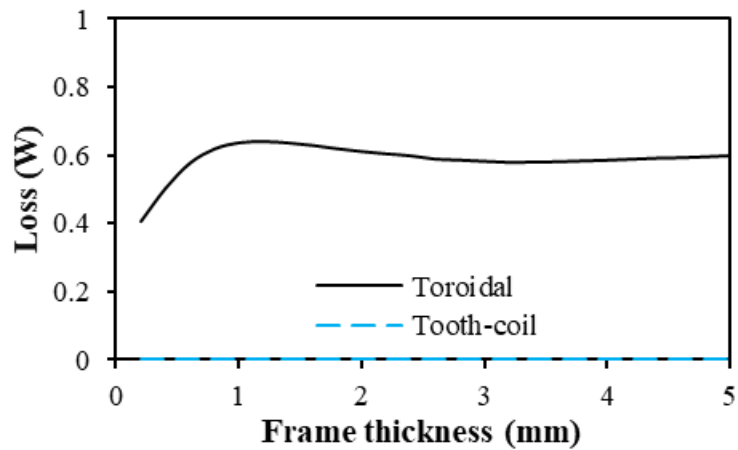


Fig. 5.37. Variation of frame losses with frame thickness of motors with toroidal and tooth-coil windings.

5). Winding inductances

The comparison of winding inductances between motors with toroidal and tooth-coil windings is investigated. The winding inductances are calculated by FEM using the same method as section 5.2.3. It can be seen that the motor with tooth-coil windings has significantly larger self- and mutual-inductance than the motor with toroidal windings, Table 5.8, but has positive mutual-inductance since the two different phase conductors with the same connection polarity are located at the sides of the slot, Fig. 5.23(b). Since toroidal windings and tooth-coil windings have short end-winding, end-winding inductance is neglected in this chapter.

Table 5.8
Winding Inductances for HSPM Motors (μH)

	Toroidal	Tooth-coil
Self-inductance	22.80	53.32
Mutual-inductance	-1.97	21.24
Phase inductance	24.77	32.08

5.4 Conclusion

In this chapter, 2-pole slotted and slotless HSPM motors with toroidal windings are optimized by FEM, and their electromagnetic and mechanical performances are compared. The results show that the slotted motor has advantages of high torque and torque per PM volume, lower AC copper loss, and relatively suitable winding inductance. Although the slotless motor can offer advantages such as low stator iron loss and low rotor loss, its high AC copper loss and very small winding inductances should be considered carefully for high-speed applications. In addition, 6s/2p HSPM motor with toroidal and tooth-coil windings are optimized and compared

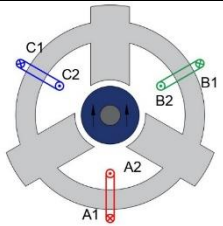
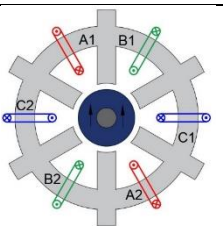
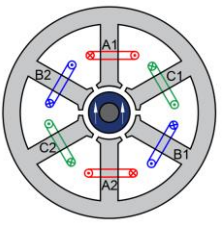
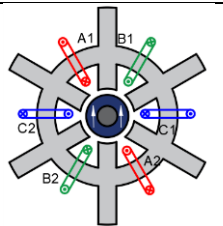
using the same method. Compared with tooth-coil windings, the 6s/2p HSPM motor with toroidal windings has higher torque and PM utilization, but smaller winding inductances.

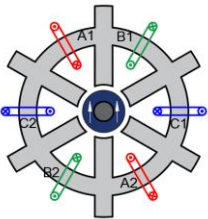
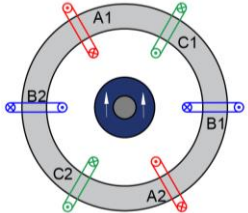
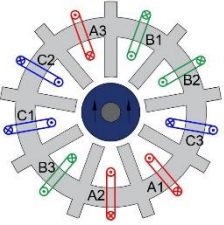
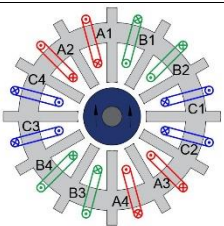
CHAPTER 6

GENERAL CONCLUSION AND FUTURE WORK

In this thesis, small-size low-power slotted 2-pole toroidally wound HSPM motors have been designed and investigated in terms of electromagnetic performance. Toroidal windings with non-overlapping end-windings can not only reduce the end-winding axial length but also achieve the modular design.

Table 6.1
All Motor Topologies in This Thesis

	Stator structures	Slot ratios	Winding Configurations	Cross-sections
3-slot/2-pole	Slotted	0.5	Toroidal	
6-slot/2-pole	Slotted	0.5	Toroidal	
		-	Tooth-coil	
		< 0.5	Toroidal	

		> 0.5		
	Slotless	0.5	Toroidal	
9-slot/2-pole	Slotted	0.5	Toroidal	
12-slot/2-pole	Slotted	0.5	Toroidal	

6.1 Motor Design and Comparison

The influence of slot numbers on electromagnetic performance of 2-pole toroidally wound HSPM motors is investigated by FEM in Chapter 2. Fig. 6.1 shows four machine topologies of 2-pole HSPM motors with slot numbers of 3, 6, 9, and 12, respectively. Then, Chapter 3 analyses the optimal split ratio of $6s/2p$ HSPM motors with toroidal windings, considering the effect of slot ratio, maximum stator iron flux density, and tooth-tip. Three machine topologies of $6s/2p$ HSPM motors with different slot ratio are shown in Fig. 6.2. The 2-pole HSPM motors with slotless/slotted stator structures and tooth-coil/toroidal winding configurations is compared in Chapter 4, and their machine topologies are shown in Fig. 6.3.

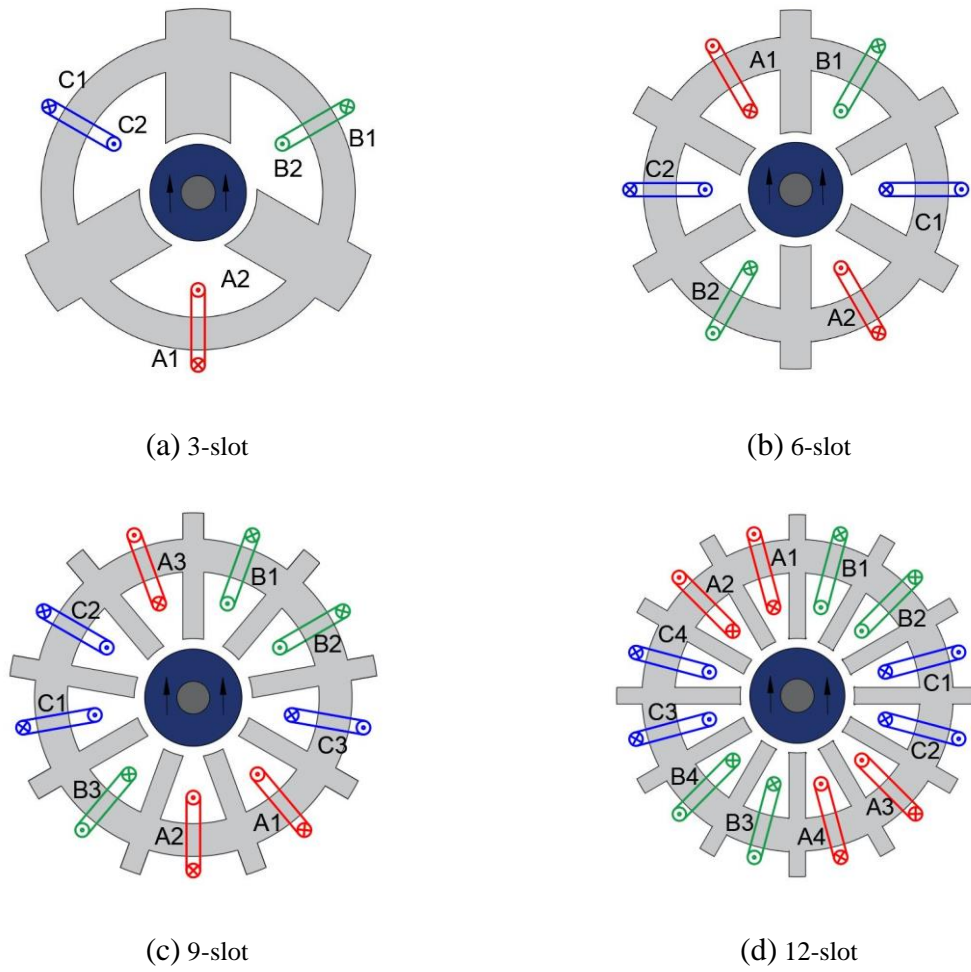


Fig. 6.1. Cross-sections of 2-pole high-speed motors with toroidal windings.

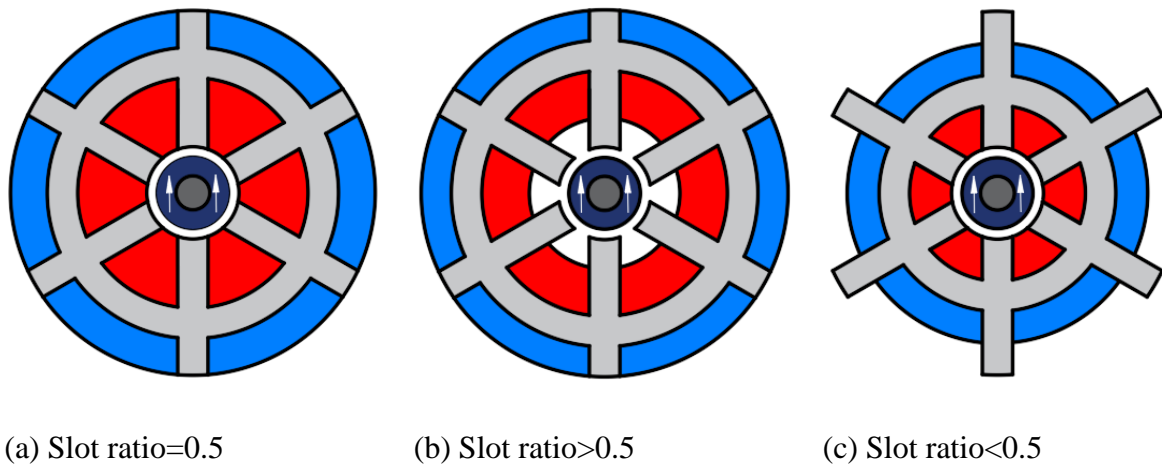


Fig. 6.2. 6s/2p toroidally-wound HSPM motors with different slot ratios.

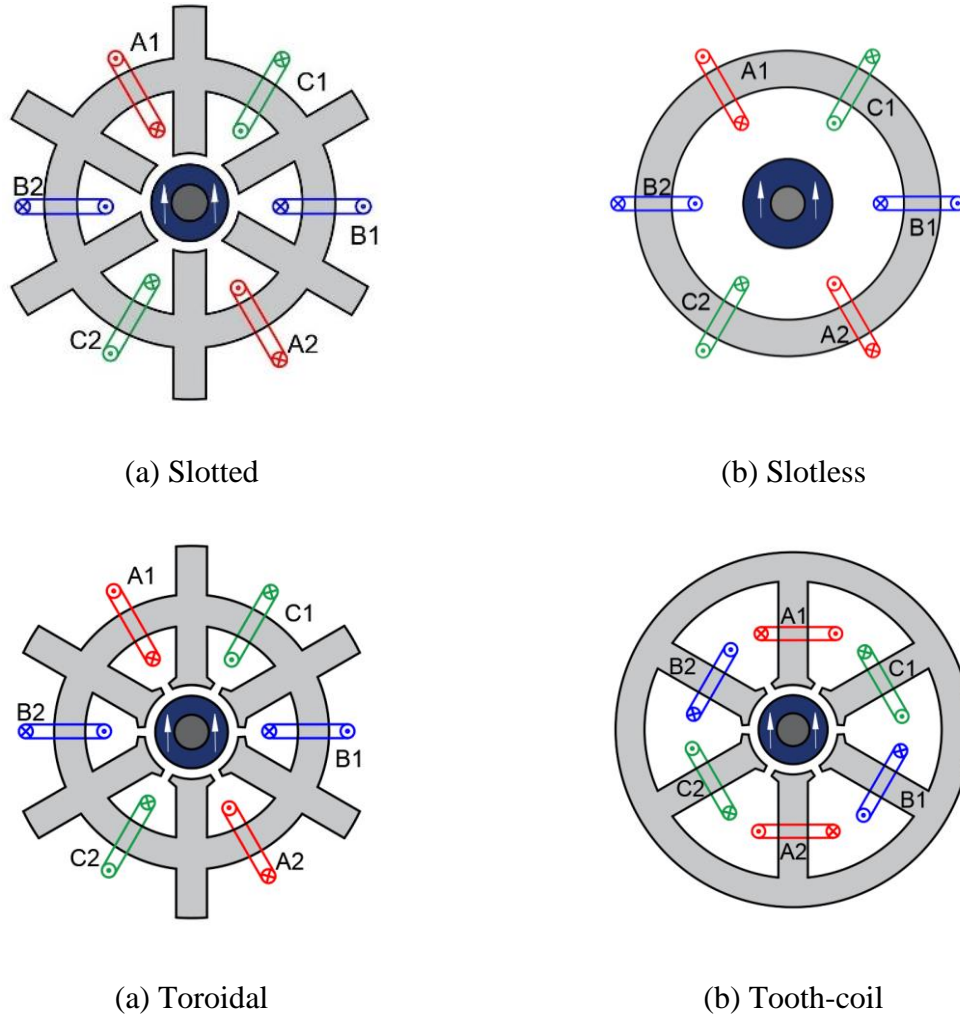


Fig. 6.3. Cross-sections of two 2-pole HSPM motors with different windings.

Firstly, the winding configurations and winding factors of 2-pole toroidally-wounded HSPM motors with 3-, 6-, 9-, 12-slot stator structures are analysed and calculated, respectively. Fixing maximum current density and limiting stator loss, four motors have been optimised for maximum torque. Then, their electromagnetic performances are compared, including air-gap flux density, back-EMF, cogging torque, electromagnetic torque, winding inductances, UMF, and various loss components. The results show that compared with the 3-slot and 9-slot stator structures, 6-slot and 12-slot motors are more suitable for high-speed applications due to non-existence of UMF and low rotor loss. Compared with the 12-slot motor, the 6-slot motor has less iron loss and larger torque due to larger winding factor, which is a better choice for high-speed application.

Secondly, the optimal split ratio of the 6s/2p HSPM motor with toroidal windings has been investigated by analytical method considering the stator iron loss. In addition, the influence of

slot ratio, i.e. the ratio of inner slot area to total slot area, maximum stator iron flux density, and tooth-tip is analysed. The results can be summarised as follow:

- With the fixed stator loss, the considered stator iron loss leads to the decrease of maximum average torque and optimal split ratio due to the reduced copper loss and electric loading.
- When the inner slot area equals to the outer slot area, the maximum average torque can be achieved under an optimal combination of split ratio and maximum stator iron flux density.
- The optimal split ratio decreases with the increase of slot ratio, and the results are affected by the maximum stator iron flux density.
- For a given iron flux density, tooth-tips have almost no influence on the variations of maximum torque and optimal split ratio with slot ratio.

Thirdly, 2-pole slotted and slotless HSPM motors with toroidal windings are optimised for maximum torque and their electromagnetic performance are compared. It shows that the slotted motor has advantages of high torque and torque per PM volume, and lower AC copper loss. The slotless motor can offer advantages such as low stator iron loss and low rotor loss due to no slotting effect. However, the slotless motor has high AC copper loss and very small winding inductances, which should be considered carefully for high-speed applications. In addition, the 6s/2p HSPM motors with toroidal and tooth-coil windings are compared. The results show that compared with tooth-coil windings, toroidal windings have higher torque and PM utilization, but smaller winding inductances.

6.2 Manufacturing Tolerances

The influence of stator segment gap and stator misaligned segments, which occur during modular manufactory process of 6s/2p HSPM motor with toroidal windings, on electromagnetic performance is investigated as shown in Fig. 6.4. The results are summarised as follows:

- The stator gap mainly affects the equivalent air-gap length and magnetic reluctance, which decrease the fundamental magnitude of air-gap flux density, flux linkage, back-EMF, and average on-load torque.

- The stator gap changes the equivalent combination of slot and pole numbers, which increases the harmonic contents of air-gap flux density and peak cogging torque significantly.
- Due to uneven equivalent air-gap distribution, stator gap leads to unbalanced three phase back-EMFs (both amplitudes and phase angles) and self-/ mutual-inductances.
- The stator gap increases the total motor loss due to the increase of rotor PM loss.
- When the stator gap is less than 1mm, the influence of stator gap on total loss can be neglected.
- The misaligned stator segments with gaps result in asymmetric air-gap length and winding configuration which affect the electromagnetic performance significantly.
- The misalignment of two stator parts mainly affects the uneven equivalent air-gap and symmetry of winding configuration, which leads to unbalanced three phase back-EMFs, especially phase angles, and self- /mutual-inductances.
- The misalignment increases the total motor loss due to the increase of rotor PM loss and has negligible influence on stator iron loss.

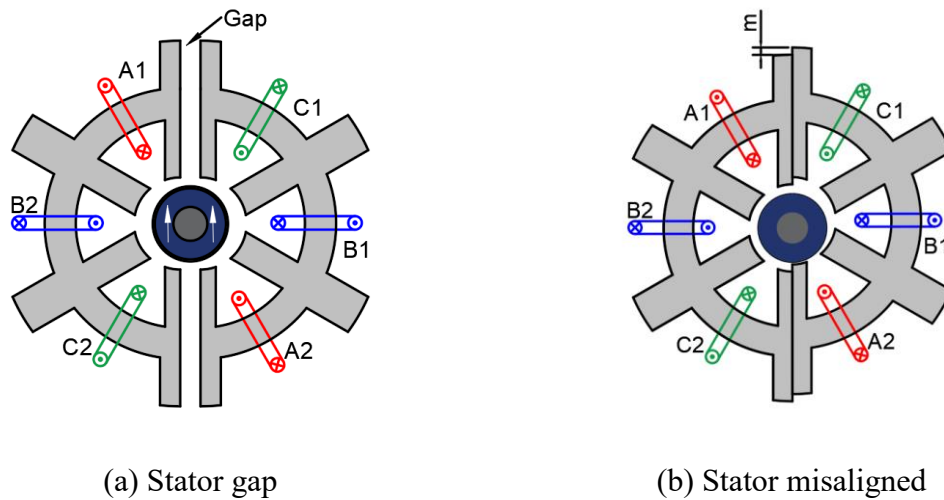


Fig. 6.4 6s/2p HSPM motors with toroidal windings.

6.3 Future Work

In this thesis, the research only focuses on the electromagnetic performance of 2-pole toroidally wound HSPM motors. Therefore, multiphysics design and optimization can be investigated in

the future, including thermal field, mechanical stress, rotor dynamics, and vibration.

In literature [BIA04], the overall heat transfer coefficient of the slotted motor is twice higher than that of the slotless motor with forced-air cooling, which can be verified by the thermal analyses of slotted and slotless 2-pole motors with forced-air cooling. In addition, different winding configurations also can be compared in terms of temperature rise.

Since the 6s/2p HSPM motor with toroidal windings has small winding inductance, the influence of low winding inductance on the high-speed sensorless control can be investigated in the future, together with the electromagnetic torque and rotor loss.

REFERENCES

- [AHN17] J. Ahn, J. Choi, C. H. Park, C. Han, C. Kim, and T. Yoon, "Correlation between rotor vibration and mechanical stress in ultra-high-speed permanent magnet synchronous motors," *IEEE Trans. Magn.*, vol. 53, no. 11, pp. 1-6, Nov. 2017.
- [AHN18] J. Ahn, C. Han, C. Kim, and J. Choi, "Rotor design of high-speed permanent magnet synchronous motors considering rotor magnet and sleeve materials," *IEEE Trans. Appl. Supercond.*, vol. 28, no. 3, pp. 1-4, Apr. 2018.
- [ARU16] P. Arumugam, Z. Xu, A. Rocca, G. Vakil, M. Dickinson, E. Amankwah, T. Hamiti, S. Bozhko, C. Gerada, and S. Pickering, "High-speed solid rotor permanent magnet machines: concept and design," *IEEE Trans. Transport. Electric.*, vol. 2, no. 3, pp. 391–400, Sep. 2016.
- [ATA92] K. Atallah, Z. Q. Zhu, and D. Howe, "An improved method for predicting iron losses in brushless permanent magnet DC drives," *IEEE Trans. Magn.*, vol. 28, no. 5, pp. 2997-2999, 1992.
- [ATA98] K. Atallah, Z.Q. Zhu, and D. Howe, "Armature reaction field and winding inductances of slotless permanent-magnet brushless machines," *IEEE Trans. Magn.*, vol. 34, no. 5, pp. 3737-3744, Sept. 1998.
- [BEN18] R. Benlamine, T. Hamiti, F. Vangraefschep, and D. Lhotellier, "Electromagnetic, structural and thermal analyses of high-speed PM machines for aircraft application," *International Conference on Electrical Machines (ICEM)*, Greece, 2018, pp. 212-217.
- [BER16] N. Bernard, R. Missoum, L. Dang, N. Bekka, H. Ben Ahmed, and M. E. Zaïm, "Design methodology for high-speed permanent magnet synchronous machines," *IEEE Trans. Energy Convers.*, vol. 31, no. 2, pp. 477-485, Jun. 2016.
- [BER88] G. Bertotti, "General properties of power losses in soft ferromagnetic materials," *IEEE Trans. Magn.*, vol. 24, no. 1, pp. 621-630, Jan. 1988.
- [BIA04] N. Bianchi, S. Bolognani, and F. Luise, "Potentials and limits of high-speed

- PM motors,” *IEEE Trans. Ind. Appl.*, vol. 40, no. 6, pp. 1570–1578, Nov. 2004.
- [BIA05] N. Bianchi, S. Bolognani, and F. Luise, “Analysis and design of a PM brushless motor for high-speed operations,” *IEEE Trans. Energy Convers.*, vol. 20, no. 3, pp. 629-637, Sept. 2005.
- [BIA06] N. Bianchi, S. Bolognani, and F. Luise, "High speed drive using a slotless PM motor," *IEEE Trans. Power Electron.*, vol. 21, no. 4, pp. 1083-1090, July 2006.
- [BIN06] A. Binder, T. Schneider, and M. Klohr, "Fixation of buried and surface-mounted magnets in high-speed permanent-magnet synchronous machines," *IEEE Trans. Ind. Appl.*, vol. 42, no. 4, pp. 1031-1037, Jul.-Aug. 2006.
- [BOR10] A. Borisavljevic, H. Polinder, and J. A. Ferreira, “On the speed limits of permanent-magnet machines,” *IEEE Trans. Ind. Electron.*, vol. 57, no. 1, pp. 220-227, Jan. 2010.
- [BOR14] A. Borisavljevic, S. Jumayev, and E. Lomonova, “Toroidally-wound permanent magnet machines in high-speed applications,” *International Conference on Electrical Machines (ICEM)*, Berlin, Germany, 2014, pp. 2588-2593.
- [BUR17] G. Burnand, D. M. Araujo, and Y. Perriard, "Very-high-speed permanent magnet motors: Mechanical rotor stresses analytical model," *IEEE International Electric Machines and Drives Conference (IEMDC)*, Miami, USA, 2017, pp. 1-7.
- [BUR19] G. Burnand and Y. Perriard, "Very-high-speed miniaturized permanent magnet motors: design and optimization," *IEEE Energy Conversion Congress and Exposition (ECCE)*, Baltimore, USA, 2019, pp. 5258-5264.
- [BUR20] G. Burnand, A. Thabuis, D. M. Araujo, and Y. Perriard, "Novel optimized shape and topology for slotless windings in BLDC machines," *IEEE Trans. Ind. Appl.*, vol. 56, no. 2, pp. 1275-1283, Mar.-Apr. 2020.
- [CHA93] F. B. Chaaban, “Determination of the optimum rotor/stator diameter ratio of permanent magnet machines,” *Electrical Machines and Power Systems*, vol.

22. pp. 521-531.1993.

- [CHA00] F. B. Chaaban and A. El-Hajj, "A cost effective design approach for permanent magnet brushless machines," *Electric machines and power Systems*, vol. 28, pp. 893-900, 2000.
- [CHA10] S. H. Chai, B. Y. Lee, J. J. Lee, and J. P. Hong, "Reduction eddy current loss design and analysis of in-wheel type vehicle traction motor," *International Conference on Electrical Machines and Systems (ICEMS)*, Incheon, South Korea, 2010, pp. 1264-1267.
- [CHE07] A. Chebak, P. Viarouge, and J. Cros, "Analytical model for design of high-speed slotless brushless machines with SMC stators," *IEEE International Electric Machines and Drives Conference (IEMDC)*, Antalya, USA, 2007, pp. 159-164.
- [CHE09] A. Chebak, P. Viarouge, and J. Cros, "Analytical Computation of the full load magnetic losses in the soft magnetic composite stator of high-speed slotless permanent magnet machines," *IEEE Trans. Magn.*, vol. 45, no. 3, pp. 952-955, Mar. 2009.
- [CHE11] F. Cheng, H. Xu, and S. Xue, "Study on the design method of high speed permanent magnet synchronous machine," *International Conference on Electrical Machines and Systems (ICEMS)*, Beijing, China, 2011, pp. 1-6.
- [CHE15] A. Chebak, P. Viarouge, and J. Cros, "Improved analytical model for predicting the magnetic field distribution in high-speed slotless permanent-magnet machines," *IEEE Trans. Magn.*, vol. 51, no. 3, pp. 1-4, Mar. 2015.
- [CHE19] X. Cheng, W. Xu, G. Du, G. Zeng, and J. Zhu, "Novel rotors with low eddy current loss for high speed permanent magnet machines," *CES Trans. Electrical Machines and Systems*, vol. 3, no. 2, pp. 187-194, Jun. 2019.
- [CHE95] Z. Chen and E. Spooner, "A modular, permanent-magnet generator for variable speed wind turbines," *International Conference on Electrical Machines and Systems (ICEMS)*, Sep. 1995, pp. 453-457.

- [CHE97] Y. Chen, J. Shen, and Z. Fang, "Topology and preliminary design of slotless brushless DC motor," *IEEE International Electric Machines and Drives Conference Record*, 1997, pp. WB2/7.1-WB2/7.3.
- [CHE98] Y.S. Chen, Z.Q. Zhu, and D. Howe, "Investigation of slotless brushless permanent magnet machines," *Proc.15th Int. Workshop on Rare-Earth Magnets and Their Applications*, Germany, 1998, pp.737-745.
- [CHE99] Y. S. Chen, Z. Q. Zhu, and D. Howe, "Slotless brushless permanent magnet machines: influence of design parameters," *IEEE Trans. Energy Convers.*, vol. 14, no. 3, pp. 686-691, Sept. 1999.
- [DAM16] A. Damiano, A. Floris, G. Fois, M. Porru, and A. Serpi, "Modelling and design of PM retention sleeves for high-speed PM synchronous machines," *IEEE International Electric Drives Production Conference (EDPC)*, Nuremberg, Germany, 2016, pp. 118-125.
- [DON14a] J. Dong, Y. Huang, L. Jin, H. Lin, and H. Yang, "Thermal optimization of a high-speed permanent magnet motor," *IEEE Trans. Magn.*, vol. 50, no. 2, Feb. 2014.
- [DON14b] J. Dong, Y. Huang, L. Jin, B. Guo, H. Lin, J. Dong, M. Cheng, and H. Yang, "Electromagnetic and thermal analysis of open-circuit air cooled high-speed permanent magnet machines with gramme ring windings," *IEEE Trans. Magn.*, vol. 50, no. 11, Nov. 2014.
- [DON16a] M. S. Donea and D. Gerling, "Design and calculation of a 300 kW high-speed PM motor for aircraft application," *International Symposium on Power Electronics, Electrical Drives, Automation and Motion (SPEEDAM)*, Capri, Italy, 2016, pp. 1-6.
- [DON16c] J. Dong, Y. Huang, L. Jin, and H. Lin, "Comparative study of surface-mounted and interior permanent-magnet motors for high-speed applications," *IEEE Trans. Appl. Supercond.*, vol. 26, no. 4, pp. 1-4, Jun. 2016.
- [DUG19] G. Du, W. Xu, J. Zhu, and N. Huang, "Rotor stress analysis for high-speed permanent magnet machines considering assembly gap and temperature

- gradient," *IEEE Trans. Energy Convers.*, vol. 34, no. 4, pp. 2276-2285, Dec. 2019.
- [DUG20a] G. Du, W. Xu, J. Zhu, and N. Huang, "Effects of design parameters on the multiphysics performance of high-speed permanent magnet machines," *IEEE Trans. Ind. Electron.*, vol. 67, no. 5, pp. 3472-3483, May 2020.
- [DUG20b] G. Du, Q. Zhou, S. Liu, N. Huang, and X. Chen, "Multiphysics design and multiobjective optimization for high-speed permanent magnet machines," *IEEE Trans. Transport. Electrification*, vol. 6, no. 3, pp. 1084-1092, Sept. 2020.
- [DUG21] G. Du, N. Huang, Y. Zhao, G. Lei, and J. Zhu, "Comprehensive sensitivity analysis and multiphysics optimization of the rotor for a high speed permanent magnet machine," *IEEE Trans. Energy Convers.*, vol. 36, no. 1, pp. 358-367, Mar. 2021.
- [EDE01] J.D. Ede, Z.Q. Zhu, and D. Howe, "Optimal split ratio for high speed permanent magnet brushless dc motors," *International Conference on Electrical Machines (ICEM)*, August, 2001, pp.909-912.
- [EDE02] J. D. Ede, Z. Q. Zhu, and D. Howe, "Rotor resonances of high-speed permanent-magnet brushless machines," *IEEE Trans. Ind. Appl.*, vol. 38, no. 6, pp. 1542-1548, Nov.-Dec. 2002.
- [EVA83] P. Evans and J. Eastham, "Slotless-disc alternator with AC-side excitation," *IEE Proc. Electr. Power Appl.*, vol. 130, no. 6, pp. 399-406, 1983.
- [FAN15] J. Fang, X. Liu, B. Han, and K. Wang, "Analysis of circulating current loss for high-speed permanent magnet motor," *IEEE Trans. Magn.*, vol. 51, no. 1, Jan. 2015.
- [FAN17] H. Fang, R. Qu, J. Li, P. Zheng, and X. Fan, "Rotor design for a high-speed high-power permanent-magnet synchronous machine," *IEEE Energy Conversion Congress and Exposition (ECCE)*, Montreal, Canada, 2015, pp. 4405-4412.

- [FAN19] H. Fang, D. Li, R. Qu, J. Li, C. Wang, and B. Song, "Rotor design and eddy-current loss suppression for high-speed machines with a solid-PM rotor," *IEEE Trans. Ind. Appl.*, vol. 55, no. 1, pp. 448-457, Jan.-Feb. 2019.
- [FOD14] D. Fodorean, D. C. Popa, P. Minciunescu, C. Irimia, and L. Szabó, "Study of a high-speed motorization for electric vehicle based on PMSM, IM and VRSM," *International Conference on Electrical Machines (ICEM)*, Berlin, Germany, 2014, pp. 2577-2582.
- [FOD14a] D. Fodorean, "Study of a high-speed motorization with improved performances dedicated for an electric vehicle," *IEEE Trans. Magn.*, vol. 50, no. 2, pp. 921-924, Feb. 2014.
- [GAL15] S. J. Galioto, P. B. Reddy, A. M. EL-Refaie, and J. P. Alexander, "Effect of magnet types on performance of high-speed spoke interior-permanent-magnet machines designed for traction applications," *IEEE Trans. Ind. Appl.*, vol. 51, no. 3, pp. 2148-2160, May-Jun. 2015.
- [GER14] D. Gerada, A. Mebarki, N. L. Brown, C. Gerada, A. Cavagnino, and A. Boglietti, "High-speed electrical machines: technologies, trends, and developments," *IEEE Trans. Ind. Electron.*, vol. 61, no. 6, pp. 2946-2959, Jun. 2014.
- [GIE14] J. F. Gieras, "Design of permanent magnet brushless motors for high speed applications," *International Conference on Electrical Machines and Systems (ICEMS)*, Hangzhou, China, 2014, pp. 1-16.
- [GIL15] A. Gilson, S. Tavernier, M. Gerber, C. Espanet, F. Dubas, and D. Depernet, "Design of a cost-efficient high-speed high-efficiency PM machine for compressor applications," *IEEE Energy Conversion Congress and Exposition (ECCE)*, Montreal, Canada, 2015, pp. 3852-3856.
- [GIL16] A. Gilson, F. Dubas, D. Depernet, and C. Espanet, "Comparison of high-speed PM machine topologies for electrically-assisted turbocharger applications," *International Conference on Electrical Machines and Systems (ICEMS)*, Chiba, Japan, 2016, pp. 13-16.

- [GIL17] A. Gilson, G. Verez, F. Dubas, D. Depernet, and C. Espanet, "Design of a high-speed permanent-magnet machine for electrically-assisted turbocharger applications with reduced noise emissions," *International Electric Machines and Drives Conference (IEMDC)*, Miami, USA, 2017, pp. 1-6.
- [GON14] D. A. Gonzalez and D. M. Saban, "Study of the copper losses in a high-speed permanent-magnet machine with form-wound windings," *IEEE Trans. Ind. Electron.*, vol. 61, no. 6, pp. 3038-3045, Jun. 2014.
- [HAN03] D. Hanselman, "Brushless motor fundamentals" in *Brushless permanent magnet motor design*, 2nd ed., Lebanon, USA: Magna Physics Publishing, 2003, pp. 92-94.
- [HAN18] T. Han, Y. Wang, X. Qin, and J. Shen, "Investigation of various rotor retaining sleeve structures in high-speed PM brushless motors," *International Conference on Electrical Machines and Systems (ICEMS)*, Jeju, South Korea, 2018, pp. 109-114.
- [HES82] D. E. Hesmondhalgh and D. Tipping, "Slotless construction for small synchronous motors using samarium cobalt magnets," *IEE Proc. Electr. Power Appl.*, vol.129, no.5, pp. 251-261, Sept. 1982.
- [HES87] D. E. Hesmondhalgh, D. Tipping, and M. Amrani, "Design and construction of a high-speed high-performance direct-drive handpiece," *IEE Proc. B-Elec. Power Appl.*, vol. 134, no. 6, pp. 286-296, Nov. 1987.
- [HE21] T. R. He, Z. Q. Zhu, F. Xu, Y. Wang, H. Bin, and L. M. Gong, "Electromagnetic performance analysis of 6-slot/2-pole high-speed permanent magnet motors with coil-pitch of two slot-pitches," *IEEE Trans. Energy Convers.*, Nov. 2021.
- [HE21a] T. R. He, Z. Q. Zhu, Fan Xu, Hong Bin, Di Wu, Liming Gong, and Jintao Chen, "Comparative study of 6-slot/2-pole high-speed permanent magnet motors with different winding configurations," *IEEE Trans. Ind. Appl.*, vol.57, no.6, pp.5864-5875, Nov.-Dec. 2021.

- [HON09] D. Hong, B. Woo, C. Ahn, and D. Koo, "Unbalance analysis of 15kW, 120krpm, ultra high speed permanent magnet synchronous motor," *International Conference on Electromagnetic Field Problems and Applications (ICEF)*, Dalian, China, 2012, pp. 1-4.
- [HON13] D. Hong, D. Joo, B. Woo, Y. Jeo, D. Koo, C. Ahn, and Y. Cho, "Performance verification of a high speed motor-generator for a microturbine generator," *International Journal of Precision Engineering and Manufacturing*, vol. 14, no.7, pp. 1237-1244, Jul. 2013.
- [HON18] D. Hong, T. Lee, and Y. Jeong, "Design and experimental validation of a high-speed electric turbocharger motor considering variation of the L/D ratio," *IEEE Trans. Magn.*, vol. 54, no. 11, pp. 1-4, Nov. 2018.
- [HON97] Y. Honda, S. Yokote, T. Higaki, and Y. Takeda, "Using the Halbach magnet array to develop an ultra high-speed spindle motor for machine tools," *IAS '97. Conference Record of the 1997 IEEE Industry Applications Conference Thirty-Second IAS Annual Meeting*, 1997, pp. 56-60 vol.1.
- [HUA10] W. Y. Huang, A. Bettayeb, R. Kaczmarek, and J. C. Vannier, "Optimization of magnet segmentation for reduction of eddy current losses in permanent synchronous machine," *IEEE Trans. Energy Convers.*, vol. 25, no. 2, pp. 381-387, Jun. 2010.
- [HUA16] Z. Huang and J. Fang, "Multiphysics design and optimization of high-speed permanent-magnet electrical machines for air blower applications," *IEEE Trans. Ind. Electron.*, vol. 63, no. 5, pp. 2766-2774, May 2016.
- [HUY15] Y. Hu and T. Wu, "Comprehensive design and modeling of a super high-speed permanent magnet motor," *IEEE Workshop on Electrical Machines Design, Control and Diagnosis (WEMDCD)*, 2015, pp. 28-33.
- [HWA14] C. Hwang, S. Hung, C. Liu, and S. Cheng, "Optimal design of a high speed SPM motor for machine tool applications," *IEEE Trans. Magn.*, vol. 50, no. 1, pp. 1-4, Jan. 2014.

- [IID20] T. Iida, M. Takemoto, S. Ogasawra and K. Orikawa, I. Sato, H. Kokubun, A. Toba, and M. Syuto, "Investigation of enhancing output power density in ultra-high-speed motors with concentrated winding structure," *IEEE Energy Conversion Congress and Exposition (ECCE)*, Detroit, USA, 2020, pp. 262-269.
- [ISM18] F. R. Ismagilov, V. E. Vavilov, and D. V. Gusakov, "High-speed electric machine with a speed of 1.2 million rpm," *International Symposium on Power Electronics, Electrical Drives, Automation and Motion (SPEEDAM)*, Amalfi, Italy, 2018, pp. 1159-1164.
- [JAN07] S. Jang, H. Cho, and S. Choi, "Design and analysis of a high-speed brushless dc motor for centrifugal compressor," *IEEE Trans. Magn.*, vol. 43, no. 6, pp. 2573-2575, Jun. 2007.
- [JAN09] S. Jang, U. Lee, D. You, J. Lee, and S. Choi, "Operating torque estimation of high-speed slotless brushless dc machine considering power loss," *IEEE Trans. Magn.*, vol. 45, no. 10, pp. 4539-4542, Oct. 2009.
- [JAN11a] S. Jang, M. Koo, Y. Park, J. Choi, and S. Lee, "Characteristic analysis of permanent magnet synchronous machines under different construction conditions of rotor magnetic circuits by using electromagnetic transfer relations," *IEEE Trans. Magn.*, vol. 47, no. 10, pp. 3665-3668, Oct. 2011.
- [JAN11b] X. Jannot, J. Vannier, C. Marchand, M. Gabsi, J. Saint-Michel, and D. Sadarnac, "Multiphysic modeling of a high-speed interior permanent-magnet synchronous machine for a multiobjective optimal design," *IEEE Trans. Energy Convers.*, vol. 26, no. 2, pp. 457-467, Jun. 2011.
- [JAN18] G. Jang, J. Ahn, B. Kim, D. Lee, J. Bang, and J. Choi, "Design and characteristic analysis of a high-speed permanent magnet synchronous motor considering the mechanical structure for high-speed and high-head centrifugal pumps," *IEEE Trans. Magn.*, vol. 54, no. 11, pp. 1-6, Nov. 2018.
- [JAS17] R. P. Jastrzebski, P. Jaatinen, O. Pyrhönen, and A. Chiba, "Design of 6-slot inset PM bearingless motor for high-speed and higher than 100kW applications," *2017 IEEE International Electric Machines and Drives*

Conference (IEMDC), Miami, USA, 2017, pp. 1-6.

- [JEN12] B. B. Jensen, A. G. Jack, G. J. Atkinson, and B. C. Mecrow, "Performance of a folded-strip toroidally wound induction machine," *IEEE Trans. Ind. Electron.*, vol. 59, no. 5, pp. 2217–2226, May 2012.
- [JUM14] S. Jumayev, A. Borisavljevic, K. Boynov, E. A. Lomonova, and J. Pyrhönen, "Analysis of rotor eddy current losses in slotless high-speed permanent magnet machines," *European Conference on Power Electronics and Applications (ECCE)*, Lappeenranta, Finland, 2014, pp. 1-10.
- [JUM15] S. Jumayev, M. Merdzan, K. O. Boynov, J. J. H. Paulides, J. Pyrhönen, and E. A. Lomonova, "The effect of PWM on rotor eddy-current losses in high-speed permanent magnet machines," *IEEE Trans. Magn.*, vol. 51, no. 11, pp. 1-4, Nov. 2015.
- [JUM16] S. Jumayev, K. O. Boynov, J. J. H. Paulides, E. A. Lomonova, and J. Pyrhönen, "Slotless PM machines with skewed winding shapes: 3-D electromagnetic semianalytical model," *IEEE Trans. on Magn.*, vol. 52, no. 11, pp. 1-12, Nov. 2016.
- [JUM18] S. Jumayev, K. O. Boynov, E. A. Lomonova, and J. Pyrhonen, "High-speed slotless permanent magnet machines: modelling and design frameworks," *International Power Electronics Conference (IPEC)*, Niigata, Japan, 2018, pp. 161-168.
- [JUN15] H. Jun, J. Lee, H. Lee, and W. Kim, "Study on the optimal rotor retaining sleeve structure for the reduction of eddy-current loss in high-speed SPMSM," *IEEE Trans. Magn.*, vol. 51, no. 3, pp. 1-4, Mar. 2015.
- [JUN18] D. Jung, J. Lee, J. Kim, I. Jang, J. Lee, and H. Lee, "Design method of an ultrahigh speed PM motor/generator for electric-turbo compounding system," *IEEE Trans. Appl. Supercond.*, vol. 28, no. 3, pp. 1-4, Apr. 2018.
- [JUN19] G. Jungmayr, E. Marth, and G. Segon, "Magnetic-gear motor in side-by-side arrangement - concept and design," *IEEE International Electric Machines & Drives Conference (IEMDC)*, San Diego, USA, 2019, pp. 847-853.

- [KAZ16] K. Kazerooni, A. Rahideh, and J. Aghaei, "Experimental optimal design of slotless brushless PM machines based on 2-D analytical model," *IEEE Trans. Magn.*, vol. 52, no. 5, pp. 1-16, May 2016.
- [KOL11] Z. Kolondzovski, A. Arkkio, J. Larjola, and P. Sallinen, "Power limits of high-speed permanent-magnet electrical machines for compressor applications," *IEEE Trans. Energy Convers.*, vol. 26, no. 1, pp. 73-82, Mar. 2011.
- [KOL13] R. Kolano, K. Krykowski, A. Kolano-Burian, M. Polak, J. Szynowski, and P. Zackiewicz, "Amorphous soft magnetic materials for the stator of a novel high-speed PMBLDC motor," *IEEE Trans. Magn.*, vol. 49, no. 4, pp. 1367-1371, Apr. 2013.
- [KOL16] R. Kolano, A. Kolano-Burian, K. Krykowski, J. Hetmanczyk, M. Hreczka, M. Polka, and J. Szynowski, "Amorphous soft magnetic core for the stator of the high-speed PMBLDC motor with half-open slots," *IEEE Trans. Magn.*, vol. 52, no. 6, pp. 1-5, Jun. 2016.
- [KRA17] C. T. Krasopoulos, M. E. Beniakar, and A. G. Kladas, "Robust optimization of high-speed pm motor design," *IEEE Trans. Magn.*, vol. 53, no. 6, pp. 1-4, Jun. 2017.
- [LEE06] J.Y. Lee, B. K. Lee, T. Sun, J. P. Hong, and W. T. Lee, "Dynamic analysis of toroidal winding switched reluctance motor driven by 6-switch converter," *IEEE Trans. Magn.*, vol. 42, no. 4, pp. 1275–1278, Apr. 2006.
- [LEE17] H. Lee, E. Lee, S. Kwon, and J. Hong, "A study on brushless PM slotless motor with toroidal winding," *International Electric Machines and Drives Conference (IEMDC)*, Miami, USA, 2017, pp. 1-6.
- [LEE20] J. Lee, K. Shin, T. Bang, B. Choi, B. Kim, and J. Choi, "Experiments and design criteria for a high-speed permanent magnet synchronous generator with magnetic bearing considering mechanical aspects," *IEEE Trans. Appl. Supercond.*, vol. 30, no. 4, pp. 1-5, Jun. 2020.
- [LIB06] F. Libert and J. Soulard, "Manufacturing methods of stator cores with concentrated windings," *3rd IET Int. Conf. Power Electron., Mach. Drives,*

2006, pp. 676–680.

- [LID15] D. Li, R. Qu, J. Li, and W. Xu, “Consequent-pole toroidal-winding outer-rotor Vernier permanent-magnet machines,” *IEEE Trans. Ind. Appl.*, vol. 51, no. 6, pp. 4470–4481, Nov.-Dec. 2015.
- [LIG14] G. J. Li and Z. Q. Zhu, “Analytical modelling of modular and unequal tooth width surface-mounted permanent magnet machines,” *IEEE Trans. Magn.*, vol. 51, no. 9, pp. 1-9, Sept. 2015.
- [LIG15] G. J. Li and Z. Q. Zhu, “Analytical modelling of modular and unequal tooth width surface-mounted permanent magnet machines,” *IEEE Trans. Magn.*, vol. 51, no. 9, pp. 1-9, Sept. 2015.
- [LIH20] H. Li, Z. Q. Zhu, and H. Hua, “Comparative analysis of flux reversal permanent magnet machines with toroidal and concentrated windings,” *IEEE Trans. Ind. Electron.*, vol. 67, no. 7, pp. 5278-5290, Jul. 2020.
- [LIM17] M. Lim, J. Kim, Y. Hwang, and J. Hong, "Design of an ultra-high-speed permanent-magnet motor for an electric turbocharger considering speed response characteristics," *IEEE/ASME Trans. Mechatronics*, vol. 22, no. 2, pp. 774-784, Apr. 2017.
- [LIQ15] Q. Li, M. Dou, and C. Fang, "Analytical determination of optimal split ratio for high-speed permanent magnet brushless motors," *International Conference on Electrical Machines and Systems (ICEMS)*, Pattaya, Thailand, 2015, pp. 636-640.
- [LIS16] S. Li, Y. Li, W. Choi, and B. Sarlioglu, "High-speed electric machines: challenges and design considerations," *IEEE Trans. Transp. Electrification*, vol. 2, no. 1, pp. 2-13, Mar. 2016.
- [LIU18] Y. Liu, J. Ou, M. Schiefer, P. Breining, F. Grilli, and M. Doppelbauer, "Application of an amorphous core to an ultra-high-speed sleeve-free interior permanent-magnet rotor," *IEEE Trans. Power Electron.*, vol. 65, no. 11, pp. 8498-8509, Nov. 2018.

- [LIW13] W. Li, X. Zhang, S. Cheng, and J. Cao, "Thermal optimization for a HSPMG used for distributed generation systems," *IEEE Trans. Ind. Electron.*, vol. 60, no. 2, pp. 474-482, Feb. 2013.
- [LIW14] W. Li, H. Qiu, X. Zhang, J. Cao, and R. Yi, "Analyses on electromagnetic and temperature fields of super high-speed permanent-magnet generator with different sleeve materials," *IEEE Trans. Ind. Electron.*, vol. 61, no. 6, pp. 3056-3063, Jun. 2014.
- [LOO10] A. Looser, T. Baumgartner, C. Zwyssig, and J. W. Kolar, "Analysis and measurement of 3D torque and forces for permanent magnet motors with slotless windings," *IEEE Energy Conversion Congress and Exposition (ECCE)*, Atlanta, USA, 2010, pp. 3792-3797.
- [LUO09] J. Luomi, C. Zwyssig, A. Looser, and J. W. Kolar, "Efficiency optimization of a 100-W 500 000-r/min permanent-magnet machine including air-friction losses," *IEEE Trans. Ind. Appl.*, vol. 45, no. 4, pp. 1368-1377, Jul.-Aug. 2009.
- [MA17] J. Ma, L. Wu, and Z. Q. Zhu, "Effect of magnet thickness on electromagnetic performance of high speed permanent magnet machines," *IEEE International Electric Machines and Drives Conference (IEMDC)*, Miami, USA, 2017, pp. 1-7.
- [MA18] J. Ma and Z. Q. Zhu, "Mitigation of unbalanced magnetic force in a PM machine with asymmetric winding by inserting auxiliary slots," *IEEE Trans. Ind. Appl.*, vol. 54, no. 5, pp. 4133-4146, Sept.-Oct. 2018.
- [MA19a] J. Ma and Z. Q. Zhu, "Magnet eddy current loss reduction in permanent magnet machines," *IEEE Trans. Ind. Appl.*, vol. 55, no. 2, pp. 1309-1320, Mar.-Apr. 2019.
- [MA19b] J. Ma and Z. Q. Zhu, "Optimal split ratio in small high speed PM machines considering both stator and rotor limitations," *CES Trans. on Electrical Machines and Systems*, vol.3, no.1, pp.3-11, Apr. 2019.
- [MER15] M. Merdzan, J. J. H. Paulides, and E. A. Lomonova, "Comparative analysis of rotor losses in high-speed permanent magnet machines with different winding

configurations considering the influence of the inverter PWM," *International Conference Ecological Vehicles Renew. Energies (EVER)*, Monte Carlo, Monaco, 2015, pp. 1–8.

- [MIL16] J. Millinger, J. Soulard, and O. Wallmark, "Influence of shaft relative permeability on rotor losses in 2-pole slotless high-speed motor," *International Conference on Electrical Machines (ICEM)*, Lausanne, Switzerland, 2016, pp. 405-411.
- [MIR08] M. Mirzaei, and A. Binder, "Permanent magnet savings in high speed electrical motors," *International Symposium on Power Electronics, Electrical Drives, Automation and Motion (SPEEDAM)*, Ischia, Italy, 2008, pp. 1276-1281.
- [MLO15] A. Mlot, M. Lukaniszyn, and M. Korkosz, "Influence of an end-winding size on proximity losses in a high-speed PM synchronous motor," *Selected Problems of Electrical Engineering and Electronics (WZEE)*, Kielce, Poland, 2015, pp. 1-6.
- [MUL99] E. Muljadi, C. P. Butterfield, and Y. H. Wan, "Axial-flux modular permanent-magnet generator with a toroidal winding for wind-turbine applications," *IEEE Trans. Ind. Appl.*, vol. 35, no. 4, pp. 831–836, Jul.-Aug. 1999.
- [MUN10] G. Munteanu, A. Binder, T. Schneider, and B. Funieru, "No-load tests of a 40 kW high-speed bearingless permanent magnet synchronous motor," *International Symposium on Power Electronics, Electrical Drives, Automation and Motion (SPEEDAM)*, Pisa, Italy, 2010, pp. 1460-1465.
- [NIU12] S. Niu, S. L. Ho, W. N. Fu, and J. Zhu, "Eddy current reduction in high-speed machines and eddy current loss analysis with multislice time-stepping finite-element method," *IEEE Trans. Magn.*, vol. 48, no. 2, pp. 1007-1010, Feb. 2012.
- [NOG05] T. Noguchi, Y. Takata, Y. Yamashita, Y. Komatsu, and S. Ibaraki, "220000 r/min, 2kW PM motor drive for turbocharger," *IEEEJ Trans. on Ind. Appl.*, vol. 125, No. 9, pp. 854-861, Aug. 2005.
- [NOG09] T. Noguchi and T. Wada, "1.5-kW, 150,000-r/min ultra high-speed PM motor fed by 12-V power supply for automotive supercharger," *European*

Conference on Power Electronics and Applications (EPE), Barcelona, Spain, 2009, pp. 1-10.

- [OYA03] J. Oyama, T. Higuchi, T. Abe, K. Shigematsu, X. Yang, and E. Matsuo, "A trial production of small size ultra-high speed drive system," *IEEE International Electric Machines and Drives Conference (IEMDC)*, Madison, USA, 2003, pp. 31-36 vol. 1.
- [PAN06] Y. Pang, Z. Q. Zhu, and D. Howe, "Analytical determination of optimal split ratio for permanent magnet brushless motors," *IEE Proceedings Elec. Power Appl.*, vol. 153, no. 1, pp. 7-13, 1 Jan. 2006.
- [PAN14] Y. Pang and Z.Q. Zhu, "Reduction of unbalanced magnetic force in 2-pole 3-slot permanent magnet machine," *IET International Conference on Power Electronics Machines and Drives (PEMD)*, Manchester, UK, 2014, pp. 1-6.
- [PFI10] P. Pfister and Y. Perriard, "Very-high-speed slotless permanent-magnet motors: analytical modeling, optimization, design, and torque measurement methods," *IEEE Trans. Ind. Electron.*, vol. 57, no. 1, pp. 296-303, Jan. 2010.
- [POP13] M. Popescu and D. G. Dorrell, "Proximity losses in the windings of high speed brushless permanent magnet AC motors with single tooth windings and parallel paths," *IEEE Trans. Magn.*, vol. 49, no. 7, pp. 3913-3916, Jul. 2013.
- [REI13] T. Reichert, T. Nussbaumer, and J. W. Kolar, "Split ratio optimization for high-torque PM motors considering global and local thermal limitations," *IEEE Trans. Energy Convers.*, vol. 28, no. 3, pp. 493-501, Sept. 2013.
- [SCH17] M. Schuck, A. Da Silva Fernandes, D. Steinert, and J. W. Kolar, "A high speed millimeter-scale slotless bearingless slice motor," *International Electric Machines and Drives Conference (IEMDC)*, Miami, USA, 2017, pp. 1-7.
- [SCH97] N. Schofield, K. Ng, Z. Q. Zhu, and D. Howe, "Parasitic rotor losses in a brushless permanent magnet traction machine," *International Conference on Electrical Machines and Drives*, 1997, pp. 200-204.
- [SHA09] M. R. Shah and A. M. EL-Refaie, "Eddy-current loss minimization in conducting sleeves of surface PM machine rotors with fractional-slot

concentrated armature windings by optimal axial segmentation and copper cladding," *IEEE Trans. Ind. Appl.*, vol. 45, no. 2, pp. 720-728, Mar.-Apr. 2009.

- [SHE13] J. Shen, H. Hao, M. Jin, and C. Yuan, "Reduction of rotor eddy current loss in high speed pm brushless machines by grooving retaining sleeve," *IEEE Trans. Magn.*, vol. 49, no. 7, pp. 3973-3976, Jul. 2013.
- [SHE18] J. Shen, X. Qin, and Y. Wang, "High-speed permanent magnet electrical machines — applications, key issues and challenges," *CES Trans. on Electrical Machines and Systems*, vol. 2, no. 1, pp. 23-33, Mar. 2018.
- [SHI04] K. Shigematsu, J. Oyama, T. Higuchi, T. Abe, and Y. Ueno, "The study of eddy current in rotor and circuit coupling analysis for small size and ultra-high speed motor," *International Power Electronics and Motion Control Conference (IPEMC)*, Xi'an, China, 2004, pp. 275-279.
- [SNE18] S. Neethu, S. P. Nikam, S. Pal, A. K. Wankhede, and B. G. Fernandes, "Toroidal winding with fictitious slots for high speed permanent magnet synchronous motors," *IEEE International Conference on Industrial Technology (ICIT)*, Lyon, France, 2018, pp. 546-550.
- [SPO91] E. Spooner, B. J. Chalmers, M. M. El-Missiry, Wu Wei, and A. C. Renfrew, "Motoring performance of the toroidal permanent-magnet machine 'Torus'," *International Conference on Electrical Machines and Drives*, London, UK, 1991, pp. 36-40.
- [SPO96] E. Spooner, A. C. Williamson, and G. Catto, "Modular design of permanent-magnet generators for wind turbines," *IEE Proc. Elec. Power Appl.*, vol. 143, no. 5, pp. 388-395, Sep. 1996.
- [SPO96a] E. Spooner and A. Williamson, "Modular, permanent-magnet wind turbine generators," *Conf. Rec. IEEE Ind. Appl. Conf. 31st IAS Annu. Meeting*, Oct. 1996, pp. 497-502.
- [SPO98] E. Spooner and C. Williamson, "Electromagnetic machine with at least one pair concentric rings having modularized magnets and yokes," U.S. Patent 5 844 341, Dec. 1998.

- [SUZ16] M. Suzuki and K. Sakai, "Reduction of torque ripple for PM motor with toroidal winding," *International Conference on Electrical Machines and Systems (ICEMS)*, Chiba, Japan, 2016, pp. 1-6.
- [TAK94] I. Takahashi, T. Koganezawa, G. Su, and K. Ohyama, "A super high speed PM motor drive system by a quasi-current source inverter," *IEEE Trans. Ind. Appl.*, vol. 30, no. 3, pp. 683-690, May-Jun. 1994.
- [TEN14] A. Tenconi, S. Vaschetto, and A. Vigliani, "Electrical machines for high-speed applications: design considerations and tradeoffs," *IEEE Trans. Ind. Electron.*, vol. 61, no. 6, pp.3022-3029, Jun. 2014.
- [TOB99] A. Toba and T. A. Lipo, "Novel dual-excitation permanent magnet Vernier PM machine," *Conf. Rec. IEEE IAS Annu. Meeting*, 1999, pp. 2539–2544.
- [TUY15] A. Tüysüz, M. Steichen, C. Zwyssig, and J. W. Kolar, "Advanced cooling concepts for ultra-high-speed machines," *International Conference on Power Electronics and ECCE Asia (ICPE-ECCE Asia)*, Seoul, South Korea, 2015, pp. 2194-2202.
- [TUY17] A. Tüysüz, F. Meyer, M. Steichen, C. Zwyssig, and J. W. Kolar, "Advanced cooling methods for high-speed electrical machines," *IEEE Trans. Ind. Appl.*, vol. 53, no. 3, pp. 2077-2087, May-Jun. 2017.
- [UZH14] N. Uzhegov, J. Nerg, and J. Pyrhönen, "Design of 6-slot 2-pole high-speed permanent magnet synchronous machines with tooth-coil windings," *International Conference on Electrical Machines (ICEM)*, Berlin, Germany, 2014, pp. 2537-2542.
- [UZH16] N. Uzhegov, E. Kurvinen, J. Nerg, J. Pyrhönen, J. T. Sopenan, and S. Shirinskii, "Multidisciplinary design process of a 6-slot/2-pole high-speed permanent-magnet synchronous machine," *IEEE Trans. on Ind. Elec.*, vol. 63, no. 2, pp. 784-795, Feb. 2016.
- [VET15] M. Vetuschi and F. Cupertino, "Minimization of proximity losses in electrical machines with tooth-wound coils," *IEEE Trans. Ind. Appl.*, vol. 51, no. 4, pp. 3068-3076, Jul.-Aug. 2015.

- [VIL13] B. Virlan, S. Benelghali, A. Simion, L. Livadaru, R. Outbib, and A. Munteanu, "Induction motor with outer rotor and ring stator winding for multispeed applications," *IEEE Trans. Energy Convers.*, vol. 28, no. 4, pp. 999–1007, Dec. 2013.
- [VRA68] J. Vrancik, "Prediction of windage power loss in alternators," NASA Technical Note, 1968.
- [WAL09] O. Wallmark, P. Kjellqvist, and F. Meier, "Analysis of axial leakage in high-speed slotless PM motors for industrial hand tools," *IEEE Trans. Ind. Appl.*, vol. 45, no. 5, pp. 1815-1820, Sept.-Oct. 2009.
- [WAN03] F. Wang, M. Zong, W. Zheng, and E. Guan, "Design features of high speed PM machines," *International Conference on Electrical Machines and Systems (ICEMS)*, Beijing, China, 2003, pp. 66-70 vol. 1.
- [WAN09] F. Wang, D. Zhang, J. Xing, and Y. Xu, "Study on air friction loss of high speed PM machine," *IEEE International Conference on Industrial Technology (ICIT)*, Victoria, Australia, 2009, pp. 1-4.
- [WAN10a] K. Wang, M. J. Jin, J. X. Shen, and H. Hao, "Study on rotor structure with different magnet assembly in high-speed sensorless brushless DC motors," *Electric Power Applications, IET*, vol. 4, no. 4, pp. 241–248, Mar. 2010.
- [WAN10b] X. Wang, X. Zhang, S. Yan, X. Wang, and C. Zhang, "The analysis of high speed slotless permanent magnet brushless DC motor based on soft magnetic ferrite," *International Conference on Electrical Machines and Systems (ICEMS)*, Incheon, South Korea, 2010, pp. 1061-1064.
- [WAN18] Y. Wang, J. H. Feng, S. Y. Guo, Y. F. Li, Z. C. Che, Y. Wang, and Z. Q. Zhu, "Investigation of optimal split ratio for high-speed permanent-magnet brushless machines," *IEEE Trans. Magn.*, vol. 54, no. 11, pp. 1-5, Nov. 2018.
- [WAN20] Y. Wan, Q. Li, J. Guo, and S. Cui, "Thermal analysis of a Gramme-ring-winding high-speed permanent-magnet motor for pulsed alternator using CFD," *Electric Power Applications, IET*, vol. 14, no. 11, pp. 2202-2211, Jun. 2020.

- [WAN21] Y. Wang, Z. Q. Zhu, J. Feng, S. Guo, Y. Li, and Y. Wang, "Rotor stress analysis of high-speed permanent magnet machines with segmented magnets retained by carbon-fibre sleeve," *IEEE Trans. Energy Convers.*, vol. 36, no. 2, pp. 971-983, Jun. 2021.
- [WRO10] R. Wrobel, A. Mlot, and P. H. Mellor, "Investigation of end-winding proximity losses in electromagnetic devices," *International Conference on Electrical Machines (ICEM)*, Rome, Italy, 2010, pp. 1-6.
- [XIN10] J. Xing, F. Wang, T. Wang, and Y. Zhang, "Study on anti-demagnetization of magnet for high speed permanent magnet machine," *IEEE Trans. Appl. Supercond.*, vol. 20, no. 3, pp. 856-860, Jun. 2010.
- [XUE12] S. Xue, H. Xu, and C. Fang, "The effect of stator slot and air gap length on high speed brushless PM motor," *Proceedings of The 7th International Power Electronics and Motion Control Conference*, Harbin, China, 2012, pp. 281-285.
- [XU11] J. Xu and C. Liu, "Research on high-speed permanent magnet generator for a miniature turbojet," *IEEE Conference on Industrial Electronics and Applications*, Beijing, China, 2011, pp. 2783-2786.
- [XU12] G. Xu, L. Jian, W. Gong, and W. Zhao, "Quantitative comparison of flux modulated interior permanent magnet machines with distributed winding and concentrated windings," *Progr. Electromagn. Res.*, vol. 129, pp. 109–123, Jun. 2012.
- [XU20] F. Xu, T. R. He, Z. Q. Zhu, Y. Wang, S. Cai, H. Bin, D. Wu, L. M. Gong, and J. T. Chen, "Influence of slot number on electromagnetic performance of 2-pole high-speed permanent magnet motors with toroidal windings," *International Conference on Ecological Vehicles and Renewable Energies (EVER)*, Monte Carlo, Monaco, 2020, pp. 1-7.
- [XU21] F. Xu, T. R. He, Z. Q. Zhu, Y. Wang, S. Cai, H. Bin, D. Wu, L. M. Gong, and J. T. Chen, "Influence of slot number on electromagnetic performance of 2-

pole high-speed permanent magnet motors with toroidal windings," *IEEE Trans. Ind. Appl.*, vol. 57, no. 6, pp. 6023-6033, Nov.-Dec. 2021.

- [YAM09] K. Yamazaki, M. Shina, Y. Kanou, M. Miwa, and J. Hagiwara, "Effect of eddy current loss reduction by segmentation of magnets in synchronous motors: Difference between interior and surface types," *IEEE Trans. Magn.*, vol. 45, no. 10, pp. 4756-4959, Oct. 2009.
- [YAN12] G. Yan, R. Lin, and M. Jian, "Improvement on the core loss of high speed slotless PMSM motor and its measurement," *International Conference on Electrical Machines and Systems (ICEMS)*, Sapporo, Japan, 2012, pp. 1-4.
- [YON12] J. M. Yon, P. H. Mellor, R. Wrobel, J. D. Booker, and S. G. Burrow, "Analysis of semipermeable containment sleeve technology for high-speed permanent magnet machines," *IEEE Trans. Energy Convers.*, vol. 27, no. 3, pp. 646-653, Sept. 2012.
- [YOU08] D. You, S. Jang, J. Lee, and T. Sung, "Dynamic performance estimation of high-power fess using the operating torque of a PM synchronous motor/generator," *IEEE Trans. Magn.*, vol. 44, no. 11, pp. 4155-4158, Nov. 2008.
- [ZHA13] F. Zhang, S. Song, G. Du, and Y. Li, "Analysis of the 3D steady temperature field of MW high speed permanent magnet motor," *International Conference on Electrical Machines and Systems (ICEMS)*, Busan, South Korea, 2013, pp. 1351-1354
- [ZHA15] X. Zhang, W. Li, B. Kou, J. Cao, H. Cao, C. Gerada, and H. Zhang, "Electro-thermal combined optimization on notch in air-cooled high-speed permanent-magnet generator," *IEEE Trans. Magn.*, vol. 51, no. 1, pp. 1-10, Jan. 2015.
- [ZHA15a] F. Zhang, G. Du, T. Wang, G. Liu, and W. Cao, "Rotor retaining sleeve design for a 1.12-MW high-speed PM machine," *IEEE Trans. Ind. Appl.*, vol. 51, no. 5, pp. 3675-3685, Sept.-Oct. 2015.

- [ZHA15d] J. Zhang, W. Chen, X. Huang, Y. Fang, J. Zhang, J. Ma, and W. Cao, "Evaluation of applying retaining shield rotor for high-speed interior permanent magnet motors," *IEEE Trans. Magn.*, vol. 51, no. 3, pp. 1-4, Mar. 2015.
- [ZHA15e] X. Zhang, W. Li, B. Kou, J. Cao, H. Cao, C. Gerada, and H. Zhang, "Electrothermal combined optimization on notch in air-cooled high-speed permanent-magnet generator," *IEEE Trans. Magn.*, vol. 51, no. 1, pp. 1-10, Jan. 2014.
- [ZHA15h] H. Zhang, X. Zhang, C. Gerada, M. Galea, D. Gerada, and J. Li, "Design considerations for the tooth shoe shape for high-speed permanent magnet generators," *IEEE Trans. Magn.*, vol. 51, no. 11, pp. 1-4, Nov. 2015.
- [ZHA16a] F. Zhang, G. Du, T. Wang, F. Wang, W. Cao, and J. L. Kirtley, "Electromagnetic design and loss calculations of a 1.12-MW high-speed permanent-magnet motor for compressor applications," *IEEE Trans. Energy Convers.*, vol. 31, no. 1, pp. 132-140, Mar. 2016.
- [ZHA16c] X. Zhang, W. Li, H. Zhang, C. Gerada, M. Galea, and Jing Li, "Topology investigation on high speed PM generator with back wound windings," *International Symposium on Industrial Electronics (ISIE)*, Santa Clara, CA, 2016, pp. 234-239.
- [ZHA17a] Y. Zhang, S. McLoone, and W. Cao, "High speed permanent magnet motor design and power loss analysis," *IEEE Transportation Electrification Conference and Expo, Asia-Pacific (ITEC Asia-Pacific)*, Harbin, China, 2017, pp. 1-6.
- [ZHA17b] Y. Zhang, S. McLoone, W. Cao, F. Qiu, and C. Gerada, "Power loss and thermal analysis of a mw high-speed permanent magnet synchronous machine," *IEEE Trans. Energy Convers.*, vol. 32, no. 4, pp. 1468-1478, Dec. 2017.

- [ZHA18] W. Zhao, X. Wang, C. Gerada, H. Zhang, C. Liu, and Y. Wang, "Multi-physics and multi-objective optimization of a high speed PMSM for high performance applications," *IEEE Trans. Magn.*, vol. 54, no. 11, pp. 1-5, Nov. 2018.
- [ZHA21] F. Zhao, Z. Yu, J. Cao, and L. Li, "Design and optimization of a high-speed permanent magnet synchronous machine for gas compressors," *IEEE Trans. Magn.*, vol. 58, no. 2, pp. 1-5, Feb. 2022.
- [ZHE05] L. Zheng, T. X. Wu, D. Acharya, K. B. Sundaram, J. Vaidya, L. Zhao, L. Zhou, C. H. Ham, N. Arakere, J. Kapat, and L. Chow, "Design of a super high speed cryogenic permanent magnet motor," *IEEE Trans. Magn.*, vol. 41, no. 10, pp. 3823-3825, Oct. 2005.
- [ZHO06] F. Zhou, J. Shen, W. Fei, and R. Lin, "Study of retaining sleeve and conductive shield and their influence on rotor loss in high-speed PM BLDC motors," *IEEE Trans. Magn.*, vol. 42, no. 10, pp. 3398-3400, Oct. 2006.
- [ZHU01] Z. Q. Zhu, J. D. Ede, and D. Howe, "Design criteria for brushless dc motors for high-speed sensorless operation," *Int. J. Appl. Electromagn. Mech.*, vol. 15, pp. 79-87, 2001/2002.
- [ZHU01a] Z. Q. Zhu, K. B. Ng, N. Schofield, and D. Howe, "Analytical prediction of rotor eddy current loss in brushless machines equipped with surface-mounted permanent magnets. ii. accounting for eddy current reaction field," *Proceedings of the Fifth International Conference on Electrical Machines and Systems (ICEMS)*, Shenyang, China, 2001, pp. 806–809, vol.2.
- [ZHU04] Z. Q. Zhu, K. Ng, N. Schofield, and D. Howe, "Improved analytical modelling of rotor eddy current loss in brushless machines equipped with surface-mounted permanent magnets," *Electric Power Applications, IEE Proceedings*, vol. 151, no. 6, pp. 641–650, Nov. 2004.
- [ZHU06] Z. Q. Zhu, D. Ishak, and D. Howe, "Modular permanent magnet brushless machines having a fractional number of slots per pole - influence of stator teeth and back-iron," *International Conference on Electrical Machines and Systems (ICEMS)*, Nagasaki, Japan, 2006, pp. 1–4.

- [ZHU08] D. Zhu, X. Qiu, N. Zhou, and Y. Yan, "A comparative study of winding factors between distributed windings and non-overlapping concentrated windings," *International Conference on Electric Utility Deregulation and Restructuring and Power Technologies*, Nanjing, China, 2008, pp.2725-2729.
- [ZHU09] Z. Q. Zhu, "A simple method for measuring cogging torque in permanent magnet machines," *IEEE Power Energy Soc. General Meeting*, Calgary, AB, Canada, 2009, pp. 1–4.
- [ZHU12] Z. Q. Zhu, Z. Azar, and G. Ombach, "Influence of additional air gaps between stator segments on cogging torque of permanent-magnet machines having modular stators," *IEEE Trans. Magn.*, vol. 48, no. 6, pp. 2049–2055, Jun. 2012.
- [ZHU18] Z. Q. Zhu and Y. X. Li, "Modularity techniques in high performance permanent magnet machines and applications," *CES Trans. on Electrical Machines and Systems*, vol. 2, no. 1, pp. 93-103, Mar. 2018.
- [ZHU95] Z. Q. Zhu, D. Howe, and J. K. Mitchell, "Magnetic field analysis and inductances of brushless DC machines with surface-mounted magnets and non-overlapping stator windings," *IEEE Trans. Magn*, vol. 31, no. 3, pp. 2115-2118, May 1995.
- [ZHU97] Z. Q. Zhu, K. Ng, and D. Howe, "Design and analysis of high-speed brushless permanent magnet motors," *International Conference on Electrical Machines and Drives (Conf. Publ. No. 444)*, Cambridge, UK, 1997, pp. 381-385.
- [ZHU97] Z. Q. Zhu and D. Howe, "Winding inductances of brushless machines with surface-mounted magnets," *IEEE International Electric Machines and Drives Conference Record*, Milwaukee, WI, USA, 1997, pp. WB2/2.1-WB2/2.3.
- [ZWY05] C. Zwyssig, J. W. Kolar, W. Thaler, and M. Vohrer, "Design of a 100W, 500000 rpm permanent-magnet generator for mesoscale gas turbines," *IEEE Industry Applications Society Annual Meeting (IAS)*, Hong Kong, China, 2005, pp. 253–260.

APPENDIX I

PUBLICATION RESULTED FROM PHD STUDY

Journal Publication:

- [1] **F. Xu**, Z. Q. Zhu, T. R. He, Y. Wang, H. Bin, D. Wu, L. M. Gong, and J. T. Chen, "Influence of stator gap on electromagnetic performance of 6-slot/2-pole modular high speed permanent magnet motor with toroidal windings," *IEEE Access*, vol. 9, pp. 94470-94494, 2021.
- [2] **F. Xu**, T. R. He, Z. Q. Zhu, Y. Wang, S. Cai, H. Bin, D. Wu, L. M. Gong, and J. T. Chen, "Influence of slot number on electromagnetic performance of 2-pole high-speed permanent magnet motors with toroidal windings," *IEEE Trans. Ind. Appl.*, vol. 57, no. 6, pp. 6023-6033, Nov.-Dec. 2021.
- [3] T. R. He, Z. Q. Zhu, **F. Xu**, Y. Wang, H. Bin, and L. M. Gong, "Electromagnetic performance analysis of 6-slot/2-pole high-speed permanent magnet motors with coil-pitch of two slot-pitches," *IEEE Trans. Energy Convers.*, Nov. 2021.
- [4] T. R. He, Z. Q. Zhu, **F. Xu**, Hong Bin, Di Wu, Liming Gong, and Jintao Chen, "Comparative study of 6-slot/2-pole high-speed permanent magnet motors with different winding configurations," *IEEE Trans. Ind. Appl.*, vol.57, no.6, pp.5864-5875, Nov.-Dec. 2021.
- [5] T. R. He, Z. Q. Zhu, **F. Xu**, Y. Wang, H. Bin and L. M. Gong, "Influence of rotor eccentricity on electromagnetic performance of 2-pole/3-slot PM motors," *IEEE Trans. Energy Convers.*, vol. 37, no. 1, pp. 696-706, Mar. 2022.
- [6] **F. Xu**, T. R. He, Z. Q. Zhu, H. Bin, D. Wu, L. M. Gong, and J. T. Chen, "Split ratio optimization for 6-slot/2-pole high-speed permanent magnet motor with toroidal windings," to be submitted.

Conference Publications:

- [1] **F. Xu**, T. R. He, Z. Q. Zhu, Y. Wang, S. Cai, H. Bin, D. Wu, L. M. Gong, and J. T. Chen, "Influence of slot number on electromagnetic performance of 2-pole high-speed permanent magnet motors with toroidal windings," *2020 Fifteenth International*

Conference on Ecological Vehicles and Renewable Energies (EVER), Monte Carlo, Monaco, 2020, pp. 1-7.

- [2] T. R. He, Z. Q. Zhu, **F. Xu**, H. Bin, D. Wu, L. M. Gong, and J. T. Chen, “Comparison of 6-slot/2-pole High-Speed Permanent Magnet Motors with Different Winding Configurations,” *2020 Fifteenth International Conference on Ecological Vehicles and Renewable Energies (EVER)*, Monte Carlo, Monaco, 2020, pp. 1-8.
- [3] **F. Xu**, T. R. He, Z. Q. Zhu, H. Bin, D. Wu, L. M. Gong, and J. T. Chen, “Comparison of 2-pole slotted high-speed motors with toroidal and tooth-coil windings,” submitted to *2022 IEEE 5th International Electrical and Energy Conference (CIEEC2022)*/ Accepted.
- [4] **F. Xu**, T. R. He, Z. Q. Zhu, H. Bin, D. Wu, L. M. Gong, and J. T. Chen, “Comparison of slotted and slotless high-speed permanent magnet motors with toroidal windings,” submitted to *2022 IEEE Energy Conversion Congress and Exposition (ECCE 2022)*/ Under review
- [5] T. R. He, Z. Q. Zhu, **F. Xu**, H. Bin, D. Wu, L. M. Gong, and J. T. Chen, “Influence of circulating currents on electromagnetic performance of 6-slot/2-pole high-speed PM motors with rotor eccentricity,” submitted to *2022 IEEE Energy Conversion Congress and Exposition (ECCE 2022)*/ Under review.